Samuel I.C. Daminabo

Filament Fabrication and FDM 3D Printing of PLA/BioPBS-based Composite Materials for Advanced Sustainable Manufacturing Applications

School of Aerospace, Transport and Manufacturing (SATM)

PhD

Academic Year: 2019 - 2023

Supervisor: Dr Alex Skordos
Associate Supervisor: Dr Vijay Kumar Thakur
June 2023

School of Aerospace, Transport and Manufacturing (SATM)

PhD Production and Manufacturing Engineering

Academic Year 2019 - 2023

Samuel I.C. Daminabo

Filament Fabrication and FDM 3D Printing of PLA/BioPBS-based Composite Materials for Advanced Sustainable Manufacturing Applications

Supervisor: Dr Alex Skordos
Associate Supervisor: Dr Vijay Kumar Thakur
June 2023

© Cranfield University 2023. All rights reserved. No part of this publication may be reproduced without the written permission of the copyright owner.

ABSTRACT

With the limited range of commercially viable biobased and biodegradable filament materials available for fused deposition modelling (FDM)-based additive manufacturing (AM), this work aims to advance the knowledge and potential of sustainable polymer-based materials for 3D printing (3DP) applications. This work investigates polymer phase changes in 80 wt.% poly lactic acid (PLA)/20 wt.% biobased polybutylene succinate (BioPBS)-based blends after a direct or two-step filament fabrication process. 3DP filaments made of 80 wt.% PLA /20 wt.% BioPBS blends and their nanocomposites containing either hydrophilic bentonite nano clay (HbnC) or reduced graphene oxide (rGO) at 1 part per hundred resins (phr) are compared for polymer phase properties and rheological behaviour. Subsequently, 'Power law' and 'Arrhenius' models are combined to develop complex viscosity master-curves as a predictive model for each material formulation; while each fabricated filament is applied with developed 3D printing strategies to produce tensile and interlayer-bond test materials.

Findings show that between the two filament fabrication methods, the multi-step filament fabrication route causes a higher PLA phase crystallinity of about 27%. However, the multi-step processing route and inclusion of rGO in the PLA80/BioPBS20 material matrix increases PLA crystallinity to about 34%. Moreover, rGO is found to limit the recrystallization of the BioPBS phase. Furthermore, following a successful development of complex viscosity master curve models for PLA80/BioPBS20-based formulations, tensile-fractured 3D-printed parts were also found to show an improved compatibilization of the immiscible PLA and BioPBS phases upon addition of either nanomaterial, hence offering a promising outlook for the use of PLA80/BioPBS20-based materials for sustainable and multifunctional part productions.

Keywords: 3D printing, biocomposites, melt-processing, crystallinity, viscosity, tensile, mechanical, multifunctional.

ACKNOWLEDGEMENTS

I would like to highly acknowledge my project supervisors, Dr Alex Skordos and Dr Vijay Kumar Thakur, who have contributed most significantly to my professional development while also contributing to the thesis project development, project management, extensive technical discussions and project delivery with integrity and commitment.

Further acknowledgements go to the academic and technical staff at Cranfield University's Department of Manufacturing and Materials in their efforts to support my individual project plans between June 2019 and June 2023; most especially as the COVID19 pandemic created significant disruptions and uncertainties around the project. Huge acknowledgements go to Mr Jim Hurley, Dr David Ayre, Mr Lukasz Zak Rzewski, Mr Krutarth Jani, Mr Ben Hopper, Dr Andrea Giampiccolo, Dr Diane Johnson, Mr Steve Pope, Miss Christine Kimpton, Mr Çağhan Tuncer, and Mr Kristopher Bramley for their contributions to my professional and technical development, and for facilitating my experimental research campaigns and result analyses.

To my family, friends, and loved ones who have also played crucial parts in supporting my progress and personal development, I would love to take this opportunity to acknowledge their support, understanding, care, and motivation in my pursuit to contribute insights and knowledge that would facilitate the adoption of sustainable AM materials and technologies.

In all, I would also like to acknowledge the efforts of the wider Cranfield University network; for its role in developing future leaders in the fields of science, engineering, design, technology, and management. Thank you.

TABLE OF CONTENTS

ABSTRACT i
ACKNOWLEDGEMENTS iii
LIST OF FIGURES viii
LIST OF TABLES xiv
LIST OF EQUATIONS xvi
LIST OF ABBREVIATIONS xvii
1 Introduction 1
1.1 Motivation 1
1.1.1 Development multifunctional material systems 2
1.1.2 Achieving sustainable development goals (SDGs) 3
1.2 Aims and objectives. 6
1.3 Thesis structure 7
2 Literature review 9
2.1 Introduction 9
2.2 Heat-assisted extrusion-based AM using thermoplastic-based materials. 9
2.3 FDM: The underlying technique for extrusion-based 3DP 12
2.3.1 FDM 3DP machines and developments 12
2.3.2 Factors Affecting the FDM process: CAM, FDM 3DP Machine, and Material Resources 16
2.3.3 Potential limitations in FDM-based 3D-printed parts 23
2.4 Commercially available thermoplastic-based materials for FDM-based AM 24
2.5 Bio-based thermoplastics and composites for FDM-based AM 26
2.5.1 PLA-based materials for FDM-based AM 27
2.5.2 State of the art research on PLA-based composites for FDM-based AM applications 27
2.6 Summary of literature review 40
3 Project methodology 43
3.1 Materials 43
3.1.1 Filament formulations and nomenclature 43
3.1.2 Pre-processing conditioning 44
3.1.3 Filament fabrication of PLA80/BioPBS20-based composites 45
3.2 Experimental plan 48
3.3 Fabrication of 3D-printed and cast parts. 52
3.3.1 FDM-based 3DP of dog-bone parts 52
3.3.2 Casting of PLA/BioPBS-based cylindrical plates for rheometric testing 56
3.4 Material and fabricated filament characterization and part testing 57

3.4.1 Thermogravimetric analysis (TGA) of materials and fabricated filaments 57
3.4.2 Differential scanning calorimetry (DSC) of materials and fabricated filaments 57
3.4.3 Scanning electron microscopy (SEM) and energy dissipative x-ray spectroscopy (EDS) of materials and fabricated filaments 59
3.4.4 Rotational rheometric testing of cast PLA80/BioPBS20-based cylindrical plates. 60
3.4.5 Tensile property and interlayer strength testing of 3D-printed parts using ISO 527-2/1BA standard 63
4 Thermodynamic properties and phase changes in fabricated biopolymer composite filaments 65
4.1 Introduction 65
4.2 Thermodynamic behaviour of thermoplastic polymers 65
4.2.1 Thermal degradation results of received thermoplastic polymers under nitrogen-rich and air-rich atmospheres 65
4.2.2 Calorimetric transitions and phase change behaviour of received thermoplastic biopolymers 68
4.3 Calorimetric results of biopolymer phases in fabricated composite filaments 70
4.3.1 Calorimetric results of biopolymer phases in fabricated composite filaments produced using direct filament fabrication route. 71
4.3.2 Calorimetric properties of biopolymer phases in fabricated composite filaments produced using MB-FE filament fabrication route. 72
4.3.3 Calorimetric properties of PLA and BioPBS phases in fabricated composite filaments 76
4.4 Recrystallization of biopolymer phases in the fabricated composite blends and nanocomposite filaments 82
4.5 Concluding remarks 85
5 Microscopic and rheological properties of fabricated composite formulations 88
5.1 Introduction 88
5.2 SEM results of the cross-sectional surface area of fabricated and cryo-fractured filament formulations 88
5.2.1 Cross-sectional microscopic results for composite blend filament 88
5.2.2 Cross-sectional microscopic results for composite filament containing HbnC 90
5.2.3 Cross-sectional microscopic results for composite filaments containing rGO. 91
5.3 Rheological characterization of fabricated filament formulations under FDM-based 3DP conditions. 95

5.3.1 Complex viscosity and viscoelastic behaviour of cast cylindrical plates made from fabricated filament formulations. 95
5.3.2 Determination of complex viscosity values using master curves and true shear frequency values 105
5.4 Concluding remarks 116
6 Printability, tensile mechanical properties, and fractured surface assessment of composite parts. 118
6.1 Introduction 118
6.2 Printability of dog-bone specimens using fabricated blend and nanocomposite filaments. 118
6.2.1 Challenges in 3DP of dog-bone parts using blends and nanocomposite filament formulations. 118
6.3 Tensile mechanical properties of 3D-pinted parts 122
6.3.1 Tensile modulus of 3D-printed parts 122
6.3.2 Ultimate tensile strength of 3D-printed parts 125
6.3.3 Strain at failure of printed parts 127
6.4 Fracture surface assessment of horizontally oriented 3D-printed parts. 130
6.4.1 Fracture surfaces of 3D-printed parts from Strategy 1 130
6.4.2 Fracture surfaces of 3D-printed parts from Strategy 2 133
6.4.3 Fracture surfaces of 3D-printed parts from Strategy 3 136
6.4.4 Fracture surfaces of 3D-printed parts from Strategy 4 141
6.4.5 Main findings for tensile mechanical and fracture surface results of 3D-printed parts 145
6.5 Interlayer mechanical properties of vertically oriented 3D-printed parts. 146
6.6 Concluding remarks 150
7 Overall discussion 152
7.1 Introduction 152
7.2 Discussion of findings and limitations 152
7.2.1 Effects of filament fabrication route and nanomaterial additions on BioPBS phase crystallinity 152
7.2.2 Complex viscosity of the composite formulations 153
7.2.3 Printability, tensile mechanical and interlayer bond properties of the biopolymer composites 155
7.2.4 Limitations of the study 157
7.3 Impact 158
8 Conclusions and Recommendations 161
8.1 Conclusions 161
8.2. Recommendations for future work 162
9 References 164
Appendix A 182
Appendix B 186

LIST OF FIGURES

Figure 1-1 Achieving multifunctional 3D-printed composite products (reproduced with permission from [23])..... 2

Figure 1-2 Industries utilizing AM technologies. Adapted from [6]..... 4

Figure 2-1 Hot-melt extrusion machine used in fabrication of single and composite filament materials. Reprinted with permission from [44]. 10

Figure 2-2 Cross sectional view of single and twin-screw extrusion machines. Adapted with permission from [45]. 10

Figure 2-3 Material properties to consider upon extrusion-based AM of structures and parts (Reprinted with permission from [10]). 11

Figure 2-4 Typical FDM machine design with a printed part on an immovable print bed/hot plate (Reprinted with permission from [57]). 13

Figure 2-5 Important aspects in material flow during an FDM process (Reprinted with permission from [51])..... 13

Figure 2-6 Development of FDM for advanced 3DP fabrication capabilities [39]. 14

Figure 2-7 shows a raster of parallel roads deposited to form a layer. Also shows the raster angle of relative roads in a rectilinear road pattern Reprinted with permission from [51]). 20

Figure 2-8 Important stages of an extrusion-based 3DP process..... 21

Figure 2-9 (a) Complex viscosities of PLA/BioPBS (70/30) blends as a function of angular frequency; (b) FDM-Printed dog-bone specimen printed at 220 °C , using PLA/BioPBS (70/30) filament formulation showing delamination, and (c) FDM-Printed dog-bone specimen printed (reprinted with permission from [138]..... 38

Figure 3-1 Filabot EX2 equipped with a set of cooling fans, diameter measuring device, and filament winder and spooling unit. 45

Figure 3-2 Twin-screw extrusion setup for production of PLA80/BioPBS20-based blend and composites..... 46

Figure 3-3 Material formulations and processing routes for filament fabrication and FDM-based 3DP. 47

Figure 3-4 ISO 527-2/1BA tensile-testing standard - for horizontally and vertically oriented specimens. Reprinted from [147]. 52

Figure 3-5 Set up of horizontally oriented specimens for FDM-based 3DP of dog-bone parts as seen from top view of Cura software..... 54

Figure 3-6 Vertically oriented dog-bone part setup for FDM-based 3DP using Any Cubic Chiron. 55

Figure 3-7 Tooling components (left) and final setup (right) for casting of PLA80/BioPBS20-based cylindrical plates. 56

Figure 3-8 As-fabricated cylindrical plates for use in the rheological characterisation of designated filament material formulations 57

Figure 3-9 Representative DSC curve for PLA material showing calorimetric profile obtained during heating and cooling cycles at a rate of 10 °C/min. 58

Figure 3-10 Tensile mechanical testing machine setup using laser extensometer. 64

Figure 4-1 Degradation profile of as-R PLA and as-R BioPBS polymers under nitrogen-rich and air-rich atmosphere using a heating rate of 10 °C/min. .. 66

Figure 4-2 1st heating scan curve for as-R PLA and as-R BioPBS - showing glass, cold crystallisation and melting transitions. 69

Figure 4-3 1st Heating curve for PLA80/BioPBS20 FE filament - showing heat flow against temperature profile. 71

Figure 4-4 1st Heating curve for PLA80/BioPBS20 MB-FE filament - showing heat-flow against temperature profile. 73

Figure 4-5 1st heating scan of fabricated PLA80/BioPBS20/HbnC1 MC-FE filament. 77

Figure 4-6 Heat-flow/Temperature of fabricated PLA80/BioPBS20/rGO1 (MB-FE) filament. 80

Figure 4-7 Calorimetric profile of PLA80/BioPBS20 FE, PLA80/BioPBS20 MB-FE, PLA80/BioPBS20/HbnC1 MC-FE, and PLA80/BioPBS20/rGO1 MC-FE filaments. 83

Figure 4-8 Percentage crystallinity of the PLA and BioPBS phases in the fabricated PLA80/BioPBS20-based blends and nanocomposite filaments. 87

Figure 5-1 SEM results of fabricated and cryo-fractured filaments of PLA80/BioPBS20 composites showing cross-sectional surface for: (a) PLA80/BioPBS20 FE; (b) PLA80/BioPBS20 MB-FE. 89

Figure 5-2 SEM image of fabricated and cryo-fractured PLA80/BioPBS20/HbnC1 filament showing cross-sectional surface features. 90

Figure 5-3 EDS results showing elemental dispersions for carbon (a), aluminium (b), oxygen (c), and calcium (d) - on the cross-sectional surface of the PLA80/BioPBS20/HbnC1 filament material in Figure 5-2. 91

Figure 5-4 Microscopic images at 20 µm (a) and 10 µm resolutions (b): of the cross-sectional surface of the PLA80/BioPB20/hbnC1 filament. 92

Figure 5-5 Fabricated PLA80/bioPBS20/rGO1 filament showing: possible rGO platelet and degrading regions (a), embedded rGO platelet (b), dispersed rGO platelets (c), more electron voltage-induced degradation (d), and limitedly-exfoliated graphitic structures (e). 94

Figure 5-6 Log-log plot of complex viscosity against angular shear frequency for the cast PLA80/BioPBS20 blend formulation. 97

Figure 5-7 Log-log plot of complex viscosity against angular frequency for the cast PLA80/BioPBS20/HbnC1 composite formulation. 98

Figure 5-8 log-log plot of complex viscosity against angular frequency for the cast PLA80/BioPBS20/rGO1 composite formulation. 100

Figure 5-9 log-log plot of storage modulus against angular frequency for the cast PLA80/BioPBS20 blend formulation. 101

Figure 5-10 Log-log plot of loss modulus against angular frequency for the cast PLA80/BioPBS20 blend formulation. 102

Figure 5-11 log-log plot of storage modulus against angular frequency for the cast PLA80/BioPBS20/HbnC1 composite formulation. 103

Figure 5-12 log-log plot of loss modulus against angular frequency for the Cast PLA80/BioPBS20/HbnC1 composite formulation. 103

Figure 5-13 log-log plot of storage modulus against angular frequency for the cast PLA80/BioPBS20/rGO1 composite formulation. 104

Figure 5-14 log-log plot of loss modulus against angular frequency for the cast PLA80/BioPBS20/rGO1 composite formulation. 104

Figure 5-15 Comparing power law parameter for PLA80/BioPBS-based formulation at 210 °C, 220 °C and 230 °C. 107

Figure 5-16 Shift factor (a_T) against inverse temperature(1/T) for PLA80/BioPBS20-based formulations at reference temperature of 220 °C. 112

Figure 5-17 Comparing master curves for the PLA80/BioPBS20-based formulations at 220 °C. 114

Figure 5-18 Complex viscosity of PLA80/BioPBS20-based formulations at 220 °C. 116

Figure 6-1 Delamination and warping effects shown by PLA80/BioPBS20 blends during 3DP of horizontally oriented dog-bone parts. 120

Figure 6-2 Effective printer-bed adhesion shown by PLA80/BioPBS20/HbnC1 MC-FE filament material but with stringing behaviour. 120

Figure 6-3 Stringing effect shown by nano clay-containing filament formulation during FDM-based 3DP of vertically oriented dog-bone parts. 121

Figure 6-4 Average tensile modulus for each 3DP strategy. 123

Figure 6-5 Average UTS for each 3DP strategy. 126

Figure 6-6 Average strain at failure for each 3DP strategy. 128

Figure 6-7 Representative tensile mechanical response of PLA and PLA80/BioPBS20-based blends and composites using 3DP strategy 1.. 130

Figure 6-8 Secondary electron (left) and back-scattered (right) SEM images of representative tensile-fractured surfaces of 3D-printed composite parts produced using 3DP strategy 1; for PLA100 FE-3DP (a and a')..... 131

Figure 6-9 Secondary electron (left) and back-scattered (right) SEM images of tensile-fractured surfaces of 3D-printed composite parts produced using 3DP strategy 1; for PLA80/BioPBS20 FE-3DP (a and a'), PLA80/BioPBS20 MB-FE-3DP (b and b')..... 132

Figure 6-10 Secondary electron (left) and back-scattered (right) SEM images of tensile-fractured surfaces of 3D-printed composite parts produced using 3DP strategy 1; for PLA80/BioPBS20/HbnC1 MC-FE-3DP (a and a'), and PLA80/BioPBS20/rGO1 MC-FE-3DP (b and b'). 133

Figure 6-11 Secondary electron (left) and back-scattered (right) SEM images of representative tensile-fractured surfaces of 3D-printed composite parts produced using 3DP strategy 2; for PLA100 FE-3DP (a and a')..... 134

Figure 6-12 Secondary electron (left) and back-scattered (right) SEM images of tensile-fractured surfaces of 3D-printed composite parts produced using 3DP strategy 2; for PLA80/BioPBS20 FE-3DP (a and a'), PLA80/BioPBS20 MB-FE-3DP (b and b')..... 135

Figure 6-13 Secondary electron (left) and back-scattered (right) SEM images of tensile-fractured surfaces of 3D-printed composite parts produced using 3DP strategy 2; for PLA80/BioPBS20/HbnC1 MC-FE-3DP (a and a'), and PLA80/BioPBS20/rGO1 MC-FE-3DP (b and b'). 136

Figure 6-14 Secondary electron (left) and back-scattered (right) SEM images of representative tensile-fractured surfaces of 3D-printed composite parts produced using 3DP strategy 3; for PLA100 FE-3DP (a and a')..... 137

Figure 6-15 Secondary electron (left) and back-scattered (right) SEM images of tensile-fractured surfaces of 3D-printed composite parts produced using 3DP strategy 3; for PLA80/BioPBS20 FE-3DP (a and a'), PLA80/BioPBS20 MB-FE-3DP (b and b')..... 139

Figure 6-16 Secondary electron (left) and back-scattered (right) SEM images of tensile-fractured surfaces of 3D-printed composite parts produced using 3DP strategy 3; for PLA80/BioPBS20/HbnC1 MC-FE-3DP (a and a'), and PLA80/BioPBS20/rGO1 MC-FE-3DP (b and b') 140

Figure 6-17 Secondary electron (left) and back-scattered (right) SEM images of representative tensile-fractured surfaces of 3D-printed composite parts produced using 3DP strategy 4; for PLA100 FE-3DP (a and a')..... 141

Figure 6-18 Secondary electron (left) and back-scattered (right) SEM images of tensile-fractured surfaces of 3D-printed composite parts produced using 3DP strategy 4; for PLA80/BioPBS20 FE-3DP (a and a'), PLA80/BioPBS20 MB-FE-3DP (b and b')..... 142

Figure 6-19 Secondary electron (left) and back-scattered (right) SEM images of tensile-fractured surfaces of 3D-printed composite parts produced using 3DP strategy 4; for PLA80/BioPBS20/HbnC1 MC-FE (a and a'), and PLA80/BioPBS20/rGO1 MC-FE (b and b') 143

Figure 6-20 Tensile modulus of vertically oriented PLA100 FE-3DP, PLA80/BioPBS20 and PLA80/BioPBS20/HbnC1 MC-FE-3DP parts. 147

Figure 6-21 UTS strength of vertically oriented PLA100 FE-3DP, PLA80/BioPBS20 and PLA80/BioPBS20/HbnC1 MC-FE-3DP parts. 148

Figure 6-22 UTS Strain at failure of vertically oriented PLA100 FE-3DP, PLA80/BioPBS20 and PLA80/BioPBS20/HbnC1 MC-FE-3DP parts. 148

Figure 6-23 Stress-strain curve for vertically oriented PLA and PLA80/BioPBS-based parts. 150

Figure 9-1 A.1 Log-log plots of angular shear rate against true viscosity for the fabricated composite at 210 °C..... 182

Figure 9-2 Log-log plots of angular shear rate against true viscosity for the fabricated composite at 210 °C..... 182

Figure 9-3 Log-log plots of angular shear rate against true viscosity for the fabricated composite at 210 °C..... 183

Figure 9-4 A.2 Log-log plots of angular shear rate against true viscosity for the fabricated composites at 220 °C. 183

Figure 9-5 Log-log plots of angular shear rate against true viscosity for the fabricated composites at 220 °C. 184

Figure 9-6 Log-log plots of angular shear rate against true viscosity for the fabricated composites at 220 °C. 184

Figure 9-7 Log-log plots of angular shear rate against viscosity for the fabricated composites at 230 °C. 185

Figure 9-8 Log-log plots of angular shear rate against viscosity for the fabricated composites at 230 °C. 185

Figure 9-9 Log-log plots of angular shear rate against true viscosity for the fabricated composites at 230 °C. 186

Figure 9-10 Tensile modulus of 3D-printed parts (by material category)..... 186

Figure 9-11 UTS of 3D-printed parts (by material category)..... 187
Figure 9-12 Strain at failure of 3D-printed parts (by material category)..... 187

LIST OF TABLES

Table 2-1 Important resource factors and key aspects of extrusion (FDM-based) 3DP process [6][10][48][62] 17

Table 2-2 Standard thermoplastics and typical tensile mechanical properties of 3D-printed and injection moulded materials..... 25

Table 2-3 Properties of PLA and BioPBS from suppliers [129], [130]..... 31

Table 2-4 Reported parametric conditions used for filament fabrication and FDM 3DP' of PLA/PBS (or BioPBS)-based composites [52], [138]. 37

Table 2-5 PLA/BioPBS formulations with corresponding results of their injection moulded [52] and 3D-printed [113] part's mechanical properties..... 38

Table 2-6 Existing information on Interlayer strength of PLA/BioPBS-based parts (using specific 3DP strategy) [52] 40

Table 3-1 Experimental research plan for fabrication of composite filaments. . 49

Table 3-2 Nomenclature for neat as-R materials, extruded filaments, and 3D-printed parts either used or fabricated at different experimental stages. ... 51

Table 3-3 Specifications of specimen dimensions based on ISO 527-2/1BA shown in Figure 3-3. 53

Table 3-4 Constant controls set for all FDM-based 3DP. 54

Table 3-5 Systematically developed parametric controls for assessing the effect of 3DP strategies on horizontally oriented 3D-printed dog-bone parts, (PT: Print Temperature, PS: Print Speed, and LH: Layer Height). 55

Table 3-6 3DP strategies for vertically oriented parts. 56

Table 4-1 Degradation metrics for as-R PLA and as-R BioPBS polymers under nitrogen-rich and air-rich atmospheres. 67

Table 4-2 DSC results from 1st heating scan of as-R PLA and as-R BioPBS polymers. Analysed using TRIOS Software. 70

Table 4-3 DSC results from 1st heating scan of fabricated PLA80/BioPBS20 composite filament processed via FE. 72

Table 4-4 DSC (Heat flow) results of 1st heating cycle of fabricated PLA/BioPBS20 composite filament processed via MB-FE..... 75

Table 4-5 DSC results from first heating scan of the fabricated PLA/BioPBS20/HbnC1 MC-FE filament..... 78

Table 4-6 Results from first DSC heating scan of fabricated PLA/BioPBS20/rGO1 (MC-FE) filament. 81

Table 4-7 Deduced information on the exothermic recrystallization transitions of the BioPBS phases in the fabricated filaments. 84

Table 5-1 Power law parameters for each filament material formulation at selected test temperatures 106

Table 5-2 Estimated shear rate and power law-corrected angular frequency occurring for 3DP at 220 °C for PLA80/BioPBS20 formulation. 108

Table 5-3 Estimated shear rate and power law-corrected angular frequency occurring for 3DP at 220 °C for PLA80/BioPBS20/HbnC1 formulation. ... 108

Table 5-4 Estimated shear rate and power law-corrected angular frequency occurring for 3DP at 220 °C for PLA80/BioPBS20/rGO1 formulation. 108

Table 5-5 Horizontal shift factor and activation energy of PLA80/BioPBS20-based formulation at 220 °C 110

Table 6-1 Average tensile modulus (MPa) and standard deviation in brackets obtained for 3D-printed parts using selected 3DP Strategies. 123

Table 6-2 Average UTS (MPa) and standard deviation in brackets of 3D-printed parts obtained using selected 3DP Strategies. 126

Table 6-3 Average strain at failure of 3D-printed parts obtained using selected 3DP Strategies. 128

Table 6-4 Impressions of the effects of material and 3DP strategy on nature of fracture, void content, and interlayer bonding results 144

Table 7-1 Comparative results of the tensile mechanical properties of injection moulded parts [52] and horizontally oriented 3D-printed dog-bone parts [138] obtained from different research works. 156

LIST OF EQUATIONS

Equation 3-1 59
Equation 3-2 60
Equation 3-3 60
Equation 3-4 61
Equation 3-5 61
Equation 3-6 61
Equation 3-7 62
Equation 3-8 62
Equation 3-9 62
Equation 3-10 62
Equation 3-11 63
Equation 5-1 106
Equation 5-2 109

LIST OF ABBREVIATIONS

3D	3-dimensional
3DP	3D printing
AM	Additive manufacturing
ABS	Acrylonitrile butadiene styrene
ABSi	Acrylonitrile butadiene styrene
ABSplus	Acrylonitrile butadiene styrene-plus
As-R	As received
ASA	Acrylonitrile styrene
ASTM	American society of testing materials
BAAM	Big area additive manufacturing
BioPBS	Bio-based poly butylene succinate
MFMS	Multi-functional material Systems
ISO	International Organization for Standardization
FDM	Fused deposition modelling
CAM	Computer aided manufacturing
CAD	Computer aided design
CF	Carbon fibre
cFF	Continuous flax fibre
CLTE	Coefficient of linear thermal expansion
CNC	Computer numerical control
CNTs	Carbon nano tubes
CT	Computed tomography
DSC	Differential scanning calorimetry
EPO	Epoxidized palm oil
EDS	Energy dissipative x-ray spectroscopy
ESD7	Electro-static dissipative-7
ETC	Environmental temperature chamber
FE	Filament extrusion
FFF	Fused filament fabrication
FLM	Fused layer manufacturing
FRPs	Fibre reinforced polymers
GnPs	Graphene nano platelets

HbnC	Hydrophilic bentonite nano clay
HIPS	High impact poly styrene
LEV	Local exhaust ventilation
LLC	Limited liability company
MB	Melt blending
MC	Melt compounding
MRI	Magnetic resonance imaging
PA	Poly amide
PBS	Poly butylene succinate
PC	Poly carbonate
PLA	Poly lactic acid
PLLA	Poly l-lactic acid
PPSF	Poly phenyl sulfone
PC/ABS	Polycarbonate/Acrylonitrile butadiene styrene
PEG	Polyethylene glycol
PBSL	Poly butylene succinate co-lactate
PHB	Poly hydroxy butyrate
PBAT	Poly butylene co-adipate co-terephthalate
phr	Parts per hundred resins
rGO	Reduced graphene oxide
SEM	Scanning electron microscopy
TFC	Twice functionalized clay
TGA	Thermogravimetric analysis
TiO_2	Titanium dioxide
TPU	Thermoplastic urethane
TTSP	Time-temperature superposition principle
VFR	Volumetric flow rate
XRD	X-ray diffraction

1 Introduction

1.1 Motivation

The paradigm of additive manufacturing (AM) that is commonly referred to as rapid prototyping (RP) or free-form fabrication is governed by a set of 3D printing (3DP) technologies that use a layer-by-layer approach to build parts or products either top-down or bottom-up. Importantly, 3DP technologies do not require a mould tool unlike in formative-manufacturing technology; and offer near-net-shape manufacturing in a relatively short period of time, usually with the aid of digital information and technology systems, which contributes to more robust and decentralized manufacturing systems. Commercially, AM or 3DP projects usually involve very small to medium-size batch production of complex and tailored geometries that are more costly and time-consuming to produce otherwise [1]–[13]. Such beneficial characteristics have been identified to be most relevant in the biomedical industry, and furthermore in the aerospace, construction, automotive, food, and healthcare industries, where customization is highly desirable [1]–[4], [6]–[14].

Polymer-based composite manufacturing is driving state of the art research into advanced polymer-based composites for traditional and additive manufacturing systems in pursuit of more advanced manufacturing applications [15]–[17]. Meanwhile, improved metrological methods [18] have created more opportunities for exploring material system properties and potential applications; particularly for research and development in nanomaterials, biopolymers, and biopolymer composites [7],[15]. Such capabilities are advancing the growth of multifunctional material systems (MFMSs), which form an advanced class of material systems that includes polymer composites (i.e. polymer blends and reinforced polymer-matrix composites), and has emerged as a promising area for driving product developments that meet the eco-sustainable, application-specific, high-performance requirements of global supply chains in the light of rising population demands and toughening environmental regulations (ISO 14001) - including bans on single use plastics [19],[20]. This therefore presents the challenge of limiting waste generation with the aid of 3DP technologies; and choosing constituent

materials that improve manufacturing process efficiency and effectiveness, part/product functionality, product performance, and process/product circularity [21].

1.1.1 Development multifunctional material systems

Multifunctional material systems (MFMSs) are material or products with multiple functionalities, which help to create more autonomous systems [22] and allow savings in the number of parts or amount of material required for addressing operational needs. Such a capability of MFMSs can therefore help manufacturers improve inefficient transformational operations that usually have corresponding time and cost-resource implications. The effective multifunctional capabilities of a material, composite and/or structure, should therefore enable the elimination of inefficient/ineffective product components like connectors and bulky units, thereby leading to significant weight and size savings for improved system-level efficiency. Figure 1-1 portrays the idea of using tailored 3D-printed polymer-based composites for delivering multi-functionality in products.

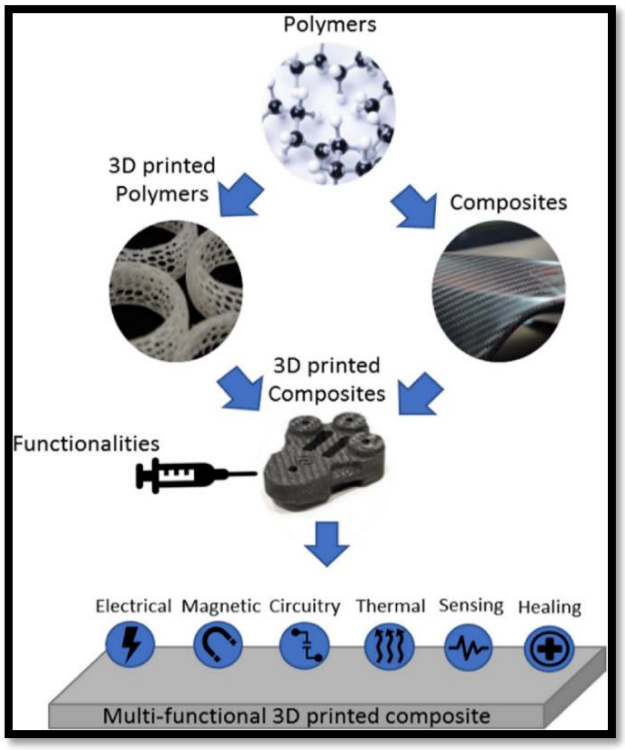

Figure 1-1 Achieving multifunctional 3D-printed composite products (reproduced with permission from [23])

The multifunctionality of a part/product is theoretically achievable in cases where constituting material phases and structural component behaviour and interactions lead to physical and chemical properties or responses that deliver a range of useful functionalities for the end user [21][22]. With such possibilities, there has been an increasing demand by industry to harness more functional and sustainable materials as candidates for future AM processes [24][25], especially as AM techniques have primarily been used for applications that do not require a high level of part functionality and/or performance [27]; like in prototypes, toys, and fixtures. Broadening the processability and functional applicability of AM materials and technologies through optimized material design, part design and/or process design remains a goal for industrial fabrication and manufacturing [11] [28]. Such developments are therefore critical for the effective realization of the next industrial revolutions (industry 4.0 & 5.0) [29]; often characterized by increased automation and collaboration between information technology and manufacturing/product systems. Consequently and critically, there has also been a rising interest in software development for data protection and security within AM/3DP systems [30]–[32], which indicates the growing level of cybersecurity risks associated with more digitally-enabled manufacturing processes and systems; one that must be tackled appropriately for the protection of intellectual property within and amongst businesses, organizations, and governments.

1.1.2 Achieving sustainable development goals (SDGs)

The International Organization for Standardization (ISO)/American Society for Testing and Materials (ASTM) 52900:2015 identify that there are 7 main categories of AM/3DP techniques available [9][27][33], i.e., material extrusion, under which this work falls via the fused deposition modelling (FDM) technology; material jetting; binder jetting; sheet lamination; vat photo polymerisation; powder bed fusion; and direct energy deposition. Consistently, these AM/3DP techniques show the capability of offering design freedom for mass product customization, waste minimization for lower environmental footprint, and decentralized rapid prototyping or manufacturing processes that can support the growth of more sustainable business and supply chain models. Consequently, the development

of AM and 3DP technologies has created opportunities for improved design, production, and end-product functionality that may help with moving effectively towards global sustainable development goals (SDGs); a factor that is expected to affect the choice of products and services with attractive market potential. It is highly relevant because, globally, at least 350 million tons of plastics are consumed per annum [34], which creates an increasing concern for their disposal, environmental contamination, and eco-toxicity, thereby driving the development of bio-based and biodegradable polymer material systems, most especially as polymers play an innovative and integral role in the manufacturing of energy efficient products and systems. Figure 1-2 highlights the global proportion of industries utilizing AM technologies, and it suggests that the medical/dental, consumer products/electronics, industrial machines, aerospace, and automotive industrial sectors form the majority AM technology users through which blue-ocean manufacturing strategies can be developed for more innovative business models. Specifically, material extrusion-based AM techniques have shown the best capability for processing a variety of materials. This category of AM technology uses polymers, hydrogels, cementitious mixtures, bio-inks, and polymer composites for 3DP [36] [37], which highlights a strong advantage over other 3DP techniques; one that will ensure that extrusion-based AM maintains strong relevance in the field of sustainable research developments.

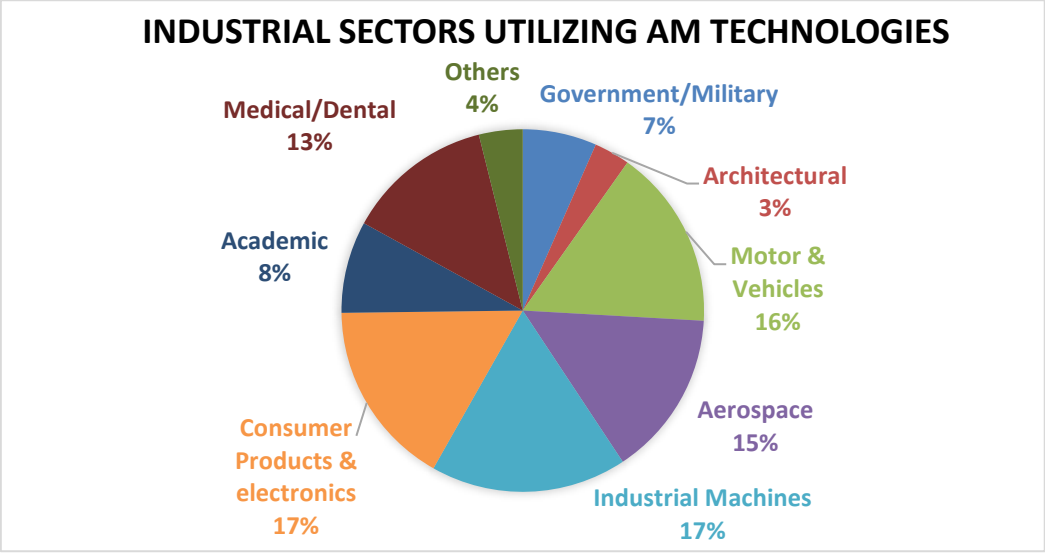

Figure 1-2 Industries utilizing AM technologies. Adapted from [6].

Furthermore, the relevance of material cost should be considered in the sustainable development of AM, especially as the low cost of non-biobased polymers creates a barrier for transitioning business operations to the use of more sustainable polymer material solutions. For instance, traditional non-bio-based polymers like polyethylene and polyamide can respectively cost about $1-$1.2 and $1-$3 per kg [1], while that of the most popular renewable and biodegradable PLA can cost about $4-20 per kg [1], and hence highlights the sort of costing gap that product manufacturers must bridge in order to competitively adopt bio-based polymers; either through economies of scale or the utilisation of more cost-effective manufacturing equipment and processes.

With the sustainability targets agreed at recent United Nations (UN) Climate Summits [38], there are several opportunities for impactful research, particularly in areas that can potentially deliver more eco-sustainable manufacturing systems while supporting socio-economic and environmental growth towards a Net-Zero future. Therefore, promising biopolymer-based materials need to be extensively explored in terms of properties and processing routes to help promote their use in eco-friendlier supply chains; particularly for use in the cost-effective and scalable extrusion-based AM process. Such an extrusion-based AM process is called fused deposition modelling (FDM) and has led to the development of fused filament fabrication (FFF), fused layer modelling (FLM), and big area additive manufacturing (BAAM) techniques, amongst others.

Sustainable extrusion (FDM)-based AM material options currently include brittle and plasticized poly lactic acid (PLA) filament materials that are being developed to form a very limited range of effectively processable, bio-based, biodegradable and multifunctional polymer-based filament materials for viable industrial and commercial applications [39]. Consequently, PLA-based material systems are the subject of significant research interest and activities, especially with respect to PLA/polybutylene succinate (PBS)-based composites, which show increased tensile toughness, strain-at-break, and biodegradability compared to pure PLA [40]. In this space, the literature examining the interdependencies between filament formulation, filament processing, filament property, printability, and final

part property in FDM (extrusion)-based AM is very limited, and therefore requires further work. This research project therefore addresses this gap by exploring a set of PLA/PBS-based formulations, filament fabrication routes, processing controls/limits, and 3D printing strategies that contribute to manufacturing cost-efficiency, filament material processability, thermal behaviour, 3D-printability, and end-product tensile mechanical properties. The use of processing methods such as in-situ polymerization, in-situ melt blending/intercalation, and ultrasonic-assisted solvent/solution mixing are initially considered for eco-sustainable filament fabrication. Nonetheless, strong emphasis is given to physical (crystalline, compositional, rheological, morphological, and mechanical) properties of PLA/PBS-based filaments and/or parts to establish their through-process lifecycle behaviour leading up to part fabrication for a simple and cost-effective FDM (extrusion)-based AM route.

1.2 Aims and objectives.

The overall aim of this work is the development of more industrially and commercially viable biobased/biodegradable filament materials with functional and multifunctional capabilities for extrusion (FDM)-based AM. This involves systematic investigation and optimization of the PLA/PBS-based composite materials and filament formulations, processing route, processing limits, and 3DP strategy for application in scalable FDM-based 3DP and includes using PLA/BioPBS-based blends and nano-composite filament formulations with sustainable and eco-friendly processability. To achieve this aim, the following objectives are addressed:

- Identification and justification of PLA/PBS-based material compositions for filament material formulation.
- Fabrication of PLA and PLA/PBS-based 3DP filaments using simple and cost-effective manufacturing methods.
- Elucidation of the links between material composition/processing route/processing limits and resulting 3DP filament properties.
- Assessment of the rheological properties of PLA/PBS-based materials for material formulation development and printing process optimization.

- Characterization of in-plane and interlayer properties of 3D-printed PLA/BioPBS-based composites.
- Explanation of the links between PLA/PBS-based filament formulation, fabrication route, filament printability, 3DP strategy and part performance.
- Identification of useful conditions for utilizing PLA/PBS-based filament formulations in FDM (extrusion)-based 3DP.

1.3 Thesis structure

Chapter 2 of this thesis gives an overview of commercially available thermoplastic filaments and then goes on to identify existing research activities surrounding the use of advanced thermoplastic bio-composites; specifically focusing on PLA/BioPBS-based composites used for heat-assisted FDM-based 3DP applications. Chapter 3 introduces the methodologies applied throughout this work and highlights key experimental approaches and characterization methods used to evaluate the results of the experimental campaign. Chapter 4 focuses on the results related to the thermodynamic properties of PLA and BioPBS materials, and furthermore, on the crystallization and recrystallization behaviour of fabricated 3DP filaments made from PLA80/BioPBS20-based filaments. This helps to understand the state of the filament material prior to 3DP, and then aids in understanding the influence of each filament formulation state on 3D-printed part properties. Chapter 5 examines the surface morphology and rheological properties of each filament formulation with the aid of Cast cylindrical plates made from each of the specified filament formulation. This assessment leads to development of a rheological master curve that aids in the prediction of complex viscosity values for PLA80/BioPBS20-based formulations at given temperature and shear rate conditions corresponding to 3DP processing. Chapter 6, which is the last of the results chapters, uses microscopy to provide insights of the qualitative challenges attributed to the PLA80/BioPBS20-based filaments. Furthermore, the tensile mechanical properties of each PLA80/BioPBS20-based filament and 3DP strategy combination, as well as their fracture surface features are presented and critically discussed to aid in elucidating the links between filament formulation, processing route, 3DP strategy and fabricated part property.

Chapter 7 provides an overall discussion of the results and discusses the potential contributions and impacts of the research activities carried out. Conclusions obtained from the main findings are summarized in Chapter 8, followed by relevant recommendations for future research activities.

2 Literature review

2.1 Introduction

The extent of material consideration for extrusion-based AM should be broad and especially inclusive of advanced materials that may contribute significant improvements in the realization of multifunctional and sustainable part properties. So far, thermoplastics and thermoplastic-based composite materials have received the most interest for commercial adoption of extrusion-based AM techniques (including FDM-based processes), which was found to be due to the benefits of its cost-effective and sustainable AM approach. In this chapter, state-of-the-art thermoplastics and thermoplastic composites used for FDM extrusion-based AM are considered to aid with material system selection for extrusion-based AM development. Critically, the choice of a thermoplastic-based material used for an FDM-based 3DP project needs to achieve properties that enable the 3DP material resource to be delivered controllably into a print volume and onto a print bed while maintaining the desired geometry, position, and form throughout the 3DP process cycle. This ultimately helps to optimize interlayer and trans layer interactions, bond formation, and dimensional accuracy, which supports the layer-by-layer construction of simple to complex functional products [10], [41].

2.2 Heat-assisted extrusion-based AM using thermoplastic-based materials.

Thermoplastics and their composites are among the most processable materials for extrusion-based AM. Heat-assisted extrusion-based AM materials comprise of polymeric material systems that have inherently strong enough intermolecular bonds and therefore require a relatively higher endothermic reaction to weaken the bonds and cause sufficient material flow for the extrusion processing cycles [42]. The overall suitability of thermoplastic and thermoplastic composites for heat-assisted processing and 3DP (i.e., for material formulation, filament fabrication, hot-melt extrusion, deposition, printability, and post-processability) can however be limited to certain materials or composites [43], and necessitates significant breadth and depth of process-property relationship definition that would inform the advanced manufacturing of advanced product systems. In heat-

assisted material processing, an extruder, as depicted in Figure 2-1, is typically used for hot-melt processing and filament fabrication process [44]. Figure 2-2 shows a cross-sectional view of a single and twin-screw extruder's barrel section used to process material into an extrudate or filament material.

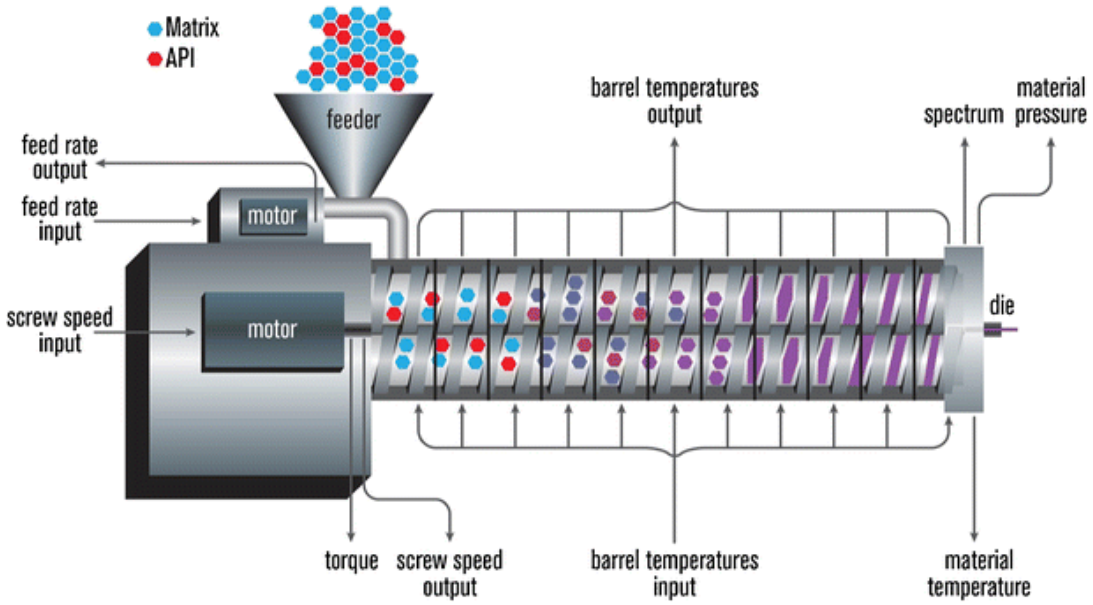

Figure 2-1 Hot-melt extrusion machine used in fabrication of single and composite filament materials. Reprinted with permission from [44]**.**

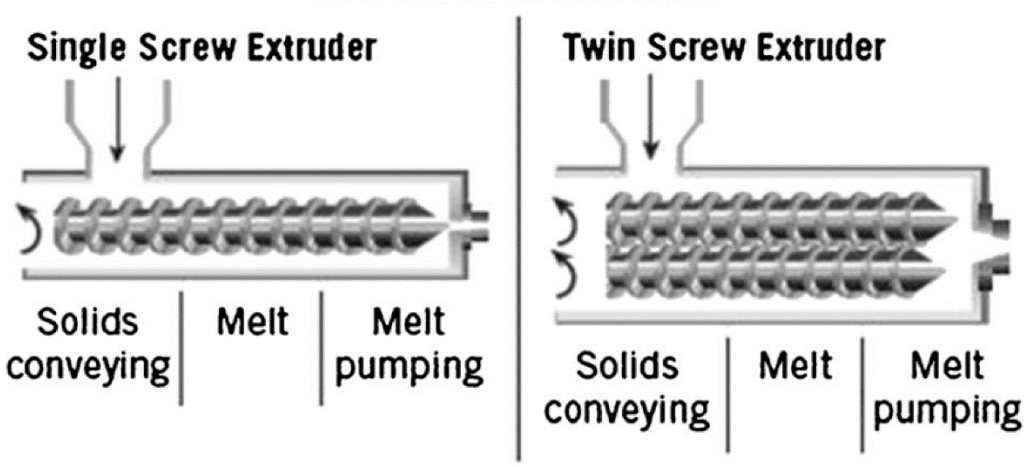

Figure 2-2 Cross sectional view of single and twin-screw extrusion machines. Adapted with permission from [45]**.**

Popular heat-assisted extrusion-based AM materials tend to have a relatively broad thermal processing window and sufficient thermal stability that allow them

to withstand the thermodynamic cycles experienced during the processing and functional life cycle of the materials. Interestingly, the suitability of polypropylene (PP), PLA and PLA-based composites have been investigated for hot-melt extrusion processing [42], [46], [47]. Drummer et al. [46]; in using PLA/tricalcium phosphate (TCP) composite to produce scaffold with optimal functional mechanical properties (at 225 °C) found a remarkable link between nozzle temperature and final part morphology and crystallinity. Meanwhile, Kumar et. al. [45] successfully demonstrated the suitability of printing with PP and ethylene vinyl acetate (EVA) around 210 °C and 110 °C respectively. Other studies often include physicochemical and rheological characterisation that aims to identify correlations with printability, end-part applicability, and post-processability – as depicted in Figure 2-3. Hence, the suitability of thermoplastic-based materials can be strongly considered to depend on factors such as the glass transition, melting, crystallization, wetting, rheological, and structural mechanical properties exhibited by the material throughout the thermal cycles involved in filament/pellet processing and extrusion-printing processes. These factors are therefore of critical significance in the development of heat-assisted thermoplastic and thermoplastic composite materials for extrusion-based AM, especially because composites introduce complex multi-material considerations for their use in manufacturing processes.

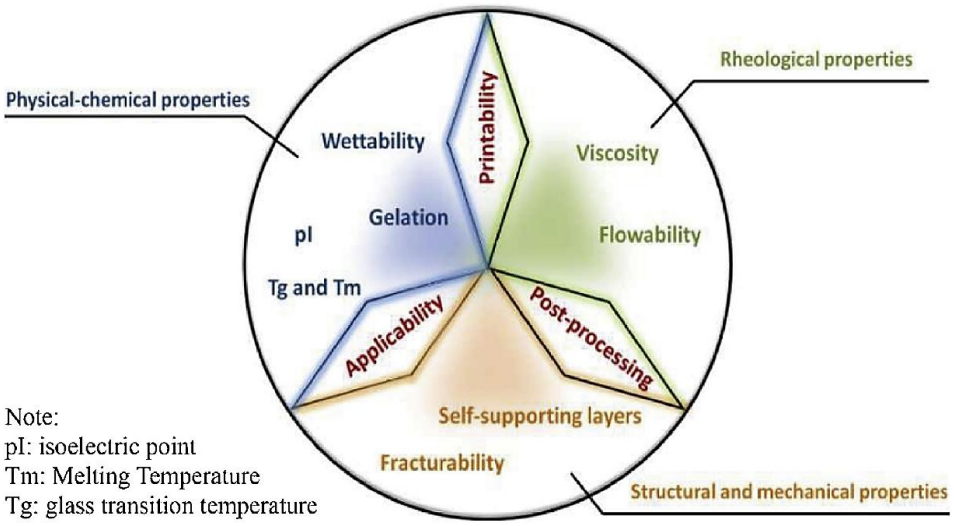

Figure 2-3 Material properties to consider upon extrusion-based AM of structures and parts (Reprinted with permission from [10]**).**

2.3 FDM: The underlying technique for extrusion-based 3DP

Extrusion-based AM methods generally execute a process where a feedstock; usually a pre-formed filament; is fed to the head of a printing system by an electrical or hydraulic motor-controlled pinch roller mechanism [48]. In the head, the filament is heated and extruded in a molten material form onto a platform to create a 2D layer. Repeatedly, this 2D layer, one on top of another, creates a 3D part that follows a design specification [6][48][49]. In other words, material extrusion techniques, which are based on fused filament fabrication (FFF) along with fused deposition modelling (FDM) processes [50], can be described as a 3DP manufacturing technique involving a thermoplastic material in filament or pellet form being extruded through one or more heated nozzles [50]. The viscous material or melt emerging from the nozzle(s) is deposited on either a moveable or immoveable build plate, before solidifying to form a part, with dimensional accuracy in the order of 100 μm [51].

2.3.1 FDM 3DP machines and developments

Stratasys patented the name fused deposition modelling (FDM) in 1989, and in recent times FDM-based printers have emerged as the most popular 3D printers used in printing thermoplastic polymers and composites [6][52][53]. Industrially, FDM machines (Figure 2-4) are also considered to have significant advantages in terms of cost-efficiency and simplicity [54]. An FDM machine can be directly related to conventional, extrusion-based polymer processing machines [55]. In its basic form, the FDM technology uses only a thermoplastic filament [56]. The printer head, which holds the heating element, extruder, and nozzle, operates at a relatively high temperature (150 – 250 °C) before extruding and depositing the molten thermoplastic material to form 2D layers and consequently, 3D printed parts. As seen in Figure 2-5, each unit of polymer extruded is considered a road/bead and can undergo swelling that must be controlled partly by adequate heat distribution for the printing of dimensionally accurate parts. Also, prior to deposition, buckling or structural failure of the filament may occur too. These highlights other aspects of the FDM process that must be controlled correctly. The ability of the extruded material to maintain a predetermined diameter, shape or structure throughout the printing stage is therefore highly desired.

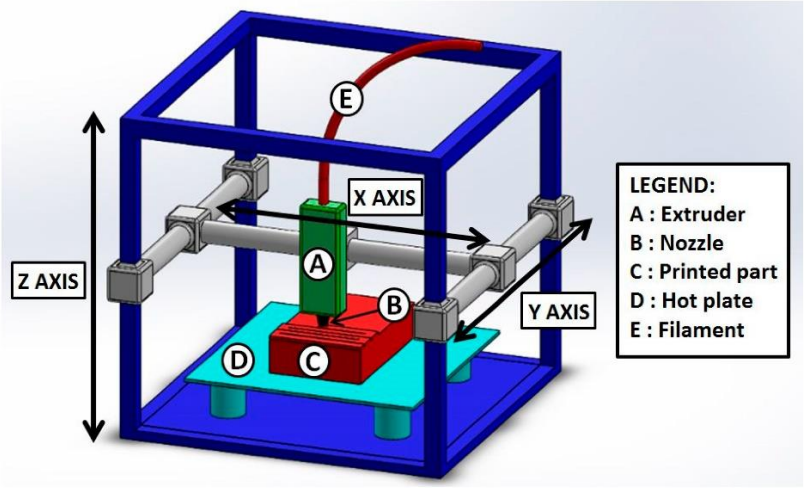

Figure 2-4 Typical FDM machine design with a printed part on an immovable print bed/hot plate (Reprinted with permission from [57]**).**

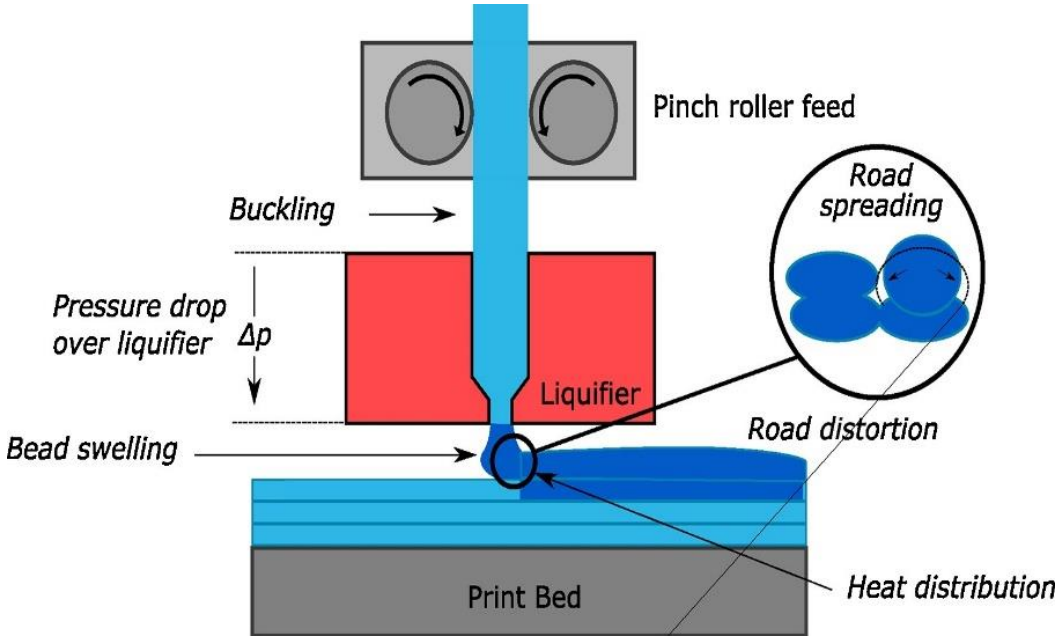

Figure 2-5 Important aspects in material flow during an FDM process (Reprinted with permission from [51]**).**

The simplicity of the actual process has led to rapid adaptations made to suit developing material systems other than pure thermoplastics. Figure 2-6 shows the different forms in which FDM machines have been adapted to produce multi- or composite material systems and parts [58]. The single head design of FDM machines is the basic form of the technology, allowing only one material system

to be printed at relatively high processing temperatures. When a compatible polymer-based composite material system is obtained as a filament; composite blends can be printed in this way, hence obtaining a composite product. Alternatively, printing can be done on a reinforcement material, which can be introduced by another external system like a human or robotic/automated system.

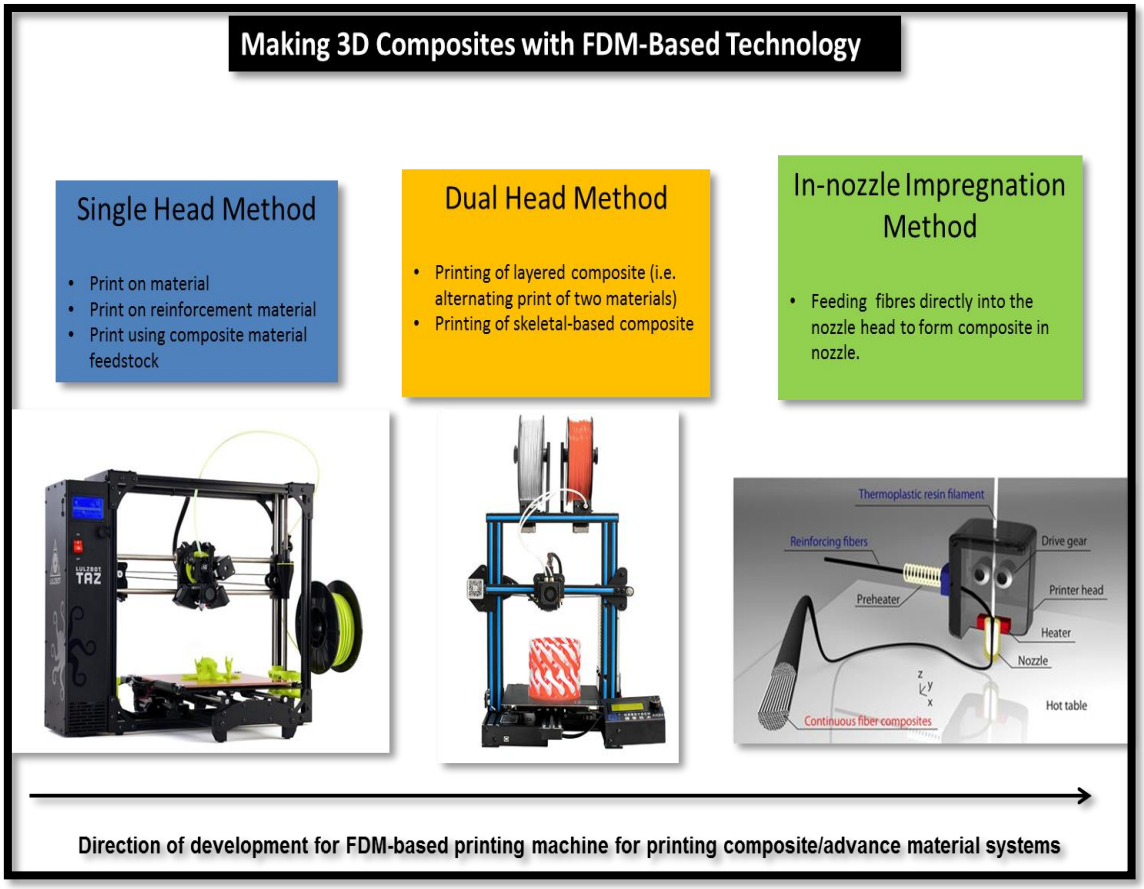

Figure 2-6 Development of FDM for advanced 3DP fabrication capabilities [39]**.**

Dual head FDM printers make the production of polymer composites a simpler problem to solve as they can alternate the printing of two material systems. These printers offer the capability of printing with support structures. It can also be applied in the printing of layered and skeletal based composites. Additionally, in special cases, multiple parts can be printed faster by using both printer heads simultaneously, and can therefore, lead to at least a 50% improvement in time-efficiency, thereby making it a great option for small-sized, multiple component fabrication activities using FDM. The in-nozzle impregnation technique is a

recently developed type of extrusion-based 3DP method that introduces the heated reinforcing material, usually fibres, into the nozzle head to facilitate better mixing and incorporation of the fibres into the polymeric filament matrix [11] [59]. These are being developed as a unique option for printing short and continuous fibre reinforced polymer (FRP) composites [13], however, due to the short distances travelled by the polymer composite's constituent materials, i.e., from nozzle to extruder, there is limited time available for interactions between polymer melt and fibre materials. This limits the formation of a more robust polymer composite material, and as a result, forms such a limitations that hinders the use of the in-nozzle impregnation method for production of commercially and industrially viable parts [18][60]. The progress in FDM machine design has led to greater interest in the development of processes that allow advanced composites, and bio-based materials to be processed correctly. 3D bio plotting and direct ink writing are examples of other forms of extrusion-based 3DP techniques that have been more recently developed via process and material optimization of the FDM technology; to deliver parts and products with more advanced material systems for advanced and bioprinting applications [61].

Achieving a 3D printed part involves creating a part or product from a 3D computer model; either designed in 3D software or scanned using available scanning methods like computed tomography (CT) and magnetic resonance imaging (MRI). Nonetheless, in the use of a specific 3DP technique, also considering their post-printing processes, there is a need for the 3D manufacturing system to be tailored to that specific 3DP category. This enables the appropriate design of configuration that affects the specific 3D printing process and part properties. Hence, the following sections highlight and discuss the configuration and control factors of an AM process design based on the CAM system, 3DP machine and material resource involved in an extrusion-based 3DP process. These sections also cover the actual 3D printing process including insights into the material feedstock and filament production process. These provide an understanding of the material and process aspects and the technicalities that affect the final part quality of extrusion 3D-printed parts.

2.3.2 Factors Affecting the FDM process: CAM, FDM 3DP Machine, and Material Resources

Table 2-1 summarizes the factors that are responsible for the quality of parts produced using FDM-based 3DP with respect to the design and control system, printing process and material resource as they affect process quality, surface finish, mechanical properties, and dimensional accuracy of printed parts and/or products. Highlighting these therefore gives a breakdown of key factors and aspects to consider during experimental review and future experimental design processes. They include aspects of computer model design, machine design, and material design used in modern manufacturing processes to aid in predicting and defining the part or product output. Overall, as reflected in Table 2-1, process efficiency and effectiveness embody an overarching output that is affected by the various factors and their aspects. For example, a fabricated 3D part with insufficient mechanical strength for its intended application is a result of an ineffective process, and hence, an optimally inefficient process. Similarly, a part with unsatisfactory dimensions also renders the manufacturing process ineffective and to some certain extent, inefficient.

The shell and infill design, part orientation, and path planning aspects are understood to be a dimensionally accurate digital model of the intended processing run and final part features/properties, and therefore has a relatively important role in determining and controlling the form and shape of 3D-printed parts. Meanwhile, the pressure and temperature gradients around the printing environment, nozzle design, and dispensing process step determines how well the CAM design aspects are executed to physically form the 3D-printed part. Both categories of CAM and 3DP machine aspects are therefore found to affect the output (3D-printed) part from a source that is external to the part and material. However, from a material (polymer) resource perspective, intrinsic crystalline properties and behaviour strongly influences the mechanical properties of printed structures. Moreover, the material's melt viscosity can significantly impact the accurate deposition of material for the realisation of dimensionally accurate 3D-printed parts. Material viscosity can also be increased by the addition of additives, which can influence the long chain branching of the polymer matrix material, and

in turn influence the crystallisation behaviour and physical properties of the polymer. Due to the fundamental and intrinsic material resource effects on processing quality, processed material property, and final 3D-printed part property, the material aspects are considered to most broadly and impactfully affect properties of a final 3D-printed part.

Table 2-1 Important resource factors and key aspects of extrusion (FDM-based) 3DP process [6][10][48][62]**.**

Factors	Aspects	Affecting
CAM: design & Information system (i.e., control system)	• Shell and infill design. • part orientation. • path planning	Part mechanical properties Surface finish Process efficiency and effectiveness
FDM 3DP machine	• speed of 3D dispensing or filament feed. • pressure and temperature gradient. • nozzle design.	Part dimensional accuracy Part mechanical properties Process efficiency and effectiveness
Materials	• die swelling. • long-chain branching • melt viscosity. • crystallization rate of melt material.	Part surface finish Part dimensional accuracy Part mechanical properties

	• shear-thinning induced by tailored molar mass distributions. • addition of stabilizers and other additives.	Process efficiency and effectiveness

2.3.2.1 Computer Aided Manufacturing: for part and process design and control.

A CAM system is an embodiment of part and process design system software and/or functionalities, which typically enables a streamlined part production process to be executed - from part design to production. CAM systems allow the user to control the part/model design, and process parameters, which ultimately determine the quality of the extrusion process, and especially the printed part quality. Prior to printing, the CAM system uses a CAD or 3D model in tessellated file format, e.g. .stl, to define a tool-path in G-code [48][49]. This is followed by the nozzle tip during the extrusion and deposition stage of the 3DP process. The G-code is a computer language that can be understood by CNC-based machines, such as those used for extrusion-based processes [48][49]. Other processing information regarding the individual filament width and height can be set before or after printing starts. Various deposition strategies can be exploited and developed during the slicing stage with several parameters available to the user. Once a strategy has been developed and set in the slicing software, e.g. Cura, Quickslice, slices - i.e. cross-sections of the part model are developed in the CAM system, and a tool path is defined as a G-code; before being communicated to the extrusion-based 3D printer [48][49]. If support structures are required, they can also be included prior to slicing the model. Essentially, as the varying process factors are updated, the tool path and G-code are updated accordingly, to reflect the orientation, size, or any other process factor change that causes a change in point location. The G-code and tool path should, therefore, be well considered, as they have a significant effect on the thermal stress accumulation in the deposited material. This signifies that various CAM programs using the same inputs may produce parts with different responses to the environmental stresses experienced by the extruded material. A. C. Abbott et

al. [62] used two open-sourced G-code programs, Slic3r 1.2 and Voxelizer 1.4, with differing G-code generating algorithms (i.e., for tool path control), but the same input values (i.e., process parameters) - to check the effect that different CAM programs have on the properties of identical 3D-printed parts [48]. Consequently, it was found that the same specimens created using different CAM programs exhibited different fracture morphologies [48]. This finding shows that, in choosing an optimal printing and deposition strategy, the G-code and tool path must be optimized for specific designs and 3DP machines so that more reliable sets of results can be obtained. Usually, a good deposition strategy mentioned in literature involves depositing continuous contours of the 2D-layers boundary for a given cross-section of the 3D model, before filling the spaces in between them with a choice of infill patterns [49]. This can enable the design of deposition strategies that achieve a desired mechanical performance that can be repeatable, while also offering better opportunity for functional optimisation.

2.3.2.1.1 Part orientation and path planning

The orientation of a part; in relation to the infill orientation and to the printing system's main axes of movement for Cartesian 3D printers plays an important role in the mechanical behaviour, dimensional accuracy, and surface finish of the final part [48]. Also importantly, part orientation can further define the need or extent to which support structures are needed, which is important for managing the cost efficiency of the process. An important aspect of path planning is the choice of infill patterns. When using a rectilinear pattern, each individual layer is filled with a raster of parallel roads with the next adjacent raster layers at a fixed alternating angle of 90° between them as depicted in Figure 2-7. Adjusting the infill density affects the level of occupied space in the hollow sections of the part, and can therefore create a scantier or denser part with bigger or smaller distances between the extruded roads [48]. A slightly negative raster to raster distance; corresponding to fibre overlapping, has been found to limit void density and increase the contact area among filaments, hence leading to stronger filament to filament bonds. However, the excessive build-up of polymer material at the layer perimeters can significantly affect the dimensional accuracy of the part in the XY

plane. This highlights the considerations needed to be made when deciding on the many factors in FDM or extrusion-based 3DP processes.

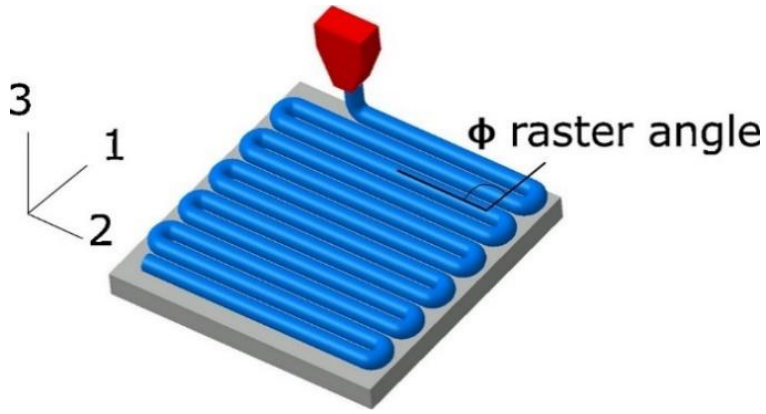

Figure 2-7 shows a raster of parallel roads deposited to form a layer. Also shows the raster angle of relative roads in a rectilinear road pattern Reprinted with permission from [51]**).**

2.3.2.2 Fused deposition modelling (FDM)

Fused deposition modelling (FDM) involves three main stages highlighted in Figure 2-8: i.e., pre-deposition, deposition, and post-deposition. Extrusion-based 3DP techniques are like conventional extrusion processes, using the same mechanism as in other extrusion-based manufacturing processes like injection moulding. However, in FDM-based 3DP, moulds are unnecessary, and the extrusion nozzle is vertically mounted to print on a print-bed. Nonetheless, both conventional and FDM-based AM techniques are temperature-dependent processes; requiring relatively higher energy input at the pre-deposition stages of the process to help achieve better control of the feed material's rheology and deposition performance. The pre-deposition and deposition stages, respectively involving filament in-feed and molten material flow through the melting reservoir and nozzle of the print head is a pressure-driven flow of material mass. This controlled flow is mainly related to nozzle geometry [63][51][48], pressure gradient [63][51][48], and the melt's apparent viscosity, and can, at the point of extrusion, be a fully-developed laminar flow of polymer through a capillary die with a generally circular cross-section [63][51][48].

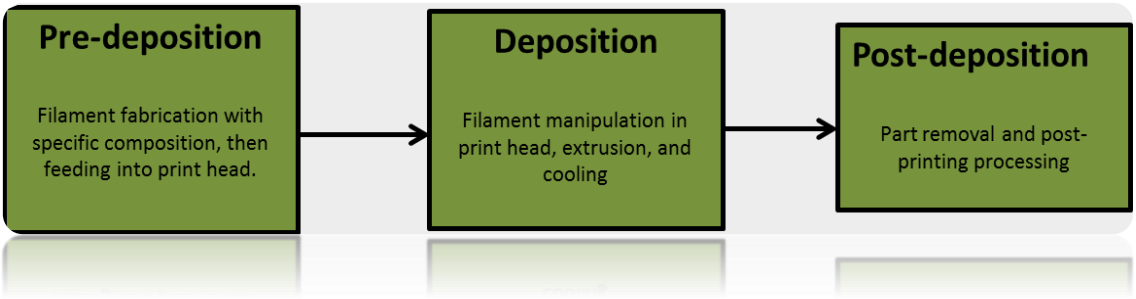

Figure 2-8 Important stages of an extrusion-based 3DP process.

The desired pressure for polymer extrusion at the nozzle tip is applied by the pre-heated parts of the 3D printing filament, acting as a piston as it is being pushed by a pinch-roller feeding mechanism into the melting reservoir of the printer head [48]. This helps in a successfully controlled extrusion and deposition process of semi-molten thermoplastic roads on a fixed or spatially translatable platform. Some important process parameters, using example values for PLA include filament feed velocity (e.g., 15-30 mm/s), extrusion temperature (e.g., 160-210 °C), cooling rate (e.g., 20% cooling fan speed), print bed temperature (e.g., 0-60 °C), print area/chamber temperature (e.g., 0-60 °C), and volumetric flow rate (e.g. 10 mm^3/s). As printing initiates, the rate at which the filament is fed to the liquefier/melting reservoir is dynamically controlled and connected to velocity changes of the print head, thereby allowing the printing system to maintain a constant material volume fraction. The amount of melt material that is present in the reservoir chamber, the melt temperature, and consequently, the viscosity and surface energy of the melt are inherent material factors that control the feed rate/feed velocity of the extruded molten polymer. On extrusion, the print head generally exhibits a constant linear movement; where the extruder motor within the print head is set at a speed that is proportional to the printing speed, therefore enabling an indirect control of feed and extrusion velocity of the thermoplastic polymer material.

The extrusion temperature and feed/deposition rate represent the most important process parameters influencing the inter-layer and intra-layer bonding of deposited roads as each layer is deposited on a previously deposited layer/road of material [51][48]. Once an extruded filament contacts other previously deposited roads, heat exchange by conduction occurs as well as convection and

radiation with their surroundings to facilitate or hinder the bonding process. This consequently creates new physical-chemical interactions that lead to the formation of bonds among individual filaments via coupled heat and mass transfer phenomena, which also involve phase changes, and thermal and mechanical stress development within the printed structure. During the heat transfer and bond formation process, air traps can also be developed between contiguous filaments depending on the level of bonding achieved. The degree of bonding depends on the neck growth between adjacent fibres, and the molecular diffusion at each interface [63][51]. When heat transfer and bonding processes are limited, partial bonds are created, which consequently leads to a printed part with inherent pores - hence producing a part with lower integrity. This phenomenon, which occurs after the deposition at the post-deposition stage is a critical stage of the process in which the printed fibres or roads can be further controlled by thermal, chemical and/or atmospheric conditions surrounding the print bed governing the extent of control that can be achieved during the FDM process. This post-deposition control feature can be used during the extrusion printing process to address issues like air traps, non-uniform cooling and poor inter or intra-layer bonding.

The extrusion process affects the maximum strain during material extrusion through the nozzle as the polymer chains are subjected to stress-induced orientation that causes some straining of the extruded polymer fibre. This potentially reduces the elongation characteristics of the extruded polymer fibre material [57], and furthermore, due to the directional bias in the extrusion process, there is development of anisotropic properties in the printed part. In a typical case of FDM-printed parts showing anisotropic properties, fully dense PLA blocks were fabricated by [64], from which cut-out samples of parts were tested. Nonetheless, Wittbrodt et al. [65] printed parts using a RepRap printer that used the proprietary FDM-based technology. In obtained parts were found to match and even outperform commercial 3D printers in terms of the tensile strength for the same polymer material used [65]. However, the tensile strength of the parts show variability, which is suggestive of the ease with which slight changes in fabrication method and specifications can affect the reliability of printed part quality.

In summary, an AM part is created by superimposing a predefined number of 2D layers in a pattern defined by a G-code. The printer head uses the G-code for each 2D layer to generate a specific pattern of fibres with predefined widths and heights. Achieving a functional, robust part involves optimum control of filament production, 3DP extrusion temperature, deposition rate, and print-bed area conditions, amongst several other factors that favour the best inter and intralayer bonding of a given material system. These factors will also have implications on the total print time, which is an important factor when considering the cost of production, and other resources available for the job.

2.3.3 Potential limitations in FDM-based 3D-printed parts

Some of the most common challenges or drawbacks associated with printing parts with the FDM technology are discussed in this section. Stepped layers [8] [53], which is a key limitation amongst others, is a result of visible trails of deposited material inherently caused by the distances between printed layer edges. They can be improved through reduction of the diameter of the extruder or by minimizing the thickness of the printing layers used. However, such a solution would also lead to longer print times, which increases the cost of the process. Overhanging and bridging [8] also cause concern for printing of part designs that have elements set at an angle greater than 45° to the vertical axis. In this case, the filament may not have support upon extrusion, and would thereby lead to a collapse of the overhanging sections. To address this challenge, support should be generated at the model preparation stage to prevent the part from breakdown and damage during and after printing. A bridge is highly similar to an overhang but has support at both ends. Therefore, a bridge characterized by a long overhanging part usually requires auxiliary supports added during the design stage and subsequently removed through the final machining of the print. Stringing [8], another issue that occurs when the extruder is moving between two discontinuous points, results in leakage of some of the plasticized filament material from the nozzle due to gravitational forces or loading from the filament. Removing this effect usually involves an appropriate retraction of the filament back into the nozzle to limit any acting forces. Warping [8] is one of the most common defect in traditional polymer processing. It occurs when the lines,

edges and corners of the printed model deflects because of shrinkage of material and/or uneven temperature distribution across the printed part. This is a common issue with polymer-based fabrication processes like injection and compression moulding, and can be addressed by controlling the cooling rate, print path, and material formulation used. Another potential challenge for 3D-printed parts is one of hygroscopicity [8] [53], which refers to occluded or precipitated porosity which makes the material more prone to absorbing moisture from the air, and is a factor that could significantly affect the mechanical properties of 3D-printed parts. It can be effectively improved by proper storage of 3DP materials or thermal conditioning of materials before use in 3DP. Additionally, the heterogeneity of structure particle size and/or insufficient density of a filament material has been found to cause another 3DP limitation characterised by structural inhomogeneity [8]. This effect causes selective filament material deposition on the print bed with differing temperature and road-bonding effects but can be addressed by reducing the lengths between spits of extruded filament material [8].

2.4 Commercially available thermoplastic-based materials for FDM-based AM

Acrylonitrile butadiene styrene (ABS) and polylactic acid (PLA), having typical bulk strengths between 30 - 100 MPa, and elastic moduli in the range of 1.3 - 3.6 GPa, are the most established materials for extrusion-based AM machines [51], [66]. Other commonly used polymeric materials include polycarbonate (PC), polyamide (nylon), high-impact polystyrene (HIPS), and poly phenyl sulfone (PPSF), which include engineering and high-performance thermoplastics. In achieving the material extrusion process, a form of polymer-based material feedstock; either in the form of pellet or filament is required. However, filaments are most common because they can produce a more consistent flow of material. Table 2-2 highlights the range of commercially available standard filament materials used in FDM-based 3DP and helps to highlight the mechanical properties of their FDM-based 3D-printed parts in relation to their respective injection moulded parts. It is useful to highlight that the performance of FDM-based 3D-printed parts (for a specific design) may vary depending on the part’s

orientation and utilised printing strategy. Interestingly, parts printed flat in the XY (horizontal plane) appear prominent when compared to parts printed in the XZ (on edge) and ZX (upright) orientations. Moreover, Table 2-2 is mainly populated based on parts printed in the XY plane, which typically show a comparable mechanical performance to parts made by injection moulding. Hence, FDM-based 3DP technologies show significant promise for greater adoption in the production of mechanically functional products across various industries. However, the limited range of material options that offer combined structural, renewable, and biodegradable capabilities creates a significant research gap for advancing FDM-based 3DP filament materials and process understanding.

Table 2-2 Standard thermoplastics and typical tensile mechanical properties of 3D-printed and injection moulded materials.

	FDM 3D-printed			**Injection moulded**		
Material	Tensile strength (MPa)	Tensile modulus (MPa)	Failure Strain (%)	Tensile Strength (MPa)	Tensile Modulus (MPa)	Failure Strain (%)
ABS [67], [68]	33.9	1681.5	4.8	45	2500	25
PLA [69], [70]	46	3039	2.5	60	3600	6
PET [71], [72]	59.4	2560	5.2	57	2420	-
PETG [73], [74]	45	1650	24	50	2100	100
HIPS [75], [76]	25.7	1990	10	24	1650	60

TPU 95A [77], [78]	39	26	552	42	-	515
PP [79], [80]	10.2	273	>800	33	1400	150

With the prevalent use of commodity plastics across several industries, bio-based and biodegradable polymeric materials like PLA, PBS, polyhydroxy alkanoates (PHA), cellulose, and lignin have recently emerged as important materials for the development of advanced biopolymer-based material systems with functionalities that are directly or indirectly in significant demand for more sustainable developments [81], [82]. Although bio-based polymeric materials might not completely replace petroleum-based plastics, they can play a crucial role in minimizing the carbon footprint of relevant products and process life cycles. And consequently, depending on the target industry, certain key aspects of the value chain must be developed towards realising successful adoptions. For example, the biomedical industry requires innovative biopolymer systems that are printable, and biocompatible, with acceptable degradation kinetics and degradation by-products [10]. Alternatively, in the automotive industry, emphasis is on the part weight, part complexity, and speed of production [83]. For each case nonetheless, the material, process, and performance need to outperform the traditionally fabricated thermoplastic parts sufficiently and sustainably.

2.5 Bio-based thermoplastics and composites for FDM-based AM

ABS, ABS blends, and other fossil fuel-based thermoplastic blends and composites have been the most frequently encountered materials in FDM-based AM, which still make up key research topics [84]–[88], [89], [90], even though PLA has emerged as a promising material for filament fabrication and 3DP of advanced composite materials. PLA is promising because of its renewable and biodegradable characteristics amongst others [48], [91] and has been identified as the most widely used renewable polymer in tissue engineering because of a variety of benefits such as biocompatibility, low cost, non-toxicity, excellent

mechanics, biodegradability, ease of processing, and green synthesis routes [35], [92]. PLA is continuously making up more of the FDM 3D printing feedstock, and although the mentioned benefits of PLA render it suitable for sustainable applications in several industries, it also has some disadvantageous properties. These include its lack of recurring cellular patterns with well-defined function; hydrophobic nature; low average molecular weight; low ultimate elongation strain; and acidic by-products upon degradation [91], [93].

2.5.1 PLA-based materials for FDM-based AM

As the growing use of biopolymer-based material resources is focused strongly on poly lactic acid (PLA), which has useful mechanical, thermal, and optical properties [94], [95]. However, PLA is relatively more expensive than established petroleum-based thermoplastics [95]–[97]. In addition, PLA exhibits low thermal resistance/stability, brittleness, low crystallization rate, and poor gas barrier properties, which pose limitations to its processability and end-product applicability [98]–[101] [102]. As a means of overcoming these challenges, while retaining eco-friendliness, other materials like plasticizers, clay, cellulose, ceramics and carbon-based nanomaterials have been used to improve the processing and properties of PLA-based materials [101], [103]–[111]. Critically, the weaknesses of PLA have led to limited applicability in biomedical products, biodegradable parts, and tough structural units, and is driving the development of improved PLA-based bio-blends and bio-composites.

2.5.2 State of the art research on PLA-based composites for FDM-based AM applications

In a research work by Gireesh et al. [112], two PLA-based nanocomposite films were fabricated using the solvent casting method; with one containing graphene oxide (GO), and the other containing reduced graphene oxide (rGO). The results showed about a 20% and 38% increase in Young's modulus for the PLA-GO and PLA-rGO nanocomposites respectively; and about a 17% and 67% increase in tensile strength respectively. However, Chieng et al. [113] found that the addition of rGO to PLA hardly changed the tensile strength, but its addition to plasticized-PLA (using poly ethylene glycol (PEG) and epoxidized palm oil (EPO) as plasticizers) resulted in at least a 28% decrease in tensile strength, which was

attributed to the plasticizer addition However, when comparing between the plasticised PLA/graphene nanoplatelet (GnP) and plasticised PLA/rGO nanocomposites, the latter shows about 5% higher tensile strength. Additionally, Chieng et al. [113] found that there is improved thermal stability (degradation onset) of about 30 – 64 °C for the PLA/rGO and EPO-plasticized PLA/rGO composite systems, which show increasingly homogenous and uniform morphology with increasing rGO content.

Matsuzaki et al. experimented with fibrous composite materials; i.e. fibres infused into PLA for 3D printing, targeting improved physical properties for the printed parts [11]. A modified FDM printer was developed to help impregnate the filament with composite fibres before extrusion. In these experiments, the reinforcing fibre was heated using a nichrome wire before it entered the nozzle head; to enable and enhance the permeation of the fibre bundles with the thermoplastic resin. The heater inside the nozzle, further helps to consolidate the heating and to promote better mixing of the fibres and the resin in the heating chamber. Critically, the resulting 3D printed part's tensile mechanical results showed superior Young's modulus (around 19.5 GPa) and tensile strength (around 185 MPa) when compared with unreinforced PLA, which shows a Young's modulus of 3 GPa, and tensile strength of 48 MPa [11].

Another study involved the production of FDM 3D-printed porous composite scaffolds made from PLA and 15 wt. % hydroxyapatite (HA), which has shape memory effects targeting use for self-fitting implants. According to Senatov et al., the addition of HA nanoparticles into the PLA matrix causes a change in the alignment of polymer molecular chains, which results in an alteration of the frictional forces occurring between molecular chains [114]. This effectively provides stationary phases within the composite microstructure to govern shape memory effects. The 3D-printed porous PLA-HA scaffold was found to assist the survival of mesenchymal stromal cells, while also stimulating their active proliferation to help with vascularization of implants, as required for successful bone prosthesis [114].

Foster et al. [115] used a PLA/graphene filament to fabricate 3D electrode discs of 1 mm thickness using a conventional RepRap FDM 3D printer. It was characterized both electrochemically and physico-chemically for applicability as negative electrode in Li-ion batteries, and for which it was found that the PLA/graphene composite thermally degraded at over 200 °C below that of an industry standard PLA. Furthermore, due to the low ratio of active material in the formulation, i.e. 8 wt.% graphene content, translating to 103 mg of active material per cm^3 of composite, relatively low discharge specific capacities of 15.8, 6.2, 2.6, 1.1, and 0.6 mAh g^{-1} of active material were reached at current densities of 10, 50, 70,100, and 200 mA g^{-1} respectively [115]. In another study by J. Luo et al. [116], PLA/MWCNT composites were found to be suitable for printing by FDM. In this work, high electrical conductivity was achieved in the 3D printed products containing 5% MWCNTs; with conductivity of 0.4 ± 0.2 S/cm. Meanwhile, tensile strength and elongation were reported to increase from 18.8 (± 2.1) MPa to 78.4 (± 12.4) MPa, and from 26.2 (±3.4) to 94.4% (± 14.3), respectively; in relation to the pure PLA material [116]. These mechanical results are however considered to be controversial because of the typical mechanical properties of industry standard PLA.

Furthermore, Le Duigou et al. [13] used a continuous flax fibre (cFF) composite filament using PLA as matrix for FDM 3DP. The results suggested that the obtained part showed considerably higher tensile strength and tensile modulus when compared to other 3D printed PLA composites with either short or continuous fibres [13]. Crucially, the 3D printed cFF/PLA composites showed tensile modulus and strength values that surpassed the only other published result on continuous natural fibre printed composites at the time by ≥ 4.5x [13]. The tensile properties of 3D printed cFF/PLA composite were comparable to that of 3D-printed continuous glass fibre/polyamide (PA) composites. However, their transverse properties remained lower than similar flax/PLA composites that are thermo-compressed [13].

In summary, plasticisers, nanofillers, short and continuous fibres have been used to improve the properties and performance of PLA-based composite materials.

The most recently highlighted research findings indicate the sort of improved part properties that are achievable with the development of advanced PLA-based composite materials [117] [118]. Consequently, PBS has importantly been another material that is found to generally offer great complementarity of properties for the development of PLA-PBS based blends and composites with the aim of achieving useful processing, mechanical, thermal, and biodegradable properties [40] [119] [120] [121].

2.5.2.1 Properties of PLA and PBS; for blend and composite formulations

PBS is an aliphatic polyester produced by the poly-condensation reaction of butylene and succinate monomers. It has found applications in films, laminates, moulded foams and injection-moulded products within various fields, especially in the agricultural and packaging industries [98] [122] [123]. The combination of PLA and PBS has attracted great interest due to their large differences in bulk properties (see Table 2-3). While PLA is a glassy thermoplastic with higher thermal degradation rate, tensile strength, and tensile modulus, PBS is a softer thermoplastic with lower thermal degradation rate (i.e., heat resistance), higher elongation at break, lower tensile strength, and lower tensile modulus [124] [125]. PBS has been found to crystallise faster than PLA, and offers lower gas and water permeability; in addition to its superior processability and biodegradability [100]. Importantly, crystallinity plays a crucial role in tailoring the properties of PLA, PBS, and their blends/composites. Hence, it is useful to highlight that PLA can exist in three distinct crystalline polymorphs, namely the α, α', and β forms, while PBS crystals are known to exist in one single crystal form. The most observed PLA crystal form is the α-form, which has a helical conformation [126] and represents the most stable crystal polymorph of PLA, which, just like any polymorphic thermoplastic crystal, can be influenced by several factors including molecular weight, stereochemistry, and thermomechanical history. As a result, rapid cooling often produces an amorphous structure, while slow cooling allows for a more crystalline formation to occur [127]. And although the crystallization rate of PLA is relatively slow, it can be accelerated by adding nucleating agents or blending with other polymers [128]. Interestingly, it has been reported that PBS can act as a nucleating agent in a PLA matrix, which induces crystallisation of

PLA in PLA/PBS blends [40]. Consequently, these findings offer a route for potentially controlling the micro and macro mechanical properties of PLA-based parts through intuitive processing methods.

Table 2-3 Properties of PLA and BioPBS from suppliers [129], [130]

Specific Property	**PLA**	**BioPBS**
Density (g/cm^3)	1.24	1.26
Elongation at break (%)	6	300 – 560
Tensile Strength (MPa)	53	35-45
Tensile Modulus (MPa)	3500	500 – 700
Flexural Modulus (MPa)	-	650
Flexural strength (MPa)	-	40
Notched Izod Impact strength (MPa)	16	10
Melting Temperature (℃)	150	115
Glass transition (℃)	55 – 65	-32
Heat distortion temperature (℃)	55	95
Heat of fusion (J/g)	93	210

2.5.2.2 Nanomaterials for polymer (PLA/PBS) nanocomposite formulations

The addition of nanoparticles or nanoplatelets to thermoplastic polymers has commonly attracted considerable attention due to the potential for significantly enhancing or modifying the properties of the base polymer [131], [132]. This enhancement is largely due to the high surface area to volume ratio and the unique properties of nanoparticles [132]. The addition of nanoparticles often results in increased tensile strength and modulus of the polymer, which is particularly pronounced for high aspect ratio fillers like nanoplatelets (e.g., clay or graphene) [132], [133]. Certain nanoparticles can also enhance the toughness of thermoplastics, especially when they are well dispersed and have good

interfacial adhesion with the polymer matrix [133]. Furthermore, nanomaterial addition to polymers can influence the rheological, electrical, optical, thermal, and crystallisation properties of the nanocomposite [134], [135]. Nonetheless, the actual effects of nanomaterial additions depend on the type and amount of nanoparticle, the nature of the polymer matrix, and the processing techniques employed [136]. Consequently, issues associated with dispersion and aggregation, interface, and interphase, can support or negate the positive effects of nanomaterial addition to base polymer formulations, and should therefore be strongly considered for the fabrication and assessment of PLA/PBS-based nanocomposites.

2.5.2.3 Further research findings on PLA-based composites for FDM-based AM applications

Most research activities on the use of PLA/PBS blends and their composites have focused on compatibility and miscibility upon mixing, and on the mechanical properties of parts produced through injection moulding, compression moulding, and electrospinning techniques. In a work by Yokohara and Yamaguchi [94], a rheological emulsion model was employed, and the interfacial tension of the immiscible blend system was evaluated and found to be 3.5 mN/m [94]. According to Park and Im [137] , the interaction parameter between PLA and PBS as derived using the Flory Huggins equation was found to be -0.15 [137], which suggested some level of miscibility, perhaps in the amorphous phase. Wu et al. [124] subsequently identified that the PBS/PLA blend is an immiscible blend system with very narrow co-continuous regions and high percolation threshold [124]. In another case, Bahia et al. concluded that the two polymers (PLA and PBS) are immiscible beyond 20% PBS content based on the evidence of two distinct melting peaks obtained from modulated Differential Scanning Calorimetry results [96]. Nonetheless, PLA/PBS blends with over 40% PBS content show crystallization-induced phase separation, which creates a strong dual phased polymer [52], [138].

In a molecular dynamic simulation by Lin et al. [139], PLA and PBS blends showed good compatibility at all compositions; a feature that was attributed to the

formation of hydrogen and van der Waals bonds between constituting elements of PLA and PBS polymer chains [139]. These findings suggest that there may be some level of miscibility between PLA and PBS, more likely at low PBS loadings and in the amorphous phase. However, with the aim of adopting PLA/PBS blends and composites as filaments for extrusion-based AM, the choice of formulation would need to provide sufficient balance between miscibility, processability, and functionality in achieving 3D printability and end-use part functionality. In other research activities that have attempted to establish and improve the compatibility, miscibility and general physical properties of PLA/PBS (or BioPBS) composites; organoclay, carbon black, carbon nanotubes (CNTs) and titanium oxide (TiO_2) have been used in some cases with compatibilising or functionalizing agents [107] [140], [141], [142], [143].

In an incompatible blend of PLLA and PBS, twice-functionalized organoclay (TFC) was melt mixed into the bio-composite PLLA/PBS blend morphology [144]. TFC was exfoliated to fill the PLLA matrix regions. At 2 wt.% TFC content, a constant domain size was observed in the PLLA matrix. However, at 5 wt.% TFC content, the dispersion of co-existing exfoliated and intercalated TFC particles were seen in both PLA and PBS domains [144]. In another case, Wang et al. [140] prepared PLA/PBS/rGO nanocomposites via in-situ thermal reduction of graphene oxide using a masterbatch melt blending approach. This study found that an increasing concentration of rGO greatly influenced the morphological and physicochemical properties, especially by improving the composite thermal stability, and compatibility between the PLA and PBS phases [140].

Carbon black has been used for PBS/PLA-based nanocomposite fabrication. In a work by Xuemei Wang et al., carbon black was used to develop a ternary material system, also made of PBS and PLA domains; with the aim of overcoming the issues of immiscibility between the two polyesters [141] . On compounding, carbon black was found to be selectively dispersed in the PBS phase, due to the rheological properties of the constituents. It was also supposed that an increasing viscosity of the PBS phase at certain temperatures prevents or limits coalescence

with the PLA phase. However, the mechanical and thermal stability properties improved [141].

Melt compounding and compression moulding methods were used to process and make bioresorbable nanocomposite samples with varying contents of CNTs and TiO_2 in a PLLA/poly butylene succinate co-lactate (PBSL) blend [142]. The PLLA/PBSL/CNT nanocomposites were found to have higher flexural strength and modulus compared to the PLLA/PBSL/TiO_2 nanocomposites at the same filler loading. However, the addition of TiO_2 nanofillers improved the bioactivity of the PLLA/PBSL blend by forming bone-like apatite particles on the surface of the nanocomposite after 7 days of immersion in simulated body fluid. In the PLLA/PBSL/TiO_2 nanocomposite, water intake was increased with increasing TiO_2 content. However, in PLLA/PBSL/CNT, water absorption increases only similarly to the PLLA/PBSL blend, thereby indicating a limiting bioresorbable behaviour of PLLA/PBSL/CNT when compared to TiO_2-filled nanocomposites.

In the research work by [107], carbon nanotube and cloisite 15A were individually and simultaneously dispersed as reinforcing fillers into PBS/PLA blend using PBSL as a compatibilizer [107]. Morphological results showed that the CNTs distributed in the PBS matrix while the cloisite 15A particles are selectively located in the dispersed PLA domains. The addition of only cloisite 15A produced a quasi-co-continuous PLA/PBS morphology, while a nucleating-effect was reported for CNTs in both the PLA and PBS domains. However, cloisite 15A only showed a nucleating effect in the PLA phase [107]. Furthermore, CNTs were also found to have greater influence on the rheological properties of the material [107]. Overall, the composites containing either 1 or 3 parts per hundred resins (phr) of Cloisite 15A or CNTs [107] lead up to 2.8x higher tensile strength, 4.2x higher tensile modulus, and 11x more electrical resistivity (at 3 phr CNT loading). Furthermore, an electrical percolation threshold was found at a 0.5phr loading of cloisite 15A. Importantly, the improved mechanical properties of the fabricated PLA/PBS-based nanocomposites strongly depend on homogeneity, dispersion state, miscibility of dispersed phases, and strength of interaction between the

polymer matrix and other composing material in the form of fibres, particles, and/or sheets [107].

2.5.2.4 State of the art research on PLA/PBS (or PLA/BioPBS)-based composites in FDM-based AM applications

Two key research groups investigated the use of PLA/PBS (or PLA/BioPBS)-based composites for FDM-based AM applications [52], [138]. Both groups focused on establishing links between composition of PLA/PBS (or PLA/BioPBS) blends without additives, compatibilizers, catalysts and 3D-printability (using FDM or FFF), with further results on the mechanical and interlayer properties of fabricated parts [52], [138]. Table 2-4 shows the approaches used for PLA and PBS or BioPBS pellet conditioning, PLA/PBS or PLA/BioPBS composite filament fabrication, and 3DP of test samples. However, the approaches reported in these works are varied, and appear to individually lack some detail required for developing filament fabrication and 3DP standards, a key aspect of furthering the effective adoption of extrusion-based AM, perhaps for specific industries and applications. Table 2-5 shows the mechanical properties of PLA/PBS or PLA/BioPBS parts produced using injection moulding by [52], and using 3D-printing by Qahtani et al. [138]. The results show highest tensile strength property for the formulation containing 10% PBS, which is comparable to that of pure PLA. However, increasing PBS or BioPBS content reduces tensile strength, while simultaneously increasing elongation at break. Furthermore, tensile modulus was found to be lower for parts with 40 wt.% PBS content when compared to parts with 20 wt.% PBS, thereby highlighting an expected effect of PBS (or BioPBS) in PLA/PBS-based composites.

From the collective research works on PLA/PBS (or BioPBS)-based composite and 3DP filaments used for extrusion-based AM via FDM-based 3DP technology, it was found that filaments with PBS or BioPBS content above 50 wt.% show an increased level of distortion of the extruded material [52], which is due to the increased coefficient of linear thermal expansion of the PBS material in the formulation, which can effectively lead to inaccurately printed parts, i.e., assuming other issues such as clumps, strings, dimensional inaccuracies, voids, and cavities, which can also limit an accurate print, are also

prevented. Furthermore, tensile strength, flexural strength, and Young's modulus all decrease with an increasing content of PBS (or BioPBS). Moreover, PBS is found to act as a nucleating agent for PLA as earlier highlighted, of which Qahtani et al. [138] established that with as little as 10 wt.% PBS content, the crystallinity of the PLA phase was increased from 7.1% to 21.2%. This results in the PLA/PBS (90/10) formulation having the greatest tensile strength of all the investigated formulations, while also showing greater elongation at break than the blend with 20 wt.% PBS. Nonetheless, upon addition of PBS (up to 50 wt.% content), the crystallinity of the PLA phase does not improve beyond 21.2%. However, increasing the PBS or BioPBS content beyond 20 wt.% causes immiscibility and incompatibility in the blends but compatibility and miscibility of BioPBS in PLA is importantly considered good around 8.4 – 10 wt.% PBS (or BioPBS). In terms of printability, 215 – 245 °C was found to be the optimum processing temperature range for FDM-based 3DP of PLA/PBS (or BioPBS) blends that contain up to 40 wt.% PBS (or BioPBS). Nonetheless, the PLA60/BioPBS40 blend was identified as an optimum composition for use in FDM 3DP [52].

Table 2-4 Reported parametric conditions used for filament fabrication and FDM 3DP' of PLA/PBS (or BioPBS)-based composites [52], [138]**.**

Authors	Pre-processing Conditioning	Melt Blending	Filament Extrusion Parameters	Controlling 3DP Parameters (for FDM)
Ou-Yang et al. (2018)	Both PLA and PBS are oven-dried at 65 °C for 12 hrs	Melt blended and extruded via temperature profile: 150-170-180-185 °C. No Screw speed information No Screw diameter information Cooled to R.T. Then Oven conditioning	Extrusion speed: 10-30 rpm Extrusion temp. profile: 145-150-160 °C (extrusion die @150 °C) Then oven conditioning	190 °C nozzle temperature 23 °C print-bed temperature Printing speed: 25 mm/s 2.9 mm layer thickness 45°/−45° raster angle.
Qahtani et al. (2019)	PLA is oven-dried at 70 °C for 4 hrs. BioPBS is oven-dried at 70 °C for 12 hrs	Melt blended and extruded at 190 °C, using screw speed of 100 rpm, Screw diameter: 27 mm, L/D: 48:1 No Cooling info.	Not reported	250 °C nozzle temperature, 60 °C print-bed temperature, Printing speed: 60 mm/s 2.25 mm layer thickness 45°/−45° raster angle.

Table 2-5 PLA/BioPBS formulations with corresponding results of their injection moulded [52] **and 3D-printed** [138] **part's mechanical properties.**

	Ou Yang et al. (2018) – used PBS [52]			**Qahtani et al. (2019) – used BioPBS** [138]	
PLA/PBS filament composition	Tensile Strength (MPa)	Tensile Modulus (GPa)	Elongation at break (%)	Tensile Strength (MPa)	Tensile Modulus (GPa)
100/0	n/a	n/a	n/a	66.2	n/a
90/10	n/a	n/a	n/a	77	n/a
80/20	55.6	2.1	93	64.9	3.0
60/40	51.2	2.0	159	57.1	2.4
0/100	41.5	0.55	324	n/a	n/a

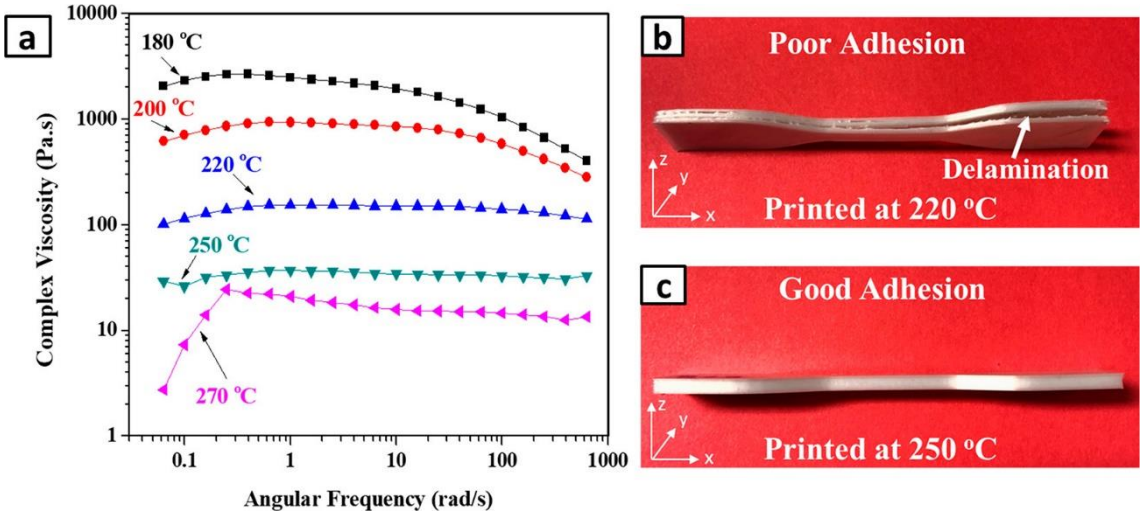

Figure 2-9 (a) Complex viscosities of PLA/BioPBS (70/30) blends as a function of angular frequency; (b) FDM-Printed dog-bone specimen printed at 220 °C , using PLA/BioPBS (70/30) filament formulation showing delamination, and (c) FDM-Printed dog-bone specimen printed (reprinted with permission from [138]**.**

Figure 2-9 shows the complex viscosity of the printable PLA70/BioPBS30 formulation with respect to prospective printing temperatures. The results indicate an effective viscosity for the PLA70/BioPBS30 filament, which is between 20 and 50 Pa.s, and represents an appropriate value for improving interlayer adhesion of resulting FDM-printed layers [138]. According to the findings, the limited compatibility between PLA and BioPBS does not hinder successful printing but may lead to limited physical and mechanical properties. The latest literature findings in Figure 2-9 also indicate that PLA70/BioPBS30 blends and filaments can be used for successful FDM-based 3DP of oriented horizontally- oriented dog-bone parts with good interlayer bonding at temperatures around 250 °C, which suggests a stronger interlayer bond strength than that of similarly oriented printed parts printed at 220 °C. However, in another set of results by Ou-yang et al. [52], the interlayer strength of vertically oriented FDM 3D-printed samples were assessed. PLA/BioPBS compositions of 0/100, 20/80, 40/60, and 60/40 were used to print vertical dog-bone structures at printing temperatures between 190 °C and 230 °C, and the results are shown in Table 2-6 [52]. At these printing temperatures, it was found that printing with PLA/BioPBS blends with higher BioPBS content resulted in better interlayer bonding strength, which was understood to be a consequence of the decrease in zero-shear viscosity of the melt blends containing more BioPBS [52]. However, considering the printed PLA/BioPBS (70/30) formulation presented in Figure 2-9 (c), and with reference to vertically (ZX) oriented PLA60/BioPBS40 parts, printed at 230 °C by [138], the vertically oriented part results show the least interlayer strength performance of the assessed formulations [138]. This is probably a result of the 230 °C processing temperature not being high enough to sufficiently reduce the zero-shear viscosity of the PLA phase, which would consequently improve interfacial interactions between layers This observation suggests that the interlayer bond quality obtained for the PLA/BioPBS (70/30) part in Figure 2-9 (c) is a function of both higher PLA content and higher (250 °C) processing temperature. Furthermore, it also shows that as the BioPBS content increases and that of PLA decreases, the interlayer bond quality depends less on higher print processing

temperature, and more so on the more-easily attainable low zero-shear viscosity of PBS in relation to PLA at typical printing temperatures.

Table 2-6 Existing information on Interlayer strength of PLA/BioPBS-based parts (using specific 3DP strategy) [52]

3DP Strategy	Filament Material Composition	Print Temperature (°C)	Interlayer Strength (MPa)
No heated print-bed Printing head speed: 25 mm/s 0.1 mm layer thickness 45°/−45° raster angle.	BioPBS100	210	25
	PLA20/BioPBS80	210	20.5
	PLA40/BioPBS60	210	19.6
	PLA60/BioPBS40	190	21.4
	PLA60/BioPBS40	200	19.5
	PLA60/BioPBS40	210	18.4
	PLA60/BioPBS40	230	16.5

2.6 Summary of literature review

Based on the literature, sufficient limitations in the application of bio-based thermoplastic composites for extrusion-based AM are present. PLA and PLA/PBS (or BioPBS) blends were found to hold some promise for expanding the range of biobased, biocompatible, and renewable resource materials used in additive manufacturing processes across diverse industries and sectors. Nonetheless, reports on the fabrication of 3DP filaments are rare, and there is very limited research and reporting covering the fabrication and use of PLA/BioPBS-based filaments in FDM extrusion-based AM. Based on the review, PLA/BioPBS-based composites with a 20 wt.% PBS loading represent an upper limit for BioPBS content, for which miscibility between the PLA and PBS components can be achieved; an important factor for printability and end-part performance reliability. The PLA/BioPBS-based composite material system was

also found to show increasing coefficient of linear thermal expansion (CLTE), which increases with increasing PBS content and thereby leading to dimensional changes upon material deposition and part formation; a result that was attributed to the inherent crystallization behaviour of PBS (or BioPBS) material. Consequently, the crystalline behaviour and state of the BioPBS phase appears to have a significant influence on the filament material processability, printability, thermomechanical and degradation ability, which are key aspects of fundamental design considerations that need to be understood during the development of a robust PLA/BioPBS-based material system that is suitable for an effective FDM extrusion-based AM process cycle.

During the production of material filaments, the entire fabrication process typically involves a direct filament extrusion (FE) process, which typically uses a short-barrel single-screw extruder. However, for blend and composite filament fabrication, a single-screw extruder with a short barrel presents limitations to effective mixing and efficient use of processing time and costs. Hence, a single or twin-screw extruder with longer-barrel is preferred for simpler and cost-effective industrial scale extrusion and composite formulation processes [95]. More specifically, fabrication of thermoplastic-based composites involves a melt blending (MB) or melt compounding (MC) type of process to create the formulated material system. In the context of melt processing, MB refers to use of only two or more thermoplastic materials, while MC refers to the use of single or multiple thermoplastics and another alternative material (e.g., ceramic, metallic or graphitic materials) in processing of thermoplastic composites. Regardless of the MB or MC approach used, most fabricators employ a specialized short-barrel single-screw filament extruder to subsequently extrude, cool, and collect the typical 1.75 mm or 2.85 mm diameter 3DP filaments required for 3DP. However, as thermoplastic polymer composites develop, there could be valid arguments for developing more specialized longer-barrel single and twin-screw filament extrusion systems that effectively facilitates the fabrication of advanced thermoplastic composite filaments.

From the perspective of developing more renewable, biodegradable, and multifunctional materials, the available literature indicates significant opportunities for creating, consolidating, validating, and developing knowledge on the thermomechanical, morphological, and end-part tensile mechanical and interlayer strength properties associated with PLA/BioPBS-based filament formulations and their FDM-based 3D-printed parts. Of the discussed PLA/BioPBS formulations, higher PBS contents in PLA/BioPBS (70/30) causes good interlayer bond strength, while lower PBS content like in PLA/BioPBS (90/10) causes good miscibility and tensile mechanical properties. Based on this understanding, and the need for processable, printable, and multifunctional materials, PLA/BioPBS (80/20)-based filament formulations are explored for filament processing and properties, rheology, printability, and 3D-printed part tensile mechanical properties. The findings obtained can ultimately be used for making deductions of process-property relationships that exist between material formulation, filament fabrication route, 3DP strategy, and part performance.

3 Project methodology

3.1 Materials

Due to environmental concerns, the most available and cost-effective renewable polymer, PLA, has been selected as matrix material for the development of PLA/BioPBS-based (80/20) blend and composites as 3D printing filament materials for FDM-based 3DP, especially as BioPBS offers great complementarity of properties for tuning the resulting material properties. Hence, for this work, transparent PLA Ingeo 2003D was obtained from Nature Works LLC, with a melt flow rate of 0.6 g/min (210°C, 2.16 kg) [129]. While BioPBS FZ91PB, a 50% bio-based PBS, was obtained from Mitsubishi Chemicals MCPP with a melt flow rate of 0.5 g/min (at 190 °C, 2.16 kg) [130]. In the formulation of PLA/BioPBS (80/20)-based composites, relatively small amounts of the advanced renewable nanomaterials, i.e., hydrophilic bentonite nano-clay (HbnC) and rGO, which can offer multifunctional capabilities, are introduced into the PLA/BioPBS (80/20)-based formulation and explored similarly to the PLA/BioPBS (80/20) blend.

HbnC was purchased from Sigma Aldrich with the chemical formular $H_2Al_2O_6Si$, a light tan to brown colour, average particle diameter of <25 µm, bulk density of 600-1500 kg/m^3, and molecular weight of 180.1 g, and was used without any pre-conditioning or functionalization steps [145]. The as received (as-R) product was stored in an airtight container and used under normal room atmospheric conditions. Meanwhile, reduced graphene oxide (rGO)**,** a very light, fluffy, and odourless black powder was obtained from Adnano technologies PLC and was reported by the supplier as having 5 – 10 wt.% oxygen content, thickness of 0.8 - 2 nm, lateral size of 5-10 µm, surface area of 80 – 200 m^2/g, and bulk density of 0.03 g/cm^3. Hydrogen, nitrogen, and sulphur were also reported to make up 1-2%, 1-2%, and <1 % of the rGO content respectively [146].

3.1.1 Filament formulations and nomenclature

As emphasised so far, this research work focuses mainly on the 80 wt.% PLA and 20 wt.% BioPBS blend and composites, which includes the PLA/BioPBS

(80/20) blend and its PLA/BioPBS-based composites made with the addition of HbnC or rGO nanomaterials. The chosen PLA/BioPBS (80/20) formulation was based on the potential for maximizing cost-effectiveness, material processability, printability, biodegradability, and printed part tensile/interlayer mechanical properties. In the formulation nomenclature, the dominant matrix material is represented first as PLA80, while, the dispersing phase, BioPBS, at 20 wt.%, is denoted as BioPBS20, and hence represented as PLA80/BioPBS20. On addition of the HbnC or rGO nanomaterials, the formulation nomenclature is represented as PLA80/BioPBS20/HbnCX or PLA80/BioPBS20/rGOX respectively, where 'X' represents the nanomaterial filler addition with units in 'part per hundred resins' (i.e., X phr). A relatively low loading of nanomaterial at about 1 phr was chosen as an appropriate composition for assessing the nanomaterial influence on processability, fabricated filament property, and final 3D-printed part properties, while reducing overall material cost, and limiting the possibility of the nanomaterial damaging the internal linings of the processing equipment.

3.1.2 Pre-processing conditioning

During the pre-processing stages, and for each filament material formulation, the as-received (as-R) PLA and as-R BioPBS materials were weighed at an 80:20 wt.% ratio respectively using a laboratory scale, and then added to a dry sample bag, which was tumbled severally to enable out-of-machine granular pellet mixing. After weighing the neat PLA and neat BioPBS pellets, the biopolymers were dried in a conventional oven at 60 °C for 20-24 hours to remove moisture and possible effects of hydrothermal degradation during processing. This was carried out before each use in either a direct filament extrusion (FE) or two-step (MB-FE or MC-FE) composite filament fabrication process. Additionally, the nanomaterials, HbnC and rGO were weighed under an externally local exhaust ventilation (LEV) system. In this study, the nanomaterials were used without any pre-conditioning treatment and were stored in a tight container to limit moisture intake, especially for the hydrophilic nano-clay material.

3.1.3 Filament fabrication of PLA80/BioPBS20-based composites

3.1.3.1 Direct filament extrusion route

During fabrication, the conditioned PLA and BioPBS polymer pellets were used to make 3DP filaments with a 1.75 mm diameter. The direct FE process route involved direct addition of either as-R PLA, as-R BioPBS, or mixed as-R PLA + as-R BioPBS pellets into the hopper of a single-screw Filabot EX2 extruder. The extruder was set to an extrusion temperature of about 170 – 180 °C (from barrel to die), which was based on the melting points of the PLA and BioPBS polymers as presented in the literature review but using a single-screw extrusion speed of about 14 rpm - based on suitability for controllable extrusion of 1.75 mm filaments. The direct FE process was carried out at room temperature in a room with limited air flow disruption. The Filabot EX2 extruder was equipped with cooling fans, a filament diameter measuring instrument, and filament winder as shown in Figure 3-1, which enables a good level of continuous filament production with sufficient diameter control.

Figure 3-1 Filabot EX2 equipped with a set of cooling fans, diameter measuring device, and filament winder and spooling unit.

3.1.3.2 Two-step filament fabrication route

In the alternative two-stage filament fabrication route, the processing of PLA80/BioPBS20, PLA80/BioPBS20/HbnC1, and PLA80/PBS20/rGO1 filaments were achieved by either melt blending (MB) of the constituting polymer materials in the PLA80/BioPBS20 formulation, or by melt compounding (MC) of the constituting polymer and nanomaterials in the PLA80/BioPBS20/HbnC1phr and PLA80/BioPBS20/rGO1phr formulations. Both MB and MC are polymer melt-mixing processes that are cost-effective for the combination of two or more

polymers in the case of making polymer blends; or for the combination of other distinct materials with polymers (e.g., ceramics) in the case of making polymer composites. In this research, the twin-screw extruder used for MB or MC was equipped with intermeshing and counter-rotating 21 mm screws that were used under a temperature profile of 130-165-170-180-190 °C (from infeed to die section) and at an extrusion speed of about 60-80 rpm – which is based on the extrusion profiles utilised by Ou-Yang et al. [52] and Qahtani et al. [138]. After the material was mixed in the barrel, it was extruded, cooled, and pelletized, ready for use in the fabrication of 1.75 mm filaments. The setup used for the MB or MC process can be visualized in Figure 3-2. Machine controls are identified by the red arrows, while the material flow path of PLA and BioPBS materials are shown in orange and green up until the realization of pelletized PLA/BioPBS-based material.

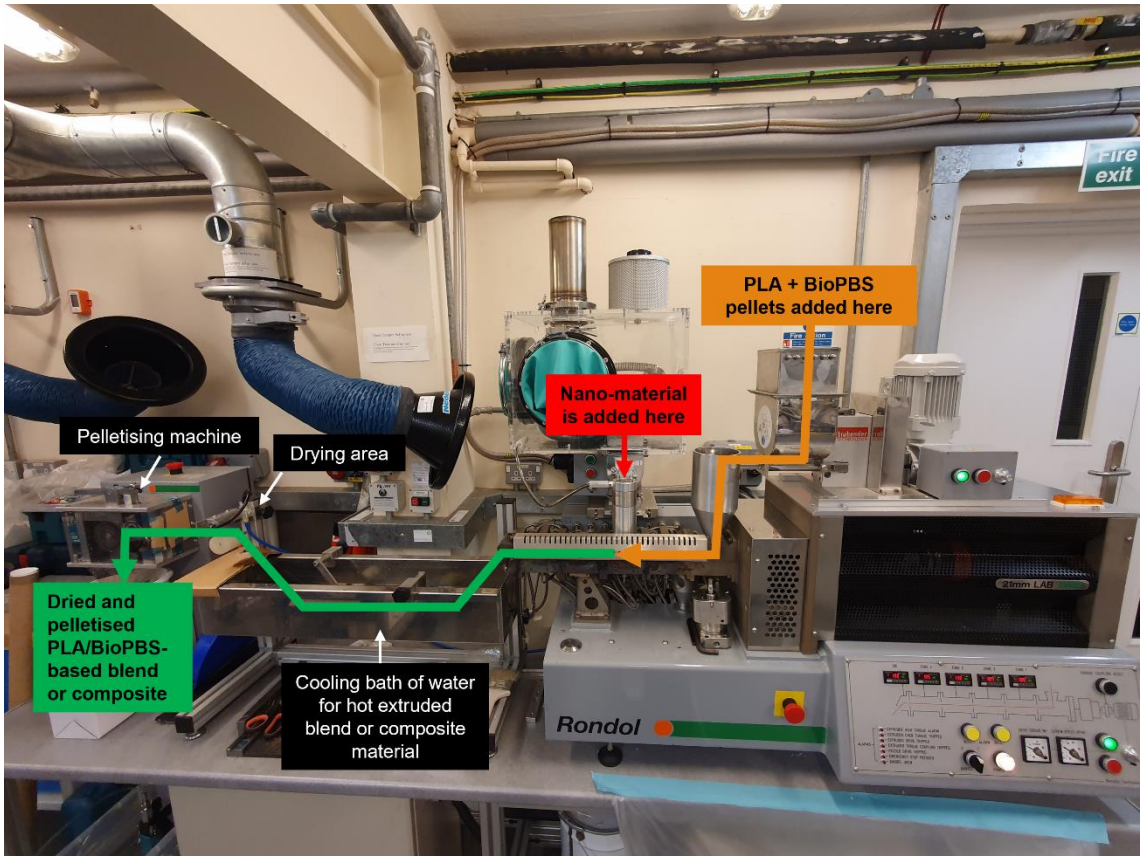

Figure 3-2 Twin-screw extrusion setup for production of PLA80/BioPBS20-based blend and composites.

For the process that used the MB approach, PLA80/BioPBS20 blends were put through the twin-screw extruder once. Meanwhile, for processes that used MC, i.e., the PLA80/BioPBS20-based composites containing HbnC or rGO, were put through the twin-screw extruder twice and thrice respectively - as depicted in more detail in Figure 3-3. The multiple pass through of the composite formulations were used to facilitate better shear mixing, nanomaterial intercalation and dispersion of HbnC or rGO fillers in the resulting composite material. Nonetheless, the objective was also to maintain a minimal number of passes through the twin-screw extruder; a useful factor for achieving shorter, simpler, and cost-effective production process cycles. The highlighted approach was helpful in developing fundamental knowledge and understanding of the effect of simple and cost-effective PLA/BioPBS20-based composite processing routes on resulting 3DP filament and their subsequently 3D-printed part properties. Following the MB or MC process, the obtained pellets were used with the Filabot EX2 extruder to produce 3DP filaments that were stored in a desiccant – ready for use in FDM-based 3DP.

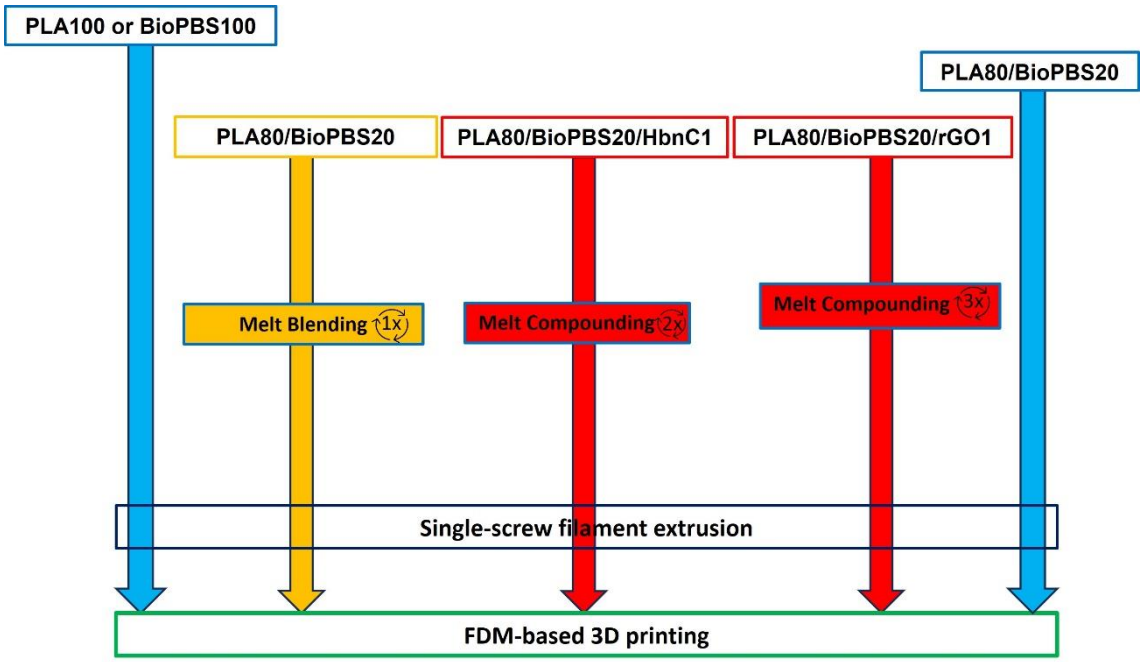

Figure 3-3 Material formulations and processing routes for filament fabrication and FDM-based 3DP.

3.2 Experimental plan

An experimental research plan was created to test the effects of relatively simple and cost-effective AM routes that can add value to the production process of PLA80/PBS20-based composites (see Table 3-1). The plan allows for production of designated filament material formulations and the characterization of their realized 3DP filament materials. The fabricated filaments were used for 3D-printing of dog-bone shaped parts that were further used to assess printability and tensile/interlayer-bond mechanical properties. In the experimental research plan, a direct FE approach is used to produce PLA100, BioPBS100, and PLA80/BioPBS20 filament formulations as reference filaments. Furthermore, the alternative two-step filament fabrication approach, i.e., via MB-FE or MC-FE was used to produce the PLA80/BioPBS20, PLA80/BioPBS20/HbnC1, and PLA80/BioPBS20/rGO1 filament formulations.

Table 3-1 Experimental research plan for fabrication of composite filaments.

	Constituent materials				Melt processing machine controls	
Filament Formulation	**PLA (%)**	**BioPBS (%)**	**HbnC (phr)**	**rGO (phr)**	**MB/MC**	**FE**
PLA100 FE	100	-	-	-	-	14 revolutions per minute (rpm), 12:1 length (L) /diameter(D) ratio, screw pitch: 1.27 cm, temperatur e. profile: 170-180 °C
BioPBS100 FE	-	100	-	-	-	14 rpm, 12:1 L/D ratio, screw pitch: 1.27 cm, temperatur e profile: 170-180 °C
PLA80/BioPB S20 FE	80	20	-	-	-	14 rpm, 12:1 L/D ratio, screw pitch: 1.27 cm, temperatur e profile:

						170-180 °C
PLA80/BioPBS20 MB-FE	80	20	-	-	70-80 rpm, 30:1 L/D ratio, temperature profile: 130-165-170-180-190 °C	14 rpm, 12:1 L/D ratio, screw pitch: 1.27 cm, temp. profile: 170-180 °C
PLA80/BioPBS20/HbnC1 MC-FE	80	20	1	-	70-80 rpm, 30:1 L/D ratio, temperature profile: 130-165-170-180-190 °C	14 rpm, 12:1 L/D ratio, screw pitch: 1.27 cm, temperature profile: 170-180 °C
PLA80/BioPBS20/rGO1 MC-FE	80	20	-	1	70-80 rpm, 30:1 L/D ratio, temperature profile: 130-165-170-180-190 °C	14 rpm, 12:1 L/D ratio, screw pitch: 1.27 cm, temperature profile: 170-180 °C

In Table 3-2, the nomenclature used to identify the as-R materials, fabricated filament, and 3D-printed parts is highlighted. From the list of nomenclatures, as-R materials represent unmodified versions of the respective constituent materials used throughout the study. Meanwhile, fabricated filaments are represented such as with PLA FE, which highlights that a 100% PLA filament material formulation processed via direct filament extrusion only is used. Alternatively, PLA80/BioPBS20 MB-FE represents a filament formulation with 80% PLA content and 20% BioPBS content processed via melt blending and then direct filament extrusion. Similarly, PLA80/BioPBS20/rGO1phr MC-FE represents a filament formulation with 80% PLA content and 20% BioPBS content processed via melt compounding and then direct filament extrusion. And lastly, the nomenclature for 3D-printed parts like PLA80/BioPBS20/HbnC1phr MC-FE-3DP represent a filament formulation with 80% PLA content and 20% BioPBS content processed via melt compounding, direct filament extrusion, and then 3DP of either in-plane or out-of-plane (90°) vertically oriented dog bone parts.

Table 3-2 Nomenclature for neat as-R materials, extruded filaments, and 3D-printed parts either used or fabricated at different experimental stages.

As-R materials	Fabricated filaments	3D-printed parts
PLA, BioPBS, HbnC, rGO.	PLA100 FE, PBS100 FE, PLA80/BioPBS20 FE, PLA80/BioPBS20 MB-FE, PLA80/BioPBS20/HbnC1 MC-FE, PLA80/BioPBS20/rGO1 MC-FE.	PLA100 FE-3DP, PLA80/BioPBS20 FE-3DP, PLA80/BioPBS20 MB-FE-3DP, PLA80/BioPBS20/HbnC1 MC-FE-3DP, PLA80/BioPBS20/rGO1 MC-FE-3DP.

3.3 Fabrication of 3D-printed and cast parts.

3.3.1 FDM-based 3DP of dog-bone parts

The FDM-based 3DP process used to produce dog-bone parts and samples commenced with the design of a 3D computer model of a dog-bone part based on ISO 527-2/1BA standard. The corresponding dimensions of the part as indicated by Figure 3-4 and Table 3-3 was used to create a computer-based 3D model. In this process, the Solid Works 2019 software was used to design and develop a 3D computer model of the identified dog-bone geometry and structure. The developed dog-bone model in Solid works file format was saved and exported in stl file format as a tessellated model of the initially developed 3D model. In a subsequent step, the tessellated model was imported into Cura (version 4.11.0/5.2.1/5.2.2) and was then oriented on-face. These were therefore horizontally oriented and duplicated as shown in Figure 3-5 to allow for the 3DP of 6 specimens in total; for which specific constant 3DP controls were set - as defined in Table 3-4; hence, also producing similar print paths and patterns.

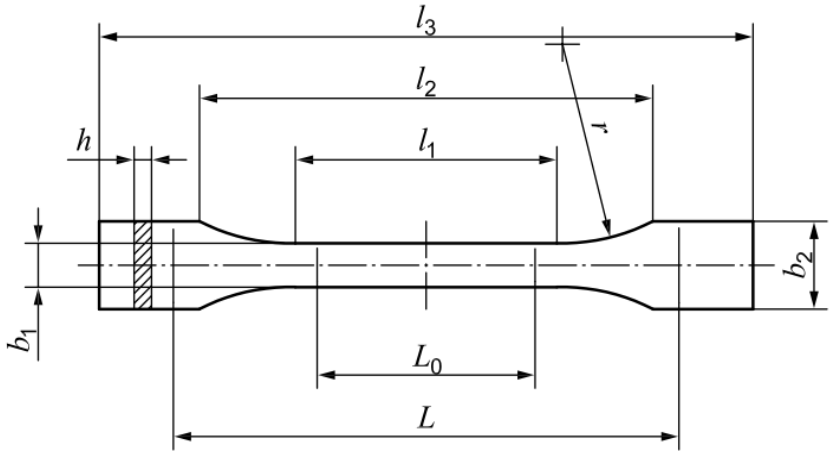

Figure 3-4 ISO 527-2/1BA tensile-testing standard - for horizontally and vertically oriented specimens. Reprinted from [147]**.**

Once all parameters were set, the Cura software was used to slice the model, creating a print-path or g-code instruction for the FDM-based 3DP machine. Then a memory card was used to transfer the G-code file to the AnyCubic Chiron FDM 3DP printer, which was equipped with a single-head nozzle and an open-design 400 × 400 × 450 mm^3 build volume. Using the fabricated PLA FE,

PLA80/BioPBS20 direct FE, PLA80/BioPBS20 MB-FE, PLA80/BioPBS20/HbnC1 MC-FE, and PLA80/BioPBS20/rGO1 MC-FE filaments, dog-bone specimens were 3D printed to enable comparative analyses of the fabricated parts. For experimental purposes, following an initial FDM-based 3DP attempt at 210 °C print temperature, 40 mm/s print speed, and 0.2 mm layer height, a set of varied FDM-based 3DP controls were sequentially developed and applied as shown in Table 3-5**.** These were used for each filament formulation and meant that four sets of samples were fabricated for each filament formulation excluding that of BioPBS100 FE filament. Notably, the BioPBS100 FE filament was not used because it was found to unsuccessfully extrude and form an accurate part during the 3DP process.

Table 3-3 Specifications of specimen dimensions based on ISO 527-2/1BA shown in Figure 3-4.

	Specimen type	**Dimensions (mm)**
l_3	Overall length	75
l_1	Length of narrow parallel-sided portion	30 ±0.5
r	Radius	30
l_2	Distance between broad parallel-sided portion	58 ± 2
b_2	Width at ends	10 ± 0.5
b_1	Width at barrow position	5 ± 0.5
h	Thickness	2
L_0	Gauge length	25 ± 0.5
L	Initial distance between grips	l_2 + 2.5 (± 0.5)
Note: The specimen type 1BA is proportionally scaled to ISO 527-2/1B with a reduction factor of 1:2		

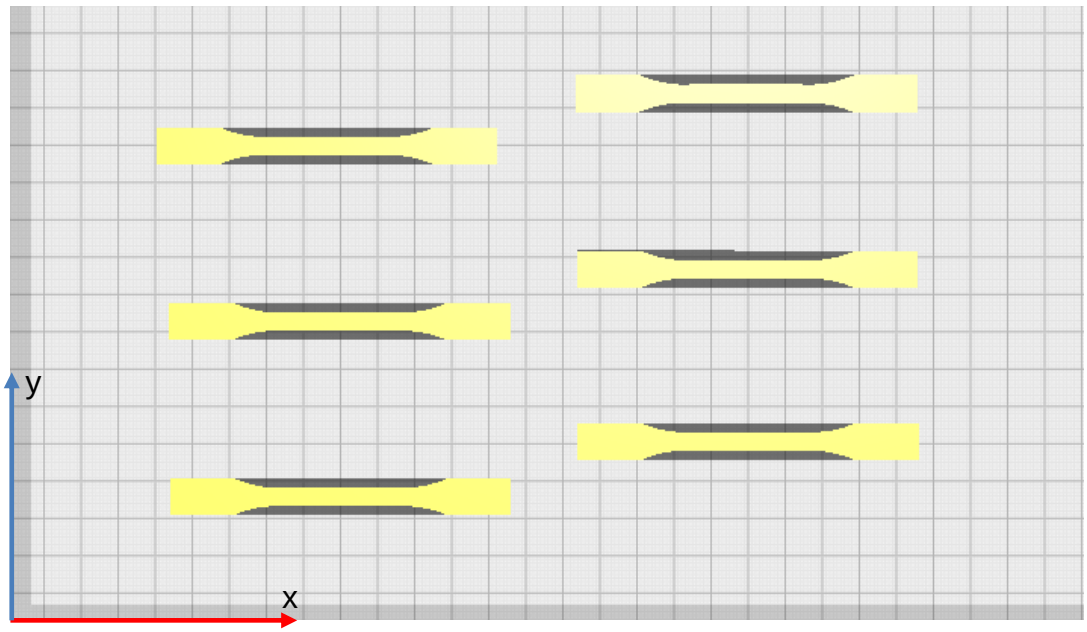

Figure 3-5 Set up of horizontally oriented specimens for FDM-based 3DP of dog-bone parts as seen from top view of Cura software.

Table 3-4 Constant controls set for all FDM-based 3DP.

Constant Machine Control	Chosen Value	Reason
Part infill	100%	for maximum mechanical strength of the part.
Bed temperature	60 °C	throughout print, for improved adhesion of part to bed
infill pattern/raster angle	45°/-45°	for improved strength in transverse y-direction
cooling fan	0%	to limit cooling rate of PLA, and allow for possibly higher PLA crystallization and crystallinity in final part

Table 3-5 Systematically developed parametric controls for assessing the effect of 3DP strategies on horizontally oriented 3D-printed dog-bone parts, (PT: Print Temperature, PS: Print Speed, and LH: Layer Height).

3DP strategy			
1	**2**	**3**	**4**
PT: 220 °C **PS**: 40 mm/s **LH**: 0.2 mm	**PT**: 230 °C **PS**: 60 mm/s **LH:** 0.2 mm	**PT**: 230 °C **PS**: 60 mm/s **LH:** 0.3 mm	**PT**: 230 °C **PS**: 40 mm/s **LH:** 0.2 mm

A vertically oriented dog bone model as shown in Figure 3-6 was also processed in the Cura software by tessellating and slicing the 3D model. This was followed by generation of a gcode file that is suitable for communicating the printing instructions to the 3DP machine. Subsequently, 3DP was attempted with each of the formulated and fabricated 3DP filaments. Based on the prescribed setup, and while similarly using the constant 3DP controls set for the horizontally oriented parts, the initially attempted (strategy 1) and updated (strategy 2) 3DP variable controls as shown in Table 3-6 were adopted to facilitate a workable printing process of vertically oriented dog bone parts. This was developed to help assess the level of printability and interlayer-bond properties associated with thin vertical structures printed with PLA/BioPBS20-based material formulations.

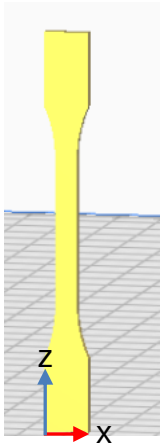

Figure 3-6 Vertically oriented dog-bone part setup for FDM-based 3DP using Any Cubic Chiron.

Table 3-6 3DP strategies for vertically oriented parts.

3DP Strategy	
1	**2**
PT: 220 °C **PS**: 40 mm/s **LH:** 0.2 mm	**PT**: 220 °C **PS**: 20 mm/s **LH:** 0.2 mm

3.3.2 Casting of PLA/BioPBS-based cylindrical plates for rheometric testing.

The rheological assessments of the developed material formulations were based on the use and therefore fabrication of cylindrical plates with a cross sectional area of about 25 mm^2. To make the cylindrical plates, a thin (1 – 1.5 mm) silicone rubber sheet with circular cut-outs of 25 mm diameter was first prepared and used with two glass plates as seen in Figure 3-7 (left), to set up a casting mould, which was further held together and secured using clips, but only after pelletised composites materials prepared by the MB or MC were loaded into the glass-backed opening of the silicone sheet. The setup, as seen in Figure 3-7 (right), was placed in an oven at 180 °C, for 45 minutes, and then removed to cool to room temperature, at room temperature. Upon cooling, the cast cylindrical plates were collected and stored. Representations of the fabricated cylindrical plates with respective nomenclature, as used in the thesis, are shown in Figure 3-8.

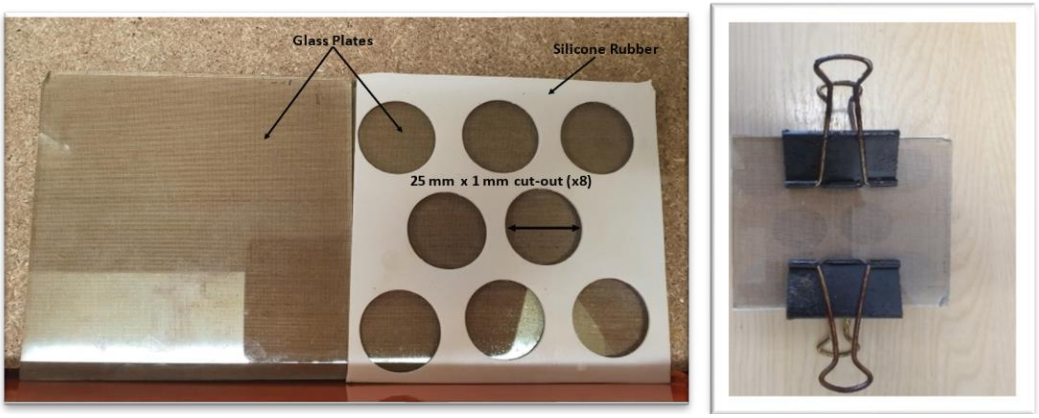

Figure 3-7 Tooling components (left) and final setup (right) for casting of PLA80/BioPBS20-based cylindrical plates.

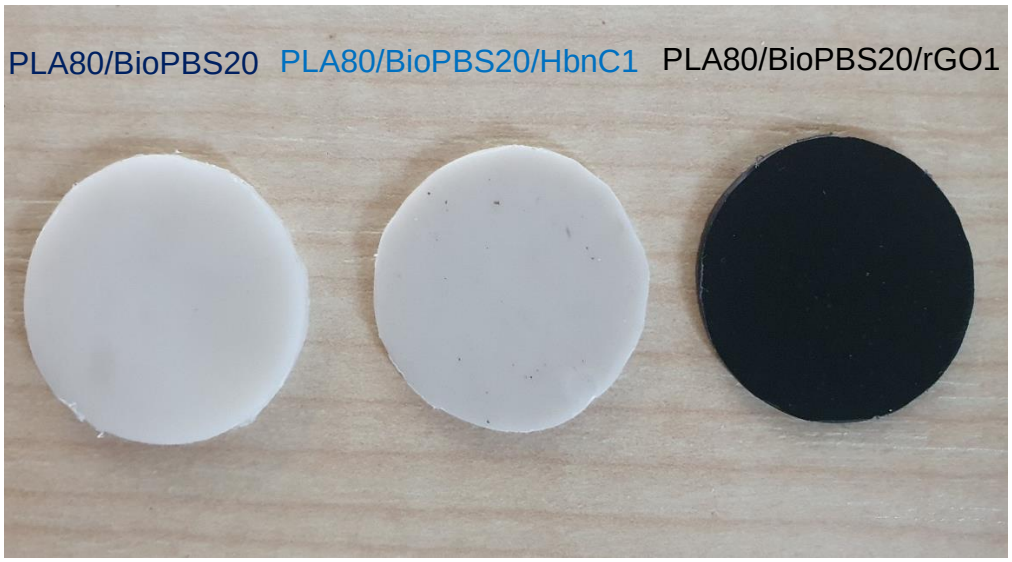

Figure 3-8 As-fabricated cylindrical plates for use in the rheological characterisation of designated filament material formulations

3.4 Material and fabricated filament characterization and part testing

3.4.1 Thermogravimetric analysis (TGA) of materials and fabricated filaments

The thermal degradation behavior of the fabricated filaments was examined using a TGA 550 from TA Instruments and was used to help identify suitable temperature limits during DSC characterization and thermal processing. In doing this, 5 – 10 mg of the filament sample was loaded onto tared platinum pans that were staged on the machine pan/specimen loading dock. Temperature ramps were set to go up to 500 °C at 10 °C/min and were run under nitrogen to allow measurements of the degradation onset temperature ($T_{deg\ (onset)}$) and degradation rates associated with the as-R PLA or as-R BioPBS material. This information was significant for defining printing temperatures and material temperature processing limits.

3.4.2 Differential scanning calorimetry (DSC) of materials and fabricated filaments

DSC was used to identify the calorimetric response of the fabricated blends and nanocomposites, with interest in changes that occurred after the pellets were put

through the filament fabrication steps. Standard aluminum pans and lids were used to create two sealed pans with one being a reference and the other being a sealed pan loaded with 5-10 mg of filament material sample. A DSC Q250 from TA Instruments, using 50 mL nitrogen supply, and a heat/cool/heat mode at 10 °C/min, was used to fingerprint three samples for each of the five fabricated filament materials. The collected heat flow and temperature data were used to determine the glass transition, cold crystallization, melting, and recrystallization behaviour of the fabricated filament materials. An illustration of the typical heating and cooling DSC curves for the as-R PLA material is shown in Figure 3-9.

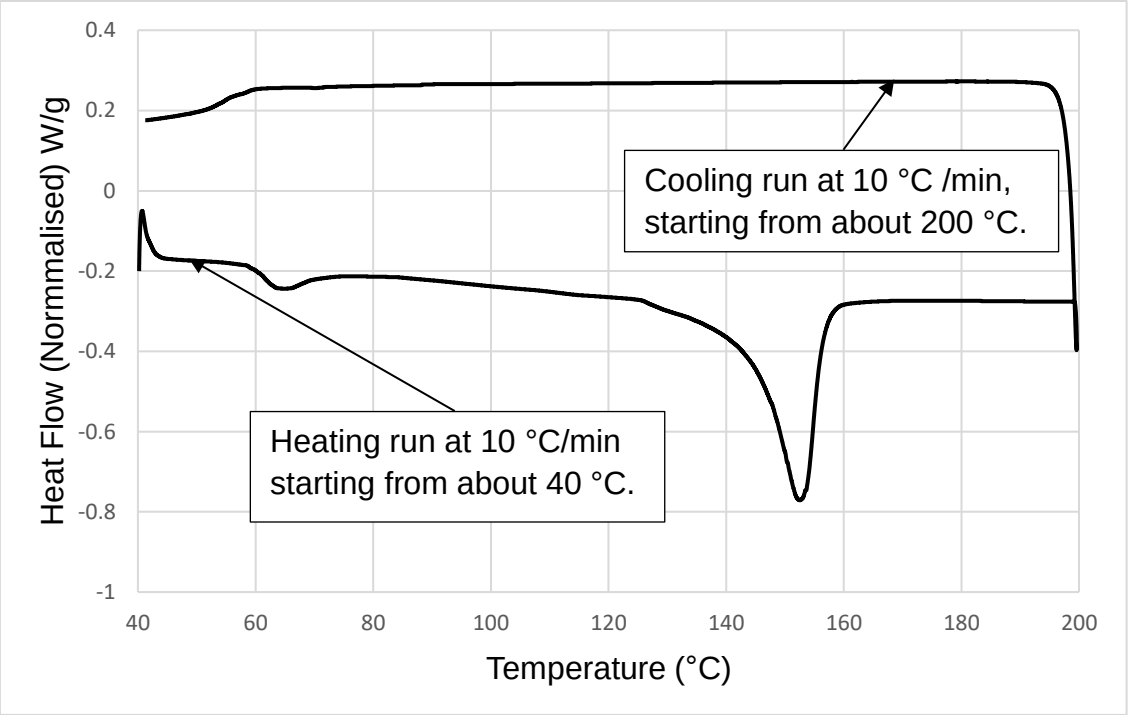

Figure 3-9 Representative DSC curve for PLA material showing calorimetric profile obtained during heating and cooling cycles at a rate of 10 °C/min.

Thermal transitions associated with T_g, onset cold crystallization temperature ($T_{cc\ (onset)}$), cold crystallization enthalpy (ΔH_{cc}), onset melting temperature ($T_{m\ (onset)}$), melting peak temperature ($T_{m\ (peak)}$), melting enthalpy (ΔH_m), recrystallization temperature (T_c), onset recrystallization temperature ($T_{c\ (onset)}$) and recrystallization enthalpy (ΔH_c) were deducible from the DSC thermographs. This was done for each category of fabricated filament materials. Consequently, this

allowed the determination of PLA and BioPBS phase crystallinity in the as-R polymeric materials; single thermoplastic filament materials; composite (PLA80/BioPBS20-based) filament materials; and nanocomposite filament material formulations. Following such results as shown in Figure 3-9, the PLA or BioPBS phase crystallinity was calculated using the formula:

$$X_c = \frac{\Delta H_m - \Delta H_{cc}}{\Delta H_f^0} \text{ x } \frac{1}{W} \text{ x } 100 \qquad \textbf{Equation 3-1}$$

where X_c is percentage crystallinity of PLA or BioPBS, ΔH_m is the enthalpy of melting, ΔH_{cc} is the enthalpy of cold crystallization, ΔH^0_f is the heat of fusion for 100% crystalline PLA (93.7 J/g) [111] or BioPBS (210 J/g) [148], and W is the weight fraction of either PLA or BioPBS in the formulation. Based on this, the calculations of PLA and BioPBS phase crystallinity were conducted using weight fraction adjustments to consider the composition of PLA and BioPBS materials for each material formulation and fabricated filament material. The results obtained were used to assess the effects of processing steps and conditions on the crystallinity of PLA and BioPBS phases in the fabricated filament, as higher BioPBS crystallinity may lead to bead or road shrinkage during printing.

3.4.3 Scanning electron microscopy (SEM) and energy dissipative x-ray spectroscopy (EDS) of materials and fabricated filaments

SEM was used for analysis of the surface morphologies obtained from cryo-fractured or tensile-fractured surfaces of fabricated PLA/BioPBS20-based filaments and their 3D-printed parts, while EDS was used to provide supporting information on the surface composition of fabricated nanomaterial-containing filament materials. A Vega 3 SEM/EDS system was used to assess the surface morphology and composition of representative cryo-fractured filaments and their tensile-fractured 3D-printed part surfaces as required. The cryo-fractured filaments were prepared at -75 °C by dipping the fabricated filament in a dewar holding about 500 ml of liquid nitrogen. The filaments were held in the dewar for 15 to 30 seconds before being removed and snapped at various points to obtain the cryo-fractured filament surfaces. Subsequently, and prior to SEM characterization, the cryo-fractured filaments were coated with a thin (10 nm)

layer of gold using a Quorum Q150T ES machine before being mounted and observed under the scanning electron microscope. For the tensile-fractured surfaces, the gold coating was also applied prior to conducting the scanning electron microscopy.

3.4.4 Rotational rheometric testing of cast PLA80/BioPBS20-based cylindrical plates.

In the rotational rheological characterization, temperature sweep tests of Cast PLA80/BioPBS20-based cylindrical plates were tested using a TA instrument Discovery HR20 instrument, equipped with an environmental temperature chamber (ETC). During this test, the cast material formulations were loaded onto a 25 mm stainless-steel plate with a drip channel, which was attached to the lower stage of the rheological testing machine. After loading the sample and closing the ETC, gaps between 1 mm and 1.5 mm were set for each sample, followed by a temperature sweep test. The temperature sweep test was started at 180 °C following a 10-second equilibration time, which was similarly repeated at subsequent intervals of 10 °C until the test was completed at 250 °C. The angular frequency applied during each sweep was set between 0.1 and 600 rad s^{-1} to aid in obtaining the complex shear viscosity values that occur at prospective 3DP temperatures. In the FDM 3DP experiments, printing/extrusion speeds of 20 - 60 mm/s were computed using the Hagen/Poiseuille formula [149]:

$$\dot{\gamma} = \frac{4V}{\pi r^3 t} \qquad \textbf{Equation 3-2}$$

where $\dot{\gamma}$ is shear rate, V is discharged volume, r is extruder nozzle radius, and t is material flow time, to calculate estimate values of the shear rate occurring during filament material melt extrusion. Upon calculation of the associated printing shear rate in hertz, the value was converted to rad/s. At this point, it was considered useful to find the power law parameters of the non-Newtonian composite by using the power law/Oswald equation [150]:

$$\eta^* = K\dot{\gamma}^{n-1} \qquad \textbf{Equation 3-3}$$

where η^* is the complex viscosity, K is a constant pre-factor or consistency index,

$\dot{\gamma}$ is the shear rate, and n is the power law index. Upon rearranging Equation 3-3, a straight-line equation was obtained as shown in Equation 3-4.

$$\log \eta^* = (n-1)\log \dot{\gamma} + \log K \qquad \textbf{Equation 3-4}$$

Before using Equation 3-4, the experimental oscillation strain rate data was collected and corrected into true shear frequency values using the Weissenberg-Rabinowicz-Mooney correction method for the point-flow-rate changes that occur at the wall of the parallel plate geometry during testing. The obtained true shear frequency was then used to calculate corresponding true viscosity values using Equation 3-5.

$$True\ viscosity = \frac{oscillation\ stress}{true\ strain\ rate} \qquad \textbf{Equation 3-5}$$

Using the angular shear frequency and true viscosity data, log-log plots of true viscosity against angular shear frequency were obtained for each PLA80/BioPBS20-based formulation at prospective printing temperatures. From these plots, $n-1$, which is the slope of the line graph, and $\log K$, which is the intercept, were used to determine the power law and consistency index values. The obtained power law parameters were used to gain insight and better understanding of the composite formulations, while importantly utilizing the power law index for correction of the calculated shear frequency (rad/s) values obtain from Equation 3-2 following developments by [151]. The corrected shear frequency was thereby ready for use in a predictive model. Consequently, a complex viscosity prediction model based on the time-temperature superposition principle (TTSP) [152] was developed to help estimate complex viscosity values of blend and nanocomposite filament formulations at chosen print temperatures and power law index-corrected shear frequency values. The Arrhenius method of TTPS was followed for constructing master curves of the polymeric materials sin the experimental tests were conducted at temperatures far greater than the material T_g. The Arrhenius equation is given below:

$$k = Ae^{\frac{-E_a}{RT}} \qquad \textbf{Equation 3-6}$$

where k is the phenomenon rate constant, E_a is the activation energy, R is the gas constant, and T is the absolute temperature of the reaction. The rate constant is a function of temperature, and between two temperatures, the equation is represented as:

$$k = Ae^{\frac{-E_a}{R}(\frac{1}{T_1}-\frac{1}{T_{ref}})} \quad \textbf{Equation 3-7}$$

where additional parameters, T_1 is the temperature sweep data to be super imposed, and T_{ref} is the reference temperature which is used for determination of the horizontal shift factor (a_T) – the key parameter required for superimposition of T_1 onto T_{ref}. Following Equation 3-7; as the controlling variable tends towards zero, k becomes approximately equal to A; hence, A becomes k_0 or k_{ref}, which is a reference reaction rate constant. Then, the equation can be rearranged as:

$$(\frac{k_1}{k_{ref}}) = e^{\frac{-E_a}{R}(\frac{1}{T_1}-\frac{1}{T_{ref}})} \quad \textbf{Equation 3-8}$$

In this equation, $\frac{k_1}{k_0}$ defines a shift factor from the reference k_0 and furthermore, by taking the logarithm of both sides of the equation, the following linear equation is obtained:

$$log_{10}(\frac{k_1}{k_{ref}}) = \frac{-E_a}{R}(\frac{1}{T_1}-\frac{1}{T_{ref}}) \quad \textbf{Equation 3-9}$$

The ratio of the rate constants in this equation can be related to the ratio of viscoelastic properties at reference and arbitrary temperatures, T_{ref} and T_1, respectively. Hence, the equation could also be rewritten as:

$$log_{10}(\frac{\mu_1}{\mu_{ref}}) = \frac{-E_a}{R}(\frac{1}{T_1}-\frac{1}{T_{ref}}) \quad \textbf{Equation 3-10}$$

Here, μ represents the apparent viscosity of the material under testing conditions. Hence, μ_1/μ_{ref} was used to calculate a_T. Consequently, the measured viscoelastic temperature sweep results were used to produce a regression model which shows the dependence of horizontal shift factor (a_T) on the temperature variable, $\frac{1}{T}$ for each PLA80/BioPBS20-based material formulation. The R^2 value

of the model was used to verify the use of the data points for master curve generation, which also validated the calculation of an associated reaction activation energy, E_a (KJ/mol), for each filament formulation. Using a reference temperature of 220 °C, the associated shift factor values of the temperature sweep results were determined and plotted against inverse temperature, according to Equation 3-11.

$$log_{10}\,(a_T) = \frac{-E_a}{R}(\frac{1}{T}) \qquad \textbf{Equation 3-11}$$

A line of best fit was used to define the activation energy, which was determined by equating the slope to $-E_a/R$. Hence, the E_a data was calculated and then further used for establishing complex viscosity values over a broader shear frequency range than was achievable from the experimental tests.

3.4.5 Tensile property and interlayer strength testing of 3D-printed parts using ISO 527-2/1BA standard.

Following filament fabrication and 3DP of parts, tensile tests were carried out to establish the tensile properties of each set of parts obtained via their specific fabrication route. Each fabricated material part included five samples each, which were measured using an electronic vernier calliper and micrometre screw gauge for deduction of dimensional values that supported calculations of tensile property values. Each specimen was mounted vertically onto an Instron 5500R 6025 machine as seen in Figure 3-10 before commencing the test. The machine was setup with a 5 KN load cell and laser extensometer to facilitate testing and data collection respectively. Consequently, load-extension data was collected for each set of 3D-printed samples that were produced according to ISO 527-2/1BA standard. Tests were carried out at strain rates of 1 mm/min. The collected data allowed the ultimate tensile stress (strength), strain at failure, tensile modulus, and tensile toughness information to be deduced for each set of samples. The interlayer test approach was carried out with the same tensile testing approach used for the horizontally oriented part; using a 1 mm/min strain rate for all 5 samples tested. The data in this case was used to determine the minimal

interlayer strength of the interlayer bonds of vertically oriented and printable PLA and PLA/BioPBS20-based parts.

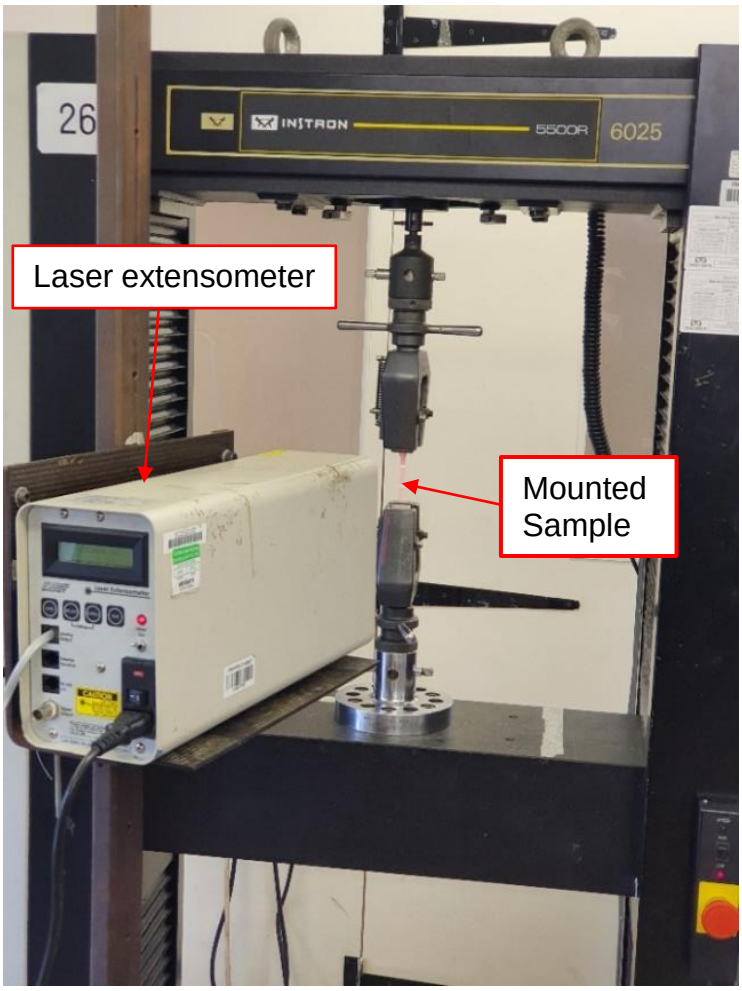

Figure 3-10 Tensile mechanical testing machine setup using laser extensometer.

4 Thermodynamic properties and phase changes in fabricated biopolymer composite filaments

4.1 Introduction

This chapter presents the thermal degradation behaviour of as-R PLA and as-R BioPBS materials under nitrogen-rich and air-rich atmosphere as well as the calorimetric response of these materials to aid in the determination of their processing temperatures and temperature limits. Furthermore, calorimetric results are also presented for PLA80/BioPBS20-based filaments and are used to explore the enthalpic phase changes that occur in the PLA and BioPBS phases within each type of 3DP filament fabricated. This is aimed at providing a better understanding of the influence of filament processing routes and nanomaterial additive on the miscibility, crystallinity, and thermal stability of the fabricated PLA80/BioPBS20-based filaments. The chapter is concluded with a summary of the identified changes in crystallinity or enthalpic response of the fabricated PLA80/BioPBS20-based 3DP filaments, which provides an understanding of material-process-property relationships that support the design of material formulation and filament fabrication processing.

4.2 Thermodynamic behaviour of thermoplastic polymers

In this section, the calorimetric and thermal degradation behaviour of as-R PLA and as-R BioPBS polymers are reported following characterization under nitrogen and air-rich atmospheres. This is used to develop knowledge on the lower and upper thermal processing limits used for PLA and BioPBS filament fabrication and 3DP processing, which further aids in the design and optimization of processing parameters.

4.2.1 Thermal degradation results of received thermoplastic polymers under nitrogen-rich and air-rich atmospheres.

Figure 4-1 and Table 4-1 show the degradation profile and mass loss results obtained for each as-R bio-based polymeric material under a nitrogen-rich and air-rich atmosphere. As observed in Figure 4-1, a single step degradation profile occurs for both the as-R PLA and as-R BioPBS polymers in both nitrogen-rich

and air-rich atmospheres. Meanwhile, Table 4-1 presents the degradation onset temperature ($T_{deg\ (onset)}$), end of degradation temperature ($T_{deg\ (end)}$), temperature at maximum degradation rate ($T_{deg\ (max\ rate)}$) and maximum degradation rate ($D_{(max\ rate)}$) of the received PLA and BioPBS polymers under nitrogen-rich and air-rich atmospheres. The results show that PLA starts degrading thermally under a nitrogen-rich atmosphere from about 341 °C. The degradation continues and reaches a maximum degradation rate at around 364 °C, at which the PLA polymer degrades at a rate of about 3.1 %/°C. Finally, the degradation process slows down reaching a plateau at around 367 °C as the mass of PLA material is completely degraded. For the as-R BioPBS polymer, it is found that under nitrogen-rich atmosphere, the onset of degradation occurs around 366 °C, and the material reaches a maximum degradation rate of about 2.3 %/°C at around 397 °C before plateauing at around 403 °C, just as the mass of the BioPBS polymer degrades completely. These findings immediately show the higher thermal stability of BioPBS, relative to PLA, both in terms of the degradation temperature and degradation rate.

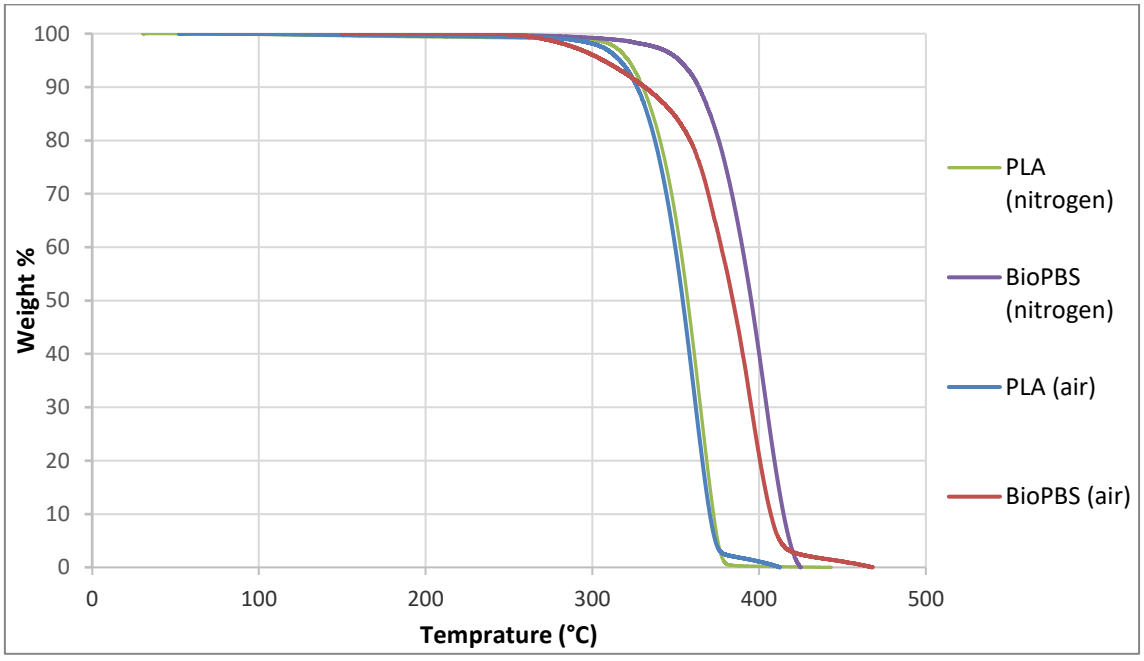

Figure 4-1 Degradation profile of as-R PLA and as-R BioPBS polymers under nitrogen-rich and air-rich atmosphere using a heating rate of 10 °C/min.

Table 4-1 Degradation metrics for as-R PLA and as-R BioPBS polymers under nitrogen-rich and air-rich atmospheres.

As-R polymer (atmosphere)	$T_{deg\ (onset)}$ (°C)	$T_{deg\ (end)}$ (°C)	$T_{deg\ (max\ rate)}$ (°C)	$D_{(max\ rate)}$ (%/°C)
PLA (nitrogen)	341 (±3.3)	367 (±3.1)	364 (±3.1)	3.1 (±0.3)
BioPBS (nitrogen)	366 (±2.4)	403 (±2.9)	397 (±0.9)	2.3 (±0.1)
PLA (air)	333 (±3.5)	367 (±2.3)	358 (±2.4)	2.6 (±0.1)
BioPBS (air)	363 (±3.1)	403 (±4)	396 (±1.7)	2.2 (±0.0)

Under air-rich atmosphere, as-R PLA starts degrading upon reaching a temperature of about 333 °C, which is about 8 °C lower than it started degrading under the nitrogen-rich atmosphere. Furthermore, the as-R PLA shows maximum degradation rate of about 2.6 %/°C occurring at around 358 °C for the as-R PLA polymer, which is about 6 °C higher than it was under the nitrogen atmosphere. Subsequently, the as-R PLA degrades completely at around 367 °C – just as it did under the nitrogen atmosphere. For the as-R BioPBS under air, the onset of degradation appears at around 363 °C. This is around the temperature that the as-R PLA degradation ends, and it highlights the impressive thermal stability of the as-R BioPBS polymer. Subsequently in the test, the as-R BioPBS reaches a maximum degradation rate of about 2.2 %/°C (around 396°C), before ending degradation around 402 °C – with almost an identical profile to its values under nitrogen atmosphere. Towards the end of both degradation processes of as-R PLA and as-R BioPBS polymers under the air-rich atmosphere, there appears to be an increase in degradation rate, which is attributed to the oxygenated degradation process.

According to the derived degradation metrics in Table 4-1, the entire thermal degradation process of the as-R PLA polymer under nitrogen begins and ends around 341 °C and 367 °C respectively, while the as-R BioPBS polymer starts and finishes its degradation around 363 °C and 403 °C respectively. This shows

a temperature range for degradation of about 26 °C for as-R PLA and about 40 °C for as-R BioPBS. Meanwhile, under air-rich atmosphere, the entire thermal degradation process starts and ends around 333 °C and 367 °C respectively for the as-R PLA polymer; and between about 363 °C and 403 °C respectively for the as-R BioPBS polymer. Therefore, the as-R PLA polymer shows a temperature range for degradation of about 34 °C while the as-R BioPBS shows a degradation range of about 40 °C. In summary, from the results obtained and discussed thus far, the $T_{deg\ (onset)}$ for the as-R BioPBS is about 25 °C higher than that of as-R PLA under nitrogen-rich atmosphere; and about 30 °C higher under air-rich atmosphere. It is also observed that the $T_{deg\ (onset)}$ for as-R BioPBS barely differs under both atmospheric conditions, while the $T_{deg\ (onset)}$ for as-R PLA decreases from about 341 °C in the nitrogen-rich atmosphere to about 333 °C in the air-rich atmosphere, and hence shows the influence of the atmospheric conditions only on as-R PLA. The results also show that while the as-R PLA has a maximum degradation rate occurring at a significantly lower temperature, i.e., about 33 °C lower – under nitrogen, and about 38 °C – under air, its degradation rate is about 0.8 %/°C and 0.4 %/°C higher than that of the as-R BioPBS polymer under nitrogen-rich and air-rich atmospheres, respectively. Hence, these results identify PLA as a more critical constituent material to consider during thermo-mechanical processing of filament materials, more especially under extended processing time frames or polymer residence times. Meanwhile, BioPBS shows a relatively impressive thermal stability performance.

4.2.2 Calorimetric transitions and phase change behaviour of received thermoplastic biopolymers.

Figure 4-2 and Table 4-2 show the heat-flow/temperature profiles and extracted data for the as-R PLA and as-R BioPBS polymers. Glass and melting (start, peak, and end) transitions for both as-R PLA and as-R BioPBS polymers are highlighted. For the as-R PLA, the glass transition occurs at around 61 °C, while the start, peak, and end of melting transitions occur at around 144 °C, 153 °C, and 160 °C respectively with an endothermic enthalpy change of 38 J/g. For the as-R BioPBS polymer, the glass transition occurs at around -35 °C, and although a limited melting peak of BioPBS crystals is observed at around 76 °C with an

enthalpy of about 3 J/g (i.e., 1.4% crystallinity), the main melting transition occurs at a start, peak and end temperature of around 107 °C, 116 °C, and 120 °C respectively with an endothermic enthalpy change of 68 J/g. Furthermore, as-R PLA and as-R BioPBS polymers show exothermic cold-crystallization peaks at around 125 °C and 91 °C respectively. However, while the exothermic enthalpy changes of the biopolymers appear negligible, that of the as-R BioPBS polymer shows a more significant exothermic enthalpy change of about 6.4 J/g. This further suggests that the latest cooling cycle of the BioPBS material led to formation of some thermally weaker amorphous BioPBS phases. Based on the estimation of ΔH_m and ΔH_{cc} of the PLA and BioPBS polymers, the percentage crystallinity (X_c) of the as-R PLA and as-R BioPBS is determined to be about 41% and 33% respectively. Furthermore, based on the findings in this section, as-R PLA, and as-R BioPBS polymers are thermodynamically processable between 170 °C and 270 °C (for PLA), and between 130 °C and 300 °C (for BioPBS) without the risk of damaging the polymer chains in each bulk polymer, particularly when exposed to the temperatures at relatively short periods of time. These ranges were defined based on the $T_{m\ (end)}$ and $T_{deg\ (onset)}$ values deduced for both of the as-R bio-based thermoplastic polymers.

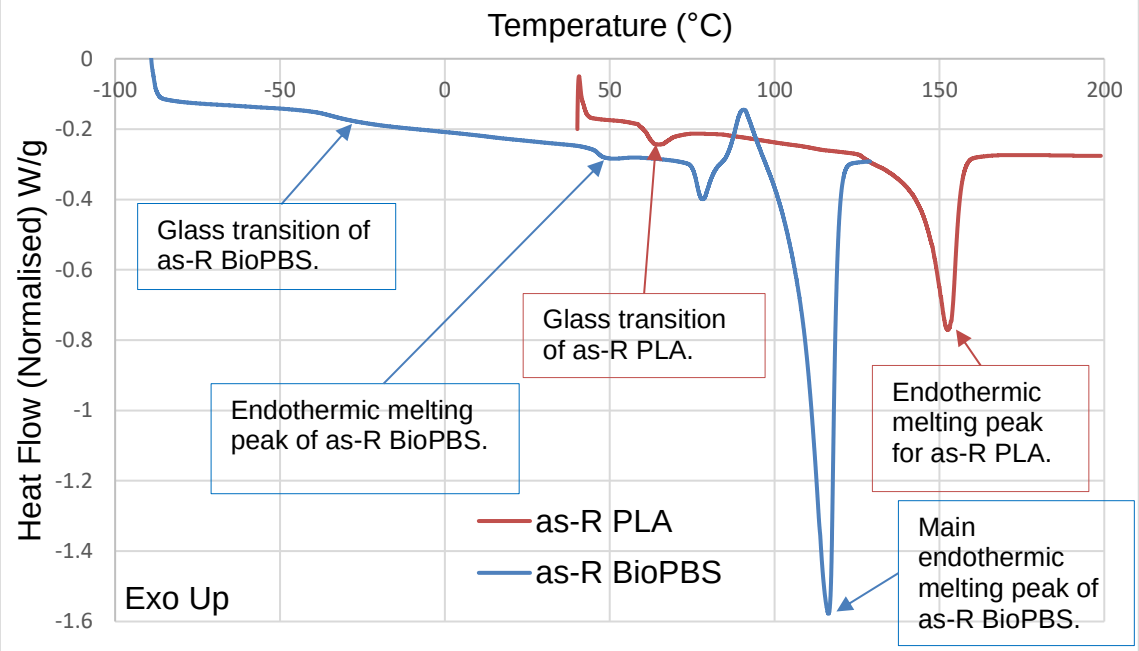

Figure 4-2 1st heating scan curve for as-R PLA and as-R BioPBS - showing glass, cold crystallisation and melting transitions.

Table 4-2 DSC results from 1st heating scan of as-R PLA and as-R BioPBS polymers. Analysed using TRIOS Software.

Polymer	T_g (°C)	$T_{m\ (start)}$ (°C)	$T_{m\ (peak)}$ (°C)	$T_{m\ (end)}$ (°C)	ΔH_m (J/g)	X_c (%)
PLA	61	144	153	160	38	40.5
BioPBS	-35	107	116	120	68	32.5

4.3 Calorimetric results of biopolymer phases in fabricated composite filaments

The thermodynamic calorimetric results of the PLA and BioPBS phase transitions occurring in the PLA80/BioPBS20-based filaments are reported following characterizations under nitrogen-rich atmosphere in this section. This is used to explore the phase crystallinity, crystalline phase stability, and crystallization rate behaviour of both PLA and BioPBS phases in the fabricated PLA80/BioPBS FE, PLA80/BioPBS20 MB-FE, PLA80/BioPBS20/HbnC1 MC-FE, and PLA80/BioPBS20/rGO1 MC-FE 3DP filaments. These results represent the state of the filament materials as obtained after the latest cooling cycle used for the filament fabrication process. In the analysis of each fabricated PLA80/BioPBS20-based filament material formulation, both crystalline phases of PLA and BioPBS are given a similarly important level of focus. However, in the amorphous phases, the amorphous PLA phase is given more attention, with little or no reference to information on the amorphous BioPBS phase. This is because the T_g of the amorphous BioPBS phase remains difficult to detect at the 20 wt.% loading and therefore does not offer reliable results that are useful for understanding miscibility and crystalline behaviour of existing PLA and BioPBS phases in the fabricated filaments.

4.3.1 Calorimetric results of biopolymer phases in fabricated composite filaments produced using direct filament fabrication route.

The DSC results for the PLA80/BioPBS20 fabricated using direct FE is processed and presented as seen in Figure 4-3 and Table 4-3. The results show that the T_g for amorphous PLA-rich phase occurs at around 55 °C and is followed by an annealing effect. Furthermore, the BioPBS-rich phase is observed to cold crystallise around 106 °C with an approximated exothermic enthalpy change of about 2 J/g. Subsequently, a uniform melting transition with a peak around 114 °C, and an endothermic enthalpy change of about 4 J/g is observed for the crystalline BioPBS phase. The next transition observed is the cold crystallization of the PLA phase around 120 °C, with an exothermic enthalpy change of about 5 J/g, which indicates the portion of the crystalline PLA-rich phase that failed to recrystallise effectively after the latest cooling cycle that occurred during filament fabrication. Lastly, the crystalline PLA phase shows uniform mode of crystal melting with endothermic enthalpy change of about 16 J/g. Hence, the crystallinity of PLA and BioPBS phases are around 16% and 4% respectively.

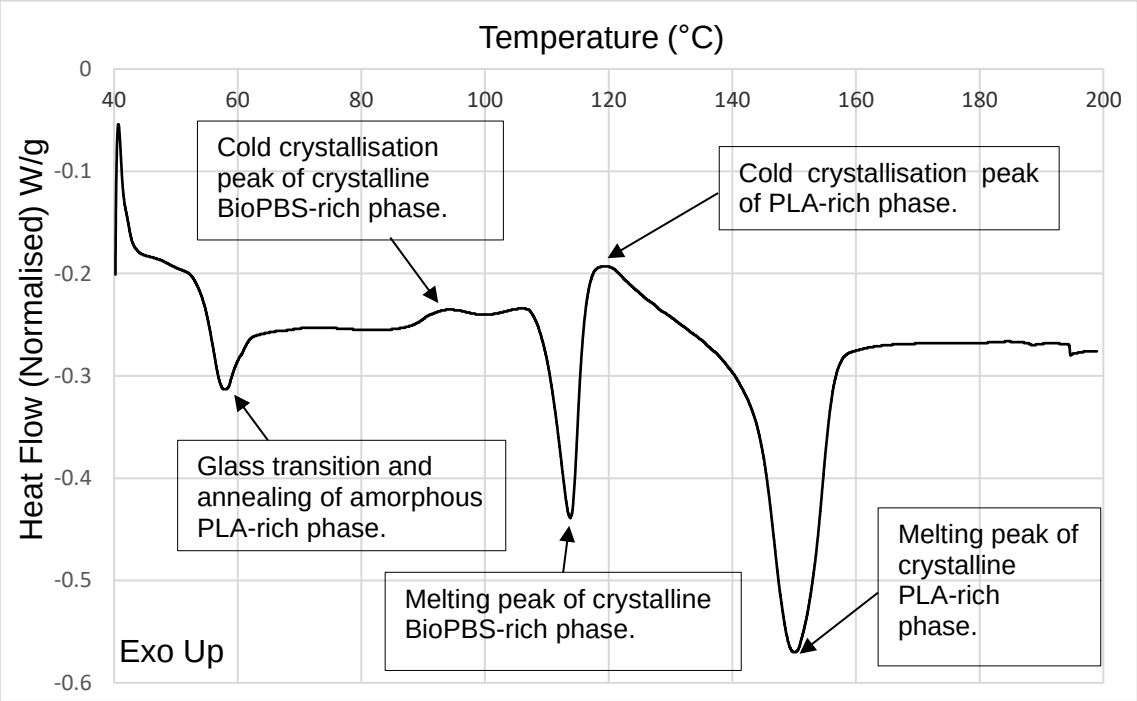

Figure 4-3 1st Heating curve for PLA80/BioPBS20 FE filament - showing heat flow against temperature profile.

Table 4-3 DSC results from 1st heating scan of fabricated PLA80/BioPBS20 composite filament processed via FE.

Polymer	T_g (°C)	$T_{cc\ (peak)}$ (°C)	ΔH_{cc} (J/g)	$T_{m\ (peak)}$ (°C)	ΔH_m (J/g)	X_c (%)
PLA	55.2 (±0.3)	120 (±0.0)	4.6 (±0.6)	150 (±0.0)	16.1 (±0.6)	16 (±0.0)
BioPBS	-	106 (±0.0)	1.7 (±0.4)	114 (±0.1)	3.9 (±0.2)	5 (±1.4)

Following the results presented in Figure 4-3 and Table 4-3, the fabricated PLA80/BioPBS20 FE filament shows two distinct melting peaks for the PLA and BioPBS phases, which suggests that the two phases do not combine well enough to form a more singular melting peak in the PLA80/BioPBS20 FE filament material. Therefore, an immiscible blend of PLA-rich and BioPBS-rich phases is formed. According to these results for the BioPBS-rich phase in the PLA80/BioPBS20 direct FE filament, a limited inhomogeneous cold crystallization effect is observed, but with a more homogeneous melting peak at around 106 °C, which has a ΔH_m of about 4 J/g and translates to a BioPBS phase crystallinity of about 5%.

4.3.2 Calorimetric properties of biopolymer phases in fabricated composite filaments produced using MB-FE filament fabrication route.

The DSC results for the PLA80/BioPBS20 filament fabricated using the MB-FE filament fabrication route are presented in Figure 4-4 and Table 4-4. Following the profile and metrics data reported, the PLA80/BioPBS20 MB-FE filament material shows a T_g of about 59 °C and a cold crystallization of the BioPBS phase occurs with a ΔH_{cc} of about 8 J/g, which peaks at around 104 °C. Furthermore, the BioPBS melting transition occurs with ΔH_m of about 6 J/g, and peaks at around 115 °C. A negligible cold crystallization transition of the crystalline PLA phase appears at about 122 °C. This is followed by a melting transition that shows a broadened peak with a maximum at around 152 °C with ΔH_m of about 19 J/g. The

enthalpy results were used to calculate the PLA and BioPBS phase crystallinity which were found to be around 27% for PLA, but negligible for the BioPBS phase. This represents an increase in PLA crystallinity for the PLA80/BioPBS20 MB-FE filament when compared to the PLA80/BioPBS20 FE filament. However, the cold crystallization of the BioPBS phase is also increased in the former and indicates a slower recrystallisation of the BioPBS phase upon final cooling of the filament fabrication process.

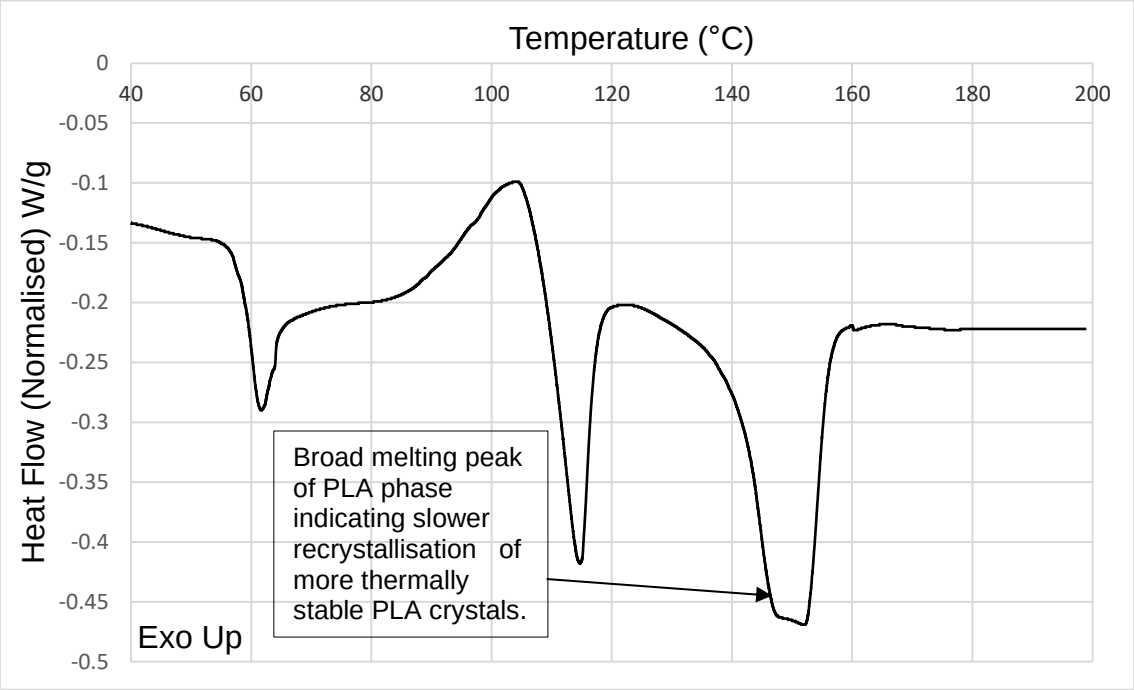

Figure 4-4 1st Heating curve for PLA80/BioPBS20 MB-FE filament - showing heat-flow against temperature profile.

According to the fabricated filament DSC results highlighted so far, the crystallinity of the PLA phase increases to about 27% in the PLA80/BioPBS20 MB-FE filament, which represents about 82% increase when compared to the crystalline PLA content of 16% in the PLA80/BioPBS20 FE filament. This increase in PLA crystallinity for the PLA80/BioPBS20 MB-FE filament is supported by its higher T_g of 59 °C, which indicates that there is a more ordered amorphous PLA phase in the fabricated filament. However, in explaining the higher crystallinity in the PLA80/BioPBS20 MB-FE filament, it may be caused by increased density of PLA polymer chain ends that arise after chain scissions that occur during the more intensive MB-FE filament fabrication process route;

producing a PLA phase with lower molecular weight, but increased polymer chain ends that act as nucleation sites for new PLA crystallite initiation and growth. Alternatively, the dispersion of BioPBS in the PLA80/BioPBS20 blend could well be responsible - as has been highlighted in a previous study [52]. Or perhaps, it is a combination of both factors. Nonetheless, the increase in PLA crystallinity could enhance the storage modulus of the filament during cold and melt-processing steps involved in FDM-based 3DP. Moreover, considering the transitions, another notable finding for the PLA80/BioPBS20 MB-FE filament is found to be the formation of a broader melting peak for the crystalline PLA phase, which, based on the T_m of about 152 °C, suggests that the crystalline PLA phase contains more thermally stable PLA crystals that are more like those present in the crystalline phase of the as-R PLA polymer. Additionally, considering the cold-crystallisation effect observed for the crystalline PLA phase in the PLA80/BioPBS20 FE filament (Figure 4-3), the ΔH_{cc} of the PLA-rich phase in the PLA80/BioPBS20 MB-FE filament appears to have been reduced to a negligible and barely distinguishable level around 121 °C to 123 °C, which indicates the realisation of a more effective recrystallisation process during fabrication of the PLA80/BioPBS20 MB-FE filament; a result of significant reordering of the PLA chains to support effective recrystallisation. For these reasons, the relative increase in PLA phase crystallinity in the PLA80/BioPBS20 MB-FE filament is attributed to the extra melt processing that forms PLA polymorphs with an improved crystal structure and atomic arrangement. Critically, while [52] and [138] processed PLA80/BioPBS20 formulations using a twin-screw extruder, with the former undergoing a more extensive processing, similar to that used in this work. The former reports a BioPBS phase crystallinity of about 10%, while the latter reports a BioPBS phase crystallinity of about 16.4%, which, based on the negligible BioPBS phase crystallinity found for the same material in this work, suggests that more melt processing and mixing causes a reduction in BioPBS phase crystallinity. However, [138] reported on the crystallinity of the PLA phase in the PLA80/BioPBS20 formulation to be about 21%, which is lower than the 27% obtained in this work, and therefore suggests that more melt processing and mixing causes an increase in PLA phase crystallinity.

Table 4-4 DSC (Heat flow) results of 1st heating cycle of fabricated PLA/BioPBS20 composite filament processed via MB-FE.

Polymer	T_g (°C)	T_{cc} (°C)	ΔH_{cc} (J/g)	$T_{m\ (peak)}$ (°C)	ΔH_m (J/g)	X_c (%)
PLA	58.5 (±0.6)	-	-	151 (±1.4)	20.1 (±1.3)	27 (±1.4)
BioPBS	-	104.6 (±0.6)	7.8 (±0.5)	114 (±0.6)	5.5 (±1.0)	0

Furthermore, in contrast to the PLA80/BioPBS20 FE filament which shows a negligible T_{cc} of the BioPBS phase, the BioPBS phase in the two-step MB-FE filament fabrication route is found to be significantly more, occurring at a $T_{cc\ (peak)}$ of 104 °C, but with a ΔH_{cc} of about 8 J/g, which is about 300% higher than the value found in the BioPBS phase of the PLA80/BioPBS20 FE filament. Additionally, the $T_{m\ (peak)}$ of the BioPBS phase in the PLA80/BioPBS20 MB-FE filament occurs at a similar temperature of about 114 °C, with a ΔH_m of about 6 J/g, which is about 60% higher than the ΔH_m value obtained for the BioPBS phase in the PLA80/BioPBS20 FE filament. This suggests that the crystalline BioPBS phase in the PLA80/BioPBS20 MB-FE filament recrystallises at a slower rate than the BioPBS crystals in the PLA80/BioPBS20 FE filament. This is possibly because the less dispersed BioPBS polymer phase in the PLA80/BioPBS20 FE filament offers limited sites for BioPBS nucleation and growth, and hence the lower enthalpy values for cold crystallisation and melting when compared to the PLA80/BioPBS20 MB-FE filament. Nonetheless, both sets of BioPBS crystals in the PLA80/BioPBS20 FE and PLA80/BioPBS20 MB-FE filaments show similar levels of thermal stability upon recrystallization. Importantly, the degree of crystallinity of the BioPBS phase in the PLA80/BioPBS20 MB-FE filament is difficult to deduce more accurately due to the lack of good baseline between the BioPBS cold crystallization and melting transitions presented in Figure 4-4. However, the similarity in ΔH_{cc} and ΔH_m peaks of the BioPBS phase suggests

that the crystallinity of the BioPBS phase is significantly low and at a negligible level in the PLA80/BioPBS20 MB-FE filament.

4.3.3 Calorimetric properties of PLA and BioPBS phases in fabricated composite filaments

4.3.3.1 Results for composite filaments containing nano clay.

The DSC results for the PLA80/BioPBS20/HbnC1 produced using the two-step MC-FE filament fabrication route are presented in Figure 4-5 and Table 4-5. According to the metric results presented in Table 4-5, a glass transition is observed around 52 °C with no annealing effects. Meanwhile, two cold crystallization peaks of the BioPBS phase are found to occur with a total enthalpy of about 7 J/g: with both transitions sequentially occurring at peak temperatures of about 109 °C and 91 °C. The cold crystallization of the BioPBS phase occurs to the extent that it overlaps with the melting transition of its crystalline phase. The melting transition of the BioPBS was estimated to occur with an enthalpy of approximately 1 J/g, with a peak around 114 °C. An overlapping cold crystallization transition of the PLA phase follows next with an exothermic enthalpy of about 4 J/g, which peaks around 117 °C and less effectively overlaps the melting transition of the crystalline PLA phase, i.e., in relation to the transitions of the crystalline BioPBS phase. In the melting transitions of the crystalline PLA phase, two peaks are formed with a combined ΔH_m of about 22 J/g. The first peak formation with higher but less stable crystalline PLA crystals occurs around 149 °C, meanwhile the secondary peak with lower but more stable PLA crystals occurs around 154 °C and represents the last observed transitions in the PLA80/BioPBS20/HbnC1 MC-FE filament. This result confirms the formation of more stable PLA polymorphs in the filaments that undergo extended melt processing – particularly when compared to the PLA80/BioPBS20 FE filament.

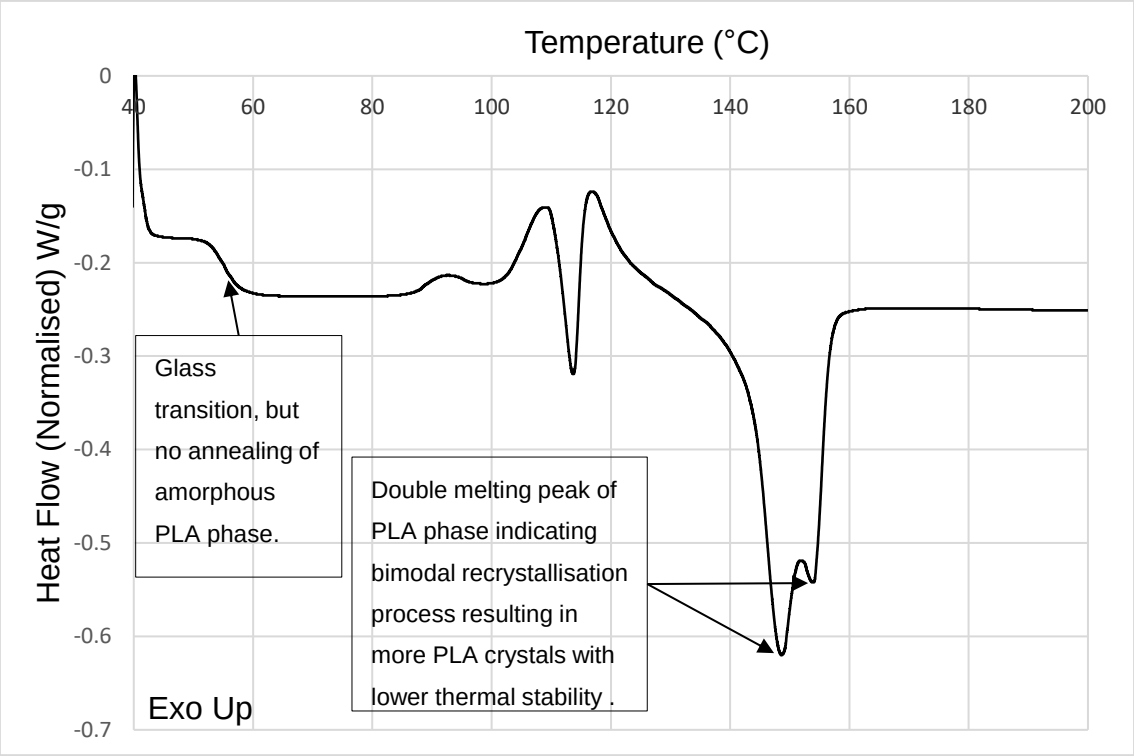

Figure 4-5 1st heating scan of fabricated PLA80/BioPBS20/HbnC1 MC-FE filament.

In another observation, there are distinct PLA and BioPBS melting peaks, which indicates immiscibility of the two phases in this fabricated filament. Furthermore, the annealing effect observed in the PLA80/BioPBS20 FE and PLA80/BioPBS20 MB-FE filaments is not present in the PLA80/BioPBS20/HbnC1 MC-FE filament. This suggests that the amorphous PLA phase in the PLA80/BioPBS20/HbnC1 MC-FE filament is stress/strain-relieved following filament fabrication, maybe because of the increased dispersion of BioPBS in the matrix, or the nucleating sites of PLA crystals, which can be induced by extensive melt-processing or HbnC addition. Furthermore, little cold crystallization of the BioPBS and PLA phases occurs, but with the typical hard-to-define baselines between the cold crystallization and melting transitions of both polymers. And following the results presented in Table 4-5**,** the crystallinity of the PLA phase is found to be around 24% in the PLA80/BioPBS20/HbnC1phr MC-FE filament, which is like the crystallinity found for the crystalline PLA phase of the PLA/BioPBS20 MB-FE filament, although slightly lower. Alternatively, in the crystalline BioPBS phase of the PLA80/BioPBS20/HbnC1phr MC-FE filament, no positive enthalpy difference

is deduced, hence resulting in a BioPBS phase where the $\Delta H_{cc} \geq \Delta H_{m,}$ thereby indicating a negligible BioPBS crystallinity in the fabricated composite filament. These findings, in terms of PLA phase crystallinity and net enthalpy change, indicates similar results to that of the PLA/BioPBS20 MB-FE filament. However, the BioPBS cold crystallization peak in the PLA80/BioPBS20/HbnC1phr MC-FE filament appears broader and indicates a reduced level of effective cold crystallization or cold crystallization rate, which is probably due to the addition of HbnC or the use of an additional melt processing cycle during the filament fabrication process. Nonetheless, with isolated evidence supporting the effect of organoclay filler on isothermal PBS crystallisation [153], there appears to be more of a case for the influence of HbnC on the recrystallisation of the BioPBS phase in the PLA80/BioPBS20/HbnC1phr MC-FE filament. Hence, the effects of HbnC addition appears to have more likely caused better recrystallization of the BioPBS phase in the PLA80/BioPBS20/HbnC1phr MC-FE filament when compared to the PLA80/BioPBS20 MB-FE or PLA/BioPBS20 FE filaments, particularly because the BioPBS cold crystallization in the PLA80/BioPBS20/HbnC1phr MC-FE filament appears to peak at a higher temperature and suggests that better recrystallization occurs in the BioPBS phase during the final cooling step of filament fabrication.

Table 4-5 DSC results from first heating scan of the fabricated PLA/BioPBS20/HbnC1 MC-FE filament.

Polymer	**T_g (°C)**	**$T_{cc\ (peak)}$ (°C)**	**ΔH_{cc} (J/g)**	**$T_{m\ (peak)}$ (°C)**	**ΔH_m (J/g)**	**X_c (%)**
PLA	52.4 (±2.5)	117.6 (±0.6)	4 (±0.8)	148.8 (±0.2)	22.3 (±0.6)	24 (±0.5)
BioPBS	-	108.9 (±0.2)	6.8 (±1.4)	114 (±0.3)	0.85 (±0.0)	0

4.3.3.2 Results for composite filament containing rGO.

Figure 4-6 and Table 4-6 shows the heat-flow/temperature profile and results obtained from the first DSC heating scan of the PLA80/BioPBS20-based

composite filament containing rGO, which was fabricated using the MC-FE fabrication route and involving 3 passes during MC. The results for this filament material shows a glass transition temperature that occurs around 56 °C with an annealing effect on the amorphous PLA phase. Following on, two exothermic peaks can be observed - representing the cold crystallization of the crystalline BioPBS phase. This is like the BioPBS recrystallization profile that is found for the PLA80/BioPBS20/HbnC1 MC-FE filament; however, a more substantially dominant proportion of the crystalline BioPBS in the PLA80/BioPBS20/rGO1 MC-FE filament results in cold crystallization with a higher enthalpy of about 15 J/g and at a lower $T_{cc\ (peak)}$ of about 104 °C, which is suggestive of a more readily crystallisable BioPBS phase. Following the BioPBS cold crystallization, an endothermic melting transition of the BioPBS phase occurs with an enthalpy of about 7 J/g, which peaks around 114 °C. This is followed by suppressed evidence of the cold crystallization peak of the crystalline PLA phase, although negligible in appearance. The subsequent reaction is an endothermic melting of the crystalline PLA phase with a total energy of about 26 J/g. The endothermic melting process of the crystalline PLA phase occurs and produces two distinct peaks during the transition. The primary and lower temperature peak occurs around 148 °C, while the secondary and higher-temperature peak occurs around 155 °C. The latter appears to make up more of the crystalline PLA phase present in the PLA80/BioPBS20/rGO1 MC-FE filament. Based on the findings presented in Table 4-6, the crystallinity of the PLA and BioPBS phases in the fabricated PLA80/BioPBS20/rGO1 MC-FE filament is found to be about 34% and negligible, respectively.

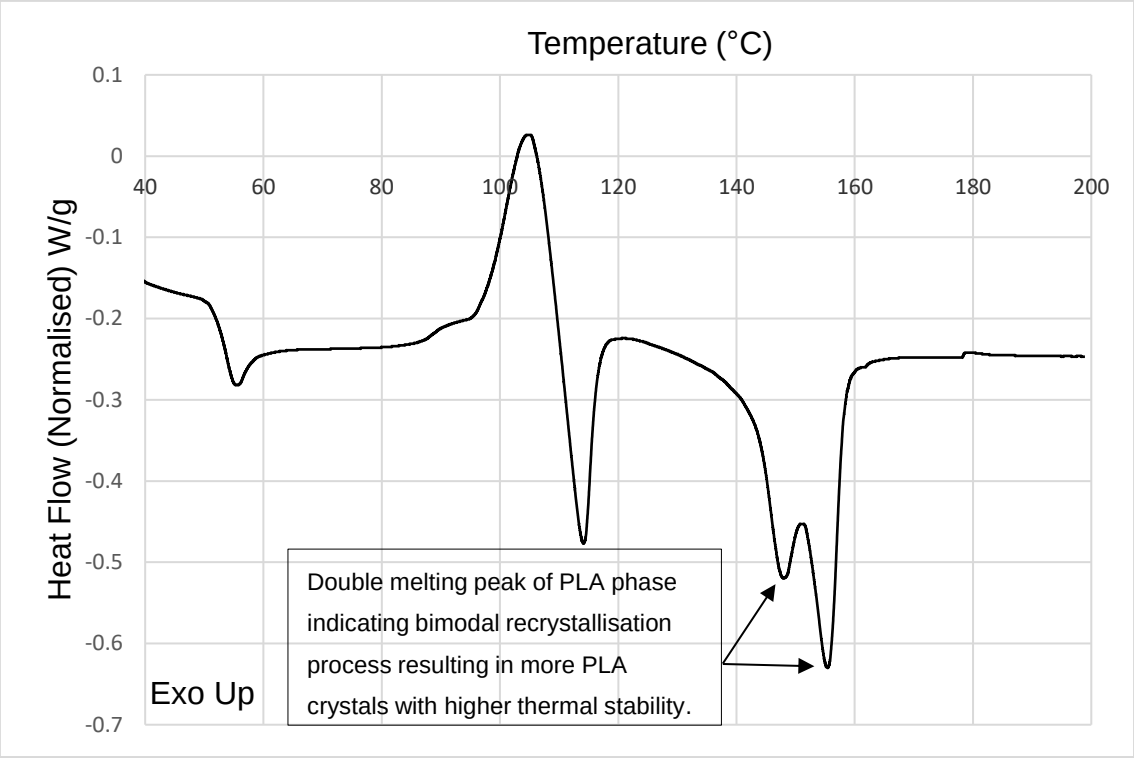

Figure 4-6 Heat-flow/Temperature of fabricated PLA80/BioPBS20/rGO1 MC-FE filament.

From the results discussed for the rGO-filled composite filament, the BioPBS phase shows the highest exothermic cold crystallization observed for any of the fabricated filaments. The trend in net enthalpy change for the BioPBS phase is exacerbated in comparison to that observed for the other blend and composite filaments. For the PLA phase, the cold crystallization enthalpy of the PLA phase is reduced when compared to the PLA80/BioPBS20/HbnC1 MC-FE filament and perhaps indicates that rGO promotes better recrystallisation results in the PLA phase, which allows more stable PLA polymorphs to form. Interestingly, the results show a bimodal PLA crystal phase formation in the PLA80/BioPBS20/rGO1 MC-FE filament and PLA80/BioPBS20/HbnC1phr MC-FE filaments. This is due to the influence of the rGO and HbnC nanomaterials in altering the recrystallisation behaviour of the PLA phase but may also be due to the potentially detrimental thermo-mechanical and thermo-oxidative effects of screw-based melt processing on molecular weight, as identified by [154]; an occurrence that can consequently support the increase of crystal nucleation sites for PLA due to chain scissions and the availability of new polymer chain ends for

PLA crystal nucleation. Moreover, it was considered that the relatively ultra-low molecular weight, low density, and nanoplatelet structure of rGO (in relation to the HbnC particle) utilises the additional melt processing cycle to position its nanosheets as effective limiters to PLA crystal grain mobility, which encourages limited crystal growth. This is especially critical between 95 and 146 °C, for which, according to the calorimetric studies of PLLA by [155] - promotes recrystallisation and crystal growth, as studied under isothermal conditions. With such effects of processing condition and nanofiller, recrystallisation and crystal growth processing upon cooling allows for more crystal reorganisation during cold crystallisation, which leads to distinct PLA crystal forms (bimodal melting peak) seen in the crystalline PLA phase of the nano-filled composite filaments.

Table 4-6 Results from first DSC heating scan of fabricated PLA/BioPBS20/rGO1 MC-FE filament.

Polymer	**T_g (°C)**	**$T_{cc\ (peak)}$ (°C)**	**ΔH_{cc} (J/g)**	**$T_{m\ (peak)}$ (°C)**	**ΔH_m (J/g)**	**X_c (%)**
PLA	56 (±0.8)	-	-	155 (±0.2)	25.4 (±0.7)	34 (±1.0)
BioPBS	-	104.2 (±0.7)	14.9 (±0.5)	114.2 (±0.3)	6.8 (±0.9)	0

In contrast to the HbnC-containing filament which is shown to have more PLA crystals melting at lower melting temperatures, the PLA80/BioPBS20/rGO1 MC-FE filament shows more PLA crystals melting at higher temperatures. Interestingly, the PLA80/BioPBS20/rGO1 MC-FE filament shows a higher T_g of about 56 °C when compared to that of the PLA80/BioPBS20/HbnC1 MC-FE filament, which is around 52 °C. Although this finding may suggest the presence of a more thermally stable amorphous PLA phase in the PLA80/BioPBS20/rGO1 MC-FE filament, the T_g of the PLA80/BioPBS20 MB-FE filament is shown to be around 59 °C, which further confirms that the conditions during MB or MC routes affects the thermal stability of the amorphous PLA phase. This explanation is considered plausible since the T_g of about 59 °C in the PLA80/BioPBS20 MB-FE

filament is higher than the T_g of about 56 °C in the as-R PLA polymer despite the addition of BioPBS, which has a glass transition temperature of about -34 °C Interestingly, the T_g of the PLA phase in the PLA80/BioPBS20 MB-FE filament is also higher than the T_g of the PLA phase in the PLA80/BioPBS20/HbnC1 MC-FE and PLA80/BioPBS20/rGO1 MC-FE filaments, which were put through more twin-screw extrusion processing cycles. In this case, however, there are further dependencies on the HbnC and rGO nanoparticles, which further influences the amorphous properties; especially when considering the differing compatibilising and crystallising effect of the BioPBS phase in the presence of the nanomaterials.

4.4 Recrystallization of biopolymer phases in the fabricated composite blends and nanocomposite filaments

After the first heating scans of each respective PLA80/BioPBS20-based filament, cooling scans were conducted at 10 °C/min for the purpose of identifying and understanding the recrystallization enthalpy changes that occur in the crystalline PLA and BioPBS phases following the hot extrusion and cooling steps of the FDM-based 3DP process. This is crucially important for understanding the crystalline BioPBS phase properties upon cooling, for which the BioPBS phase has been found to cause a reduction in dimensional stability of the final fabricated parts; a result of its significantly high CLTE. As a result, the calorimetric profile for PLA80/BioPBS20 FE, PLA80/BioPBS20 MB-FE, PLA80/BioPBS20/HbnC1 MC-FE, and PLA80/BioPBS20/rGO1 MC-FE filaments are presented in Figure 4-8. Nonetheless, it is important to recall that the filaments were cooled at room temperature with the support of cooling fans and were therefore cooled at a faster cooling rate than was used in these tests. The heat-flow and temperature data for each fabricated filament are also collected, processed, and presented in Table 4-7. In the PLA phase for each fabricated filament, no recrystallization reaction or peak is observed. This is because the cooling rate used for the test causes fast temperature changes that does not allow sufficient time for the equipment to record the recrystallisation enthalpy values. Based on this, it is therefore important to note that there is no visible exothermic recrystallization peak for the

crystalline PLA phase in any of the fabricated and tested filament samples. Hence, the observed recrystallization peaks are of the crystalline BioPBS phase.

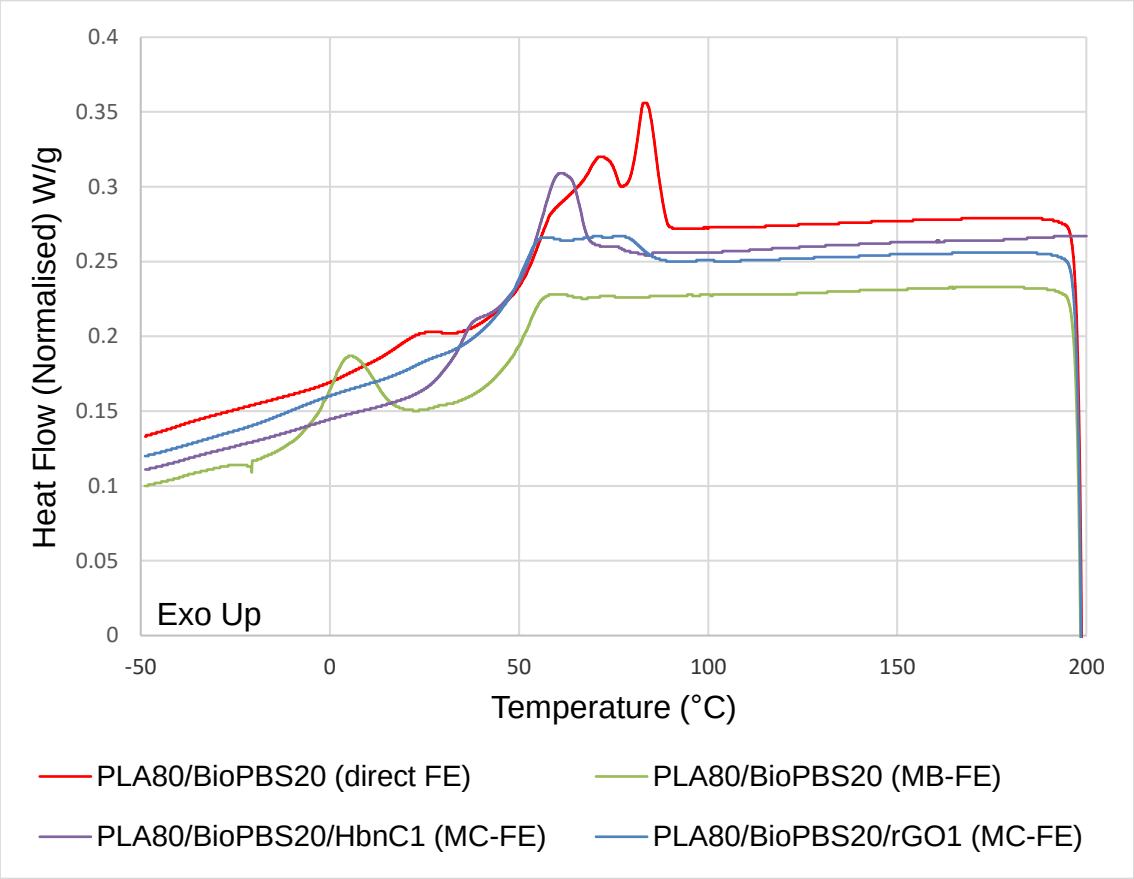

Figure 4-7 Calorimetric profile of PLA80/BioPBS20 FE, PLA80/BioPBS20 MB-FE, PLA80/BioPBS20/HbnC1 MC-FE, and PLA80/BioPBS20/rGO1 MC-FE filaments.

According to these results, the PLA80/BioPBS20 FE filament shows the highest $T_{c\ (peak)}$ of about 83 °C, with a ΔH_c of about 5 J/g, meanwhile the PLA80/BioPBS20/rGO1 MC-FE filament shows the second highest $T_{c\ (peak)}$ at about 81 °C, with a ΔH_c of about 1 J/g. In the PLA80/BioPBS20/HbnC1 MC-FE filament, the $T_{c\ (peak)}$ is around 61 °C with a ΔH_c of about 2 J/g. However, in the PLA80/BioPBS20 MB-FE filament, the $T_{c\ (peak)}$ drops to about 7 °C, with a ΔH_c of about 3 J/g. As for the calculations for crystallinity, the obtained values were used to determine the crystallinity of the recrystallised BioPBS phases in the PLA80/BioPBS20 FE, PLA80/BioPBS20 MB-FE, PLA80/BioPS20/HbnC1 MC-FE, and PLA80/BioPS20/rGO1 MC-FE filaments. Consequently, the crystallinity of the filaments is found to be around 11%, 8%, 6% and 3% respectively.

Table 4-7 Deduced information on the exothermic recrystallization transitions of the BioPBS phases in the fabricated filaments.

Fabricated Filament	$T_{c\ (onset)}$ (°C)	$T_{c\ (peak)}$ (°C)	ΔH_c (J/g)	X_c (%)
PLA80/BioPBS20 FE	88.4 (±0.1)	83.4 (±0.2)	4.7 (±0.8)	11.3 (±2.1)
PLA80/BioPBS20 MB-FE	17.2 (±0.6)	6.5 (±1.9)	3.4 (±0.2)	8.3 (±0.9)
PLA80/BioPBS20/HbnC1 MC-FE	67.8 (±0.1)	60.7 (±0.3)	2.4 (±0.3)	5.7 (±0.5)
PLA80/BioPBS20/rGO1 MC-FE	85.5 (±1.0)	80.9 (±2.7)	1.1 (±0.1)	2.7 (±0.5)

The PLA80/BioPBS20 MB-FE filament shows a significantly lower $T_{c\ (onset)}$ when compared to the PLA80/BioPBS20 FE filament, or indeed any other fabricated filament. This is most importantly attributed to the twin-screw mixing process utilised during filament fabrication of the PLA80/BioPBS20 MB-FE filament, which induces relatively increased dispersion and division (through shearing) of the BioPBS polymer chains and domains. Hence, while increasing the distance between BioPBS molecules, this effect provides the sites for BioPBS phase nucleation, but seems to result in small and significantly spaced BioPBS molecules, which contribute factors that can inhibit the onset of BioPBS phase recrystallisation in the PLA80/BioPBS20 MB-FE filament. Crucially, this result is distinctly different from that of any other fabricated filament. However, at such significantly lower BioPBS phase recrystallisation temperatures, the BioPBS phase is shown to recrystallise at a similar rate to the BioPBS phases in other fabricated filaments. It crystallises well enough to form about 8% of recrystallised BioPBS crystals, which is among the highest value of all the fabricated filaments. Furthermore, it appears that in the PLA80/BioPBS20/HbnC1 MC-FE and PLA80/BioPBS20/rGO1 MC-FE filaments, the $T_{c\ (onset)}$ values are increased back

to higher values (i.e., between 68 °C and 88 °C), which are like that of the PLA80/BioPBS20 FE filament. This is likely caused by a combination of nanofiller nucleation effects, and the melt processing conditions involved in the fabrication of the composite filaments. It appears that the additional melt processing of the composite filaments allows for new interactions between BioPBS domains, which results in creating newly developed BioPBS domains that can act as more effective nucleation sites in the recrystallisation process. Nonetheless, the results suggest that the HbnC and rGO inclusions increase the nucleation potential of BioPBS crystals. However, rGO appears to be a more effective nucleating agent than HbnC as it influences an earlier onset of recrystallisation during the cooling cycle. Furthermore, rGO also acts as an effective agent in limiting BioPBS crystal growth as is indicated by a broad and shallow recrystallisation peak for the PLA80/BioPBS20/rGO1 MC-FE filament. In summary, FDM 3D-printed parts made using the PLA80/BioPBS20/rGO1 MC-FE filament is most likely to have a more partially developed BioPBS crystalline phase, which can consequently reduce the mechanical capability of the BioPBS phase in the printed part. Meanwhile, the 3D-printed parts made from other fabricated PLA80/BioPBS20-based filaments are likely to have well-developed BioPBS crystals that support an improved mechanical performance in relation to the PLA80/BioPBS20/rGO1 MC-FE filament. However, the composition, crystalline and molecular properties of the PLA phase remain crucial for controlling the mechanical performance of the part.

4.5 Concluding remarks

In summary, the DSC scans of the PLA80/BioPBS20 FE, PLA80/BioPBS20 MB-FE, PLA80/BioPBS20/HbnC1 MC-FE, and PLA80/BioPBS20/rGO1 MC-FE filaments provide very useful information on the filament calorimetric state following fabrication. The cold crystallisation and melting peaks, melting profile, and crystallinity were used in defining the characteristics of fabricated filaments, and more importantly, for establishing the similarities and differences between each of the fabricated filament formulations. Between the PLA80/BioPBS20 FE and PLA80/BioPBS20 MB-FE filaments, the latter shows a considerably higher

PLA phase crystallinity, and hence contributes a unique comparison between PLA80/BioPBS20 filaments fabricated using different routes. Moreover, the PLA phase crystallinity of the PLA80/BioPBS20 MB-FE filament material in this work has the higher crystallinity of about 27% when compared to the 21% value reported by [138] for the same filament material formulation.

Using the PLA80/BioPBS20 MB-FE filament material as a reference, the PLA crystallinity is decreased by about 3.8% in the PLA80/BioPBS20/HbnC1 MC-FE filament but increases by about 27% in the PLA80/BioPBS20/rGO1 MC-FE filament. Figure 4-8 presents a bar chart showing a summary of the crystalline PLA and BioPBS content within each fabricated filament material. The PLA80/BioPBS20 FE filament has about 16% crystalline PLA phase, which increases by about 69% and 50% to a value of 27% and 24% crystalline PLA content in the PLA80/BioPBS20 MB-FE and PLA80/BioPBS20/HbnC1 MC-FE filaments respectively. Furthermore, the PLA phase crystallinity in the PLA80/BioPBS20/HbnC1 MC-FE filament increases by about 26% and 42% respectively to a crystalline PLA content of about 34% in the PLA80/BioPBS20/rGO1 MC-FE filament. In terms of each filament's applicability in FDM-based 3DP, the higher crystallinity levels of the dominant PLA phase impart higher stiffness in the filament. This can limit the ease of handling as the filament becomes more prone to brittle fractures; especially in the presence of a limitedly recrystallised BioPBS phase that would otherwise act to introduce some flexibility to the filament material. Nonetheless, a higher crystalline content importantly allows the filament to perform better as a piston that provides the necessary back pressure required to sustain a continuous extrusion process for FDM-based 3D printing.

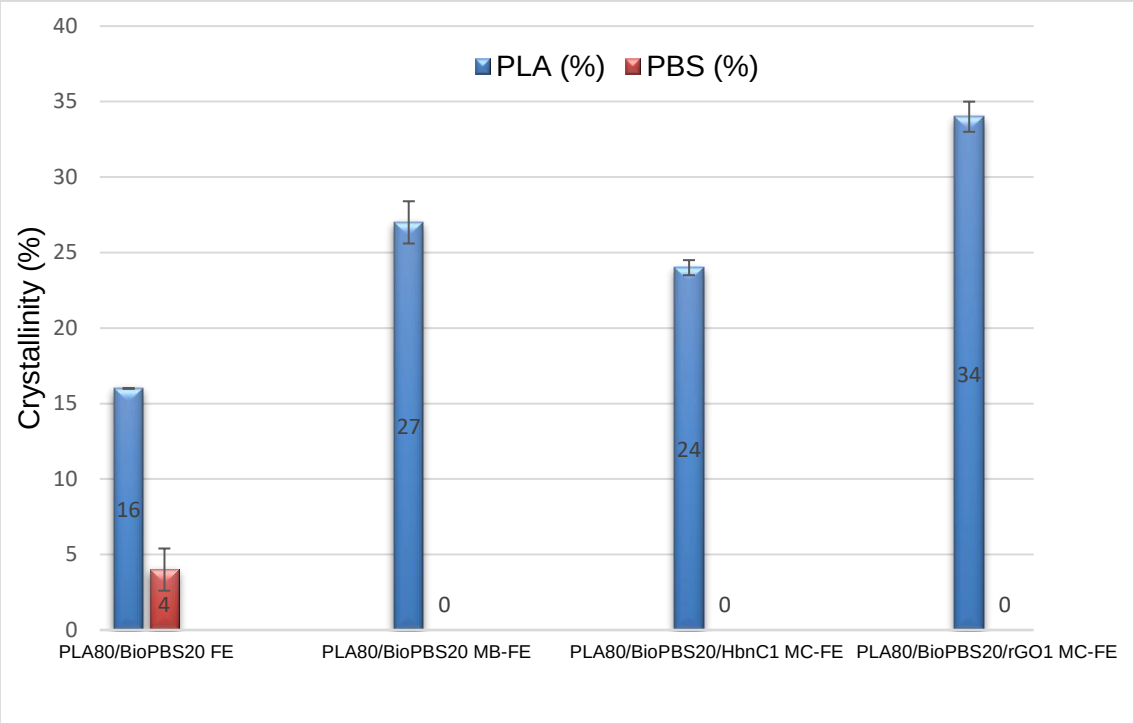

Figure 4-8 Percentage crystallinity of the PLA and BioPBS phases in the fabricated PLA80/BioPBS20-based blends and nanocomposite filaments.

Considering the BioPBS phase, its cold crystallisation is found to increase with the use of the melt blending process or the addition of rGO, which is a consequence of less effective recrystallization during the filament fabrication process. Furthermore, while the PLA80/BioPBS20/rGO1 MC-FE filament produces the most thermally stable PLA phase amongst all PLA phases in the fabricated filaments, the addition of HbnC in the PLA80/BioPBS20/HbnC1 filament also enhances PLA phase crystallinity but does not have a similar effect as the rGO on the BioPBS phase. However, if there are any effects of the HbnC on the BioPBS phase, it would involve some improvement in the recrystallisation of the BioPBS phase, i.e., in contrast to the recrystallisation process observed for the BioPBS phase in the PLA80/BioPBS20 MB-FE filament. Importantly, this shows that the BioPBS phase crystallinity can be controlled by addition of either of the nanomaterials. But nonetheless, miscibility between the PLA and BioPBS phases show immiscibility in their crystalline phase is not observed even though both phases may be miscible in their amorphous phase.

5 Microscopic and rheological properties of fabricated composite formulations

5.1 Introduction

In this chapter, the cryo-fractured surface morphology of the fabricated PLA80/BioPBS20 FE, PLA80/BioPBS20 MB-FE, PLA80/BioPBS20/HbnC1 MC-FE, and PLA80/BioPBS20/rGO1 MC-FE filaments are presented and discussed to assess the effect of the 3DP filament composition and fabrication route on each fabricated filament formulation. The morphological results are used to assess filament quality based on the material compatibility, miscibility, and porosity. Furthermore, rheological results particularly highlighting the complex viscosity properties of isothermally shear-strained PLA80/BioPBS20-based cylindrical plates are presented. The complex viscosity against angular frequency plots is explored and used in the determination of the power law index associated with each filament formulation at prospective printing temperatures. The developed power law models are used to support further analysis and extrapolation of complex viscosity results at calculated shear rates and prospective printing temperatures using time temperature superposition for the purpose of predicting and developing optimized 3DP process controls for the PLA/BioPBS20-based filament formulations in focus.

5.2 SEM results of the cross-sectional surface area of fabricated and cryo-fractured filament formulations

5.2.1 Cross-sectional microscopic results for composite blend filament

The microscopic results of the cross-sectional surfaces of the PLA80/BioPBS20 FE and PLA80/BioPBS20 MB-FE filaments are presented in Figure 5-1. The microscopic result of the PLA80/BioPBS20 FE filament surface shows the presence of globular formations identified by red arrows in Figure 5-1(a). These globular entities featuring circular droplet-like formations, for which at least 7 are identified in Figure 5-1(a), but not at all in Figure 5-1(b), indicate the presence of rich BioPBS domains, and further suggests that the direct FE route offers less

effective blending as compared to the MB-FE filament fabrication route. Overall, the imaged surfaces of both PLA80/BioPBS20 filaments have a rich and dominant PLA domain in addition to a blended PLA/BioPBS domain. However, only the PLA80/bioPBS20 FE filament shows the presence of rich BioPBS domains. Typically, the PLA/BioPBS domains appear as a secondary layer of material formed on top of the PLA-rich matrix.

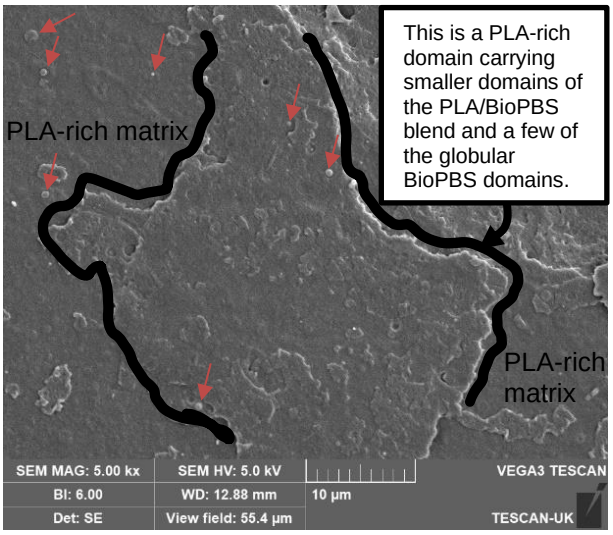

(a)

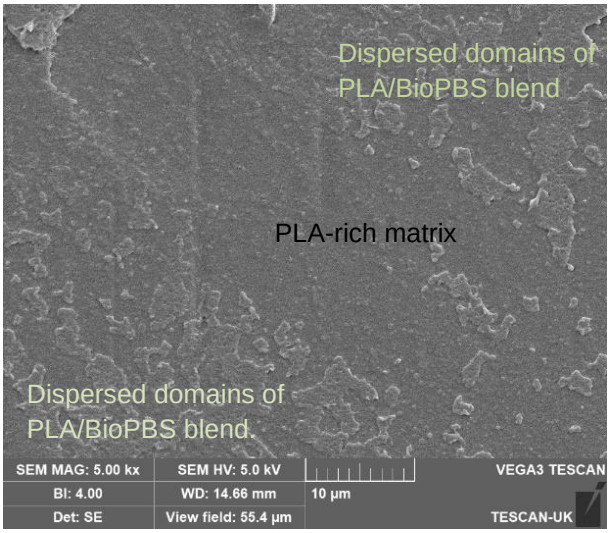

(b)

Figure 5-1 SEM results of fabricated and cryo-fractured filaments of PLA80/BioPBS20 composites showing cross-sectional surface for: (a) PLA80/BioPBS20 FE; (b) PLA80/BioPBS20 MB-FE.

5.2.2 Cross-sectional microscopic results for composite filament containing HbnC.

The morphology of the cross-sectional surface of the PLA80/BioPBS20/HbnC1 MC-FE filament is presented in Figure 5-2, in a relatively low (423×) magnification image that offers a broader view of the filament surface morphology. The cryo-fractured surface shows multiple domains indicated by the brightness, roughness, and general texture shown by domains across the surface. Figure 5-2 shows fracture lines around the filament edges, resulting from the cryo-fracture process. Further into the mid areas, a better representation of the surface morphology can be deduced. It is observed that bright particles are present at various points across the surface and appear to build-up into a relatively larger structure with a length of about 100 µm (circled with red in Figure 5-2). This finding is supported by EDS data shown in Figure 5-3, and helps to confirm that the brighter material features are dispersions of HbnC particles. Therefore, in comparing the average particle diameter of the pre-processed HbnC (i.e., < 25 µm) to the developed structure (circled with red in Figure 5-2), the latter is found to be at least 4x larger and which confirms particle agglomeration within the filament material.

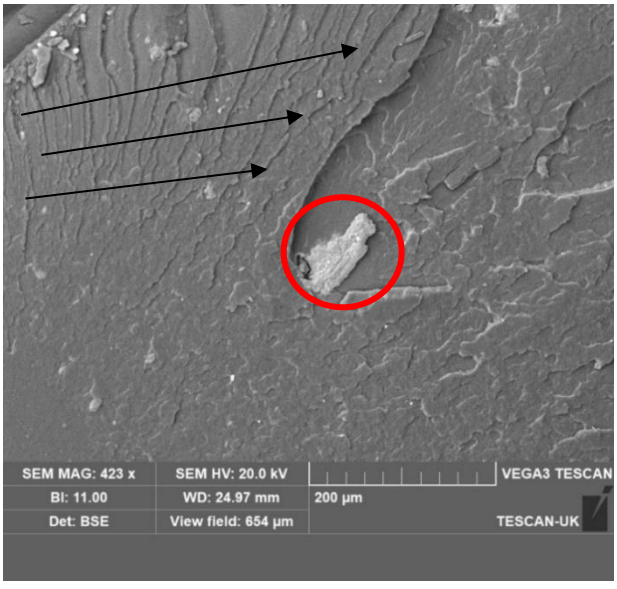

Figure 5-2 SEM image of fabricated and cryo-fractured PLA80/BioPBS20/HbnC1 filament showing cross-sectional surface features.

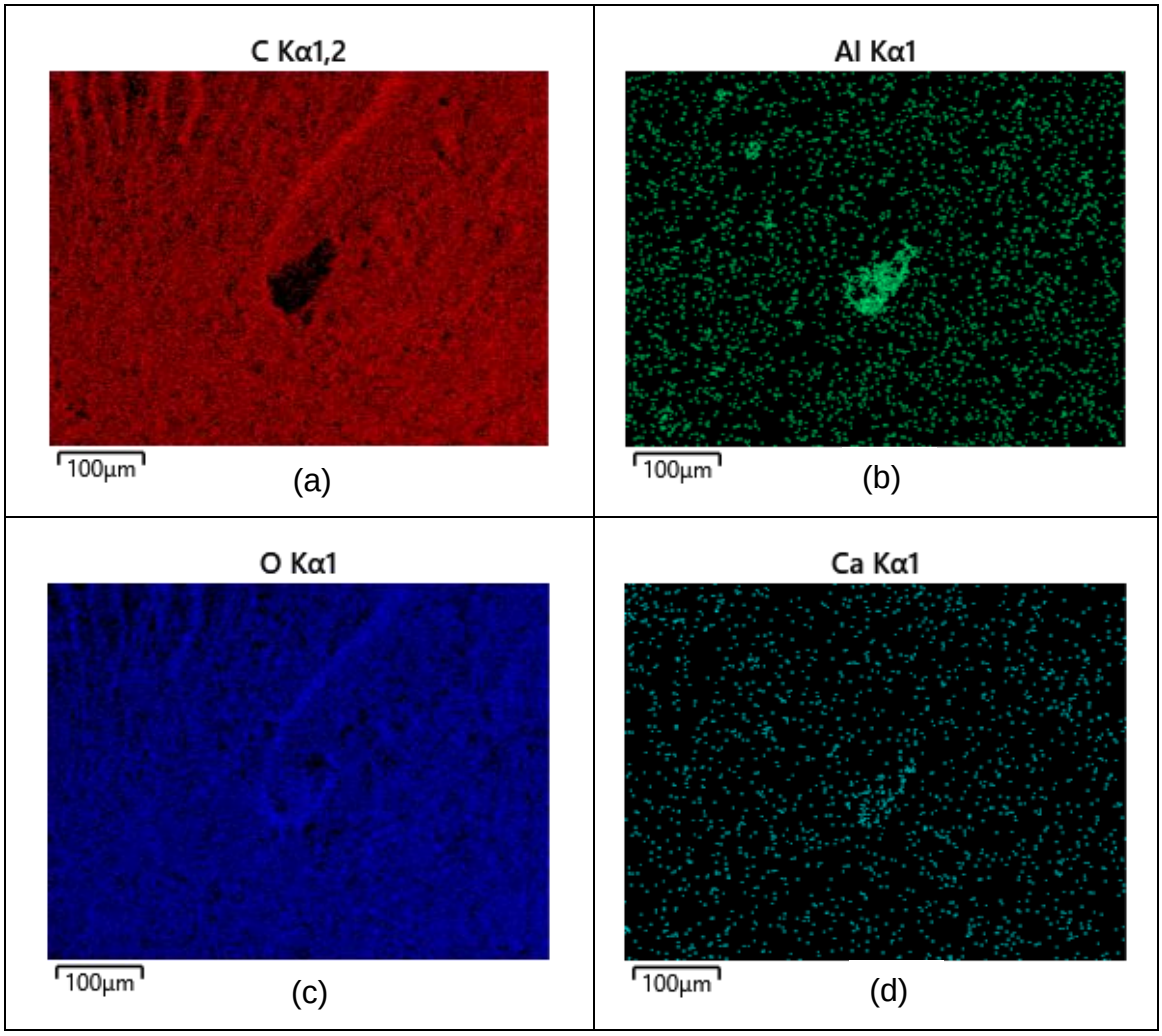

Figure 5-3 EDS results showing elemental dispersions for carbon (a), aluminium (b), oxygen (c), and calcium (d) - on the cross-sectional surface of the PLA80/BioPBS20/HbnC1 filament material in Figure 5-2.

The EDS analysis shows a strong elemental composition and distribution of carbon and oxygen based on their dominant composition in both PLA and BioPBS polymers. Additionally, silicon, aluminium and calcium are further elements identified by the EDS scan, which consequently confirms the significant presence of the constituent elements of HbnC (i.e., based on its chemical formula: $Al_2H_2O_6Si$). Figure 5-3(b) and Figure 5-3(d) show that silicone and aluminium have a strong presence in smaller- and larger-sized (agglomerated) dispersions in the PLA80/BioPBS20/HbnC1 filament surface. Nonetheless, these EDS data show that there is a good dispersion of the HbnC nanomaterial across the filament's surface. However, with the presence of some larger agglomerations of

the HbnC nanoparticles, better exfoliation and therefore dispersion can still be targeted during filament fabrication. An example of such agglomerations is seen in the area highlighted by the red-circled region in Figure 5-2, which can also be distinctly identified in the same location in the EDS map(s). Higher magnification images of the HbnC-containing filament are shown in Figure 5-4; for which, in Figure 5-4 (a), a HbnC particle of about 4 µm is identified. In Figure 5-4 (b), a relatively more blended morphology than that of the PLA80/BioPBS20 MB-FE filament is seen. Furthermore, the morphology in Figure 5-4 (b) appears to have a more developed secondary phase of polymeric structures that sits above the base surface. Moreover, in the same image - Figure 5-4 (b), the BioPBS-rich domains are more observable and show the unique sea-island morphological features that are characteristic of PLA/BioPBS blends and composites [156]. Nonetheless, the differences observed in the PLA80/BioPBS20/HbnC1 MC-FE filament is a result of increased PLA nucleation sites resulting from polymer chain scissions and nano clay particle addition. The increased PLA nucleation sites create denser regions of secondary PLA phases (i.e., structures on top of base surface) which, according to DSC data, results in a majority of partially stable PLA crystals in the PLA80/BioPBS20/HbnC1 MC-FE filament.

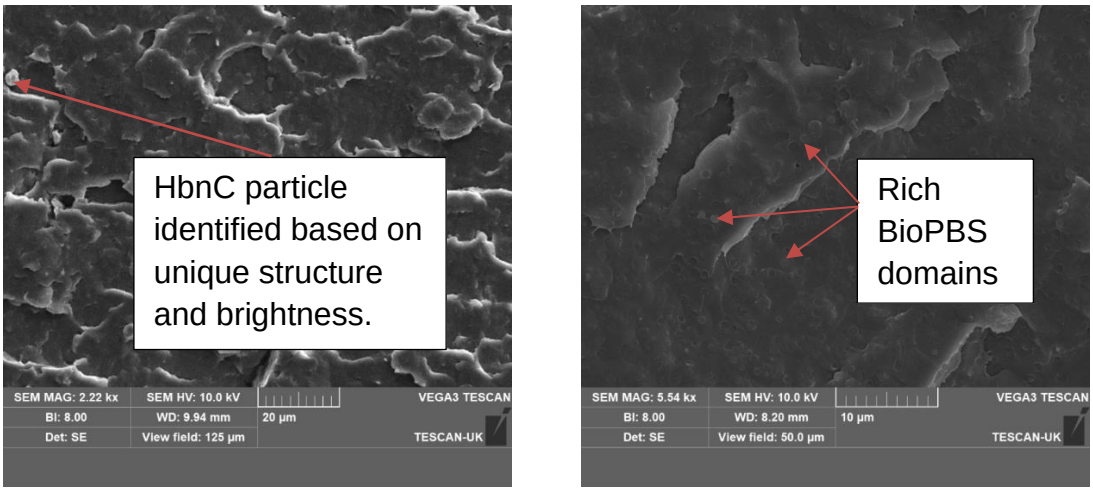

(a) (b)

Figure 5-4 Microscopic images at 20 µm (a) and 10 µm resolutions (b): of the cross-sectional surface of the PLA80/BioPB20/HbnC1 filament.

5.2.3 Cross-sectional microscopic results for composite filaments containing rGO.

Microscopic images for the fracture surface of the PLA80/BioPBS20/rGO1 MC-FE filament is presented in Figure 5-5 at relatively high (3000× – 8000×) magnification. In general, these images indicate a good dispersion of the rGO material within the filament morphology. However, there is sufficient evidence to suggest that the added rGO may also contain graphitic structures with tighter interlayer spacing. Nonetheless, there is also the possibility that the added rGO materials aggregates during production to yield less transparent graphitic structures due to multi-layer rGO sheet formations. In Figure 5-5 (a), green arrows are used to indicate positions of rGO platelets with good transparency which were identified due to their overlapping position. Additionally, other rGO platelets in the formulation can be identified as those structures like that indicated by the black arrow. The fracturing feature seen at the top region of Figure 5-5 (a), shown by red arrows, indicates the degradation of the biopolymer composite matrix material under the utilized beam intensity after a period. In Figure 5-5 (b), label ‘P’ is used to highlight a distinct platelet with a lateral size of about 10 µm in the polymer blend matrix. Meanwhile in Figure 5-5 (c) and Figure 5-5 (d), more evidence of the rGO dispersion and matrix degradation are observed respectively, and with relatively smoother matrix surface than the PLA80/BioPBS20 filaments, just as observed for the HbnC-containing filament. Irrespective of this, the distinctly identifiable domains of the BioPBS material in the HbnC-containing PLA80/bioPBS20-based filament are significantly suppressed in the PLA80/BioPBS20/rGO filament, which suggests that there is stronger phase separation in the HbnC-containing filaments. This finding supports the calorimetric results that identifies significantly reduced recrystallization of the BioPBS phase in the PLA80/BioPBS20/rGO1 filament. Furthermore, in Figure 5-5 (e), the region enclosed by the orange outline shows a site occupied by structurally rigid additive material that sits on the surface in a more vertically oriented direction. This is less intercalated and less distributed rGO that have either aggregated during the associated filament fabrication route or could be lower quality rGO material in the form of graphitic platelets.

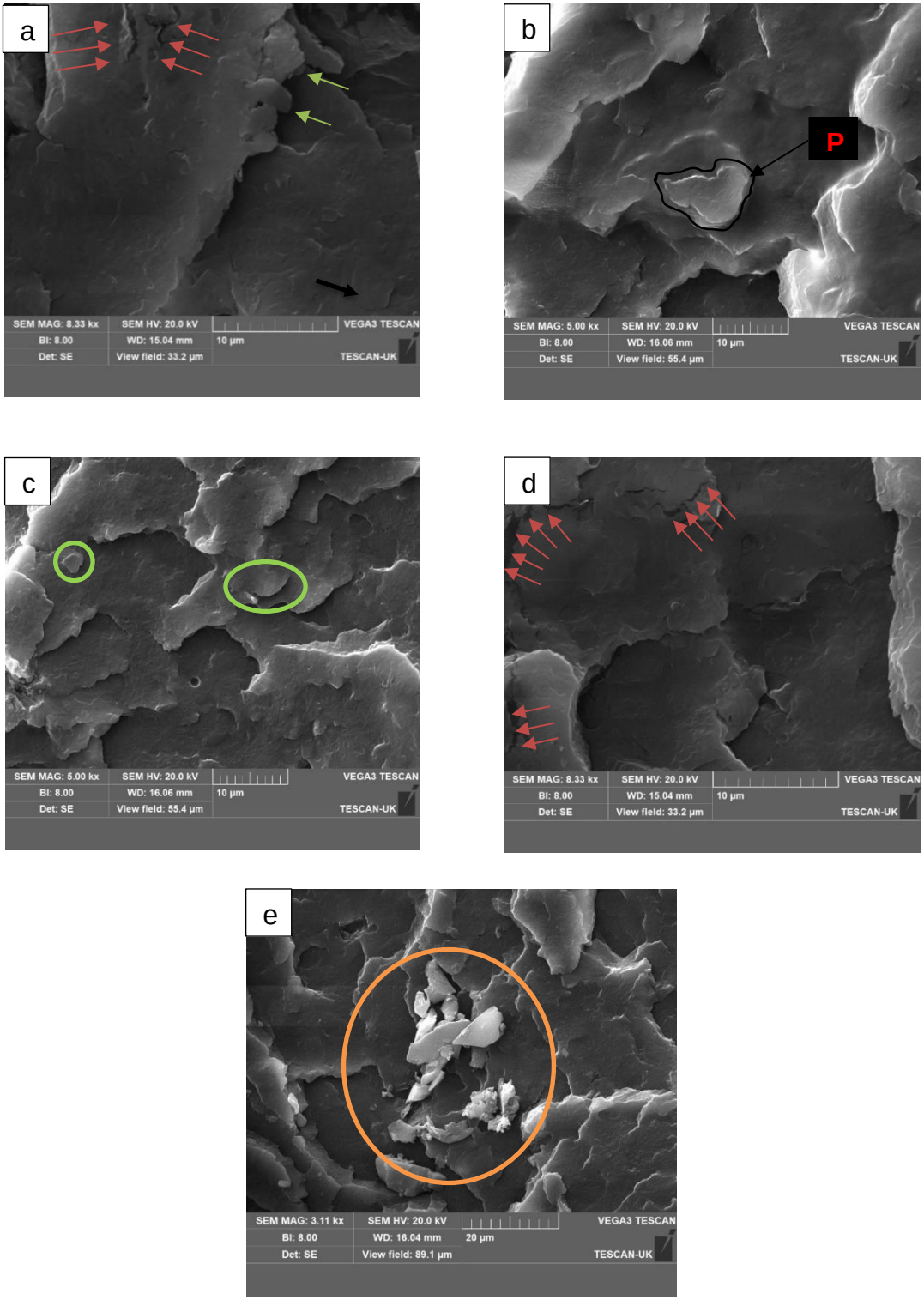

Figure 5-5 Fabricated PLA80/bioPBS20/rGO1 filament showing: possible rGO platelet and degrading regions (a), embedded rGO platelet (b), dispersed rGO platelets (c), more electron voltage-induced degradation (d), and limitedly-exfoliated graphitic structures (e).

From the SEM results, benefits of a multi-step filament fabrication route can be inferred for the dispersion of the nanomaterials in the PLA80/BioPBS20 matrix. This is even though agglomerated or non-exfoliated structures of HbnC and rGO are observed in the microscopic images. The findings in this case do show that the filament fabrication process can however be optimised for specific end-product performance. Generally, limited miscibility or compatibility of the PLA and BioPBS phases can be observed in all PLA80/BioPBS20-based filaments; however, the findings also confirm the improved nucleating effect of HbnC and rGO nanomaterials in the PLA phases of the PLA80/BioPB20-based their respective filament materials. Additionally, these findings confirm that while HbnC barely affects BioPBS recrystallization, rGO inhibits it. This indicates that the presence of rGO in the PLA/BioPBS20/rGO1 filament limits an effective recrystallisation of the BioPBS phase, which is known to cause dimensional changes and shrinkage during or after deposition on a print bed. The limited recrystallisation and recrystallisation rate of the BioPBS phase in the PLA80/BioPBS20/rGO1 MC-FE filament therefore limits the chances of positional changes of the printed roads, from which failed prints may occur. Nonetheless, for all formulations assessed via SEM, there is limited evidence of microporosity, which is an important for developing a good quality filament material.

5.3 Rheological characterization of fabricated filament formulations under FDM-based 3DP conditions.

5.3.1 Complex viscosity and viscoelastic behaviour of cast cylindrical plates made from fabricated filament formulations.

The dynamic viscoelastic results obtained from testing of cast cylindrical plates made from the melt blended and pelletised PLA80/BioPBS20 formulation are presented in Figure 5-6. In this set of results, the reducing complex viscosity values over the strain frequency range indicate non-Newtonian shear-thinning behaviour, which is typical for most thermoplastic materials. The complex viscosity values for the PLA80/BioPBS20 filament formulation at 180 °C are about 1350 Pa.s at low angular frequency of 0.1 rad/s, then drop to about 200 Pa.s at the highest tested angular frequency value of 600 rad/s. At 190 °C, the peak

complex viscosity values are reduced as expected and start at about 780 Pa.s at a strain-rate of 0.1 rad/s, which then reduces to about 140 Pa.s under a strain-rate of 600 rad/s. The complex viscosities at 200 °C, 210 °C, 220 °C, and 230 °C also show the same trend, reducing from about 380 Pa.s, 170 Pa.s, 85 Pa.s, and 40 Pa.s, respectively, to about 80 Pa.s, 45 Pa.s, 25 Pa.s, and 15 Pa.s. At 240 °C and 250°C, the complex viscosity of the materials also ranges from about 20 Pa.s and 18 Pa.s respectively, to about 10 Pa.s and 7 Pa.s. At the highest testing temperatures from 230 °C to 250 °C, there is evidence confirming that at low angular frequencies, the complex viscoelastic response changes significantly, more so with increasing temperature. This is possibly due to changing molecular weight distributions. Meanwhile, at higher strain frequency values, the viscoelastic response of the material appears to be consistent. This is because the complex viscosity becomes less dependent on molecular weight and weight distribution at higher frequencies at which the deformation is so fast that temperature and strain frequency conditions determine the viscoelastic response of the material. Furthermore, since higher temperatures induce more molecular diffusion and motion, the internal friction is significantly reduced at each temperature increment causing a stepped decrease in the complex viscosity of the blend, irrespective of strain rate. Interestingly, above an angular frequency of 100 rad/s, at 240 °C and 250 °C, a significant shear thickening or dilatant behaviour of the blend occurs and raises the question of a secondary phase response by the BioPBS domains, which occurs after the degradation of the dominant PLA phase. Nonetheless, this behaviour may also represent a high strain rate-induced phase transition of the BioPBS-rich phase, which causes the material formulation to become more viscous above a certain temperature and strain-rate. Such behaviour shows the superior thermal stability of the BioPBS phase in relation to the PLA phase. Therefore, based on specific temperature and strain rate conditions, the BioPBS phase could be used to control the storage to loss modulus ratio of an extruding PLA-based filament material at different stages of the FDM-based 3DP process. Usefully, the complex viscosity profiles obtained for the PLA80/BioPBS20 blend show a thermo-rheologically simple behaviour that allows the construction of master curves at a single reference temperature.

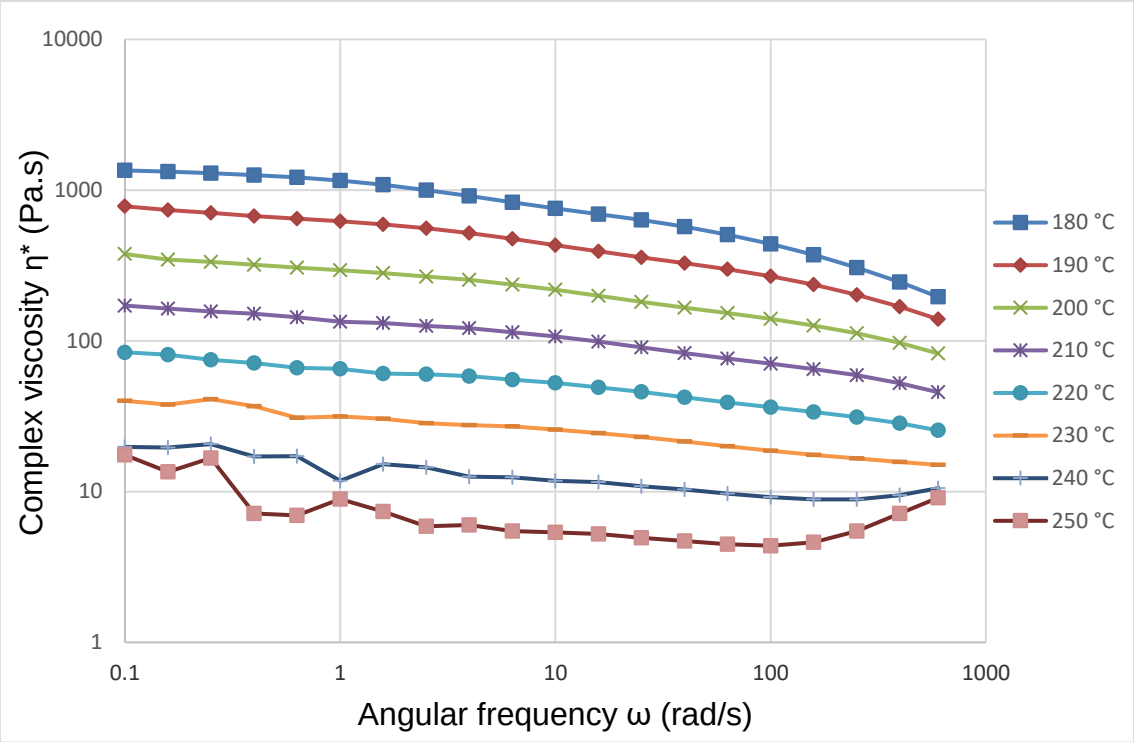

Figure 5-6 Log-log plot of complex viscosity against angular shear frequency for the cast PLA80/BioPBS20 blend formulation.

Figure 5-7 shows the dynamic viscoelastic results obtained from testing the cast cylindrical plates made of the PLA80/BioPBS20/HbnC1 composite formulation. In this result, the complex viscosities at 180 °C, 190 °C, 200 °C, 210 °C, and 220 °C show similar shear thinning behaviour as the PLA80/BioPBS20 blend, reducing from about 1650 Pa.s, 650 Pa.s, 282 Pa.s, 114 Pa.s, and 53 Pa.s, respectively, to about 221 Pa.s, 111 Pa.s, 57 Pa.s, 29 Pa.s, and 18 Pa.s, respectively. Furthermore, the complex viscosity at 230 °C reduces from about 25 Pa.s to about 13 Pa; and at 240 °C, from about 22 Pa.s to about 11 Pa.s, while at 250 °C, it reduces from about 14 Pa.s to about 11 Pa.s. Between 230 °C and 250 °C, the same possible effect of molecular weight reduction found in the blend is also observed at low strain frequencies in the nano-clay composite, and hence emphasizes the fact that some degradation occurs in the nano-clay formulation between 230 °C and 250 °C. Furthermore, at 240 °C and 250 °C, and above 100 rad/s, a shear thickening behaviour is also observed, which is intensified at the highest temperature, just as found for the PLA80/BioPBS20 blend. This behaviour may now be explained by the effect of high temperature and high shear

frequency on the PLA80/BioPBS20 matrix, which appears to be resulting in a phase transition of the PLA80/BioPBS20 matrix material. Between 10 and 100 rad/s, the complex viscosity for the nano-clay composite material is lower than that found for the composite blend formulation at 180 °C. However, above 190 °C, the complex viscosity decreases below that of the composite blend, and furthermore drops below that of the rGO-containing formulation from 200 °C without recovering against either of the other two material formulations at higher temperatures. This effect may be caused by the hydrophilic nature of the HbnC particles, which contain hydrolysable exchange cations in their molecular structure that can therefore support the absorption of surrounding moisture [27], [28]. This can facilitate the development of hydrothermal degradation sites within the tested material. Nonetheless, this characteristic of the nano-clay composite shows that it can be employed as a PLA80/BioPBS20-based formulation that yields a relatively lower viscosity value at typical printing temperatures. Importantly, however, the PLA80/BioPBS20/HbnC1 composite results suggest a thermo-rheologically simple behaviour, which allows for the construction of master curves at a single reference temperature.

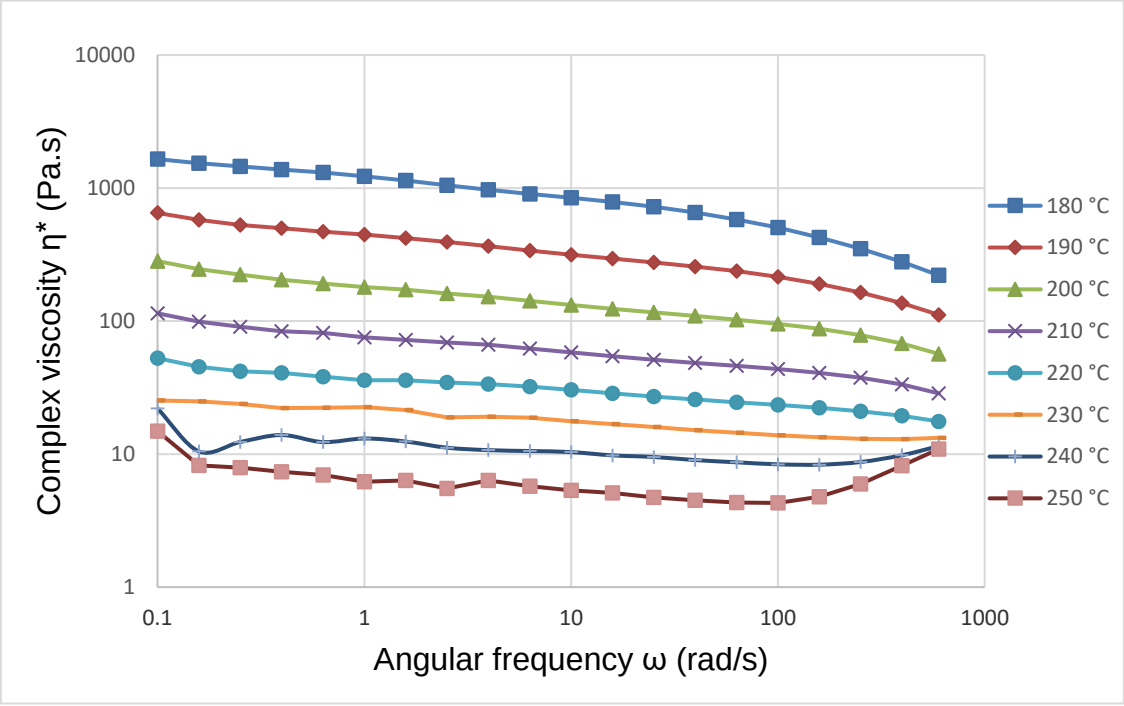

Figure 5-7 Log-log plot of complex viscosity against angular frequency for the cast PLA80/BioPBS20/HbnC1 composite formulation.

The dynamic viscoelastic results obtained from testing the cast cylindrical plates made using the PLA80/BioPBS20/rGO1 composite are presented in Figure 5-8. The complex viscosities at 180 °C, 190 °C, 200 °C, 210 °C, and 220 °C show similar shear-thinning behaviour as observed for the PLA80/bioPBS20-based composites, with complex viscosity values reducing from about 1225 Pa.s, 569 Pa.s, 315 Pa.s, 204 Pa.s, and 130 Pa.s, to about 179 Pa.s, 90 Pa.s, 69 Pa.s, 49 Pa.s, and 35 Pa.s, respectively. Between 230 °C and 250 °C, the complex viscosity at 230 °C reduces from about 86 Pa.s to about 28 Pa.s; at 240 °C, the complex viscosity is found to reduce from about 65 Pa.s to about 16 Pa.s. Meanwhile, at 250 °C, it reduces from about 53 Pa.s to about 15 Pa.s. Nonetheless, it is observed that the molecular degradation effects observed around 230 °C to 250 °C at low angular frequencies in the PLA80/BioPBS20 and PLA80/BioPBs20/HbnC1 formulations are relatively reduced in the PLA80/BioPBS20/rGO1 composite. This suggests that the rGO loading possibly provides better thermal stability for the polymer chain network, but still appears to undergo shear thickening between 230 °C and 250 °C, which again occurs most effectively at 250 °C. Other observations for the rGO-based composite suggest that it has a relatively higher strain frequency dependence, and a tighter complex viscosity range at low angular frequencies when compared to the blend and nano-clay composite formulations. Furthermore, when compared to the other two formulations, between 10 and 100 rad/s, the rGO-containing formulation offers the lowest complex viscosity value up to 200 °C where it surpasses the complex viscosity of HbnC-containing formulation. Above 210 °C, the complex viscosity of the rGO-containing filament surpasses that of the other two composite formulations. Nevertheless, the rGO-containing filament also offers the simple thermorheological behaviour that allows for the construction of master curves at a single reference temperature.

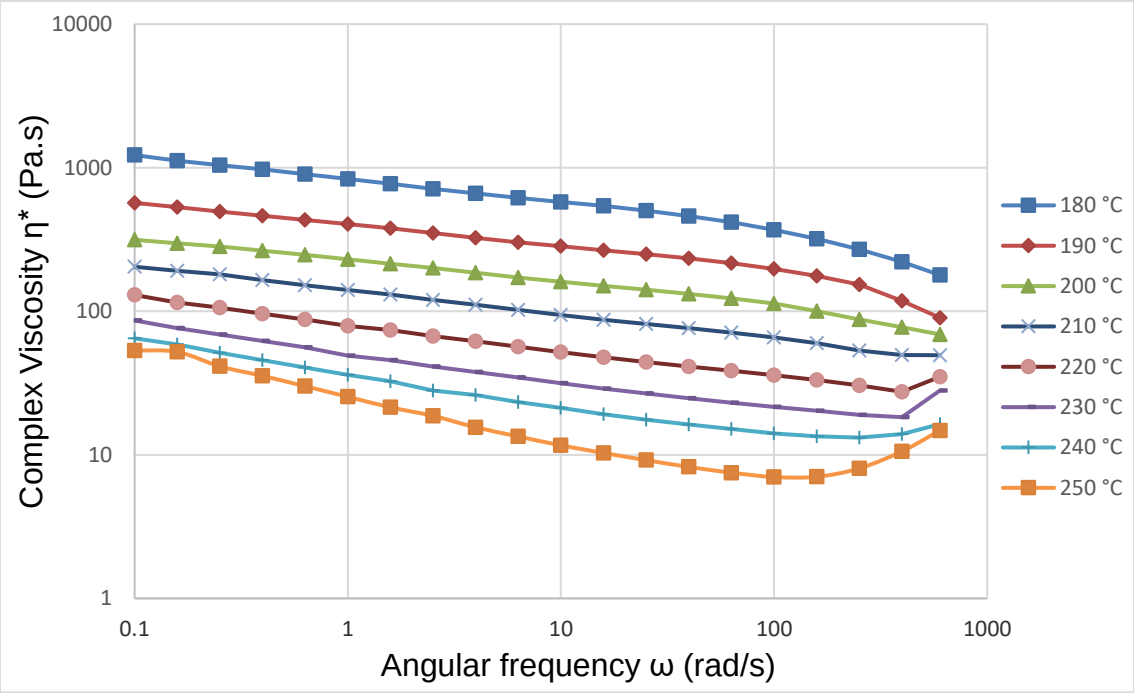

Figure 5-8 log-log plot of complex viscosity against angular frequency for the cast PLA80/BioPBS20/rGO1 composite formulation.

The viscoelastic storage modulus and loss modulus plots for each filament material formulation are presented subsequently. For the PLA80/BioPBS20 blend formulation, the storage and loss modulus plots are shown in Figure 5-9 and Figure 5-10 respectively. It can be deduced that from about 180 to 230 °C, the molecular structure is relatively well preserved, and the elasticity of the material retained up until 230 °C (and up to a limit of 100 rad/s). However, above 230 °C, the elastic storage modulus values effectively indicate phase changes during the test that lead to more transitions in complex viscosity values above 230 °C. Other storage and loss modulus plots for the tested PLA80/BioPBS20/HbnC1 and PLA80/BioPBS20/rGO1 composite formulations are therefore presented from Figure 5-11 to Figure 5-14, for further comparison.

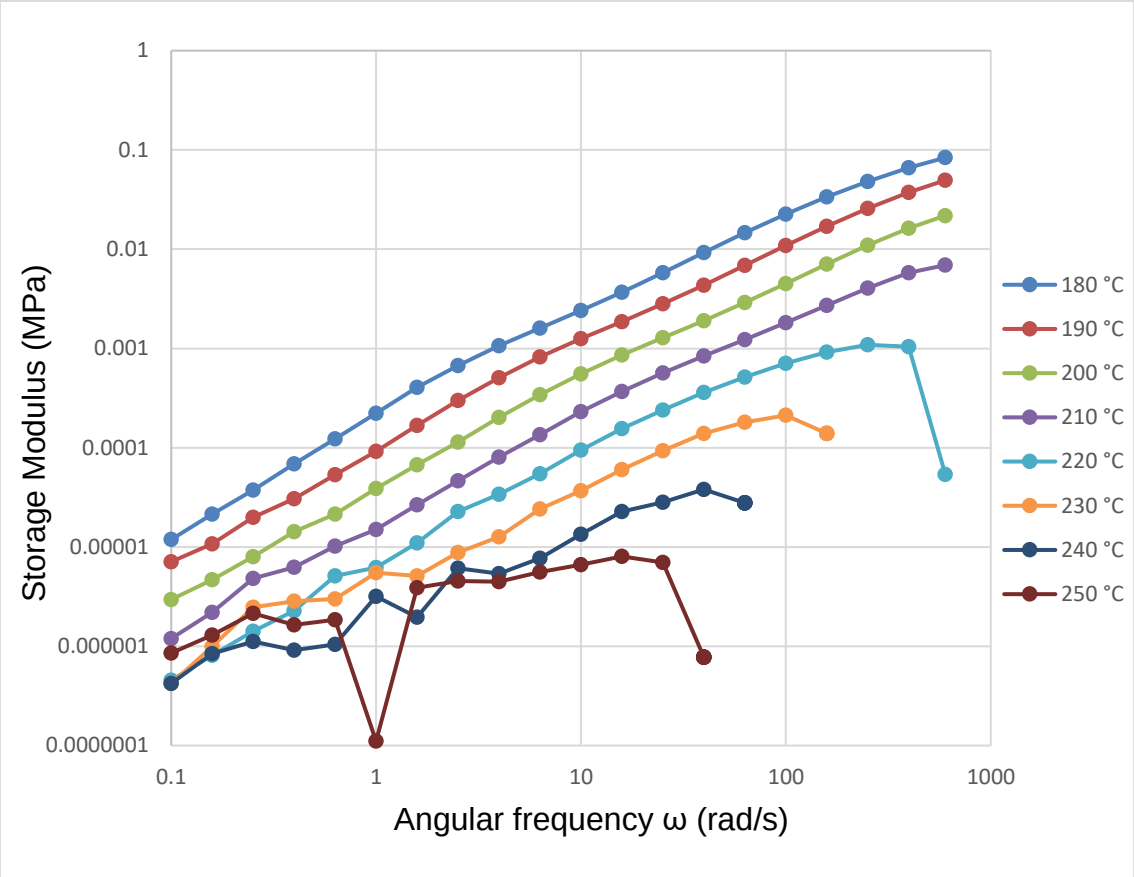

Figure 5-9 log-log plot of storage modulus against angular frequency for the cast PLA80/BioPBS20 blend formulation.

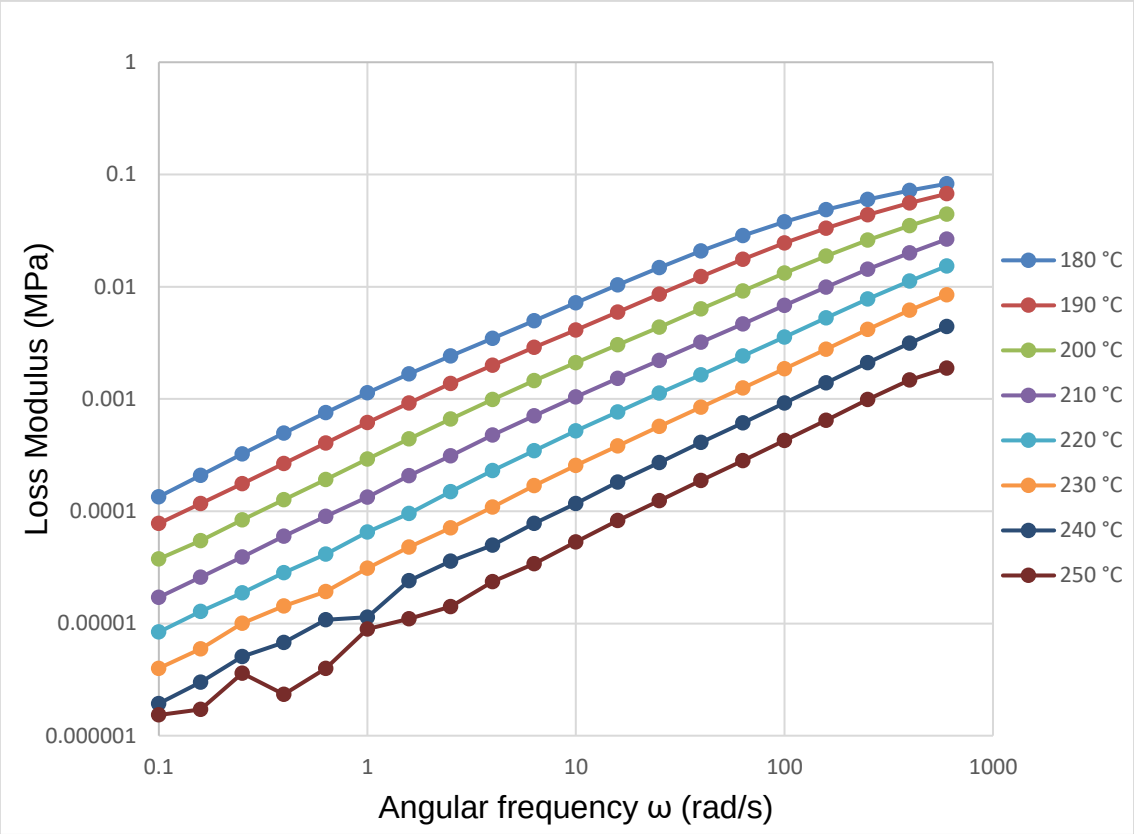

Figure 5-10 Log-log plot of loss modulus against angular frequency for the cast PLA80/BioPBS20 blend formulation.

The storage and loss modulus plots for the PLA80/BioPBS20/HbnC1 formulation are presented in Figure 5-11 and Figure 5-12 respectively, while the storage and loss modulus plots for the PLA80/BioPBS20/rGO1 formulation are presented in Figure 5-13 and Figure 5-14 respectively. These results particularly highlight the effects of HbnC and rGO on the storage and loss modulus of the PLA80/BioPBS20-based composites. In the case of HbnC, the composite shows a stronger effect of polymer chain misalignment, disentanglement, and degradation around and above 230 °C, which leads to inconsistent and unreliable storage modulus data as the viscous loss modulus component dominates the composite behaviour. However, for the rGO-containing PLA80/BioPBS-based composite under the same conditions, the effect of inconsistent storage modulus appears to be relatively and significantly improved. This result supports the suggestions that highlight rGO as acting as a thermal stabilizer for the PLA80/BioPBS20-based composite.

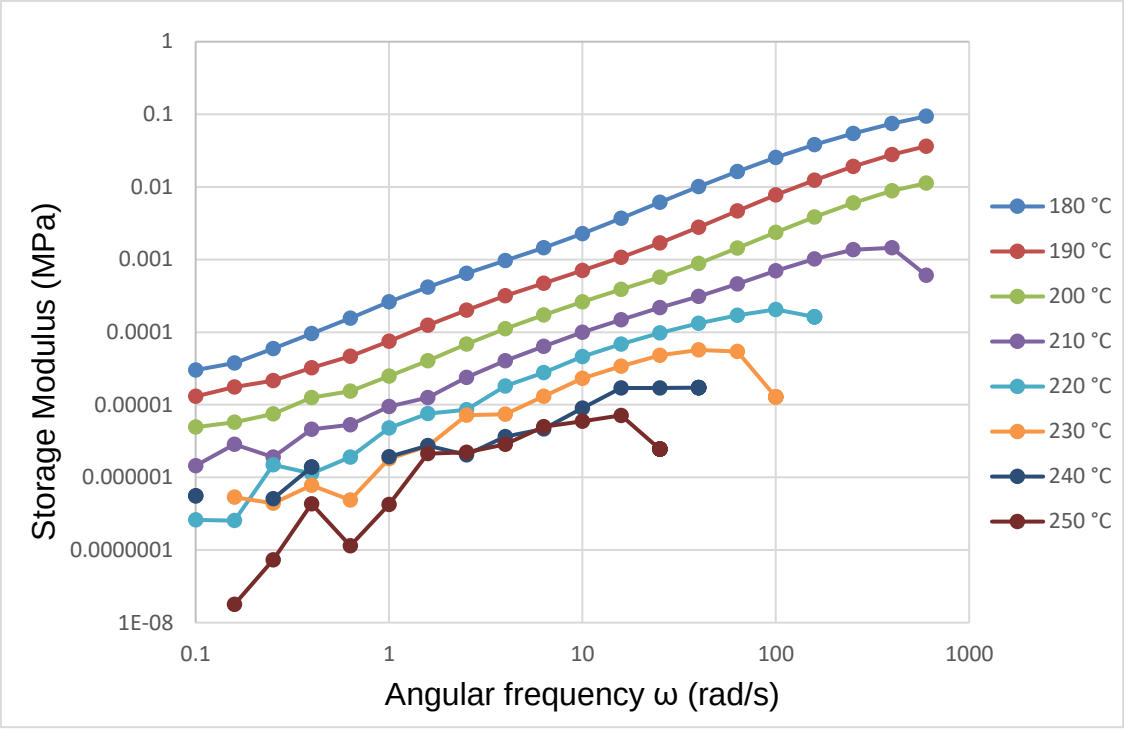

Figure 5-11 log-log plot of storage modulus against angular frequency for the cast PLA80/BioPBS20/HbnC1 composite formulation.

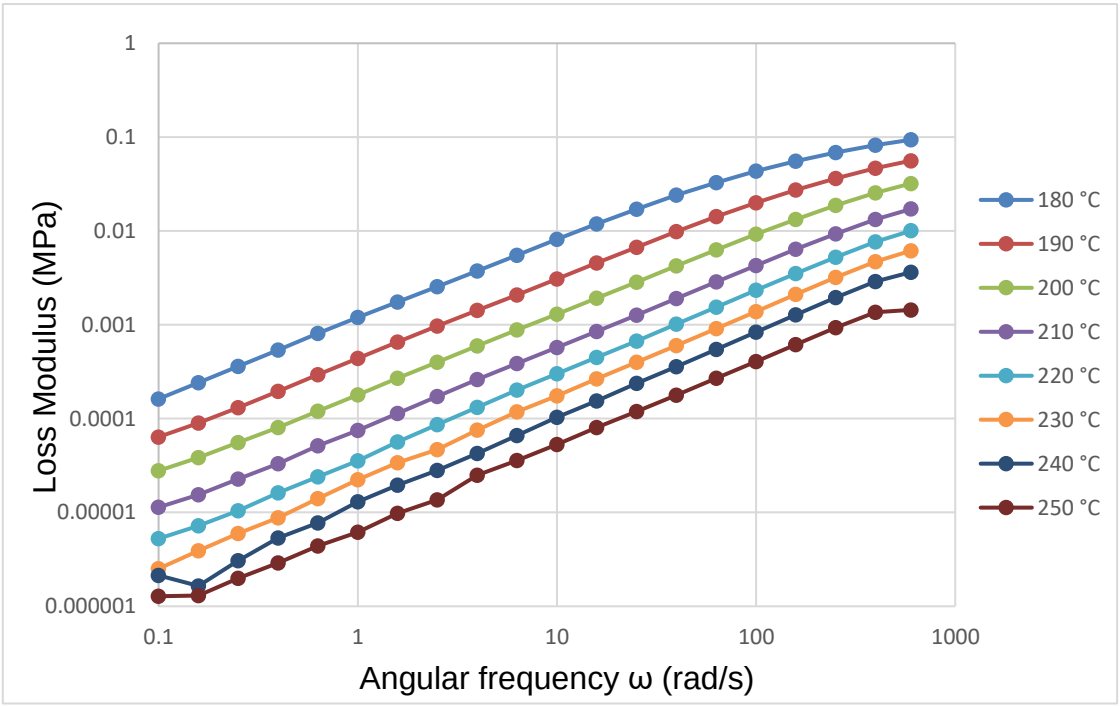

Figure 5-12 log-log plot of loss modulus against angular frequency for the Cast PLA80/BioPBS20/HbnC1 composite formulation.

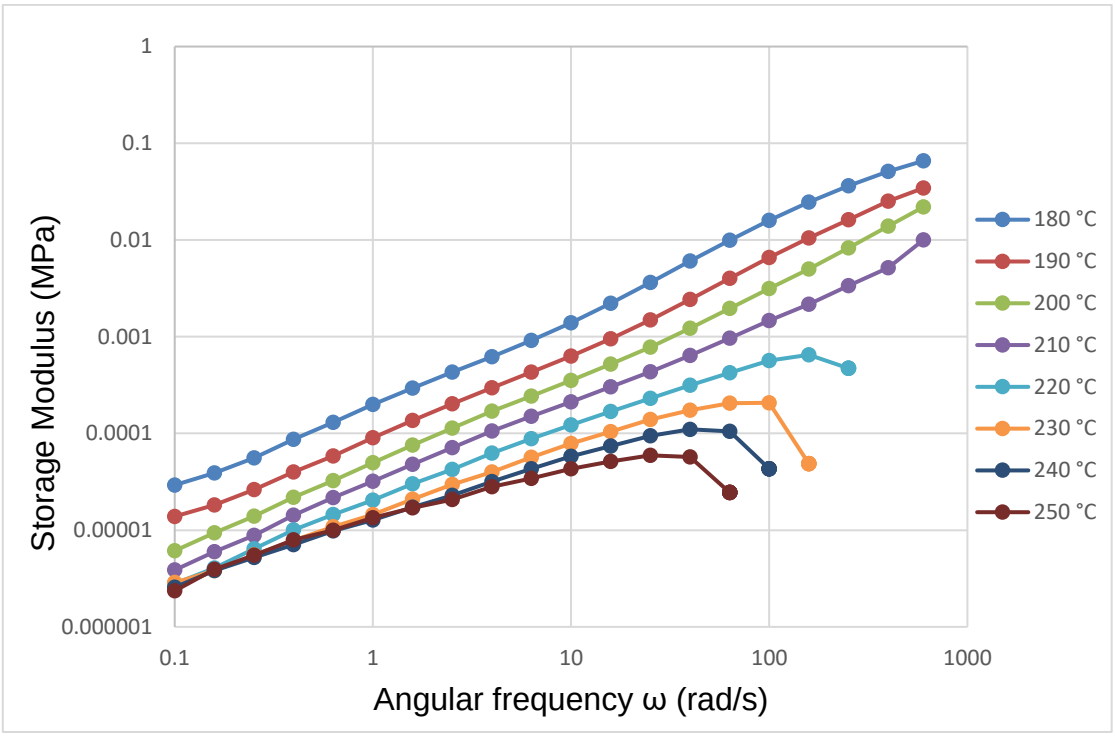

Figure 5-13 log-log plot of storage modulus against angular frequency for the cast PLA80/BioPBS20/rGO1 composite formulation.

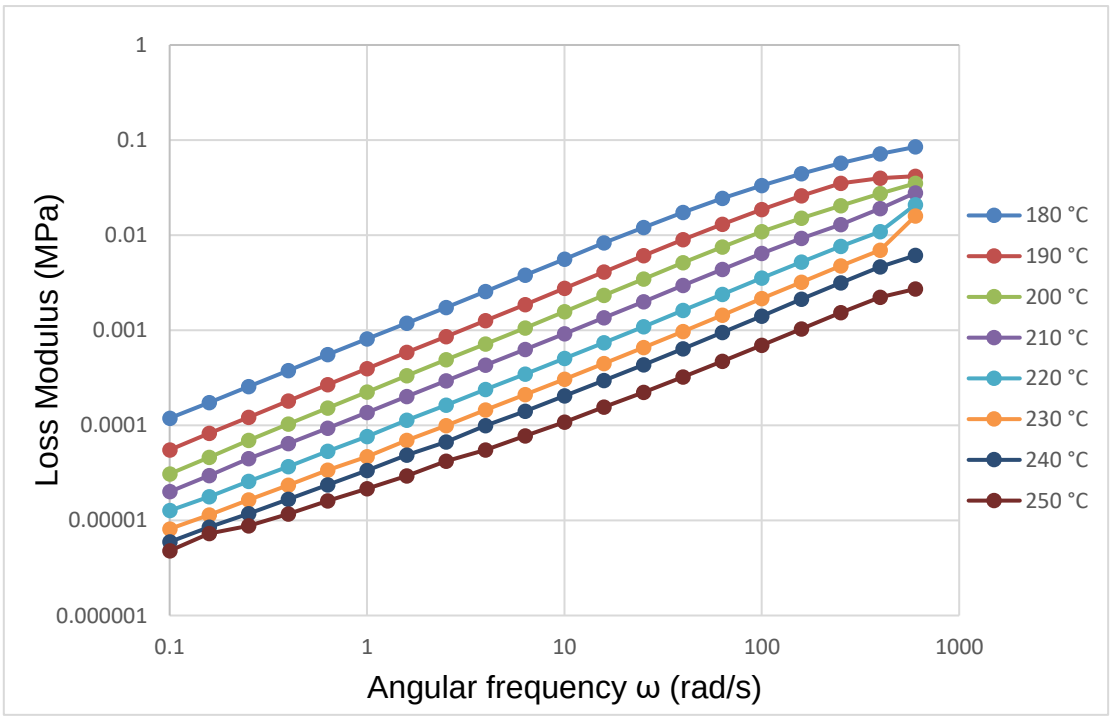

Figure 5-14 log-log plot of loss modulus against angular frequency for the cast PLA80/BioPBS20/rGO1 composite formulation.

5.3.2 Determination of complex viscosity values using master curves and true shear frequency values

The results in this section present the development of a master curve for the PLA80/BioPBS20-based formulations, which can be used to determine complex viscosity values at shear frequencies that are unattainable experimentally. However, from the deduced viscoelastic information of each composite material formulation, it is evident that none of the formulations show an effective Newtonian region before reaching the more evident shear thinning stage. This is because of the relatively high temperatures that cause the material formulations to exceed their Newtonian state under the strain and strain frequency conditions applied. Hence, the Power law model, which can be used for shear-thinning fluids, is used for identifying and comparing the shear thinning parameters and behaviour of each formulation at prospective 3DP temperatures. Determining the power law index allows for correcting the calculated apparent shear rate and providing the true shear rate values required for determining complex viscosity values form the master curve.

The power law parameters for each formulation were obtained by fitting the power law model to the experimentally obtained log-log plots of complex viscosity against angular frequency at each prospective printing temperature. For temperatures between 210 °C and 230 °C, the power law parameters, i.e., n, power law index and K, consistency parameters were obtained and are presented in Table 5-1, while the utilized log-log plots of complex viscosity against angular shear frequency are presented in Appendix A.

Table 5-1 Power law parameters for each filament material formulation at selected test temperatures

Material Formulation			
	Temperature (°C)	n	***K* (Pa s^n)**
PLA/BioPBS20	**210**	0.8	172
	220	0.83	79.8
	230	0.88	35.3
	Temperature (°C)	n	***K* (Pa s^n)**
PLA/BioPBS20/HbnC1	**210**	0.84	86.3
	220	0.89	40.7
	230	0.92	21.3
PLA/BioPBS20/rGO1	**Temperature (°C)**	n	***K* (Pa s^n)**
	210	0.83	139.8
	220	0.83	76.3
	230	0.85	43.6

Figure 5-15 compares the trend of power law index obtained for the formulations at 210 °C, 220 °C and 230 °C. According to the power law parameters obtained, the power law index is found to increase rapidly with increasing temperature for the PLA80/BioPBs20 and PLA80/BioPBS20/HbnC1 material formulation, but not for the PLA80/BioPBS20/rGO1 formulation, which maintains its power law index value of 0.83 at both 210 °C and 220 °C. These findings effectively indicate a decrease in shear thinning behaviour for the PLA80/BioPBS20 and PLA80/BioPBS20/HbnC1 formulations as these materials power index parameter moves towards that of a Newtonian fluid. The least shear thinning effect is observed for the nano-clay containing composite, while the rGO-containing composite shows a relatively preserved shear thinning behaviour within the shear frequency and temperature range. Furthermore, the deduced power law index is used in calculating the true shear frequency ($\dot{\gamma}_{true}$) using:

$$\dot{\gamma}_{n-corrected} = \dot{\gamma}(\frac{3n+1}{4n}) \qquad \textbf{Equation 5-1}$$

where $\dot{\gamma}_{n-corrected}$ is the corrected shear frequency obtained using the power law index, $\dot{\gamma}$ is the calculated shear frequency using the Hagen/Poiseuille equation, and n is the power law index at a given temperature of the non-Newtonian fluid.

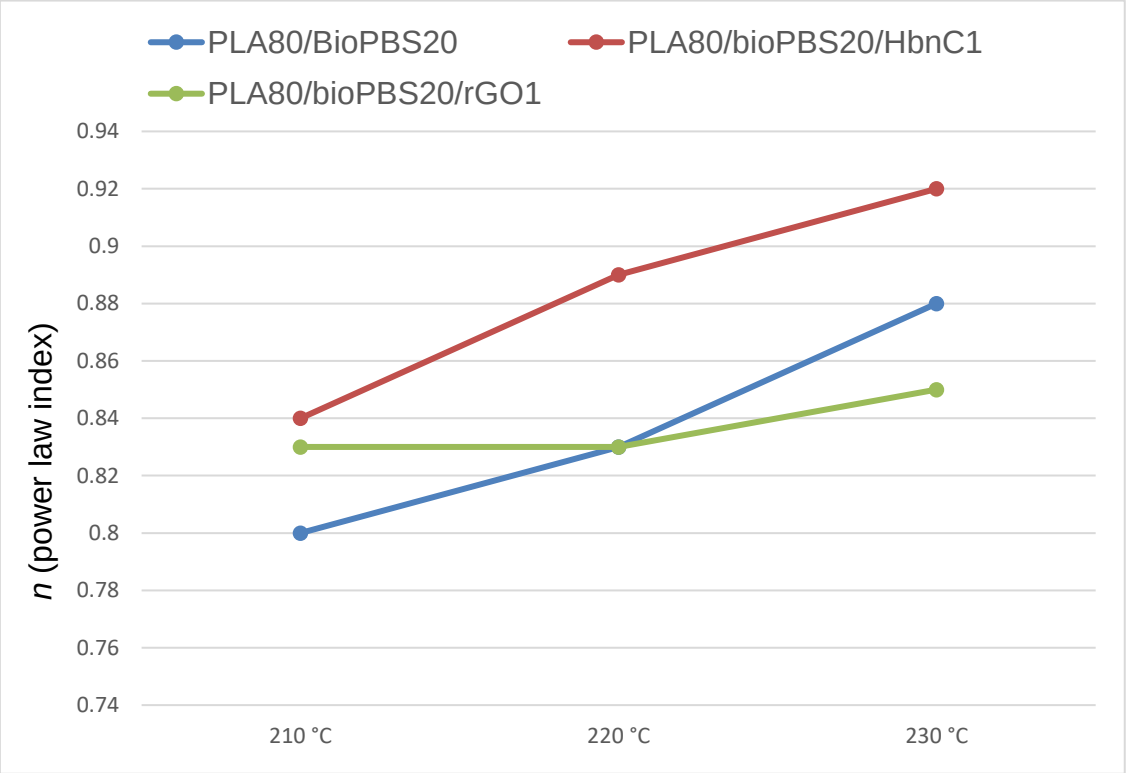

Figure 5-15 Comparing power law parameter for PLA80/BioPBS-based formulation at 210 °C, 220 °C and 230 °C.

The shear rate or frequency values for prospective 3DP extrusion speeds at 20 mm/s, 40 mm/s and 60 mm/s are calculated using the Hagen/Poiseuille formula as described in Chapter 3, and are presented alongside the corrected angular frequency values in Table 5-2, Table 5-3, and Table 5-4 for the PLA80/BioPBS20, PLA80/BioPBS20/HbnC1, and PLA80/BioPBS20/rGO1 material formulations respectively.

Table 5-2 Estimated shear rate and power law-corrected angular frequency occurring for 3DP at 220 °C for PLA80/BioPBS20 formulation.

Printing speed (mm/s)	Shear rate (s^{-1})	Angular shear frequency (rad/s)	Corrected angular shear frequency (rad/s)
20	400	2513	2642
40	800	5026	5283
60	1200	7539	7925

Table 5-3 Estimated shear rate and power law-corrected angular frequency occurring for 3DP at 220 °C for PLA80/BioPBS20/HbnC1 formulation.

Printing speed (mm/s)	Shear rate (s^{-1})	Angular shear frequency (rad/s)	Corrected angular shear frequency (rad/s)
20	400	2513	2591
40	800	5026	5181
60	1200	7539	7772

Table 5-4 Estimated shear rate and power law-corrected angular frequency occurring for 3DP at 220 °C for PLA80/BioPBS20/rGO1 formulation.

Printing speed (mm/s)	Shear rate (s^{-1})	Angular shear frequency (rad/s)	Corrected angular shear frequency (rad/s)
20	400	2513	2642
40	800	5026	5283
60	1200	7539	7925

5.3.2.1 Development of complex viscosity master curves using Arrhenius method.

Considering that the testing conditions are significantly above the glass transition points of the constituent polymer materials, the Arrhenius method, rather than the Williams-Landel-Ferry method, is preferred for carrying out the TTSP method for the development of a master curve. The TTSP is carried out with the use of complex viscosity results obtained for each filament formulation. The complex viscosity master curve represents points at which the complex viscosity values of the tested temperatures overlap with the complex viscosity values of a chosen reference temperature, which in this case is taken at 220 °C. Hence, the determined shift factor, activation energy, and developed complex viscosity master curve results for each filament formulation is outlined subsequently.

5.3.2.1.1 Master curve results for the composite formulations

The master curve is created using the reference temperature of 220 °C; partly because the use of data points at higher temperatures of 230 °C and above limits the consistency of the shift factors obtained and does not effectively offer thermos-rheologically simple data points that allows for a master curve construction. Using a 220 °C reference temperature and the derived Arrhenius-based equation:

$$log_{10}\,(a_T) = \frac{-E_a}{R}\left(\frac{1}{T}\right) \qquad \textbf{Equation 5-2}$$

the horizontal shift factors, which are obtained from complex viscosity and inverse temperature (1/K) data are obtained and presented in Table 5-5 for the three PLA80/BioPBS20-based composite formulations. Furthermore, the activation energy for each formulation is therefore calculated using the gradient, $\frac{-E_a}{R}$, which are obtained from the straight-line plots shown in Figure 5-16. Hence, the activation energy obtained for the PLA80/BioPBS20 formulation is about 129 KJ/mol, while that obtained for PLA80/BioPBS20/HbnC1 and PLA80/BioPBS20/rGO1 are about 171 KJ/mol and 108 KJ/mol respectively.

Table 5-5 Horizontal shift factor and activation energy of PLA80/BioPBS20-based formulation at 220 °C

PLA80/BioPBS20					
a_T (horizontal shift factor) At 220 °C (reference)	**T (°C)**	**T(K)**	**1/T (1/K)**	**$\frac{-E_a}{R}$ (-)**	**Activation energy (KJ/mol)**
16.17	180	453	0.002207	15462	129
8.887	190	463	0.00216		
4.501	200	473	0.002114		
2.262	210	483	0.00207		
1	220	493	0.002028		
PLA80/BioPBS20/HbnC1					
a_T (horizontal shift factor) At 220 °C (reference)	**T (°C)**	**T(K)**	**1/T (1/K)**	**$\frac{-E_a}{R}$ (-)**	**Activation energy (KJ/mol)**
48.89	180	453	0.002207	12946	171
15.38	190	463	0.00216		

5.628	200	473	0.002114		
2.148	210	483	0.00207		
1	220	493	0.002028		
0.5593	230	503			
PLA80/BioPBS20/rGO1					
a_T (horizontal shift factor) **At 220 °C (reference)**	**T (°C)**	**T(K)**	**1/T (1/K)**	**$\frac{-E_a}{R}$ (-)**	**Activation energy (KJ/mol)**
17.09	180	453	0.0022074	14946	108
7.230	190	463	0.0022		
3.647	200	473	0.0021		
1.979	210	483	0.0021		
1	220	493	0.0020		
0.5679	230	503	0.00198		
0.3549	240	513	0.00194		
0.1892	250	523	0.00191		

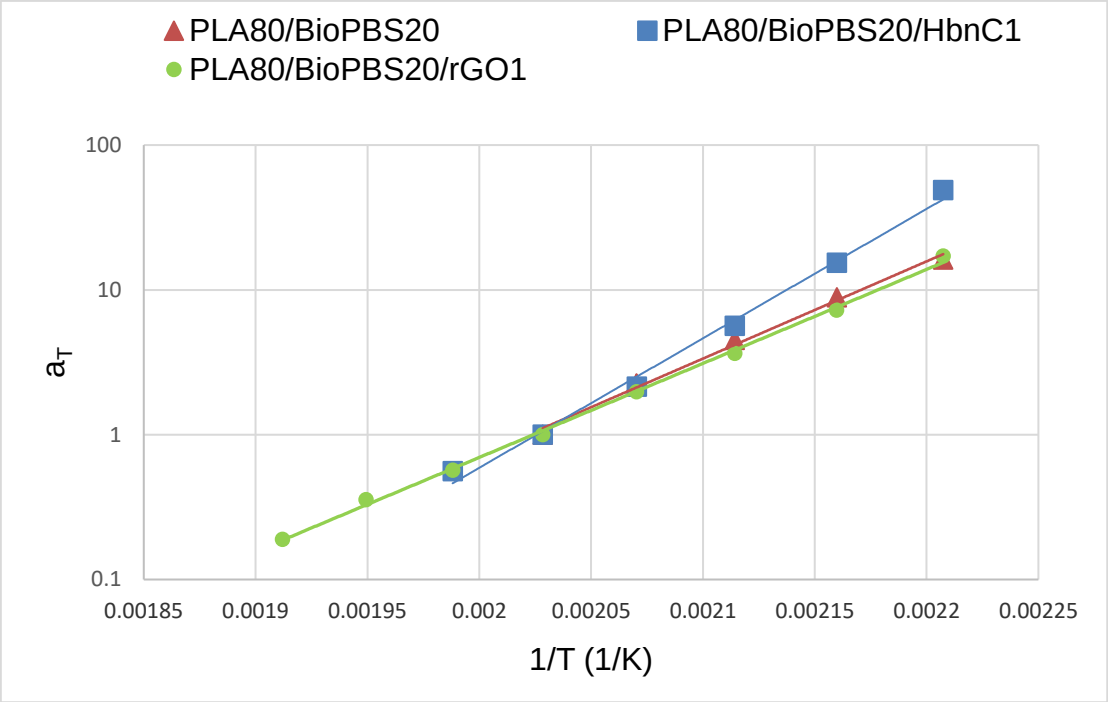

Figure 5-16 Shift factor (a_T) against inverse temperature(1/T) for PLA80/BioPBS20-based formulations at reference temperature of 220 °C.

The resulting complex viscosity master curve for the PLA80/BioPBS20, PLA80/BioPBS20/HbnC1, and PLA80/BioPBS20/rGO1 formulation is shown in Figure 5-17. From this finding, the obtained master curve for the composite blend formulation offers a tool for predicting the complex modulus of the material formulation at 180 °C, 190 °C, 200 °C, 210 °C and 220 °C, between angular strain frequencies of 0.1 rad/s and 10000 rad/s. The master curve data points presented are fitted (superimposed) at 220 °C by using the multiple complex viscosity curves of each respective material formulations - following tests conducted at 10 °C temperature intervals. Importantly, the corrected shear frequency values obtained for the specific print speeds can be utilised to estimate their associated complex viscosity value with respect to a particular PLA80/BioPBS20-based formulation. Furthermore, in relation to the master curve of the PLA80/BioPBS20 blend, the master curve for the PLA80/BioPBS20/HbnC1 composite presents a model for predicting the complex viscosity of the latter between 0.1 rad/s and 30000 rad/s; a higher range than obtained for the PLA80/BioPBS20 formulation. Meanwhile, in the case of the PLA80/BioPBS20/rGO1 formulation, the fitted

complex viscosity values for this material are found to be between 0.01 rad/s and 10000 rad/s, just as obtained for the PLA80/BioPBS20 blend. Comparatively, an additional observation surrounding the activation energy for the three formulations presented so far suggests that the PLA80/BioPBS20/rGO1 formulation requires the lowest (108 KJ/mol), while the PLA80/BioPBS20/HbnC1 formulation requires the most (171 KJ/mol). Hence, it appears that the addition of rGO reduces the activation energy value of the PLA80/BioPBS20-based formulation, meanwhile the addition of HbnC increases it. This explains the relatively higher rate of change of the complex viscosity for the PLA80/BioPBS20/rGO1 formulation at higher strain frequency and temperature conditions, i.e., when compared to the PLA80/BioPBS20 and PLA80/BioPBS20/HbnC1 formulations. In the context of this work, this finding shows that between typical extrusion speeds and strain rates of 2000 and 8000 rad/s, the PLA80/BioPBS20/rGO1 formulation offers a more variable complex viscosity than the other formulations.

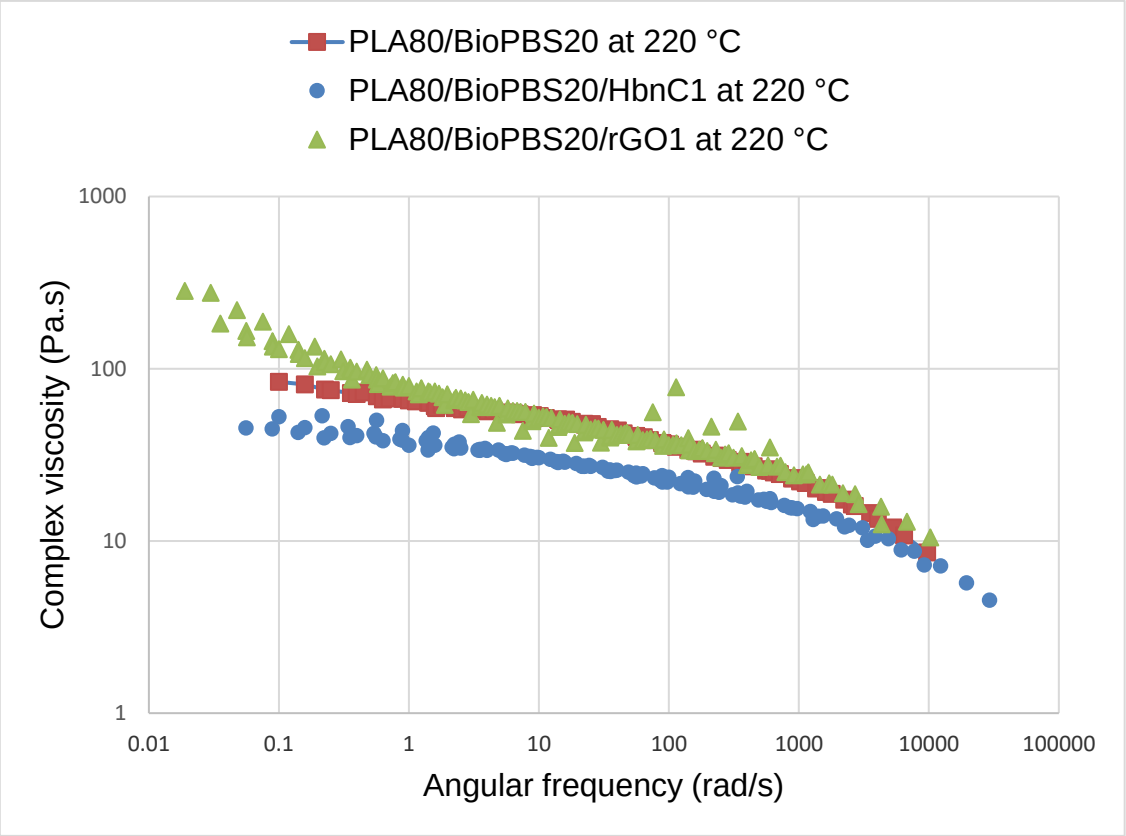

Figure 5-17 Comparing master curves for the PLA80/BioPBS20-based formulations at 220 °C.

The plot shows the complex viscosity values for the material formulations over a broad strain frequency range and helps to conclude that at the given reference temperature, the PLA80/BioPBS20/HbnC1 formulation offers the lowest complex viscosity value. Meanwhile, the complex viscosity for the PLA80/BioPBS20/rGO1 formulation appears higher than that of the PLA80/BioPBS20 formulation at low strain frequencies of about 0.1 rad/s. However, this reduces to match the complex viscosity of the PLA80/BioPBS20 formulation at higher angular frequencies between about 1 rad/s and 1000 rad/s. Finally, the complex viscosity values for the three formulations tend towards the same value as angular frequency reaches about 10000 rad/s. Ultimately, these results create a strong basis for identifying complex viscosities at given strain frequency values, for which, using the associated shift factors, can be used to obtain complex viscosity values at other temperatures. From a material property perspective, using the PLA80/BioPBS20 composite material as a reference, and extrapolating the complex viscosity

values at lower strain frequencies, it is possible to visualize the differences in the zero-shear viscosity, and the change rate of each formulation's complex viscosity upon increasing strain frequency. Furthermore, to explain the estimated differences in apparent zero shear viscosity, it seems that the relatively highest crystallinity in the crystalline PLA phase (at 33%) in the PLA80/BioPBS20/rGO1 formulation allows for more interfacial frictional forces or rigidity of the internal material structure, which therefore leads to its relatively highest zero-shear viscosity behaviour. However, while the PLA80/BioPBS20/HbnC1 formulation shows a crystallinity of about 25%, the similar but slightly higher crystallinity of the PLA80/BioPBS20 formulation at 26% seems to result in a relatively higher zero shear complex viscosity than the PLA80/BioPBS20/HbnC1 formulation. Following the analysis thus far, the corrected 3DP processing shear frequency values for the different print speeds (presented in Table 5-2, Table 5-3, and Table 5-4) is used to predict the viscosity of the PLA80/BioPBS20-based material formulations at a 220 °C print temperature. The results are presented in Figure 5-18 and confirms that the highest complex viscosity behaviour at each print speed occurs for the PLA80/BioPBS20/rGO1 formulation but also reduces most rapidly upon increasing to a 40 mm/s print speed. Nonetheless, for the 40 mm/s and 60 mm/s print speeds, the PLA80/BioPBS20/rGO1 formulation shows a similar complex viscosity value to that of the PLA80/BioPBS20 formulation. Meanwhile the PLA80/BioPBS20/HbnC1 formulation is found to have the lowest complex viscosity at all printing speeds and is strongly considered to be a result of the hydrophilic nature of HbnC, the use of water in its filaments processing route, and the presence of a rich oxygen atmosphere, which altogether promotes hydro-absorption and an effective hydrothermal oxidative degradation of the formulation during testing. While the interlayer bonding quality of dog-bone parts fabricated by Qahtani et al. [138] suggests that a suitable viscosity for the PLA70/BioPBS30 formulation is about 20 – 50 Pa.s during printing at 250 °C, a similarly suitable material viscosity for the PLA80/BioPBS20-based formulations is expected to be achieved at lower print speeds (≤ 40 mm/s) or lower print temperatures (≤ 220 °C), or a controlled combination of both.

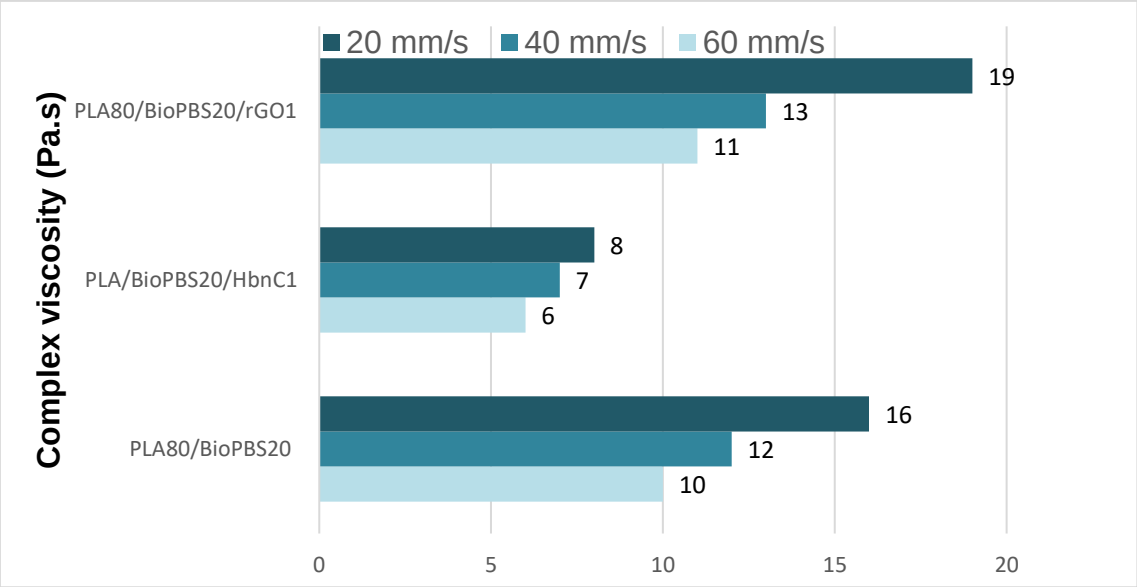

Figure 5-18 Complex viscosity of PLA80/BioPBS20-based formulations at 220 °C.

5.4 Concluding remarks

SEM results show unique features of secondary surface structures of the cryo-fractured filament surfaces, which confirm the crystallisation effects caused by adding HbnC and rGO to their respective PLA80/BioPBS20-based composite formulations, particularly in relation to the PLA80/BioPBS20 filament. These help to confirm the crystallisation and recrystallisation results of PLA and BioPBS phases as observed from DSC analysis. The SEM results confirm that significantly lower recrystallization of the BioPBS phase occurs in the PLA80/BioPBS20/rGO1 filament, which makes it a favourable choice for printing roads with limited shrinkage, warpage or dimensional changes that could disrupt the FDM-based 3DP process. Additionally, the SEM results also shows that the multi-step MB-FE filament fabrication route offers a good option for enabling cost-effective filament manufacturing of PLA80/BioPBS20-based materials for 3DP applications.

In terms of the rheological work, the complex viscosity for the PLA80/BioPBS20/rGO1 filament formulation at 220 °C is higher than that of other filament formulations at all printing speed (i.e., shear frequency) conditions applied. Furthermore, the PLA80/BioPBS20/HbnC1 filament formulation at 220

°C shows the lowest complex viscosity value at all printing speeds. This is strongly considered to be a result of the hydrophilic nature of HbnC, the use of water in its filaments processing route, and the presence of a rich oxygen atmosphere, which altogether promotes hydro-absorption and an effective hydrothermal oxidative degradation of the formulation during testing. Meanwhile, the developed rheological master curves confirm that the TTSP can be applied to PLA80/BioPBS20-based formulations for the prediction of viscoelastic properties outside the possible range of temperature and shear frequency testing. And with respect to the PLA80/BioPBS20-based materials' viscosities, lower print speeds (≤ 40 mm/s) and lower print temperatures (≤ 220 °C) appear to contribute to the favourable conditions required for maintaining the optimal viscosities for FDM-based 3DP.

6 Printability, tensile mechanical properties, and fractured surface assessment of composite parts.

6.1 Introduction

In this chapter, the printing results, and tensile mechanical properties of FDM-based 3D-printed parts are presented to enable the development of relationships between filament formulation, filament fabrication route, 3DP process strategy, and printed-part tensile properties. Subsequently, the tensile-fractured horizontally oriented dog-bone parts are presented to aid with assessments of the effects of filament material formulation, filament fabrication route, polymer phase miscibility, polymer phase crystallinity, and print strategy on the fracture surfaces of 3D-printed PLA80/BioPBS20-based parts. In addition to tensile mechanical results, this chapter includes a description of challenges related to the manufacturing of certain dog bone specimens using its initially attempted FDM-based 3DP strategy. These results provide an overview of the relationships therein that supports the identification, optimization, and adoption of certain PLA80/BioPBS20-based filament materials and related FDM-based 3DP part-fabrication strategies for advanced manufacturing processes.

6.2 Printability of dog-bone specimens using fabricated blend and nanocomposite filaments.

6.2.1 Challenges in 3DP of dog-bone parts using blends and nanocomposite filament formulations.

During the initial 3DP activities, a challenge experienced in the printing of horizontally oriented dog bone parts involved poor print bed adhesion of the PLA80/BioPBS20 FE material as shown in Figure 6-1. The printed roads of the filament material show significant warpage and delamination effects, which is due to the rapid recrystallization of the relatively larger and limitedly distributed BioPBS phases in the extruded roads. This is further supported by the fact that the roads are printed parallel to the print bed, hence causing the BioPBS crystals to grow favourably in the parallel direction as opposed to the perpendicular direction which would otherwise favour bonding to the print bed. Importantly, the

warpage and delamination effects have the potential of causing the already printed roads and structure to obstruct subsequent print-head motion, which effectively limits the accuracy of the printing process and can importantly prevent the completion of the 3DP job. Nonetheless, the optimisation of print strategy with respect to printing temperature, printing speed, and number of parts can be used to achieve printability in certain cases. However, in this case, it involved increasing the print temperature from 210 °C to 220 °C, which then allowed for successful printing of the PLA80/BioPBS20 FE filament as a result of increased residence time at higher temperatures, which allows sufficient time for the uncrystallised BioPBS phase material to form stronger interlocking bonds with the print bed before crystallising. This result and developed understanding guided the designed experimental approach (variable FDM-based 3DP controls) as defined in the methodology, which were used for each filament material formulation. Moreover, it was further found that the effects of delamination and warpage at 220 °C or higher is significantly limited for the more extensively melt-processed PLA80/BioPBS20-based materials, which could be attributed to both processing and nano-filler effects on the recrystallisation of the BioPBS phase. However, the nanoclay-containing filament shows a less concerning issue of material stringing, which is highlighted in Figure 6-2, and more obviously present during 3DP of multiple vertically oriented dog-bone parts as shown in Figure 6-3. This is understood to be caused by continuous and less viscous material flow out of the printer’s nozzle; particularly occurring between printing segments when the material extrusion process should have stopped. This issue leads to more post processing steps and an increased inefficiency of material utilization and creates an obstruction for the printer head.

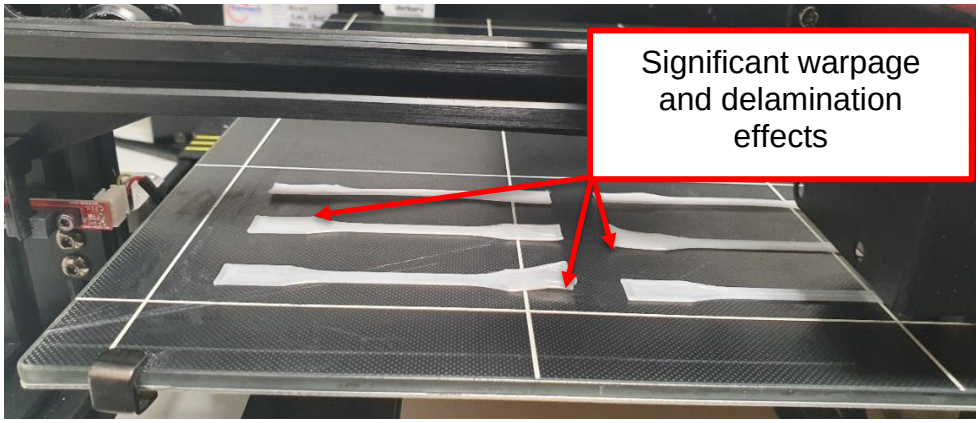

Figure 6-1 Delamination and warping effects shown by PLA80/BioPBS20 blends during 3DP of horizontally oriented dog-bone parts.

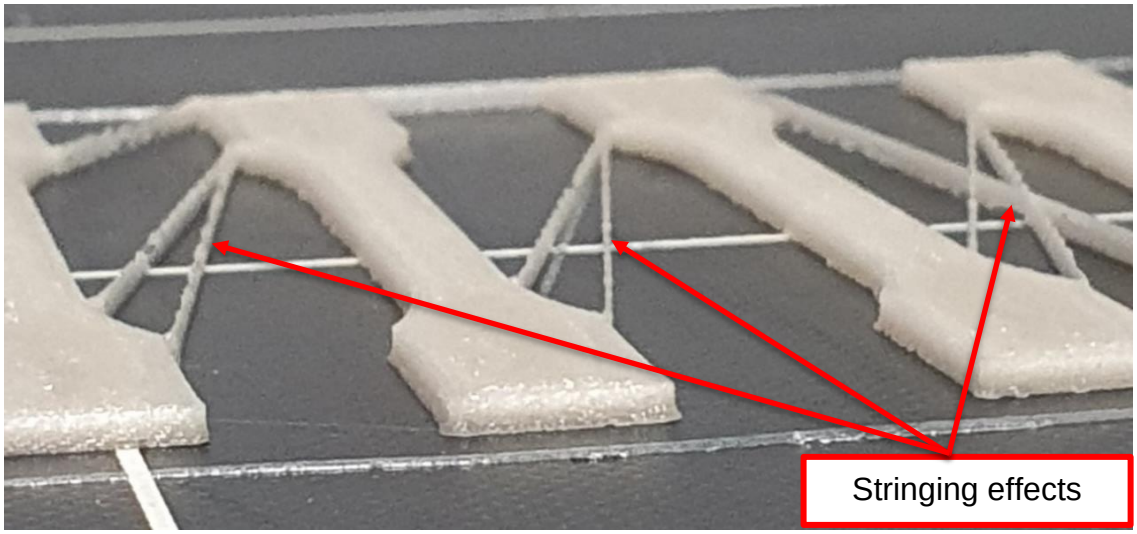

Figure 6-2 Effective printer-bed adhesion shown by PLA80/BioPBS20/HbnC1 MC-FE filament material but with stringing behaviour.

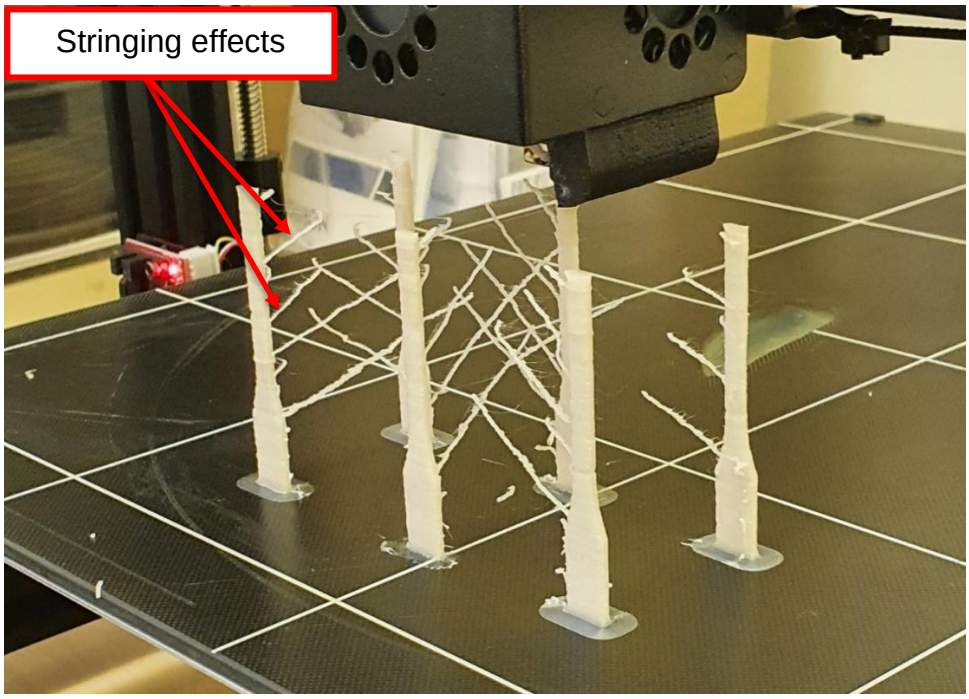

Figure 6-3 Stringing effect shown by nano clay-containing filament formulation during FDM-based 3DP of vertically oriented dog-bone parts.

Based on the presented challenges associated with the 3DP of PLA80/BioPBS20-based filament materials, the standout challenge involves the warpage and positional change of 3D-printed materials when using the PLA80/BioPBS20 FE formulation. This shows a key effect of the crystallising PLA, BioPBS, or PLA/BioPBS phases in the PLA80/BioPBS20-based formulations following extrusion. It also shows that despite the 20 wt.% content of BioPBS in relation to the 80 wt% PLA content, it appears that the rate of micromolecular recrystallisation of the BioPBS phase, which is found to be significantly higher than that of PLA, is capable of effectively and selectively causing macromolecular movements in the extruded and printed material structure. From this understanding, there is sufficient evidence suggesting that the filament material formulation and its thermomechanical properties have the most controlling influence on the fabricability and printability of the material, and hence, the effectiveness and efficiency of a 3DP process. The other influential factor: the 3DP strategy, which involves aspects like number of parts, print path, part orientation, print speed, print temperature, layer height, and infill design also determine the printability of the material. The inherent material properties of the

blend and composite filament material formulations which includes polymer phase miscibility, nanomaterial property, nanomaterial-polymer matrix interaction, and material phase crystallinity**,** therefore plays a crucial role in creating a suitable filament material formulation that functions sufficiently well under more sustainable 3DP strategies.

6.3 Tensile mechanical properties of 3D-pinted parts

In this section, the average tensile modulus, UTS, and strain at failure result obtained for each filament material formulation's 3D-printed parts are presented. These results: categorised by each applied 3DP strategy, are presented in this section with their corresponding data tables to help explore, highlight, and discuss the relative effects that each 3DP strategy has on the different material formulations (and processing route) used. The same results: categorised by material formulation (and processing route) are presented in Appendix B. The results presented in this section aids with the development of useful insights on the material-process-property relationships that exist for FDM-based 3D-printed PLA80/BioPBS20-based materials.

6.3.1 Tensile modulus of 3D-printed parts

The tensile modulus results obtained for the four utilised 3DP strategies are presented in Figure 6-4 and Table 6-1. Following the presented results, the PLA100 FE-3DP parts show the highest tensile modulus amongst all the other material parts as expected and is found to be highest for 3DP strategy 4. This is attributed to the higher print temperature, slower print speed, and lower layer height used in 3DP strategy 4. Furthermore, for all the 3DP strategies used, the tensile modulus understandably drops by about 15% upon addition of 20 wt.% BioPBS. However, upon the more extensive melt processing and/or formulation changes of the PLA80/BioPBS20 MB-FE-3DP, PLA80/BioPBS20/HbnC1 MC-FE-3DP, and PLA80/BioPBS20/rGO1 MC-FE-3DP parts, the tensile modulus of their respective parts typically remain similar across all 3DP strategies. However, the tensile modulus results of all the material parts from 3DP strategy 4 appears to surpass their counterparts from all the other 3DP strategies.

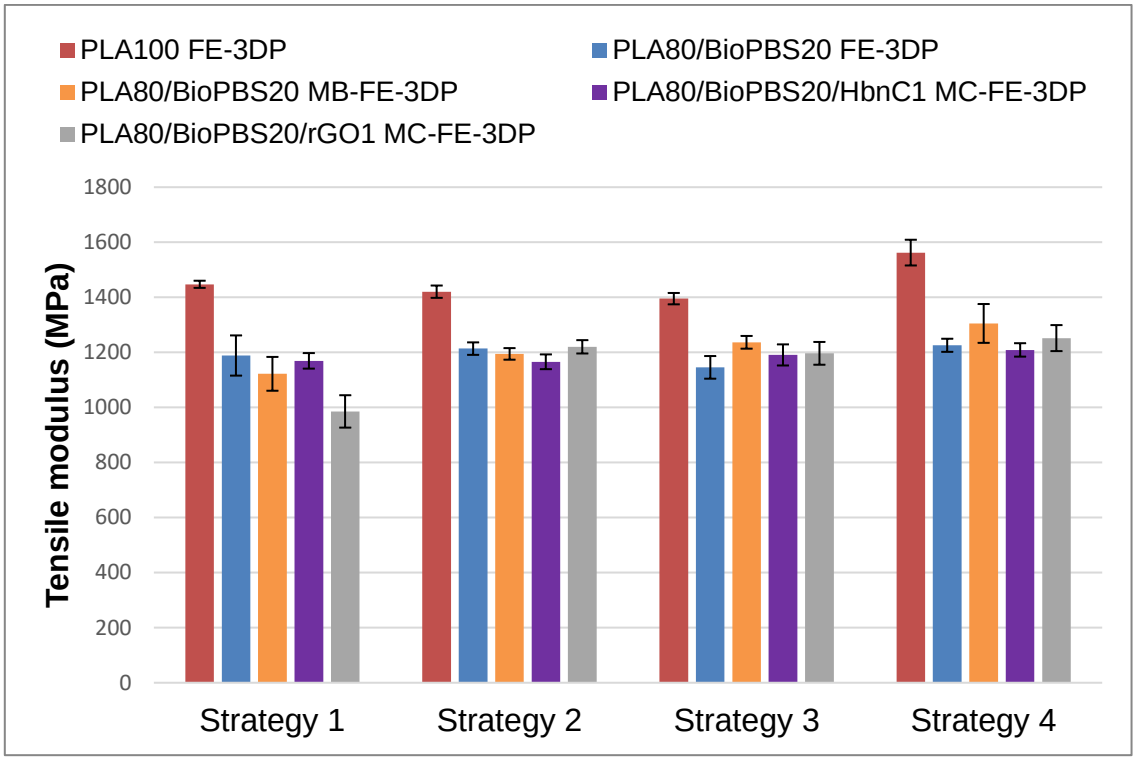

Figure 6-4 Average tensile modulus for each 3DP strategy.

Table 6-1 Average tensile modulus (MPa) and standard deviation in brackets obtained for 3D-printed parts using selected 3DP Strategies.

	Strategy 1	Strategy 2	Strategy 3	Strategy 4
PLA100 FE-3DP	1447.3 (±13)	1420.4 (±22.4)	1395.1 (±20.6)	1562.4 (±46.7)
PLA80/BioPBS20 FE-3DP	1188.6 (±73)	1213.7 (±22.7)	1145.6 (±41.1)	1225.7 (±23.8)
PLA80/BioPBS20 MB-FE-3DP	1122 (±61.4)	1194.4 (±21)	1236.6 (±23.1)	1305.1 (±70.5)
PLA80/BioPBS20/ HbnC1 MC-FE-3DP	1169.2 (±28.2)	1165.8 (±26.8)	1190.7 (±38.3)	1208.9 (±24.4)
PLA80/BioPBS20/rGO1 MC-FE-3DP	985.5 (±58.8)	1220.2 (±24.2)	1196.5 (±41.3)	1251.9 (±47.2)

Despite the similarities across all 3DP strategies, in 3DP strategy 1, the part containing rGO shows a distinctly lower average tensile modulus of about 986 MPa, which, based on the extensive melt processing route – leads to more extensive shearing and chain scission effects that generates shorter-chain/limitedly-crystallised/weaker PLA crystals when compared to other formulations and processing routes – as is confirmed by the relatively limited cold crystallisation of the PLA phase in the PLA80/BioPBS20/rGO1 material during heating (seen from DSC results). Nonetheless, the rGO-containing material shows significant scatter that is like that of the PLA80/BioPBS20 FE-3DP and PLA80/BioPBS20 MB-FE-3DP parts from 3DP strategy 1, which, when compared to the PLA100 FE-3DP parts within the same 3DP strategy, suggests that the tested samples of these materials present the most inconsistent quality alongside PLA80/BioPBS20 MB-FE-3DP and PLA80/BioPBS20/rGO1 MC-FE-3DP parts from 3DP strategy 4. However, upon comparing the tensile modulus values of parts from 3DP strategy 1 to those of other material from 3DP strategies 2, 3, and 4, there is a difference in modulus that can be attributed to print temperature, and perhaps its influence on crystallinity. These insights challenge the likelihood that melt processing is solely responsible for reducing the tensile modulus of rGO-containing parts, and instead, gives some emphasis on the effects of a lower print temperature of 3DP strategy 1 – as the more likely cause of reduced tensile modulus in the rGO-containing parts. When considering that the only difference between 3DP strategy 2 and 3DP strategy 3 is a greater layer height of 0.3 mm in the latter, the highly similar results obtained for the two sets of parts show that print temperature is the controlling influence on tensile modulus results. Moreover, for 3DP strategy 4, for which the print speed is reduced from 60 mm/s to 40 mm/s, i.e., with respect to 3DP strategy 2, the average tensile modulus shows a relative increase, even when compared to any of the other 3DP strategies. This suggests that with the slower print speed and extrusion rate, the extruded material is allowed to reach a higher temperature in the nozzle prior to extrusion and deposition and can therefore experience a broader cooling time after deposition, which allows some improved recrystallisation of the PLA phase within the extruded beads. Consequently, as subsequent layers are printed over

the previously deposited layers at these higher temperatures, these recrystallisation conditions can be recreated for the underlying layers, and therefore the material using 3DP strategy 4 shows some improvement in tensile modulus.

6.3.2 Ultimate tensile strength of 3D-printed parts

Following on; a comparative set of results is presented in Figure 6-5 and supported by Table 6-2 to explore the ultimate tensile strength (UTS) results obtained from using the specified 3DP strategies and fabricated filament materials. Generally, the UTS of parts obtained using 3DP strategies 2 and 3 are found to be lower than that obtained using 3DP strategies 1 and 4; both of which use a slower print speed of 40 mm/s, as opposed to the print speed of 60 mm/s employed by 3DP strategies 2 and 3. Nonetheless, the melt processing and fabrication route that all filament materials undergo can play a part in the mechanical strength, and can therefore be considered. However, the effect of additional melt processing steps on UTS is not clear. For example, compared to PLA80/BioPBS20 FE-3DP parts, PLA80/BioPBS20 MB-FE-3DP parts show an increase in UTS as found for 3DP strategies 3 and 4, but a slight decrease in UTS as found for 3DP strategies 1 and 2.

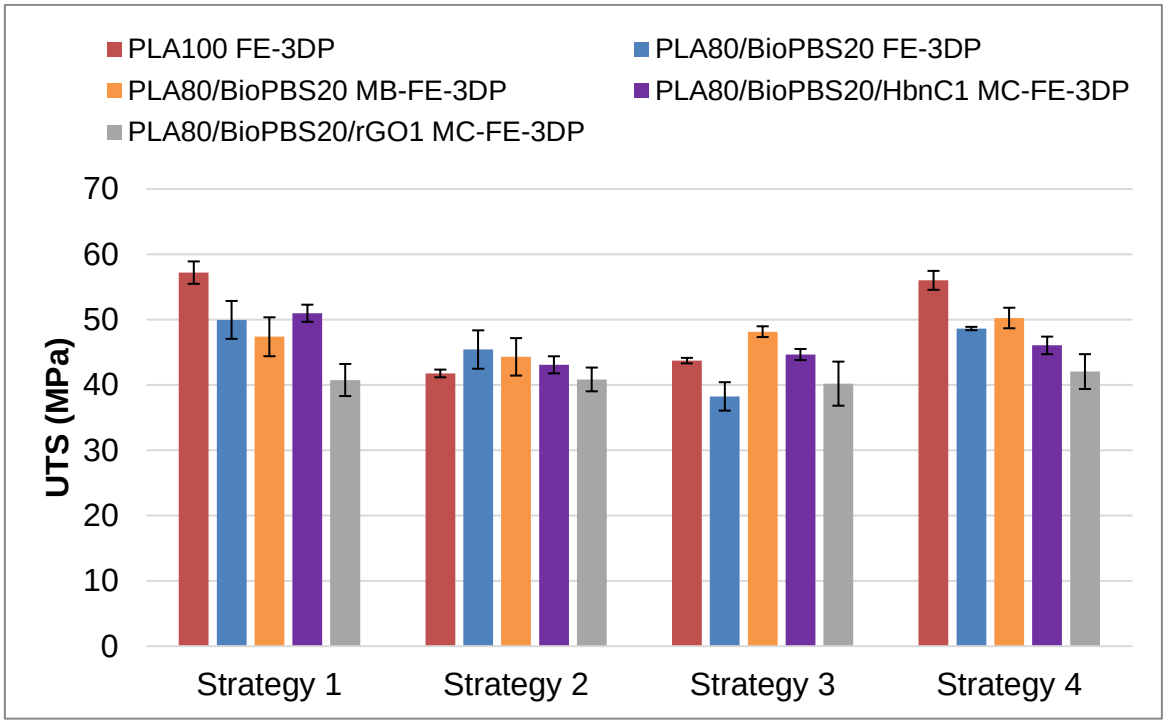

Figure 6-5 Average UTS for each 3DP strategy.

Table 6-2 Average UTS (MPa) and standard deviation in brackets of 3D-printed parts obtained using selected 3DP Strategies.

	Strategy 1	Strategy 2	Strategy 3	Strategy 4
PLA100 direct FE-3DP	57.2 (±1.7)	41.8 (±0.59)	43.7 (±0.42)	56 (±1.45)
PLA80/BioPBS20 FE-3DP	50 (±2.9)	45.4 (±2.9)	38.3 (±2.2)	48.6 (±0.3)
PLA80/BioPBS20 MB-FE-3DP	47.4 (±3)	44.3 (±2.9)	48.2 (±0.8)	50.3 (±1.6)
PLA80/BioPBS20/HbnC1 MC-FE-3DP	51 (±1.3)	43.1 (±1.3)	44.7 (±0.9)	46.1 (±1.3)
PLA80/BioPBS20/rGO1 MC-FE-3DP	40.8 (±2.5)	40.8 (±1.8)	40.2 (±3.4)	42.1 (±2.7)

Furthermore, the addition of 1 phr of HbnC particles to the PLA80/BioPBS20 blend does not seem to offer an obvious increase or decrease in UTS across all 3DP strategies, specifically when compared to PLA80/BioPBS20 FE-3DP or

PLA80/BioPBS20 MB-FE-3DP parts. PLA80/BioPBS20/HbnC1 MC-FE-3DP parts show their highest UTS of about 50 MPa and 46 MPa - for 3DP strategies 1 and 4 respectively. Additionally, for PLA80/BioPBS20/rGO1 MC-FE-3DP parts, the UTS values obtained for 3DP strategies 1 and 4 are lower than those obtained for other filament material categories within both 3DP strategies. In the case of 3DP strategy 3, the average UTS for the PLA80/BioPBS20/rGO1 MC-FE-3DP parts are inconclusively higher than that of the PLA80/BioPBS20 FE-3DP parts but clearly lower than that of the PLA80/BioPBS20 MB-FE-3DP and PLA80/BioPBS20/HbnC1 MC-FE-3DP parts. These findings, including results for 3DP strategy 4, show that PLA80/BioPBS20/rGO1 MC-FE-3DP parts offer the least UTS values amongst the fabricated parts of each 3DP strategy.

6.3.3 Strain at failure of printed parts

In this subsection, the strain at failure results for the fabricated parts are presented in Figure 6-6 and Table 6-3. In these sets of results, there is significantly more spread than obtained for the tensile modulus and UTS results. The PLA100 FE-3DP parts, as expected, shows the lowest strain at failure across all 3DP strategies - with an acceptable scatter. Furthermore, there is sufficient evidence that PLA80/BioPBS20 FE-3DP parts have an increased strain at break of at least 0.05, which is found for its material part results from 3DP strategy 3 and can possibly go up to about 0.15 in 3DP strategy 4, hence indicating a relative increase in tensile toughness for the PLA80/BioPBS20 FE-3DP parts. Similarly, for PLA80/BioPBS20 MB-FE-3DP parts, the strain at break of about 0.06 is found for its parts in 3DP strategy 1 and can possibly go up to about 0.1 as found for its parts in 3DP strategy 3. For both PLA80/BioPBS20 FE-3DP and PLA80/BioPBS20 MB-FE-3DP parts, these findings confirm an increase in tensile toughness when compared to PLA100 FE-3DP and PLA80/BioPBS20/rGO1 MC-FE-3DP parts, but nonetheless present a broad scatter of strain values.

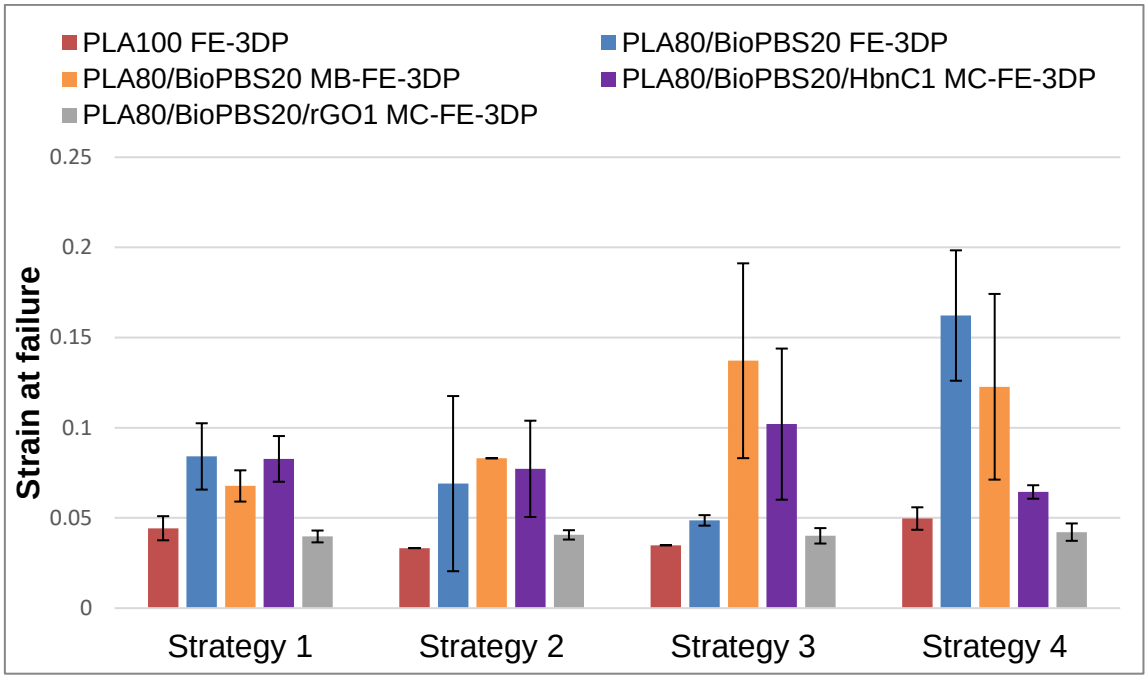

Figure 6-6 Average strain at failure for each 3DP strategy.

Table 6-3 Average strain at failure of 3D-printed parts obtained using selected 3DP Strategies.

	Strategy 1	Strategy 2	Strategy 3	Strategy 4
PLA100 direct FE-3DP	0.044 (±0.007)	0.033 (±0.00002)	0.035 (±0.00003)	0.05 (±0.006)
PLA80/BioPBS20 FE-3DP	0.084 (±0.02)	0.069 (±0.05)	0.049 (±0.003)	0.162 (±0.04)
PLA80/BioPBS20 MB-FE-3DP	0.068 (±0.009)	0.083 (±0.0001)	0.137 (±0.05)	0.122 (±0.05)
PLA80/BioPBS20/ HbnC1 MC-FE-3DP	0.083 (±0.01)	0.077 (±0.03)	0.102 (±0.04)	0.06 (±0.004)
PLA80/BioPBS20/ rGO1 MC-FE-3DP	0.040 (±0.003)	0.041 (±0.003)	0.040 (±0.004)	0.04 (±0.005)

Furthermore, for the nano-clay containing parts, the scatter of the strain at failure results observed for 3DP strategies 1, 2, and 3 remains relatively and significantly

higher when compared to PLA100 FE-3DP parts in these strategies. Nonetheless, the range of strain at failure values for the nano-clay parts remain effectively higher than those found for the PLA100 FE-3DP parts across all 3DP strategies. More specifically, the strain at failure of the PLA80/BioPBS20/HbnC1 MC-FE-3DP parts increase at least by about 20% in 3DP strategy 4 but can further increase by about 190% as found in the case of 3DP strategy 3, i.e., when compared to PLA100 FE-3DP parts in any 3DP strategy. Subsequently, for PLA80/BioPBS20/rGO1 MC-FE-3DP parts, a unique result is observed as these parts show a strain at failure of about 0.04 across all printing strategies, but also with significantly improved scatter when compared to PLA80/BioPBS20 FE-3DP, PLA80/BioPBS20 MB-FE-3DP, and PLA80/BioPBS20/HbnC1 MC-FE-3DP parts, despite also containing 20 wt.% BioPBS. Altogether, these findings help to explain the increase in strain at failure values, and the occurrence of wild variations in their values for the PLA80/BioPBS20 FE-3DP, PLA80/BioPBS20 MB-FE-3DP, and PLA80/BioPBS20/HbnC1 MC-FE-3DP parts. These results shows that the addition of BioPBS increases failure strain and toughness values but the distribution and micro-interactions of BioPBS in these parts, as governed by the extent of melt mixing and the effect of nanomaterial addition, can, in the case of larger BioPBS phase formations (i.e., limited BioPBS phase distribution), lead to a high uncertainty of failure strain and toughness values alike. However, for PLA80/BioPBS20/rGO1 MC-FE-3DP parts, this observed effect of BioPBS addition is absent, and is considered a result of the limited recrystallisation of the BioPBS phase in the presence of rGO, as was observed from DSC results. As a summary, Figure 6-7 reflects on the tensile mechanical response of PLA80/BioPBS20-based parts in relation to the PLA100 FE-3DP parts. It shows that PLA100 FE-3DP parts have the highest tensile modulus and UTS, and that the PLA80/BioPBS20-based parts experience a compliant decrease in tensile modulus and UTS. Nonetheless, for the PLA80/BioPBS20 blends and PLA80/BioPBS20/HbnC1 MC-FE-3DP parts, failure strain and toughness increase while UTS decreases. And lastly, the PLA80/BioPBS20/rGO1 MC-FE-3DP parts show the least tensile modulus and UTS performance but a comparable failure strain to the PLA100 FE-3DP parts.

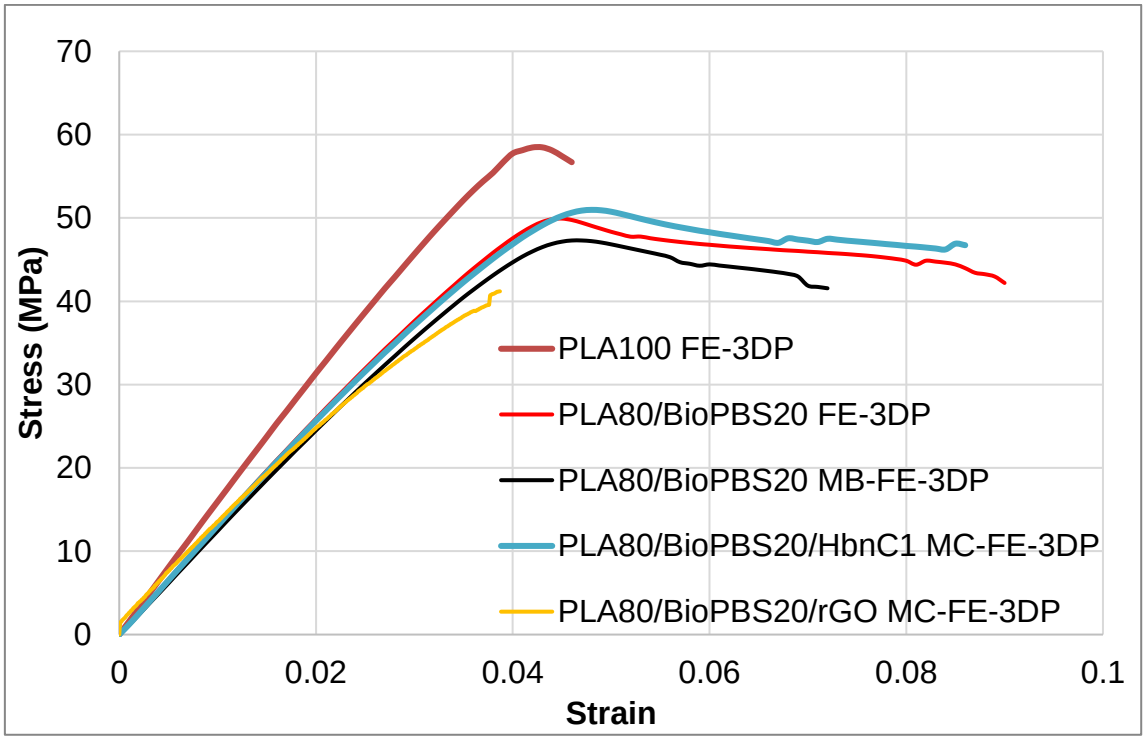

Figure 6-7 Representative tensile mechanical response of PLA and PLA80/BioPBS20-based blends and composites using 3DP strategy 1.

6.4 Fracture surface assessment of horizontally oriented 3D-printed parts.

The cross-sectional surface microscopic views of representative tensile-fractured horizontally oriented 3D-printed parts are presented in this section and are assessed for each print strategy. From these results, the apparent effects of print temperature, print speed, and layer height on void formations and interlayer bonding can be inferred. However, the effect of print speed is expected to be more complex to deduce. Generally, the voids in these parts are found either around the outer edges (walls) of the structure or inside the mid-sections for the representative PLA100 FE-3DP part, which is used as a reference for other representative horizontally oriented 3D-printed parts.

6.4.1 Fracture surfaces of 3D-printed parts from Strategy 1

For strategy 1, the five categories of materials and their representative tensile fractured surfaces are presented in Figure 6-8, Figure 6-9, and Figure 6-10. The images for the PLA100 FE-3DP part as seen in Figure 6-8 show a brittle fracture

as defined by boundaries or edges on the surface. Interestingly, the back scattered image of the sample shows a clearer position of voids across its surface. For the PLA80/BioPBS20 FE-3DP part in Figure 6-9 (a and a'), there appears to be a similar region of void formation, and then some ductile fracture in the mid-section, which is possibly caused by the distributed BioPBS-rich domains in the PLA80/BioPBS20 FE-3DP material. Alternatively, the more extensively melt-blended PLA80/BioPBS20 MB-FE-3DP part seen in Figure 6-9 (b and b') indicates relatively and significantly weaker interlayer and inter-road bonding behaviour as evidenced by the rupturing effects observed for the part. This is possibly due to the print temperature being insufficiently high enough for inducing molecular diffusion between the extruded roads and layers of the PLA80/BioPBS20 MB-FE-3DP part. However, for the nanomaterial-containing parts shown in Figure 6-10, no such ruptures are observed, and these parts show the least void content (of limited sizes) with a relatively brittle fracture surface. Nonetheless, for the rGO-containing part, there is limited interlayer bonding at the edges, for which the thermal conductivity of rGO fails to improve, and perhaps leads to the formation of a limited number of randomly developed voids.

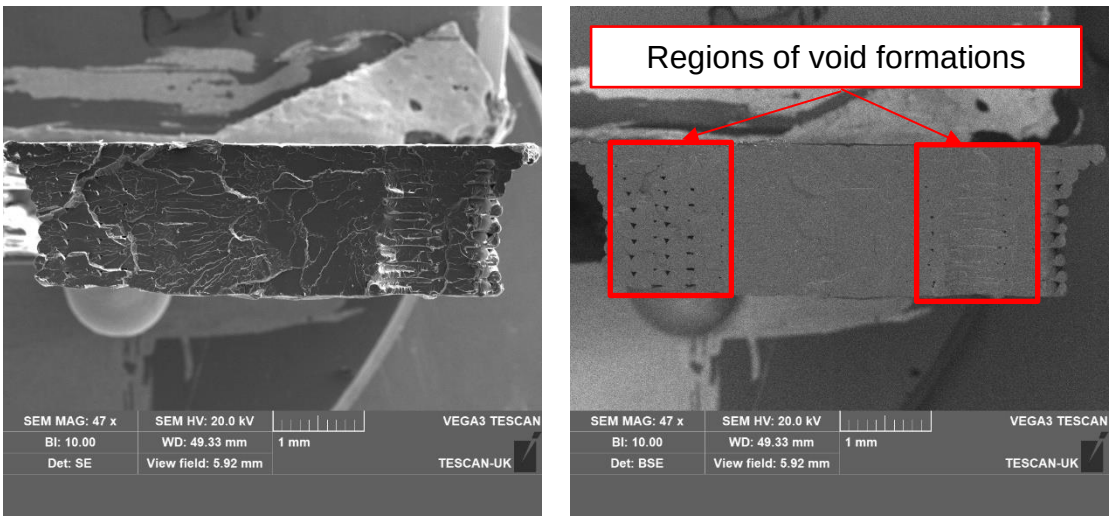

(a) (a')

Figure 6-8 Secondary electron (left) and back-scattered (right) SEM images of representative tensile-fractured surfaces of 3D-printed composite parts produced using 3DP strategy 1; for PLA100 FE-3DP (a and a')

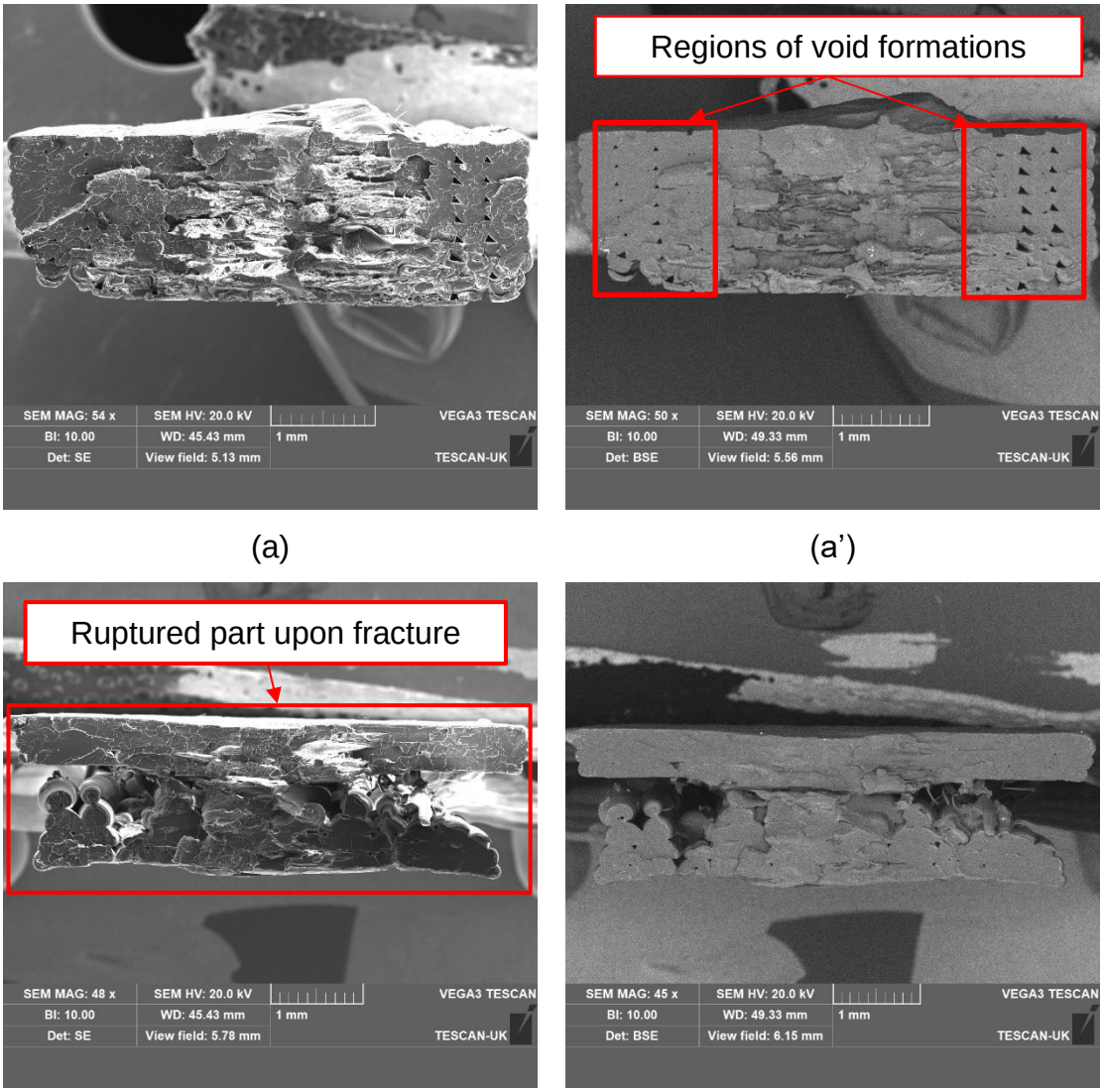

(a) (a’)

(b) (b’)

Figure 6-9 Secondary electron (left) and back-scattered (right) SEM images of tensile-fractured surfaces of 3D-printed composite parts produced using 3DP strategy 1; for PLA80/BioPBS20 FE-3DP (a and a’), PLA80/BioPBS20 MB-FE-3DP (b and b’)

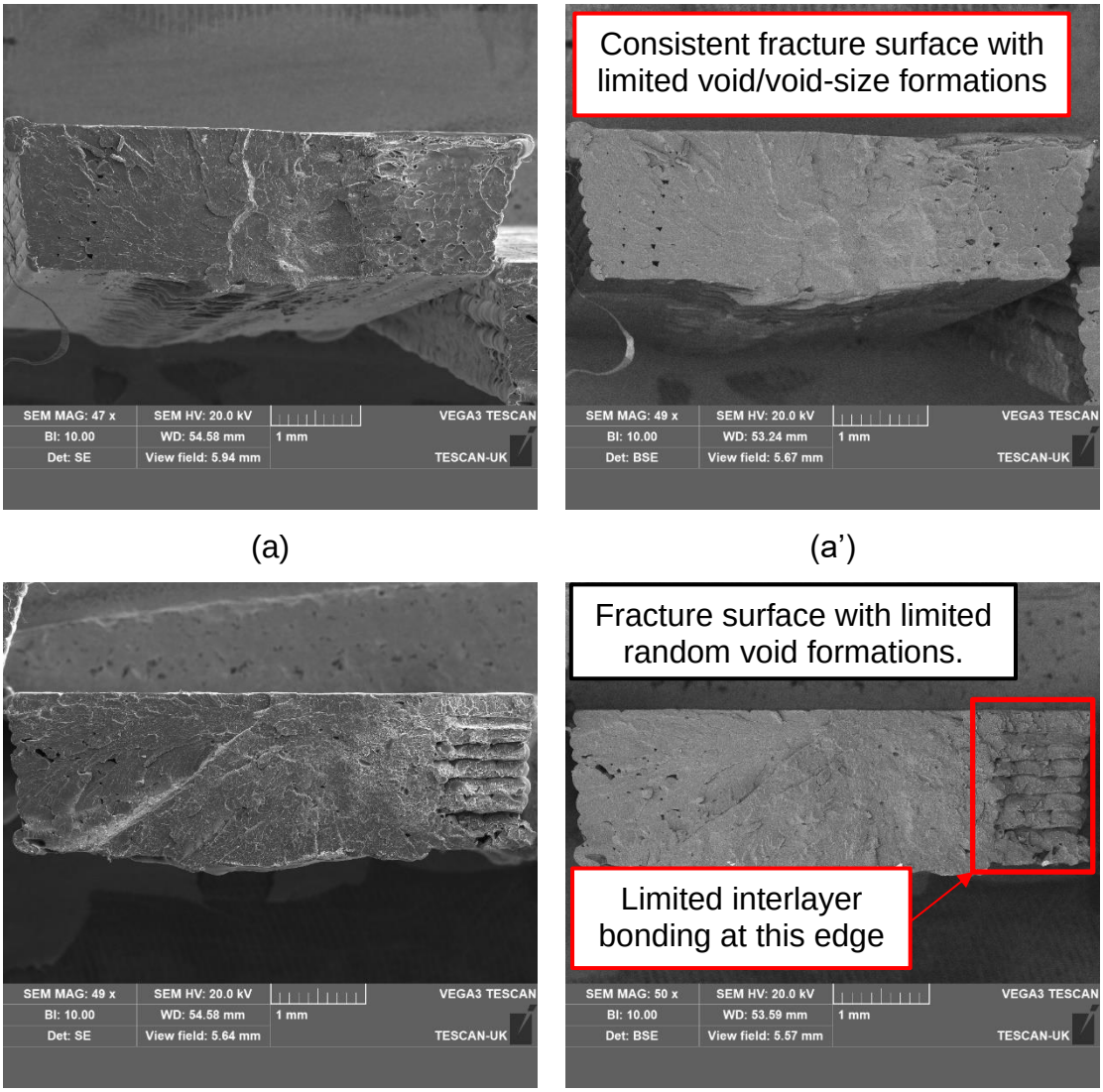

Figure 6-10 Secondary electron (left) and back-scattered (right) SEM images of tensile-fractured surfaces of 3D-printed composite parts produced using 3DP strategy 1; for PLA80/BioPBS20/HbnC1 MC-FE-3DP (a and a'), and PLA80/BioPBS20/rGO1 MC-FE-3DP (b and b').

6.4.2 Fracture surfaces of 3D-printed parts from Strategy 2

For tensile-fractured parts of PLA and PLA80/BioPBS20-based parts produced using strategy 2, their cross-sectional SEM images are presented in Figure 6-11, Figure 6-12, and Figure 6-13. This strategy appears to significantly improve the structural integrity of especially the representative tensile-fractured PLA80/BioPBS20 MB-FE-3DP part when compared to the ruptured part result of

its counterpart from strategy 1. Moreover, in Figure 6-11 (a and a'), the fractured surface of the PLA100 FE-3DP part appears more consolidated, having smaller-sized voids than its counterpart from strategy 1 – shown in Figure 6-8 (a and a'). The fracture surface results for the parts associated with the PLA80/BioPBS20 blends from strategy 2 (i.e., as shown in Figure 6-12), suggests that better interlayer/inter-bead interactions are achieved when compared to their counterparts from strategy 1. It is observed that the representative PLA80/BioPBS20 FE-3DP part from strategy 2, as seen in Figure 6-12 (a and a'), shows complete ductile fracture across its surface, with an extensive ductile failure of a printed road occurring as indicated in Figure 6-12 (a). Interestingly, for the PLA80/BioPBS20 MB-FE-3DP part from strategy 2 shown in Figure 6-12 (b and b'), a well-defined fracture surface is now obtained, and features a region of mild ductile fracture in the mid-section; although having regions of more brittle failure and some void formations around the edges.

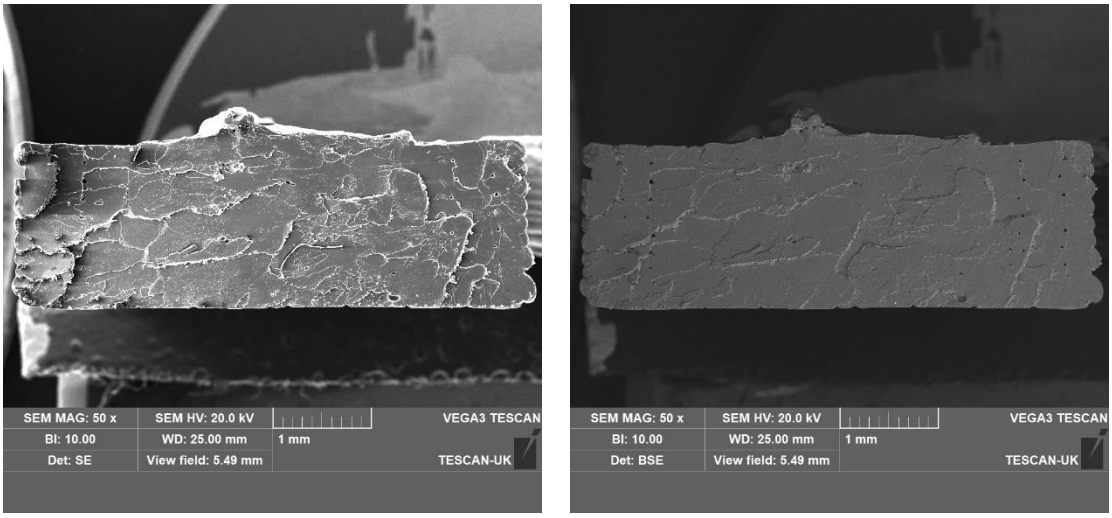

(a) (a')

Figure 6-11 Secondary electron (left) and back-scattered (right) SEM images of representative tensile-fractured surfaces of 3D-printed composite parts produced using 3DP strategy 2; for PLA100 FE-3DP (a and a')

Otherwise, for the nanocomposite parts from strategy 2 as shown in Figure 6-13, a newly developed fracture surface morphology is observed for the PLA80/BioPBS20/HbnC1 MC-FE part with respect to its counterpart from strategy 1. In this case, the PLA80/BioPBS20/HbnC1 MC-FE part's fracture

surface contains more randomly distributed void formations around the edge of the sample. This is furthermore in contrast to the more controlled fracture surface observed for the PLA80/BioPBS20/rGO1 MC-FE part, which is also interestingly without the limited interlayer bonding result observed for its counterpart in strategy 1. These results point to the increase in print temperature as the key factor controlling the achieved changes in fracture surface features.

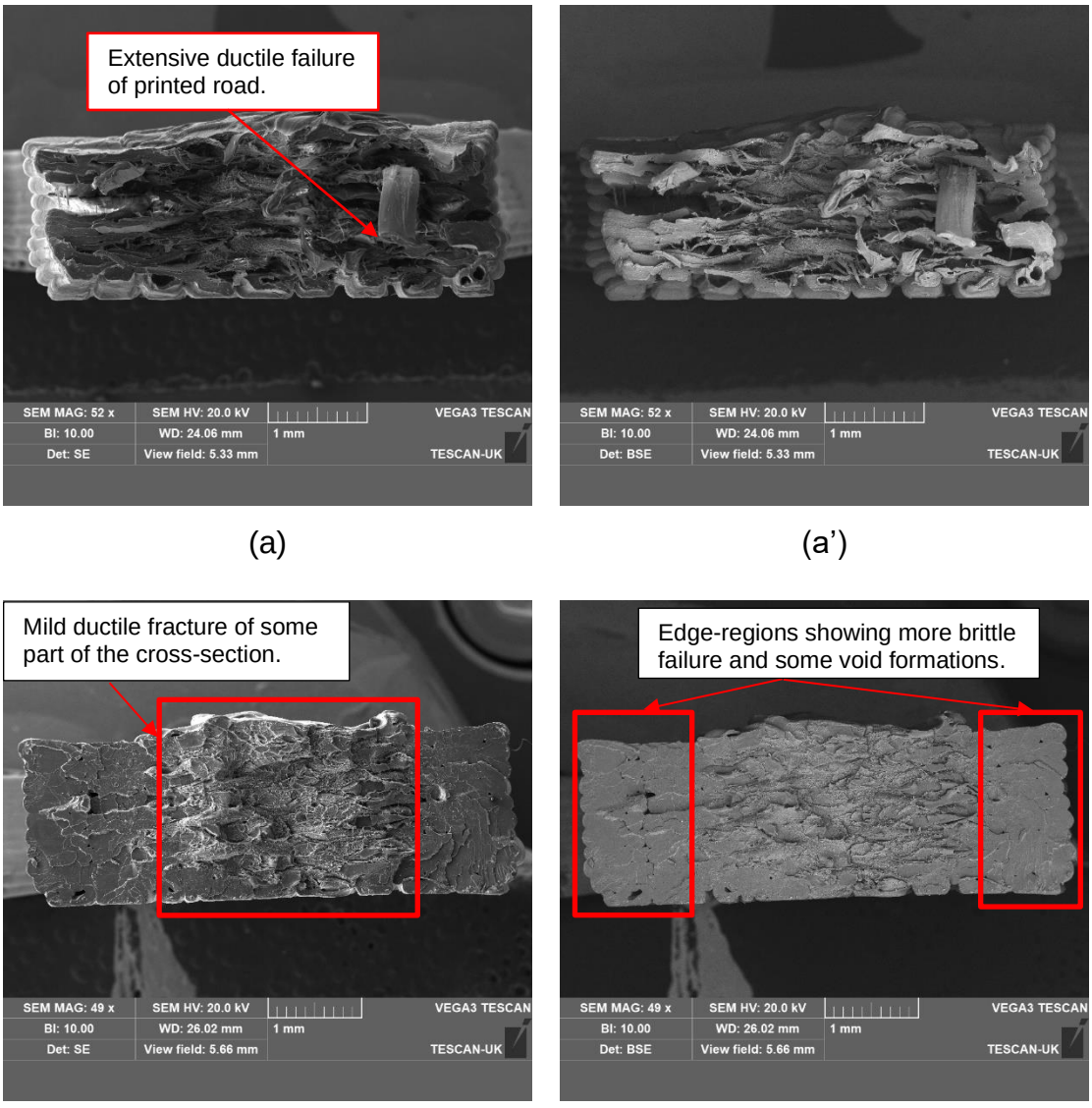

Figure 6-12 Secondary electron (left) and back-scattered (right) SEM images of tensile-fractured surfaces of 3D-printed composite parts produced using 3DP strategy 2; for PLA80/BioPBS20 FE-3DP (a and a'), PLA80/BioPBS20 MB-FE-3DP (b and b')

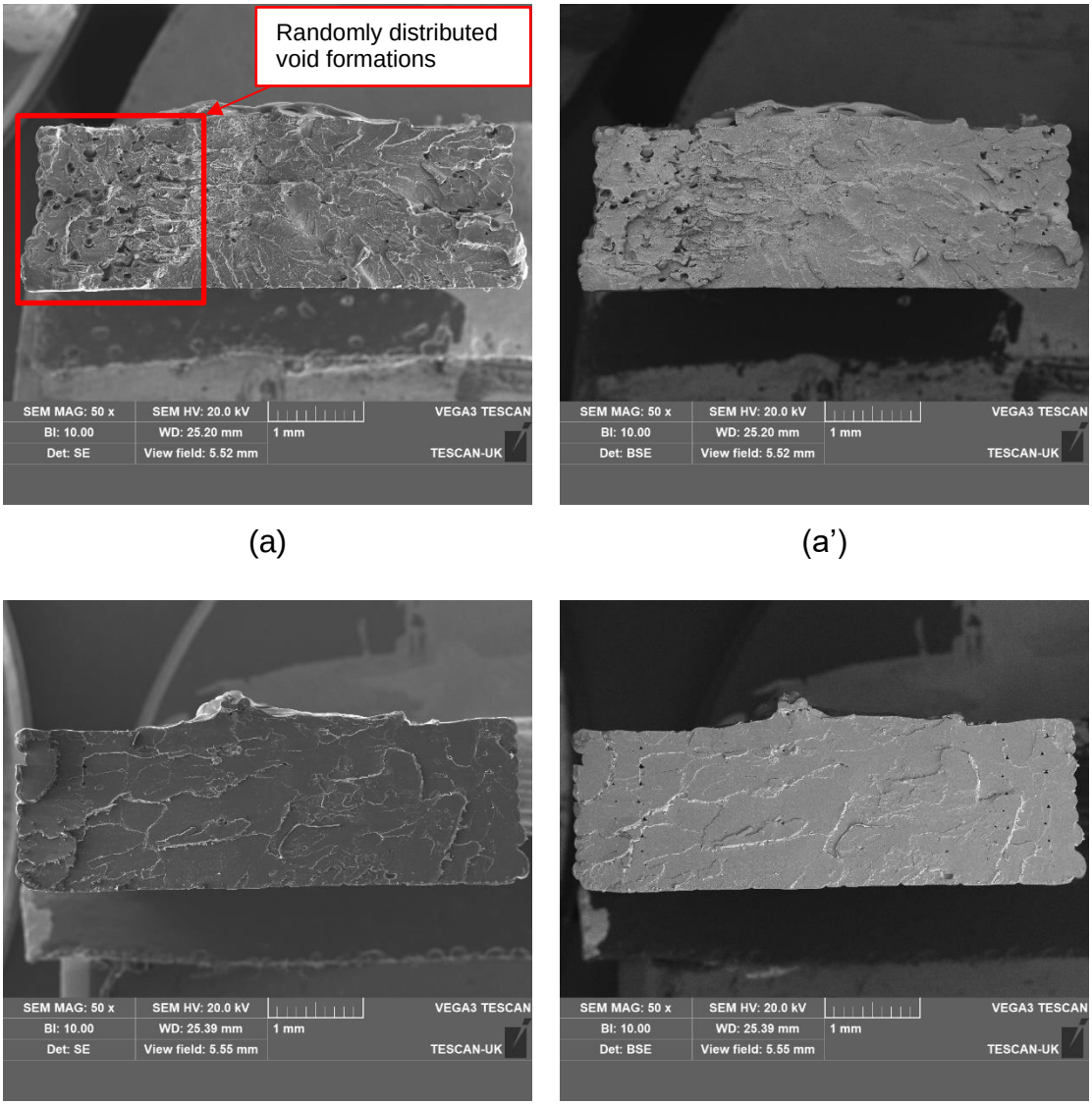

Figure 6-13 Secondary electron (left) and back-scattered (right) SEM images of tensile-fractured surfaces of 3D-printed composite parts produced using 3DP strategy 2; for PLA80/BioPBS20/HbnC1 MC-FE-3DP (a and a'), and PLA80/BioPBS20/rGO1 MC-FE-3DP (b and b').

6.4.3 Fracture surfaces of 3D-printed parts from Strategy 3

Fracture surface results from strategy 3 are presented in Figure 6-14, Figure 6-15, and Figure 6-16, for which a higher layer height is used, i.e., in contrast to strategy 2. From Figure 6-14 (a and a'), the fracture surface of the PLA100 FE-3DP material shows a brittle fracture as expected. However, the outer edges lack the good level of interlayer interaction found for its counterparts in strategy 1 and

strategy 2. Furthermore, when compared to the PLA100 FE-3DP material in strategy 1, the PLA100 FE-3DP material from strategy 3 shows a lower number of void formations on one edge, but a lower quality of interlayer interaction on the other edge; of which the latter appears to pose a greater concern for printed part integrity. This limited interlayer interaction at the edges of the PLA100 FE-3DP part from strategy 3 is importantly considered to be caused by the thicker layer height used in comparison to strategy 1 and strategy 2. It is supposed that using a 0.3 mm layer height creates a longer distance between the end surfaces of the deposited roads, thus extending the distance of heat transfer that would facilitate more effective inter-road molecular diffusion and bonding results, such as that obtained at the edges of the representative PLA100 FE-3DP part in strategy 2.

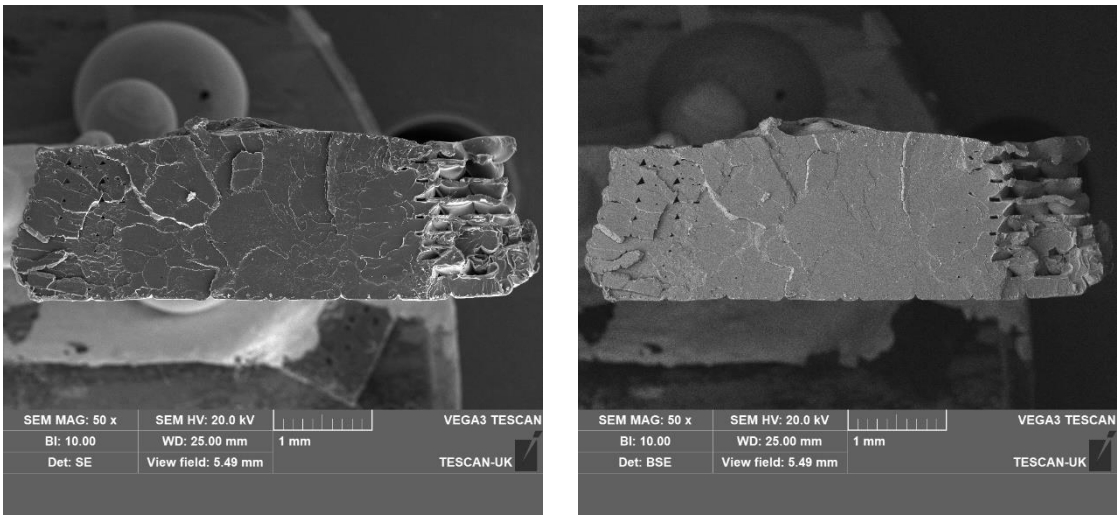

(a) (a')

Figure 6-14 Secondary electron (left) and back-scattered (right) SEM images of representative tensile-fractured surfaces of 3D-printed composite parts produced using 3DP strategy 3; for PLA100 FE-3DP (a and a')

Alternatively, for the PLA80/BioPBS20 FE-3DP and PLA80/BioPBS20 MB-FE-3DP parts presented in Figure 6-15 (a and a'), and Figure 6-15 (b and b') respectively, a significantly ductile fracture surface is obtained across the entire cross-sectional surface of both parts; showing significantly large voids and cavities. These features are especially increased for the PLA80/BioPBS20 MB-

FE-3DP part from strategy 2. The increase in temperature and print speed (from that used in strategy 1), and the use of a layer height of either 0.2 mm or 0.3 mm appears to improve the inter-road and inter-phase interactions. Interestingly, for the PLA80/BioPBS20 FE-3DP part in strategy 2, a broad scatter of strain at failure results was highlighted earlier on in this chapter and was found to significantly reduce for their counterpart in strategy 3. However, for the PLA80/BioPBS20 FE-3DP parts in strategy 3, their average strain at failure decreases by about 29% when compared to their counterpart in strategy 2, although this was inconclusive due to the broad scatter of results in the latter. Moreover, for the PLA80/BioPBS20 MB-FE-3DP parts in strategy 3, the broad scatter of the strain at failure results was found to show a significant increase when compared to its counterpart in strategy 2. However, the average strain at failure result in strategy 3 appears to be about the same, or even increased by up to 180% or more from the values found in strategy 2. Consequently, in relation to the PLA80/BioPBS20 FE-3DP parts, the findings for the PLA80/BioPBS20 MB-FE-3DP parts show at least a similar or higher strain at failure result across strategy 2 and strategy 3, and hence confirms the value of using a more extensive melt blending approach for fabrication of PLA80/BioPBS20 parts that can realise more reliable (strategy 2) and/or potentially higher (strategy 3) strain at failure results.

Furthermore, for the nano-clay containing part of strategy 3, i.e., as shown in Figure 6-16 (a and a'), visible layer lines are mainly present around one edge; a feature that is not found for its representative counterparts in strategy 1 and strategy 2, and can be explained by the higher layer height used; and its effect on limiting the effective thermal distributions that facilitates inter-road molecular diffusions and bonding. In retrospect, it is also observed that the sort of randomly distributed void formations that occur for the PLA80/BioPBS20/HbnC1 part in strategy 2 is also present around the edges of its counterpart here in strategy 3 (with potentially extended cavities overlapped by the appearance of layer lines. Moreover, in terms of the average strain at failure results obtained for the PLA80/BioPBS20/HbnC1 part in strategy 3, there is an increase from the values obtained for its counterparts in strategy 1 and strategy 2. However, the relative scatter of these results emphasize that these changes are inconclusive.

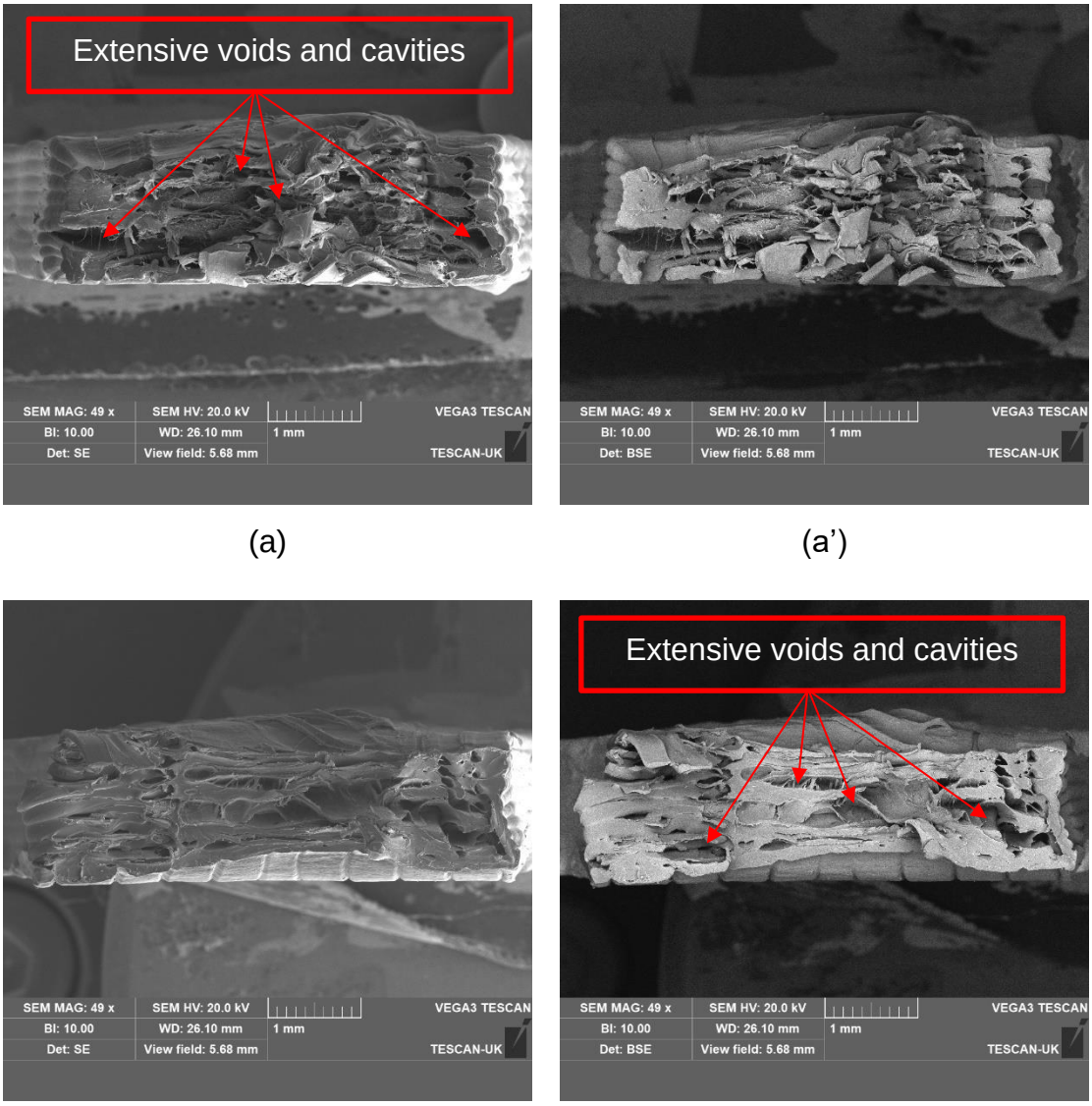

Figure 6-15 Secondary electron (left) and back-scattered (right) SEM images of tensile-fractured surfaces of 3D-printed composite parts produced using 3DP strategy 3; for PLA80/BioPBS20 FE-3DP (a and a'), PLA80/BioPBS20 MB-FE-3DP (b and b')

For the PLA80/BioPBS20/rGO1 part obtained using strategy 3, as shown in Figure 6-16 (b and b'), a higher number and distribution of voids are observed across the fractured surface, but without the sort of visible layer lines seen for the PLA80/BioPBS20/HbnC1 part (from strategy 3). In effect, the absence of layer lines could be due to better thermal conductivity of rGO, while the higher void distribution could be due to the extra melt processing step used in obtaining the

PLA80/BioPBS20/rGO1 filament. Moreover, the void formations seen in these parts are not as large or extensive as those found for either the blend or nano-clay composite parts. Hence, in terms of its strain at failure values, there is a good level of consistency and reliability across the three strategies discussed so far, which further highlights the important role of the rGO material in stabilising the PLA80/BioPBS20 microstructure.

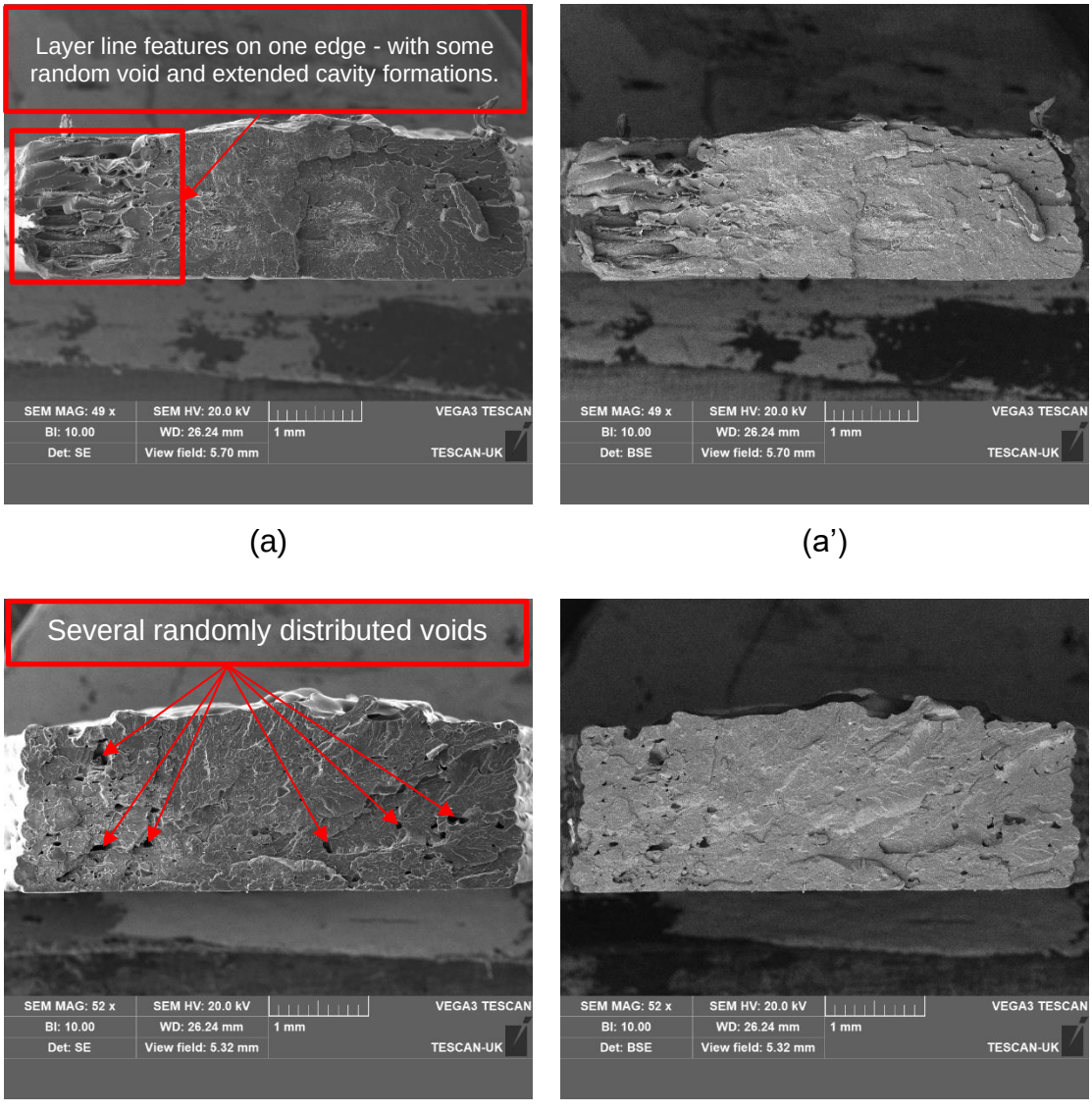

Figure 6-16 Secondary electron (left) and back-scattered (right) SEM images of tensile-fractured surfaces of 3D-printed composite parts produced using 3DP strategy 3; for PLA80/BioPBS20/HbnC1 MC-FE-3DP (a and a'), and PLA80/BioPBS20/rGO1 MC-FE-3DP (b and b')

6.4.4 Fracture surfaces of 3D-printed parts from Strategy 4

The results from strategy 4 are presented in Figure 6-17, Figure 6-18, and Figure 6-19, and it is generally observed that the interlayer bonding quality improves across all the print strategies using a 230 °C printing temperature. However, it is considered that this feature can also be improved by using a slower print speed, which gives sufficient residence time in the nozzle for the extruding material to achieve greater thermal energy for more effective molecular diffusion upon deposition. This further enhances molecular interactions between deposited roads and layers. Alternatively, this phenomenon of molecular diffusion can be improved by optimising the layer height, although with time and cost considerations in mind. For the PLA100 FE-3DP part in this strategy, significantly larger but fewer voids are formed in comparison to the representative PLA100 FE-3DP parts in other strategies. Nonetheless, this strategy offers promising tensile mechanical part results for each material in this study, and hence, the fracture surfaces of each representative material's part in this strategy will create a strong basis for making insightful conclusions.

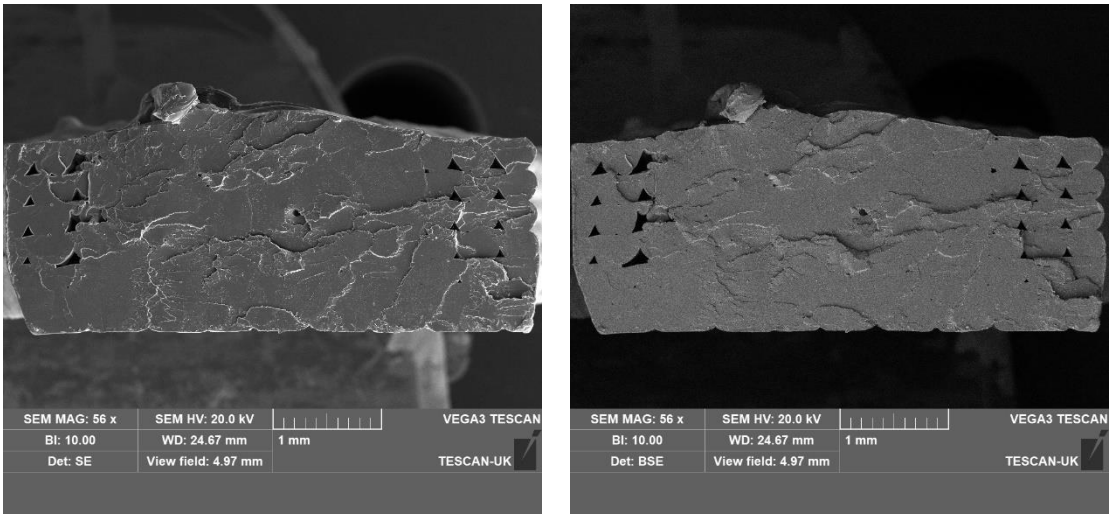

(a) (a')

Figure 6-17 Secondary electron (left) and back-scattered (right) SEM images of representative tensile-fractured surfaces of 3D-printed composite parts produced using 3DP strategy 4; for PLA100 FE-3DP (a and a')

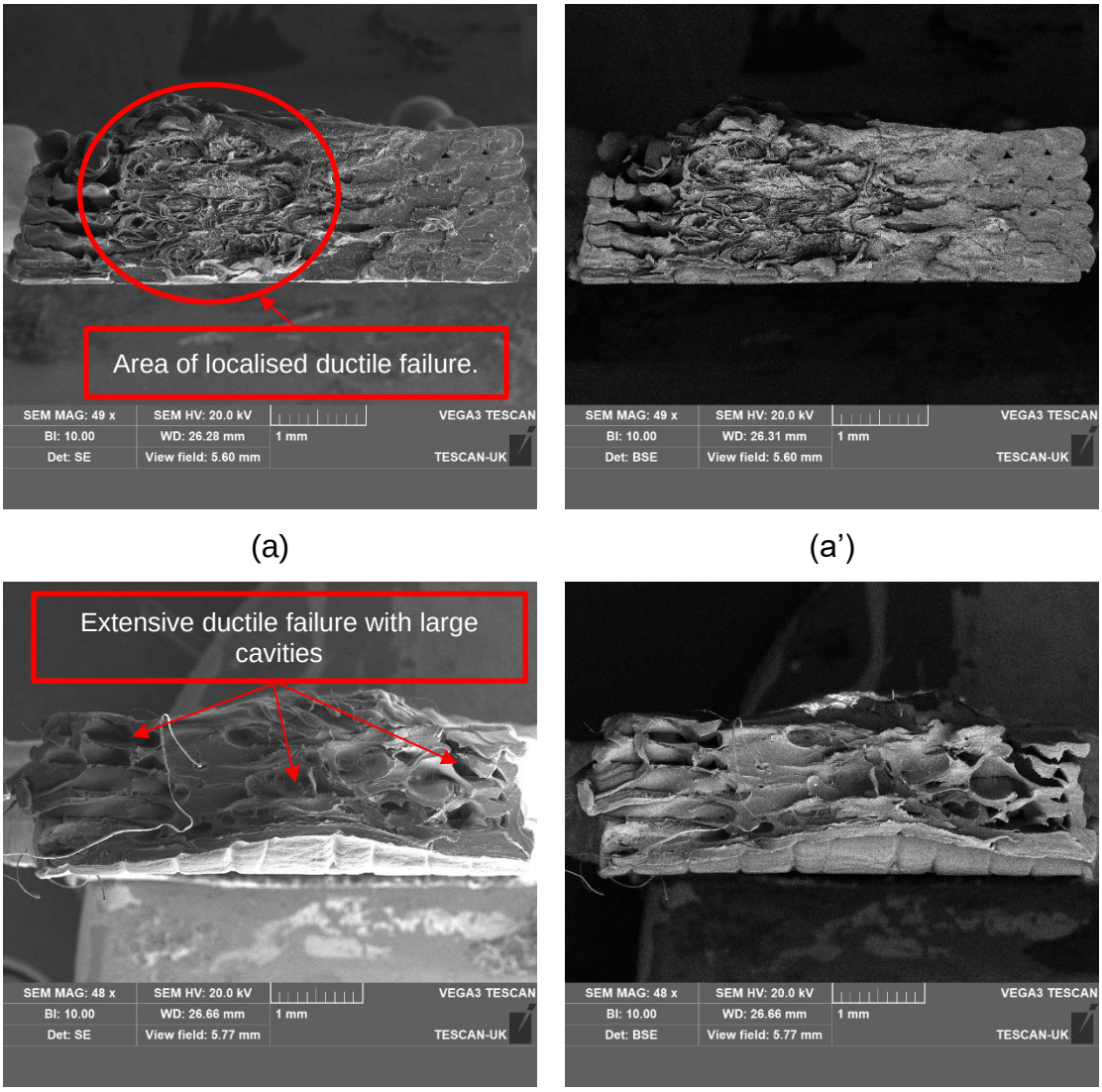

Figure 6-18 Secondary electron (left) and back-scattered (right) SEM images of tensile-fractured surfaces of 3D-printed composite parts produced using 3DP strategy 4; for PLA80/BioPBS20 FE-3DP (a and a'), PLA80/BioPBS20 MB-FE-3DP (b and b')

For the PLA80/BioPBS20 FE-3DP part in strategy 4, a feature of localised ductile fracture is present; having some similarities to the fracture surface obtained for the PLA80/BioPBS20 MB-FE-3DP part in strategy 2. Nonetheless, considering the limited blending used for the PLA80/BioPBS20 FE filament, it is likely that the rich BioPBS phase is limitedly distributed across the surface. Meanwhile, for the PLA80/BioPBS20 MB-FE-3DP part, its fracture surface shown in Figure 6-18 (b

and b') presents an entirely ductile failure similar to its counterpart results in strategy 3, which show large and extended cavities that are considered a result of good BioPBS dispersion and interphase interactions. Moreover, with the PLA80/BioPBS20 MB-FE-3DP part in strategy 4, there is some consistency that can be associated with the broad scatter of strain at failure results found for PLA80/BioPBS20-based parts without rGO.

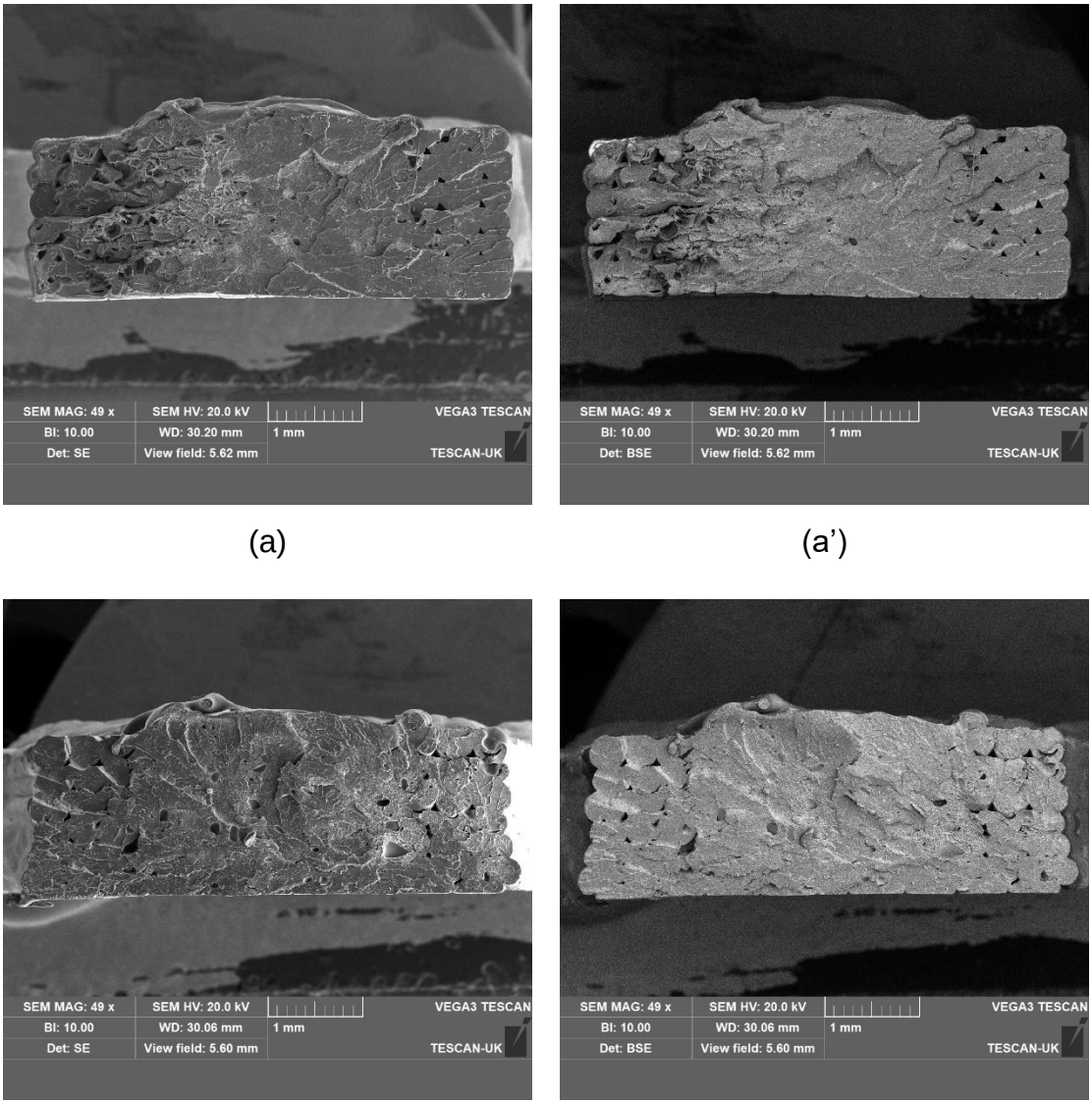

(a) (a')

(b) (b')

Figure 6-19 Secondary electron (left) and back-scattered (right) SEM images of tensile-fractured surfaces of 3D-printed composite parts produced using 3DP strategy 4; for PLA80/BioPBS20/HbnC1 MC-FE (a and a'), and PLA80/BioPBS20/rGO1 MC-FE (b and b')

For the fracture surfaces of the nanomaterial-based parts in strategy 4 - as shown in Figure 6-19, their results are consistent with those identified in their counterparts from strategy 3 and strategy 1, however, with a key difference being the absence of obvious layer lines on either of the part's fracture surface.

In summary, layer lines and relatively small-sized voids form around the edges of all parts except for the PLA80/BioPBS20 parts, which develop large cross-sectional voids upon fracture. Meanwhile, for the HbnC-containing parts, more prominent voids than those in the rGO-containing parts are formed. However, as observed for the fracture surfaces assessed for all 3DP strategies, the use of higher print temperature and lower layer height leads to fracture surfaces with the most limited layer lines. Nonetheless, to concisely highlight these deductions, Table 6-4 is provided to summarize the impressions obtained from assessing the tensile-fractured surface results for each material and 3DP strategy.

Table 6-4 Impressions of the effects of material and 3DP strategy on nature of fracture, void content, and interlayer bonding results

Factor		Nature of fracture	Void content	Interlayer bonding
Material formulation	**PLA100 FE-3DP**	Brittle	High and small-sized	Good
	PLA80/BioPBS20 FE-3DP	Ductile	Average and large-sized	Average
	PLA80/BioPBS20 MB-FE-3DP	Ductile	Average and large-sized	Average
	PLA80/BioPBS20/HbnC1 MC-FE-3DP	Mixed	Average and small-sized	Average
	PLA80/BioPBS20/rGO1 MC-FE-3DP	Brittle	Low and small-sized	Good
3DP strategy	**Strategy 1**	Brittle	Average and large-sized	Poor
	Strategy 2	Mixed	Low and average-sized	Good
	Strategy 3	Mixed	Low and average-sized	Average
	Strategy 4	Mixed	Low and average-sized	Good

6.4.5 Main findings for tensile mechanical and fracture surface results of 3D-printed parts

According to the tensile-fractured surface results presented in this chapter, strategy 4 can be considered the best 3DP strategy for realising optimal fracture surface results in the PLA80/BioPBS20-based parts, i.e., amongst the strategies attempted. In terms of tensile modulus, the general results for each material category across the four strategies show no significant difference. However, in the odd case, the modulus tends to be marginally better for the PLA80/BioPBS20 MB-FE-3DP and PLA80/BioPBS20/rGO1 MC-FE-3DP parts in strategy 4, but relatively worse for the PLA80/BioPBS20/rGO1 MC-FE-3DP part in strategy 1. Furthermore, in terms of the UTS, the parts obtained using strategy 2 and strategy 3 appear to be limited, of which is mainly attributed to the increased print speed used in these strategies alone. Furthermore, based on the features of layer lines found during the fractured-surface assessments; the use of an increased (0.3 mm) layer height in strategy 3 may also be considered a limiting factor for achieving better UTS results. Nonetheless, for all material categories, no major difference is found in UTS across the four strategies applied. However, strategy 4 offers relatively promising UTS results across all material categories.

From the strain at failure results for each respective material formulation category, that of the PLA100 FE-3DP and PLA80/BioPBS20/rGO1 MC-FE-3DP parts show the lowest values with acceptable scatter across all applied 3DP strategies. The brittle nature of these materials can be correlated with their generally well-defined fracture surface results. Alternatively, the strain at failure results for the PLA80/BioPBS20 blend materials tend to show a broad deviation from the mean, which indicates that reliable results cannot generally be concluded from the applied 3DP strategies. However, from the deviations of strain at failure results obtained for all strategies, it is possible to confirm a significant increase in strain at failure for the PLA80/BioPBS20 FE-3DP and PLA80/BioPBS20 MB-FE-3DP parts when compared to the PLA100 and PLA80/BioPBS20/rGO1 parts. Furthermore, for the nanoclay-containing part, a similar increase in strain at failure to that of the PLA80/BioPBS20 blends (also with broad scatter) is observed. However, the nanoclay-containing parts do not

similarly show the presence of stretched and elongated regions on their fracture surface. These findings, with the aid of the stress-strain curves (as shown in Figure 6-7), confirms that the tensile toughness of the blends and nanoclay composite parts are improved significantly in relation to the PLA100 FE-3DP and PLA80/BioPBS20/rGO1 MC-FE-3DP parts. However, the increased toughness is found to be most reliable for the PLA80/BioPBS20/HbnC1 parts.

6.5 Interlayer mechanical properties of vertically oriented 3D-printed parts.

The interlayer tensile-mechanical properties for successfully printed vertically oriented dog bone parts are presented in Figure 6-20, Figure 6-21 and Figure 6-22 for the tensile modulus, UTS and strain at failure. The success in printability was based on 3DP strategy 2 for the vertically oriented parts. Nonetheless, this strategy failed to successfully print a set of representative PLA80/bioPBS20/rGO1 MC-FE-3DP parts, possibly due to its more sensitive complex viscosity behaviour leading to repeated print failures. The vertically oriented PLA100 FE-3DP part is found to have the highest tensile modulus value of about 847 MPa, which upon addition of 20% wt. BioPBS; reduces to about 716 MPa, which represents a 15% reduction of tensile modulus in the PLA80/BioPBS20 MB-FE-3DP parts. However, on addition of HbnC at about 1phr, the interlayer tensile modulus of the PLA80/BioPBS20/HnC1 MC-FE-3DP part shows about a 13% increase from that of the PLA80/BioPBS20 MB-FE-3DP part: reaching levels closer to the pure PLA material.

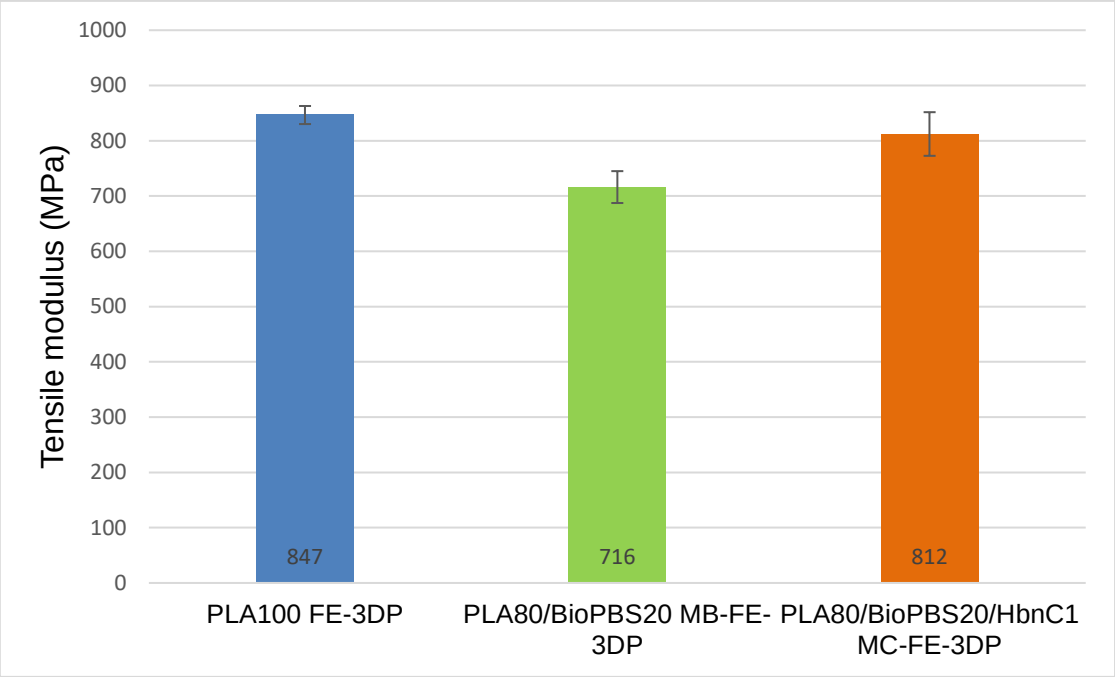

Figure 6-20 Tensile modulus of vertically oriented PLA100 FE-3DP, PLA80/BioPBS20 and PLA80/BioPBS20/HbnC1 MC-FE-3DP parts.

Figure 6-21 shows evidently that the PLA100 FE-3DP part offers the highest interlayer strength under the applied print strategy, with a value of about 27 MPa. Meanwhile, the PLA80/BioPBS20 FE-3DP part has an interlayer strength value of about 22 MPa. Both results outperform the HbnC-containing parts which shows an average and less reliable interlayer strength of about 12 MPa. The lower value obtained for the PLA80/BioPBS20/HbnC1 MC-FE-3DP part is most probably due to the presence of nanoparticles or larger formed agglomerates of the HbnC particles observed in microscopy, which may act as points of stress concentration that could facilitate tensile limitations. In the horizontally oriented parts, this effect is limited due to better material interface interactions in the direction of loading as opposed to the weaker and more susceptible interface interactions between distinct layers printed on top of one another to form the vertical structure in the loading direction. Based on the only other set of results in literature that presents interlayer properties of 3D printed PLA and BioPBS materials [52], although not directly comparable, these results contribute to the understanding of the interlayer-bond performance of PLA/BioPBS-based composite parts.

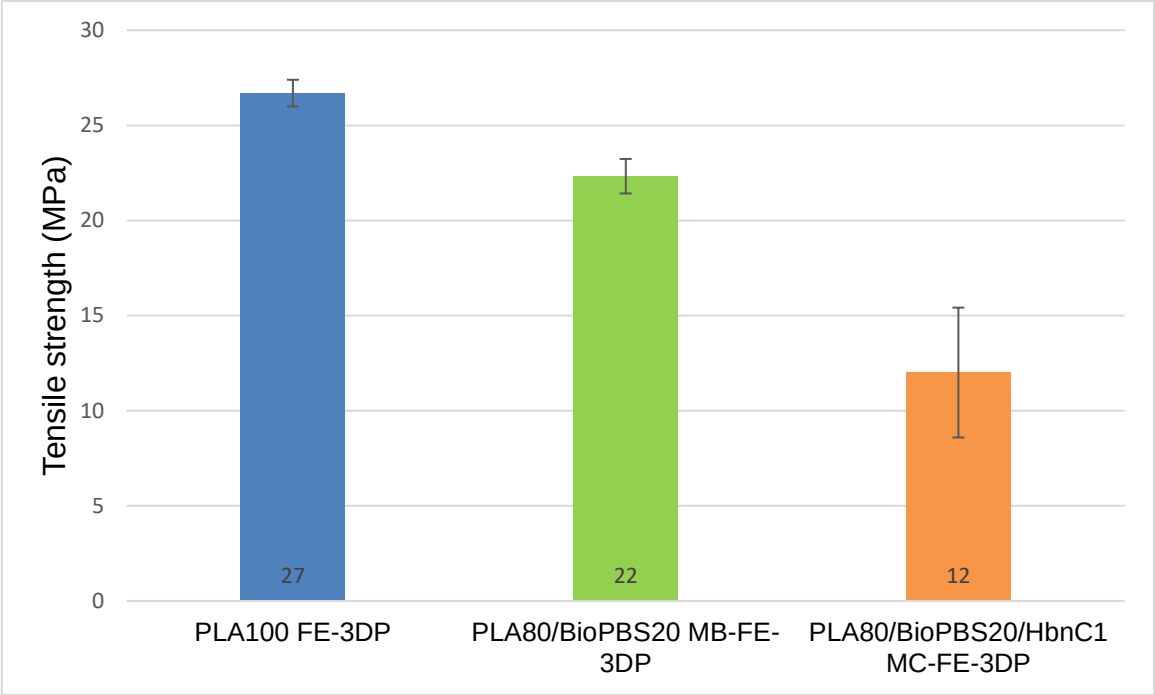

Figure 6-21 UTS strength of vertically oriented PLA100 FE-3DP, PLA80/BioPBS20 and PLA80/BioPBS20/HbnC1 MC-FE-3DP parts.

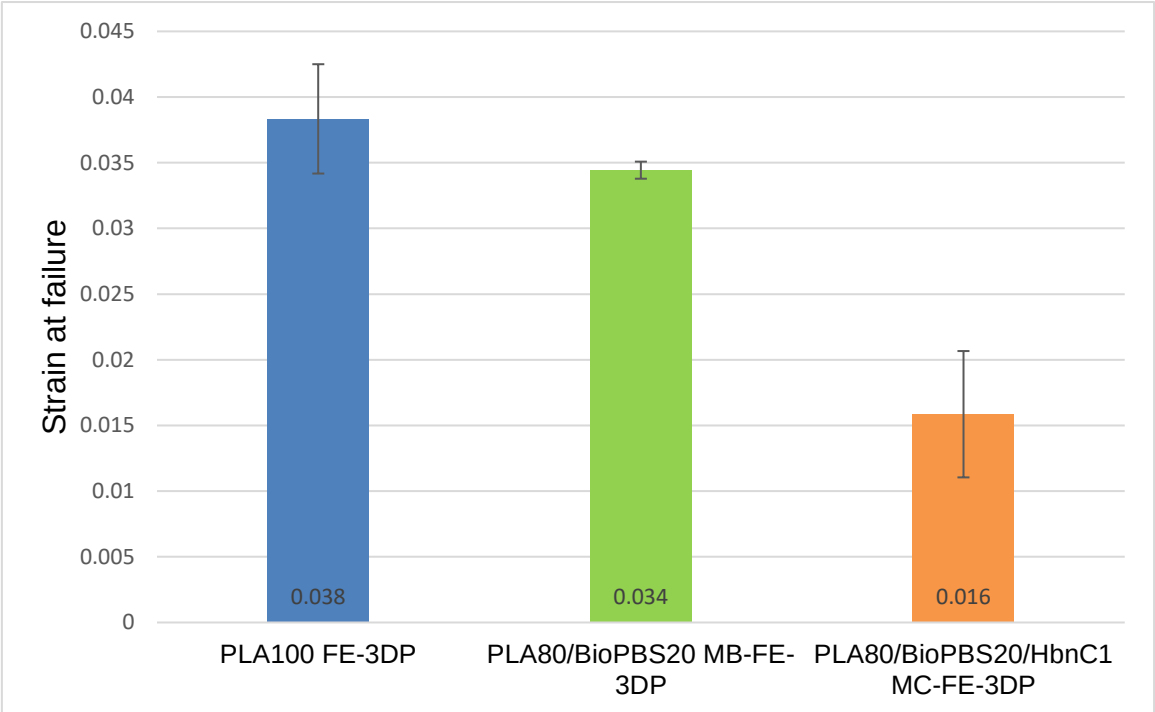

Figure 6-22 UTS Strain at failure of vertically oriented PLA100 FE-3DP, PLA80/BioPBS20 and PLA80/BioPBS20/HbnC1 MC-FE-3DP parts.

Figure 6-22 shows the strain at failure for each material. The strain for the PLA100 FE-3DP is the greatest at about 0.038, which is very similar to the strain at failure for the horizontally oriented PLA100 FE-3DP parts. Furthermore, the strain at failure for the vertically oriented PLA80/BioPBS20 MB-FE-3DP part, which uses a longer melt processing route is about 0.034 and is found to be slightly lower than that of the vertically oriented PLA100 FE-3DP part. However, in relation to the horizontally oriented PLA80/BioPBS20 composite blend parts, the vertically oriented PLA80/BioPBS20 parts show a significantly limited strain at failure, which although is dependent on the material deposition strategy and relative loading direction, may also be due to limited BioPBS-BioPBS phase interactions and limited interphase interactions between crystalline PLA and crystalline BioPBS phases. This emphasizes the dependence of strain at failure on interlayer bond quality and material phase interactions. Subsequently, in the case of the PLA80/BioPBS20/HbnC1 MC-FE-3DP parts, which show a strain at failure of about 0.016; this result is found to be about a 50% reduction in strain at failure in comparison to the vertically oriented PLA80/BioPBS20 parts. Furthermore, in comparison with the in-plane PLA80/BioPBS20/HbnC1 MC-FE-3DP parts, the strain at failure is also significantly reduced, which perhaps confirms that the interlayer bond is highly dependent on the interlayer interactions but also dependent on the composite formulation at the interlayer boundaries. Consequently, these findings also suggest that, as confirmed by the stress-strain curves in Figure 6-23, the toughness of the interlayer bond of the PLA100 FE-3DP part is highest, followed by that of the PLA80/BioPBS20 MB-FE-3DP part. Importantly, the successful strategies used in this case or other cases presented so far in literature can be adapted as a standard for testing the interlayer-bond property of vertical structures to develop the most reliable reference for defining the interlayer performance of parts printed with different filament material formulations.

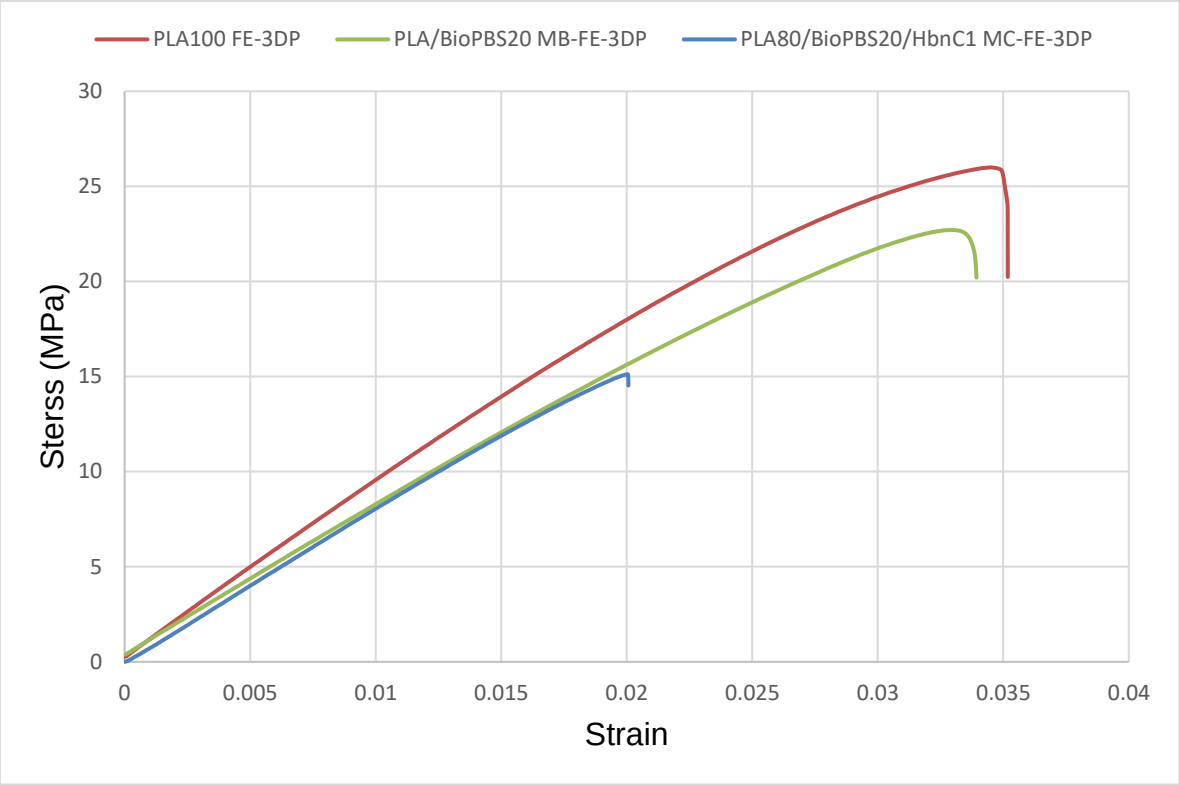

Figure 6-23 Stress-strain curve for vertically oriented PLA and PLA80/BioPBS-based parts.

6.6 Concluding remarks

The findings presented in this chapter help to conclude that PLA80/BioPBS20-based parts are printable, and that there is a strong similarity in tensile mechanical (modulus and UTS) performance for all the PLA80/BioPBS20-based parts printed using the explored 3DP strategies. However, in terms of tensile strain, the rGO-containing formulation shows a significant reduction in relation to other PLA80/BioPBS20-based formulations across all the explored 3DP strategies. Furthermore, it can be concluded that the addition of HbnC and rGO nanomaterials leads to an increase in the compatibility and uniformity of the PLA and BioPBS phases when compared to parts made of the PLA80/BioPBS20 blend. This is based on the fracture surface morphologies of the fabricated and tensile-fractured parts and is not-withstanding the fact that their DSC results show clear immiscibility between the PLA and BioPBS phases. Alternatively, another key finding is made for the in-plane PLA80/BioPBS20/HbnC1 MC-FE-3DP parts,

which show an increase in their tensile toughness property as compared to other fabricated parts. However, contrary to the findings for the in-plane PLA80/BioPBS20/HbnC1 MC-FE-3DP parts, the vertically oriented PLA80/BioPBS20/HbnC1 MC-FE-3DP parts show a significant decrease in tensile toughness, which is especially based on the limited strain at failure results obtained when compared to the vertically oriented PLA100 FE-3DP and PLA80/BioPBS20 MB-FE-3DP parts.

7 Overall discussion

7.1 Introduction

Aspects surrounding the use of PLA80/BioPBS20-based material formulations for filament fabrication, rheological complex viscosity studies, and FDM-based 3DP application have been covered in the thesis. Initially, it focuses on the effects of filament fabrication route and nanomaterial addition on the crystallinity of PLA and BioPBS phases within the filament material formulation. Furthermore, an experimental modelling approach was developed to predict the complex viscosity of the PLA80/BioPBS20-based formulations under prospective 3DP conditions of temperature and shear frequency. A developed set of 3DP strategies were applied to the PLA80/BioPBS20-based materials for the fabrication of their respective set of dog bone parts, which were assessed for their tensile mechanical and fractured surface morphological properties. In this chapter, an overall reflection and discussion of the results are presented to highlight the contribution to knowledge and potential impact derived from the findings. The findings are expected to contribute to knowledge of 1) PLA80/BioPBS20-based material crystallinity during fabrication, 2) PLA80/BioPBS20-based material rheology during extrusion, and 3) PLA80/BioPBS20-based printed part properties (tensile & fractured-surface morphology).

7.2 Discussion of findings and limitations

7.2.1 Effects of filament fabrication route and nanomaterial additions on BioPBS phase crystallinity

Based on the immiscibility between PLA and BioPBS phases, the effect of the crystallinity levels of PLA and BioPBS phases play a critical role in defining the printability of PLA/BioPBS20-based composite materials. Consequently, the fabrication route utilized in obtaining the 3DP filament material also has a considerable influence on the realized crystallinity of the PLA and BioPBS phases prior to 3DP application. Although the constituting materials are not modified due to additional processing and cost implications, the use of small amounts of additives or unique processing routes for filament fabrication can have significant

impact on the crystallinity of the PLA and/or BioPBS material phases. The use of a MB-FE process route has been found to reduce the onset recrystallisation temperature of the BioPBS phase in the PLA80/BioPBS20 MB-FE filament material by over 75 °C when compared to the onset recrystallization temperature of the BioPBS phase in the PLA80/BioPBS20 FE filament material. This is a favourable result for potentially limiting any shrinkage effects that may occur during printing, and hence creates a condition that could aid with better printability of PLA80/BioPBS20-based formulations. Moreover, the addition of HbnC or rGO and the use of associated melt processing routes do not have a similar effect of lowering the recrystallisation temperature of the BioPBS phase in either the PLA80/BioPBS20/HbnC1 or PLA80/BioPBS20/rGO1 filament materials. Nonetheless, in the latter, the recrystallization enthalpy of the BioPBS phase is limited by about 67%, which is consequently responsible for the highly brittle failure modes of PLA80/BioPBS20/rGO1 in-plane dog bone parts. Meanwhile, in the PLA80/BioPBS20/HbnC1 MC-FE formulation, the onset recrystallization temperature remains similar to that of the PLA80/BioPBS20 FE formulation and achieves similar levels of recrystallization. These are therefore responsible for the ductile and higher tensile toughness properties obtained for their respective 3D-printed parts, despite the identified potential limitations in the dispersion of HbnC nanoparticles when considering the material preparation and utilised filament fabrication route.

7.2.2 Complex viscosity of the composite formulations

The complex viscosity of PLA/BioPBS-based composites has been studied by [52] and [138] for applications in FDM-based 3DP. The former focused on the complex viscosity of various PLA/PBS blend compositions at 160 °C, while the latter focused on PLA70/BioPBS30 blend composition at temperatures between 180 and 250 °C. However, the focus in this work is on PLA80/BioPBS20-based blends and nanocomposite formulations with additions of HbnC and rGO at 1phr loading. Additionally, the experimental studies carried out on PLA80/BioPBS20-based formulations cover a temperature range of 180-250 °C and allows for the development of complex viscosity master curves. This uniquely enables the

prediction of the respective material's complex viscosity over a broader strain frequency range than experimentally possible and forms a key output of this research. For the study conducted by [52], which tested the PLA80/BioPBS20 formulation at 160 °C, the complex viscosity was found to be about 5000 Pa.s at low strain frequencies, with a strain rate dependent drop to about 500 Pa.s at higher frequencies. Nonetheless, this finding is not as comparable to this work as that obtained by [138], for which a viscosity test conducted at 220 °C for the PLA70/BioPBS30 material is reported to have a complex viscosity of about 100 Pa.s at low strain frequencies, which increases slightly and maintains a plateau at about 130-150 Pa.s in the high (400-600 rad/s) strain frequency range. However, at lower testing temperatures (180 and 200 °C), stronger strain-rate dependence is observed, which causes a decrease in complex viscosity from about 600-700 Pa.s at lower frequencies to about 300-350 Pa.s at higher frequencies. In this work, the complex viscosity results for the PLA80/BioPBS20 formulation at 220 °C is about 80 Pa.s at the lower frequencies but drops to about 17-28 Pa.s at higher frequencies (400-600 rad/s). However, the differences in the viscosity values obtained by that of [138] can also be attributed to the fact that a higher amount of the more thermally resilient BioPBS material is present in the PLA70/BioPBS30 blend, as opposed to the PLA80/BioPBS20 blend. This causes the PLA70/BioPBS30 blend to have a higher complex viscosity value especially at higher temperatures, at which the PLA phase is more thermally susceptible than the BioPBS phase.

Considering the complex viscosity results of the nanomaterial-containing PLA80/BioPBS20-based formulations, the PLA80/BioPBS20/rGO1 formulation shows the strongest dependence on strain rate at a temperature of 220 °C but has viscosity values similar to those of the PLA80/BioPBS20 formulation, particularly in the mid-range strain rate conditions. The identified strain rate dependence of PLA80/BioPBS20/rGO1 is based on the observable gradient of its master curve in relation to that of the PLA80/BioPBS20 and PLA80/BioPBS20/HbnC1 formulations and could be caused by the platelet form of rGO particles, which may reduce the coefficient of friction between polymer molecules and hence result in increasing slip-effects between the nanomaterial

platelets and polymer matrix, hence increasing the sensitivity of complex viscosity upon strain rate changes. Alternatively, it is also found that across the strain frequency conditions at 220 °C, the PLA80/BioPBS20/HbnC1 gives the weakest strain dependence and complex viscosity values at 220 °C; possibly due to the moisture adsorption properties of montmorillonite clay as reported by [158] and [157], which makes the formulation prone to more hydrothermally induced degradation and hence, lower complex viscosity properties. Nonetheless, as the two nanomaterial-based formulations show distinct influences on the viscosity behaviour, they both present interesting opportunities for adapting the PLA/BioPBS20-based formulations as an optimized composite filament material formulation that is suitable for 3DP processing and end-part functionalities supporting electrically conductive (rGO-based) and bioresorbable (HbnC-based) applications.

7.2.3 Printability, tensile mechanical and interlayer bond properties of the biopolymer composites

The extrudability and printability achieved for the PLA80/BioPBS20-based formulations is found to work for print temperature at about 210-220 °C despite showing delamination and warpage effects on some occasions at the lower-end temperature value. However, upon increasing the print temperature and adding small quantities of nanomaterials, the printability and warpage effects appear to improve; partly due to the compatibilising and stabilising effect of HbnC and rGO on the PLA80/BioPBS20-based material system. Nonetheless, the observed stringing effects need to be considered for further PLA80/BioPBS20-based nanocomposite material improvements. Subsequently, following the successful in-plane printability of the PLA80/BioPBS20-based formulations, the tensile mechanical properties show that while the PLA, as expected, performs best with modulus and UTS values of about 1.6 GPa and 56 MPa respectively, that of PLA/BioPBS20-based blends and nanocomposite formulations have a tensile modulus and UTS of about 1.2 GPa and 50 MPa respectively. Moreover, the strain at failure for the blends and HbnC-containing composite parts increases by about 40% when compared to PLA-based parts across all the attempted 3DP strategies. Furthermore, while the research conducted by [52] and [138] were

found to offer the best similarity to the current thesis in terms of the material formulations and processing involved, the tensile strength and modulus results obtained in this work are generally lower, and confirm the need for more research to comprehensively conclude on the 3D-printed tensile mechanical properties of PLA80/BioPBS20-based parts. Furthermore, the interlayer strength results of the PLA80/BioPBS20 blend, which is found to be about 22 MPa, offers an indirectly comparable result to those obtained by [52]. However, these findings should support future progress in identifying an interlayer-bond testing standard for vertically oriented 3D-printed parts, while also providing new information on the interlayer-bond performance of vertically oriented PLA80/BioPBS20-based parts.

Table 7-1 Comparative results of the tensile mechanical properties of injection moulded parts [52] **and horizontally oriented 3D-printed dog-bone parts** [138] **obtained from different research works.**

Material formulation	**Mechanical property**	**Ou Yang et al. (2018)** [52]	**Qahtani et al. (2019)** [138]	**This work**
PLA80/PBS20	**UTS (MPa)**	55.6	64.9	50
	Tensile Modulus (GPa)	2.1	3.0	1.2
	Elongation at break (%)	93	-	8

In Table 7-1, the tensile mechanical properties of injection moulded and 3D-printed PLA80/BioPBS20-based parts are presented alongside the 3D-printed part results from this work. So far, from these available results, it is found that the injection moulded parts show a much better elongation at break than the 3D-printed parts in this work; a result of voids and porous structures that can exist in

the internal sections and deposited road boundaries of 3DP parts. Nonetheless, the 3D-printed parts produced using a 250 °C print temperature by [138] are found to outperform the results from the injection-moulded PLA/BioPBS20 parts and 3D-printed parts (in this work). These findings therefore suggests that 3D-printed parts can outperform their injection moulded counterparts once optimal parameters are defined, especially with respect to printing temperature.

7.2.4 Limitations of the study

The outcomes presented so far are subject to some limitations in the manufacturing and testing methods used. Fundamentally, the use of a PLA80/BioPBS20 formulation offers a unique point for understanding PLA/BioPBS composite blend behaviour. However, the PLA80/BioPBS20 blend formulations have been found to be limited in terms of their achievable and reliable tensile mechanical performance. And from a composite processing viewpoint, it is found that the use of multiple MC thermal processing cycles for the fabrication of PLA80/BioPBS20/rGO1 composites causes limitations in their in-plane tensile mechanical performance.

Furthermore, in terms of the filament fabrication process, the use of a water bath for cooling of extruded filament material during MB and MC is considered to provide suitable conditions for moisture uptake by especially the PLA80/BioPBS20/HbnC1 parts. Similarly, during the filament fabrication (MC) process, the infeed of fluffy rGO material in the twin screw extruder poses a limitation due to its very low density, which makes it difficult to effectively transfer from the infeed hopper to the heated chamber of the twin-screw extrusion machine. This causes less material to be delivered per unit time, and hence creates the possibility of longer processing times.

In terms of filament characterisation, the use of the DSC technique alone is found to be insufficient in reliably determining the glass transition temperatures of the fabricated filament materials due to the annealing transitions that occur for some of the filament formulations during the glass transition process, and thereby creates the need for a complimentary measurement technique. Furthermore, while the DSC analysis of the filament materials is complete, the DSC analysis of

the 3D-printed parts is incomplete and is an aspect that would contribute to providing a through-process-lifecycle crystallinity map of the utilised filament material formulations.

In terms of the 3DP process and machine design, another limitation is found to be the uncontrolled temperature and pressure of the print volume, which mainly depends on standard room temperature and pressure. Although a limitation, this situation simulates the use of a basic 3DP machine in standard atmosphere, and more technically, it causes the printed roads that are positioned further away from the heated print bed to cool and crystallise differently, which can produce regions of weaker interlayer-bonds and mechanical performances of the resulting 3D-printed parts.

A last identified limitation of this work is the extent of vertically oriented parts produced for interlayer-bond strength tests. The rGO-containing formulation was not successfully and consistently 3D-printed and therefore creates a gap in the intended set of results expected from this work. Moreover, more 3DP strategies could have been applied for the printing of the in-plane and vertically oriented samples, and hence creates even more scope for further work.

7.3 Impact

The outcomes of this work expand the knowledge and understanding of the state of PLA and BioPBS material phases in a range of PLA/BioPBS composite filament materials. Consequently, researchers working on filament formulation for 3DP can gain further insight on the effect of two simple filament fabrication routes on the phase behaviour of PLA80/BioPBS20 composite filaments. Furthermore, the results obtained upon addition of rGO and HbnC can inform researchers of the potential effects of nanomaterial on the crystallisation behaviour of the PLA or BioPBS phases. This work therefore also provides sufficient evidence that will impact the research community by promoting the need for further crystallisation studies of the PLA and BioPBS phases.

This work presents a methodological approach for developing rheological master curve models, which are used for predicting the complex viscosity values of

PLA80/BioPBS20-based composite materials under 3DP conditions. This developed approach, which combines the power law and Arrhenius models, can offer evidence, and support the development of complex viscosity master curve models for other PLA/BioPBS-based material formulations. Additionally, the rheological results from this work also form a reference for further research on the rheological properties of PLA80/BioPBS20-based formulations and enable progress to be made on the development of PLA/BioPBS biocomposites for broader technical and commercial adoption.

The tensile mechanical and morphological results obtained in this work further justifies the value of PLA80/BioPBS20-based formulations for filament fabrication and 3DP processing, which will spur further interest in such sustainable 3DP material formulations. The key findings for printability, tensile mechanical properties, and morphology reflect on the choice of printing temperature, layer height and printing speed settings used, and can be applied as a basis to improve the printability and mechanical performance of future fabricated PLA80/BioPBS20-based parts, which would support further commercialization across a range of industries, especially in the medical and consumer goods sectors.

The knowledge developed in this research can be applied for the development of more biobased, biocompatible, and biodegradable 3DP material formulations for use in small to medium-sized 3D-printed structural products that can be optimized for applications in the medical, biomedical, automotive, and aerospace industries amongst others. The combined literature, including that developed in this work, is expected to produce an improved direction and vision for the development of PLA/BioPBS-based composite parts and products like stents, prosthetics, tableware, and interior automotive/aerospace parts amongst several consumer goods. The set of mechanical results presented in this research helps to develop a more reliable knowledge of the tensile mechanical properties of PLA80/BioPBS20-based 3D-printed parts and is further supported by material-process-property relationships that will inform product designers, researchers,

and process engineers towards developing the next generation of eco-sustainable processes and products with a net-zero future in mind.

8 Conclusions and Recommendations

8.1 Conclusions

The key conclusions from this work are as follows:

- In a polymer blend of 80 wt.% PLA and 20 wt.% BioPBS, the polymers are immiscible in their crystalline state but may be miscible in their amorphous state.
- Bimodal crystal formation develops upon extensive melt processing and addition of HbnC or rGO in the PLA80/BioPBS20/HbnC1 or PLA80/BioPBS20/rGO1 composites.
- The use of two-step (MB-FE) processing route for the fabrication of PLA80/BioPBS20 composite filaments lead to increasing PLA phase crystallinity. However, the additional processing and addition of rGO realises a PLA phase crystallinity of about 33%.
- With respect to all other filament materials developed in this work, the PLA80/BioPBS20/rGO1 filament material was found to develop the most thermally stable PLA phase.
- During cooling, the growth of the crystalline BioPBS phase is hindered in the PLA80/BioPBS20/rGO1 filament material formulation in contrast to other filament formulations.
- Time temperature superposition can be achieved for the PLA80/BioPBS20-based composite formulations – towards the development of a complex viscosity master curve (model) that is applicable for temperature and shear frequency-dependent complex viscosity predictions.
- PLA80/BioPBS20-based parts are printable and show similar tensile modulus and UTS performances across all the PLA80/BioPBS20-based parts and 3DP strategies used in this study. However, the rGO-containing parts show a strain at failure similar to that of PLA100-based parts.

8.2. Recommendations for future work

Material selection is key for any process and final part performance requirements. Hence, the choice of BioPBS composition should be optimised for faster biodegradability and/or improved tensile strain and toughness properties for the PLA/BioPBS-based composites. Nonetheless, considering the limited reliability of the blend's mechanical response, the addition of some HbnC or rGO should be considered. Furthermore, a combination of both nanomaterials in the same PLA/BioPBS-based filament formulation can also be considered for future work.

Fabricated filaments should be investigated under varying isothermal cooling rates to enable the development of non-isothermal crystallisation models, which will provide more information on the typical response of filament material upon extrusion and 3D-printed part formation. Next, the 3D-printed parts obtained in this study can be applied for further analysis of PLA and BioPBS phases following 3DP part production. Together, these findings would contribute to improved knowledge and understanding of the PLA and BioPBS crystalline phase changes that occur throughout its 3DP processing lifecycle.

In terms of filament fabrication, an alternative coolant instead of a water bath should also be considered for cooling the extruded material during MB or MC processing. This could be a sort of heat sink that collects and cools the extruded material but uses the heat or converts it to other forms of energy. This approach could significantly improve the energy efficiency of the MB or MC process, while preventing any limiting effects caused by hydrophilic adsorption properties of the extruding material.

There is also a consideration for the limitations associated with transferring rGO to the extrusion machine barrel. In this case, a directed pneumatic feed system can be applied to enhance the effectiveness of rGO transfer, which could have further benefits for polymer-nanomaterial interactions but also importantly limit the processing times associated with the fabrication of PLA/BioPBS/rGO-based composite filaments.

To define the glass transitions of the filament formulations more accurately and reliably, a thermal and dynamic mechanical analysis should be employed in addition to DSC. to better explore the structural capability of the material formulations. The finding is such a case can further be combined with rheological data and analysis obtained in this work. These analytical techniques can also be applied to the 3D-printed parts to provide a broad set of results that can be used to understand the physical lifecycle changes that occur in the material formulations, filaments, and end parts. In addition, studies of the dispersion of nanomaterial fillers can also be carried out using x-ray diffraction to help establish the interlayer separations between nanoparticle layers in the composite material formulations.

For 3DP of PLA/BioPBS-based parts, the application of PLA80/BioPBS20-based filaments across different types of FDM-based 3D printers would be beneficial as this would test for the compatibility of PLA80/BioPBS20 parts across 3DP machines. It would also be beneficial to use 3D printers with an enclosed print volume or temperature control unit. This could effectively limit rapid material cooling, hence offering a unique set of mechanical results for further comparison with results from this work. In lastly addressing the limitations resulting from failures of vertically oriented 3D-printed parts for the PLA80/BioPBS20/rGO1 formulation; it is recommended that a lower print temperature of about 215 °C is used for future trials; amongst other potentially successful 3DP strategies.

9 References

[1] U. Scheithauer, A. Bergner, E. Schwarzer, H.-J. Richter, and T. Moritz, “Studies on thermoplastic 3D printing of steel–zirconia composites,” *J. Mater. Res.*, vol. 29, no. 17, pp. 1931–1940, 2014.

[2] T. D. Ngo, A. Kashani, G. Imbalzano, K. T. Q. Nguyen, and D. Hui, “Additive manufacturing (3D printing): A review of materials, methods, applications and challenges,” *Composites Part B: Engineering*, vol. 143. pp. 172–196, 2018.

[3] I. T. Ozbolat and M. Hospodiuk, “Current advances and future perspectives in extrusion-based bioprinting,” *Biomaterials*, vol. 76. pp. 321–343, 2016.

[4] L. Serex, A. Bertsch, and P. Renaud, “Microfluidics: A new layer of control for extrusion-based 3D printing,” *Micromachines*, vol. 9, no. 2, 2018.

[5] A. W. Gebisa and H. G. Lemu, “Investigating effects of Fused-deposition modeling (FDM) processing parameters on flexural properties of ULTEM 9085 using designed experiment,” *Materials (Basel).*, vol. 11, no. 4, pp. 1–23, 2018.

[6] J. R. C. Dizon, A. H. Espera, Q. Chen, and R. C. Advincula, “Mechanical characterization of 3D-printed polymers,” *Addit. Manuf.*, vol. 20, pp. 44–67, 2018.

[7] S. A. M. Tofail, E. P. Koumoulos, A. Bandyopadhyay, S. Bose, L. O’Donoghue, and C. Charitidis, “Additive manufacturing: scientific and technological challenges, market uptake and opportunities,” *Mater. Today*, vol. 21, no. 1, pp. 22–37, 2018.

[8] K. Bryll, E. Piesowicz, P. Szymański, W. Ślączka, and M. Pijanowski, “Polymer Composite Manufacturing by FDM 3D Printing Technology,” *MATEC Web Conf.*, vol. 237, p. 02006, 2018.

[9] S. C. Ligon, R. Liska, J. Stampfl, M. Gurr, and R. Mülhaupt, “Polymers for

3D Printing and Customized Additive Manufacturing," *Chem. Rev.*, vol. 117, no. 15, pp. 10212–10290, Aug. 2017.

[10] J. Liu, L. Sun, W. Xu, Q. Wang, S. Yu, and J. Sun, "Current advances and future perspectives of 3D printing natural-derived biopolymers," *Carbohydr. Polym.*, vol. 207, no. June 2018, pp. 297–316, 2019.

[11] R. Matsuzaki *et al.*, "Three-dimensional printing of continuous-fiber composites by in-nozzle impregnation," *Sci. Rep.*, vol. 6, no. 1, p. 23058, Mar. 2016.

[12] R. A. Buswell, W. R. Leal de Silva, S. Z. Jones, and J. Dirrenberger, "3D printing using concrete extrusion: A roadmap for research," *Cem. Concr. Res.*, vol. 112, no. October 2017, pp. 37–49, 2018.

[13] A. Le Duigou, A. Barbé, E. Guillou, and M. Castro, "3D printing of continuous flax fibre reinforced biocomposites for structural applications," *Mater. Des.*, vol. 180, p. 107884, Oct. 2019.

[14] M. Lille, A. Nurmela, E. Nordlund, S. Metsä-Kortelainen, and N. Sozer, "Applicability of protein and fiber-rich food materials in extrusion-based 3D printing," *J. Food Eng.*, vol. 220, pp. 20–27, 2018.

[15] U. Scheithauer, E. Schwarzer, H. J. Richter, and T. Moritz, "Thermoplastic 3D printing - An additive manufacturing method for producing dense ceramics," *Int. J. Appl. Ceram. Technol.*, vol. 12, no. 1, pp. 26–31, 2015.

[16] C. González, J. J. Vilatela, J. M. Molina-Aldareguía, C. S. Lopes, and J. LLorca, "Structural composites for multifunctional applications: Current challenges and future trends," *Prog. Mater. Sci.*, vol. 89, pp. 194–251, 2017.

[17] W. Gao *et al.*, "The status, challenges, and future of additive manufacturing in engineering," *CAD Comput. Aided Des.*, vol. 69, pp. 65–89, 2015.

[18] J. F. Christ, N. Aliheidari, A. Ameli, and P. Pötschke, "3D printed highly

elastic strain sensors of multiwalled carbon nanotube/thermoplastic polyurethane nanocomposites," *Mater. Des.*, vol. 131, pp. 394–401, 2017.

[19] A. Pappu, V. K. Thakur, R. Patidar, S. R. Asolekar, and M. Saxena, "Recycling marble wastes and Jarosite wastes into sustainable hybrid composite materials and validation through Response Surface Methodology," *J. Clean. Prod.*, vol. 240, p. 118249, 2019.

[20] A. K. Thakur, A. Pappu, and V. K. Thakur, "Synthesis and characterization of new class of geopolymer hybrid composite materials from industrial wastes," *J. Clean. Prod.*, vol. 230, pp. 11–20, 2019.

[21] C. H. Kim, H. M. Cho, and M. E. Lee, "Synthesis and physical property of multi-functional siloxane protective coating materials applicable for electronic components," *Bull. Korean Chem. Soc.*, vol. 35, no. 6, pp. 1665–1669, 2014.

[22] K. Salonitis, J. Pandremenos, J. Paralikas, and G. Chryssolouris, "Multifunctional materials: Engineering applications and processing challenges," *Int. J. Adv. Manuf. Technol.*, vol. 49, no. 5–8, pp. 803–826, 2010.

[23] D. G. Bekas, Y. Hou, Y. Liu, and A. Panesar, "3D printing to enable multifunctionality in polymer-based composites: A review," *Compos. Part B Eng.*, vol. 179, no. June, p. 107540, 2019.

[24] A. D. B. L. Ferreira, P. R. O. Nóvoa, and A. T. Marques, "Multifunctional Material Systems: A state-of-the-art review," *Compos. Struct.*, vol. 151, pp. 3–35, 2016.

[25] E. M. Palmero *et al.*, "Composites based on metallic particles and tuned filling factor for 3D-printing by Fused Deposition Modeling," *Compos. Part A Appl. Sci. Manuf.*, vol. 124, 2019.

[26] "4.5. Multifunctional Materials and Their Impact on Sustainability | EME 807:" [Online]. Available: https://www.e-

education.psu.edu/eme807/node/698.

[27] K. W. A.B. Spierings, M. Voegtlin, T. Bauer, “Materials Testing Standards for Additive Manufacturing of Polymer Materials :,” *Prog Addit Manuf*, vol. 1, pp. 9–20, 2015.

[28] D. Ortiz-Acosta and T. Moore, “Functional 3D Printed Polymeric Materials,” in *Functional Materials*, IntechOpen, 2019.

[29] S. Buchholz, “Factories of the future,” *Manuf. Chem.*, vol. 82, no. 3, pp. 27–29, 2011.

[30] J. O’Heir, “Protecting a New World of 3D-Printed Products,” *The American Society of Mechanical Engineers*, 2018. [Online]. Available: https://www.asme.org/topics-resources/content/protecting-new-world-3dprinted-products.

[31] C. Nachreiner, “The security issues 3D printing should solve before going mainstream - Help Net Security,” 2018. [Online]. Available: https://www.helpnetsecurity.com/2018/08/08/security-issues-3d-printing/.

[32] G. Segalla, “Data Privacy and Security – 3D Printing: A Cybersecurity Concern,” 2018. [Online]. Available: https://dataprivacyblog.com/3d-printing-a-cybersecurity-concern/.

[33] V. C. F. Li, X. Kuang, C. M. Hamel, D. Roach, Y. Deng, and H. J. Qi, “Cellulose nanocrystals support material for 3D printing complexly shaped structures via multi-materials-multi-methods printing,” *Addit. Manuf.*, vol. 28, no. November 2018, pp. 14–22, 2019.

[34] G. E. Luckachan and C. K. S. Pillai, “Biodegradable Polymers- A Review on Recent Trends and Emerging Perspectives,” *J. Polym. Environ.*, vol. 19, no. 3, pp. 637–676, 2011.

[35] S. Kyle, Z. M. Jessop, A. Al-Sabah, and I. S. Whitaker, “‘Printability’’ of Candidate Biomaterials for Extrusion Based 3D Printing: State-of-the-Art,’”

Adv. Healthc. Mater., vol. 6, no. 16, pp. 1–16, 2017.

[36] J. K. Placone and A. J. Engler, “Recent Advances in Extrusion-Based 3D Printing for Biomedical Applications,” *Adv. Healthc. Mater.*, vol. 7, no. 8, pp. 1–11, 2018.

[37] M. H. Rahman and P. R. Bhoi, “An overview of non-biodegradable bioplastics,” *Journal of Cleaner Production*, vol. 294. Elsevier Ltd, 20-Apr-2021.

[38] J. A. Garza-Reyes, “SYNTHESIS REPORT OF THE IPCC SIXTH ASSESSMENT REPORT (AR6),” *Eur. Univ. Inst.*, no. 2, pp. 2–5, 2012.

[39] S. C. Daminabo, S. Goel, S. A. Grammatikos, H. Y. Nezhad, and V. K. Thakur, “Fused deposition modeling-based additive manufacturing (3D printing): techniques for polymer material systems,” *Mater. Today Chem.*, vol. 16, p. 100248, 2020.

[40] K. S. Su Shen, Kopitzky Rodion, Tolga Sengül, “Polylactide (PLA) and Its Blends with Poly (butylene,” *Polymers (Basel).*, pp. 1–21, 2019.

[41] G. Sotorrío, J. Alonso, N. O. E. Olsson, and J. A. Tenorio, “Printability of materials for extrusion 3D printing technologies: a review of material requirements and testin,” *Mater. Construcción*, vol. 71, no. 344, p. e267, 2021.

[42] D. Tan, M. Maniruzzaman, and A. Nokhodchi, “Advanced Pharmaceutical Applications of Hot-Melt Extrusion Coupled with Fused Deposition Modelling (FDM) 3D Printing for Personalised Drug Delivery,” *Pharmaceutics*, vol. 10, no. 4, p. 203, Oct. 2018.

[43] R. Spina and B. Cavalcante, “Preliminary Analysis of Extruded PP Filaments for FFF,” *Procedia Manuf.*, vol. 47, pp. 915–919, 2020.

[44] H. Patil, R. V. Tiwari, and M. A. Repka, “Hot-Melt Extrusion: from Theory to Application in Pharmaceutical Formulation,” *AAPS PharmSciTech*, vol. 17,

no. 1, pp. 20–42, Feb. 2016.

[45] E. H. Kamau, S. G. Nkhata, and E. O. Ayua, “Extrusion and nixtamalization conditions influence the magnitude of change in the nutrients and bioactive components of cereals and legumes,” *Food Sci. Nutr.*, vol. 8, no. 4, pp. 1753–1765, 2020.

[46] N. Kumar, P. K. Jain, P. Tandon, and P. Mohan Pandey, “Experimental investigations on suitability of polypropylene (PP) and ethylene vinyl acetate (EVA) in additive manufacturing,” *Mater. Today Proc.*, vol. 5, no. 2, pp. 4118–4127, 2018.

[47] D. Drummer, S. Cifuentes-Cuéllar, and D. Rietzel, “Suitability of PLA/TCP for fused deposition modeling,” *Rapid Prototyp. J.*, vol. 18, no. 6, pp. 500–507, 2012.

[48] E. Gkartzou, E. P. Koumoulos, and C. A. Charitidis, “Production and 3D printing processing of bio-based thermoplastic filament,” *Manuf. Rev.*, vol. 4, p. 1, 2017.

[49] S. H. Ahn, M. Montero, D. Odell, S. Roundy, and P. K. Wright, “Anisotropic material properties of fused deposition modeling ABS,” *Rapid Prototyp. J.*, vol. 8, no. 4, pp. 248–257, 2002.

[50] K. Formela, Zedler, A. Hejna, and A. Tercjak, “Reactive extrusion of bio-based polymer blends and composites–current trends and future developments,” *Express Polym. Lett.*, vol. 12, no. 1, pp. 24–57, 2018.

[51] L. G. Blok, M. L. Longana, H. Yu, and B. K. S. Woods, “An investigation into 3D printing of fibre reinforced thermoplastic composites,” *Addit. Manuf.*, vol. 22, pp. 176–186, 2018.

[52] Q. Ou-Yang, B. Guo, and J. Xu, “Preparation and Characterization of Poly(butylene succinate)/Polylactide Blends for Fused Deposition Modeling 3D Printing,” *ACS Omega*, vol. 3, no. 10, pp. 14309–14317, 2018.

[53] E. G. Gordeev, A. S. Galushko, and V. P. Ananikov, “Improvement of quality of 3D printed objects by elimination of microscopic structural defects in fused deposition modeling,” *PLoS One*, vol. 13, no. 6, 2018.

[54] A. Melocchi, F. Parietti, A. Maroni, A. Foppoli, A. Gazzaniga, and L. Zema, “Hot-melt extruded filaments based on pharmaceutical grade polymers for 3D printing by fused deposition modeling,” *Int. J. Pharm.*, vol. 509, no. 1–2, pp. 255–263, 2016.

[55] M. Harris, J. Potgieter, K. Arif, and R. Archer, “Large scale 3D printing: Feasibility of novel extrusion based process and requisite materials,” in *2017 24th International Conference on Mechatronics and Machine Vision in Practice, M2VIP 2017*, 2017, vol. 2017-Decem, pp. 1–6.

[56] A. W. Gebisa and H. G. Lemu, “Influence of 3D printing FDM process parameters on tensile property of ultem 9085,” in *Procedia Manufacturing*, 2019, vol. 30, pp. 331–338.

[57] V. Mazzanti, L. Malagutti, and F. Mollica, “FDM 3D printing of polymers containing natural fillers: A review of their mechanical properties,” *Polymers*, vol. 11, no. 7. MDPI AG, 2019.

[58] E. H. Tümer and H. Y. Erbil, “Extrusion-based 3d printing applications of pla composites: A review,” *Coatings*, vol. 11, no. 4. Multidisciplinary Digital Publishing Institute, p. 390, 29-Mar-2021.

[59] D. Kaczmarek, D. Walczyk, J. Garofalo, and M. Sobkowicz-Kline, “An investigation of in situ impregnation for additive manufacturing of thermoplastic composites,” *J. Manuf. Process.*, vol. 64, no. January, pp. 972–981, 2021.

[60] H. K. Sezer and O. Eren, “FDM 3D printing of MWCNT re-inforced ABS nano-composite parts with enhanced mechanical and electrical properties,” *J. Manuf. Process.*, vol. 37, no. July 2018, pp. 339–347, 2019.

[61] S. Wang, J. M. Lee, and W. Y. Yeong, “International journal of bioprinting,”

Int. J. Bioprinting, vol. 1, no. 1, pp. 3–14, 2015.

[62] A. C. Abbott, G. P. Tandon, R. L. Bradford, H. Koerner, and J. W. Baur, “Process-structure-property effects on ABS bond strength in fused filament fabrication,” *Addit. Manuf.*, vol. 19, pp. 29–38, 2018.

[63] Q. Wang *et al.*, *Investigation of condensation reaction during phenol liquefaction of waste woody materials*, vol. 9, no. 5. 2014.

[64] Y. Song, Y. Li, W. Song, K. Yee, K. Y. Lee, and V. L. Tagarielli, “Measurements of the mechanical response of unidirectional 3D-printed PLA,” *Mater. Des.*, vol. 123, pp. 154–164, 2017.

[65] B. Wittbrodt and J. M. Pearce, “The effects of PLA color on material properties of 3-D printed components,” *Addit. Manuf.*, vol. 8, pp. 110–116, Oct. 2015.

[66] J. T. Belter and A. M. Dollar, “Strengthening of 3D printed fused deposition manufactured parts using the fill compositing technique,” *PLoS One*, vol. 10, no. 4, p. e0122915, Apr. 2015.

[67] PLASTIM, “ABS-Technical-Data-Sheet,” Jan. 2015.

[68] Ultimaker, “Technical data sheet ABS,” Feb. 2017.

[69] Stratasys, “Ingeo™ Biopolymer 4043D Technical Data Sheet 3D Printing Monofilament-General Purpose Grade.”

[70] Stratasys, “PLA Material Data Sheet.”

[71] Ecoease, “PET - Technical Handbook.” [Online]. Available: https://ecoease.co.uk/wp-content/uploads/2018/09/PET-Technical-Handbook-1.pdf. [Accessed: 29-Dec-2023].

[72] Roffelsen Plastics, “Material Data Sheet PET General Information Physical Properties,” Jan. 2023.

[73] 3DXTECH Advanced Materials, “PETG-TDS-v03.”

[74] rigid.ink, “PETG DATA SHEET.”

[75] Stratasys, “FDM HIPS Technical Data Sheet.”

[76] Policam, “HIPS SHEETS DATA SHEET PROPERTIES,” Jan. 2014.

[77] Ultimaker, “TPU datasheet TPU 95A,” May 2017.

[78] Lubrizol, “Pearlthane ® 11H94,” 2018.

[79] Ultimaker, “PP Technical data sheet General Overview,” Apr. 2022.

[80] British Plastic Federation, “Polypropylene.” [Online]. Available: https://www.bpf.co.uk/plastipedia/polymers/PP.aspx. [Accessed: 29-Dec-2023].

[81] W. Amass, A. Amass, and B. Tighe, “A review of biodegradable polymers: Uses, current developments in the synthesis and characterization of biodegradable polyesters, blends of biodegradable polymers and recent advances in biodegradation studies,” *Polym. Int.*, vol. 47, no. 2, pp. 89–144, 1998.

[82] O. Platnieks *et al.*, “Bio-based poly(butylene succinate)/microcrystalline cellulose/nanofibrillated cellulose-based sustainable polymer composites: Thermo-mechanical and biodegradation studies,” *Polymers (Basel).*, vol. 12, no. 7, pp. 1–20, 2020.

[83] N. Shahrubudin, T. C. Lee, and R. Ramlan, “An overview on 3D printing technology: Technological, materials, and applications,” in *Procedia Manufacturing*, 2019, vol. 35, pp. 1286–1296.

[84] S. S. Luke, D. Soares, J. V. Marshall, J. Sheddden, and Ö. Keleş, “Effect of fiber content and fiber orientation on mechanical behavior of fused filament fabricated continuous-glass-fiber-reinforced nylon,” *Rapid Prototyp. J.*, vol. 27, no. 7, pp. 1346–1354, 2021.

[85] I. Papa, A. T. Silvestri, M. R. Ricciardi, V. Lopresto, and A. Squillace, “Effect of Fibre Orientation on Novel Continuous 3D-Printed Fibre-Reinforced Composites,” *Polymers (Basel).*, vol. 13, no. 15, p. 2524, 2021.

[86] P. Parnian and A. D’Amore, “Fabrication of high-performance cnt reinforced polymer composite for additive manufacturing by phase inversion technique,” *Polymers (Basel).*, vol. 13, no. 22, 2021.

[87] M. Pourali and A. M. Peterson, “Fused filament fabrication of void-free parts using low viscosity hot melt adhesives,” *Addit. Manuf.*, vol. 46, p. 102110, 2021.

[88] H. K. Sezer and O. Eren, “FDM 3D printing of MWCNT re-inforced ABS nano-composite parts with enhanced mechanical and electrical properties,” *J. Manuf. Process.*, vol. 37, no. December 2017, pp. 339–347, 2019.

[89] T. N. A. T. Rahim, A. M. Abdullah, H. M. Akil, D. Mohamad, and Z. A. Rajion, “The improvement of mechanical and thermal properties of polyamide 12 3D printed parts by fused deposition modelling,” *Express Polym. Lett.*, vol. 11, no. 12, pp. 963–982, 2017.

[90] Y. Ibrahim, A. Elkholy, J. S. Schofield, G. W. Melenka, and R. Kempers, “Effective thermal conductivity of 3D-printed continuous fiber polymer composites,” *Adv. Manuf. Polym. Compos. Sci.*, vol. 6, no. 1, pp. 17–28, 2020.

[91] J. Suganuma and H. Alexander, “Biological response of intramedullary bone to poly-L-lactic acid,” *J. Appl. Biomater.*, vol. 4, no. 1, pp. 13–27, 1993.

[92] R. Song, M. Murphy, C. Li, K. Ting, C. Soo, and Z. Zheng, “Current development of biodegradable polymeric materials for biomedical applications,” *Drug Design, Development and Therapy*, vol. 12. pp. 3117–3145, 2018.

[93] C. Schippers, J. S. Gutmann, and L. A. Tsarkova, “Revisiting the Contribution of Additives to the Long-Term Mechanical Stability and

Hydrolytic Resistance of Highly Crystalline Polylactide Fibers," *ACS Appl. Mater. Interfaces*, vol. 15, no. 1, pp. 1984–1995, Jan. 2023.

[94] T. Yokohara and M. Yamaguchi, "Structure and properties for biomass-based polyester blends of PLA and PBS," *Eur. Polym. J.*, vol. 44, no. 3, pp. 677–685, 2008.

[95] S. A. Rafiqah *et al.*, "A review on properties and application of bio-based poly(Butylene succinate)," *Polymers (Basel).*, vol. 13, no. 9, pp. 1–28, 2021.

[96] A. Bhatia, R. K. Gupta, and H. J. Choi, "Compatibility of Biodegradable Poly (lactic acid) and Poly (butylene succinate) blends for packaging application," *Korea-Australia …*, vol. 19, no. 3, pp. 125–131, 2007.

[97] V. Gigante *et al.*, "Flat die extruded biocompatible poly(lactic acid) (PLA)/poly(butylene succinate) (PBS) Based Films," *Polymers (Basel).*, vol. 11, no. 11, p. 1857, 2019.

[98] N. Stoyanova *et al.*, "Poly(l-lactide) and poly(butylene succinate) immiscible blends: From electrospinning to biologically active materials," *Mater. Sci. Eng. C*, vol. 41, pp. 119–126, Aug. 2014.

[99] E. A. M. Hassan, S. E. Elarabi, Y. Wei, and M. Yu, "Biodegradable poly (lactic acid)/poly (butylene succinate) fibers with high elongation for health care products," *Text. Res. J.*, vol. 88, no. 15, pp. 1735–1744, 2018.

[100] T. Messin *et al.*, "Biodegradable PLA/PBS multinanolayer membrane with enhanced barrier performances," *J. Memb. Sci.*, vol. 598, p. 117777, Mar. 2020.

[101] W. Prasong, A. Ishigami, S. Thumsorn, T. Kurose, and H. Ito, "Improvement of interlayer adhesion and heat resistance of biodegradable ternary blend composite 3D printing," *Polymers (Basel).*, vol. 13, no. 5, pp. 1–20, 2021.

[102] A. Dmitruk, J. Ludwiczak, M. Skwarski, P. Makuła, and P. Kaczyński,

"Influence of PBS, PBAT and TPS content on tensile and processing properties of PLA-based polymeric blends at different temperatures," *J. Mater. Sci.*, vol. 58, no. 4, pp. 1991–2004, 2023.

[103] X. Lan, X. Li, Z. Liu, Z. He, W. Yang, and M. Yang, "Composition, morphology and properties of poly(lactic acid) and poly(butylene succinate) copolymer system via coupling reaction," *J. Macromol. Sci. Part A Pure Appl. Chem.*, vol. 50, no. 8, pp. 861–870, 2013.

[104] R. Homklin and N. Hongsriphan, "Mechanical and thermal properties of PLA/PBS cocontinuous blends adding nucleating agent," *Energy Procedia*, vol. 34, pp. 871–879, 2013.

[105] A. Bhatia, R. K. Gupta, S. N. Bhattacharya, and H. J. Choi, "An investigation of melt rheology and thermal stability of poly(lactic acid)/poly(butylene succinate) nanocomposites," *J. Appl. Polym. Sci.*, vol. 114, no. 5, pp. 2837–2847, 2009.

[106] J. Zhou, Z. Yao, C. Zhou, D. Wei, and S. Li, "Mechanical properties of PLA/PBS foamed composites reinforced by organophilic montmorillonite," *J. Appl. Polym. Sci.*, vol. 131, no. 18, pp. 9319–9326, 2014.

[107] V. Sivanjineyulu, K. Behera, Y. H. Chang, and F. C. Chiu, "Selective localization of carbon nanotube and organoclay in biodegradable poly(butylene succinate)/polylactide blend-based nanocomposites with enhanced rigidity, toughness and electrical conductivity," *Compos. Part A Appl. Sci. Manuf.*, vol. 114, no. June, pp. 30–39, 2018.

[108] J. M. Campos, A. M. Ferraria, A. M. Botelho Do Rego, M. R. Ribeiro, and A. Barros-Timmons, "Studies on PLA grafting onto graphene oxide and its effect on the ensuing composite films," *Mater. Chem. Phys.*, vol. 166, pp. 122–132, 2015.

[109] M. S. Ullah, R. Yildirim, M. Kodal, and G. Ozkoc, "Reactive compatibilization of PLA/PBS bio-blends via a new generation of hybrid

nanoparticles," *J. Vinyl Addit. Technol.*, Dec. 2022.

[110] K. Oksman, M. Skrifvars, and J. F. Selin, "Natural fibres as reinforcement in polylactic acid (PLA) composites," *Compos. Sci. Technol.*, vol. 63, no. 9, pp. 1317–1324, Jul. 2003.

[111] F. A. M. M. Gonçalves, S. M. A. Cruz, J. F. J. Coelho, and A. C. Serra, "The impact of the addition of compatibilizers on poly (Lactic acid) (pla) properties after extrusion process," *Polymers (Basel).*, vol. 12, no. 11, pp. 1–18, 2020.

[112] T. K. Daya Gireesh, V. I. Anzila, T. T. Litha, and P. P. Nair, "Synthesis of Graphene-based Polymer Nanocomposites and comparison of properties," *IOP Conf. Ser. Mater. Sci. Eng.*, vol. 1248, no. 1, p. 012012, Jul. 2022.

[113] B. W. Chieng, N. A. Ibrahim, W. M. Z. W. Yunus, M. Z. Hussein, Y. Y. Then, and Y. Y. Loo, "Effects of graphene nanoplatelets and reduced graphene oxide on poly(lactic acid) and plasticized poly(lactic acid): A comparative study," *Polymers (Basel).*, vol. 6, no. 8, pp. 2232–2246, 2014.

[114] F. S. Senatov *et al.*, "Shape memory effect in 3D-printed scaffolds for self-fitting implants," *Eur. Polym. J.*, vol. 93, pp. 222–231, 2017.

[115] C. W. Foster *et al.*, "3D Printed Graphene Based Energy Storage Devices," *Sci. Rep.*, vol. 7, no. 1, p. 42233, 2017.

[116] J. Luo, H. Wang, D. Zuo, A. Ji, and Y. Liu, "Research on the application of MWCNTs/PLA composite material in the manufacturing of conductive composite products in 3D printing," *Micromachines*, vol. 9, no. 12, Nov. 2018.

[117] M. A. Vigil Fuentes, S. Thakur, F. Wu, M. Misra, S. Gregori, and A. K. Mohanty, "Study on the 3D printability of poly(3-hydroxybutyrate-co-3-hydroxyvalerate)/poly(lactic acid) blends with chain extender using fused filament fabrication," *Sci. Rep.*, vol. 10, no. 1, pp. 1–12, 2020.

[118] H. Long *et al.*, “Mechanical and thermal properties of bamboo fiber reinforced polypropylene/polylactic acid composites for 3D printing,” *Polym. Eng. Sci.*, vol. 59, no. s2, pp. E247–E260, 2019.

[119] K. Panichsombat, W. Panbangpong, N. Poompiew, and P. Potiyaraj, “Biodegradable fibers from poly (lactic acid)/poly (butylene succinate) blends,” *IOP Conf. Ser. Mater. Sci. Eng.*, vol. 600, no. 1, 2019.

[120] J. Gao *et al.*, “Toughening and Heat-Resistant Modification of Degradable PLA/PBS-Based Composites by Using Glass Fiber/Silicon Dioxide Hybrid Fillers,” *Polymers (Basel).*, vol. 14, no. 16, 2022.

[121] Z. Gu *et al.*, “Extraordinary toughness and heat resistance enhancement of biodegradable PLA/PBS blends through the formation of a small amount of interface-localized stereocomplex crystallites during melt blending,” *Polymer (Guildf).*, vol. 262, no. October, p. 125454, 2022.

[122] S. Öhman, “Characterization of biopolymers for barriers in food packaging,” *Chalmers Univ. Technol.*, 2018.

[123] A. Rodriguez-Uribe, T. Wang, A. K. Pal, F. Wu, A. K. Mohanty, and M. Misra, “Injection moldable hybrid sustainable composites of BioPBS and PHBV reinforced with talc and starch as potential alternatives to single-use plastic packaging,” *Compos. Part C Open Access*, vol. 6, p. 100201, Oct. 2021.

[124] D. Wu, L. Yuan, E. Laredo, M. Zhang, and W. Zhou, “Interfacial properties, viscoelasticity, and thermal behaviors of poly(butylene succinate)/polylactide blend,” *Ind. Eng. Chem. Res.*, vol. 51, no. 5, pp. 2290–2298, 2012.

[125] G. Gaidukova, O. Platnieks, A. Aunins, A. Barkane, C. Ingrao, and S. Gaidukovs, “Spent coffee waste as a renewable source for the production of sustainable poly(butylene succinate) biocomposites from a circular economy perspective,” *RSC Adv.*, vol. 11, no. 30, pp. 18580–18589, 2021.

[126] Y. T. Hsieh, S. Nozaki, M. Kido, K. Kamitani, K. Kojio, and A. Takahara, “Crystal polymorphism of polylactide and its composites by X-ray diffraction study,” *Polym. J. 2020 527*, vol. 52, no. 7, pp. 755–763, Apr. 2020.

[127] R. Androsch, M. L. Di Lorenzo, and C. Schick, “Optical Microscopy to Study Crystal Nucleation in Polymers Using a Fast Scanning Chip Calorimeter for Precise Control of the Nucleation Pathway,” *Macromol. Chem. Phys.*, vol. 219, no. 3, p. 1700479, Feb. 2018.

[128] J. Zhang, K. Tashiro, H. Tsuji, and A. J. Domb, “Disorder-to-order phase transition and multiple melting behavior of poly(L-lactide) investigated by simultaneous measurements of WAXD and DSC,” *Macromolecules*, vol. 41, no. 4, pp. 1352–1357, Feb. 2008.

[129] NatureWorks LLC, “Ingeo Biopolymer 2003D Technical Data Sheet,” 2004.

[130] PTT MCC Biochem, “BioPBS ™ FZ91PM / FZ91PB Technical Data Sheet,” 2020.

[131] A. C. Balazs, T. Emrick, and T. P. Russell, “Nanoparticle polymer composites: Where two small worlds meet,” *Science (80-.).*, vol. 314, no. 5802, pp. 1107–1110, Nov. 2006.

[132] J. Y. Lee, G. A. Buxton, and A. C. Balazs, “Using nanoparticles to create self-healing composites,” *J. Chem. Phys.*, vol. 121, no. 11, pp. 5531–5540, Sep. 2004.

[133] R. Krishnamoorti and R. A. Vaia, “Polymer nanocomposites,” *J. Polym. Sci. Part B Polym. Phys.*, vol. 45, no. 24, pp. 3252–3256, Dec. 2007.

[134] M. Alexandre and P. Dubois, “Polymer-layered silicate nanocomposites: preparation, properties and uses of a new class of materials.”

[135] M. Moniruzzaman and K. I. Winey, “Polymer nanocomposites containing carbon nanotubes,” *Macromolecules*, vol. 39, no. 16, pp. 5194–5205, Aug. 2006.

[136] D. R. Paul and L. M. Robeson, “Polymer nanotechnology: Nanocomposites,” *Polymer (Guildf).*, vol. 49, no. 15, pp. 3187–3204, Jul. 2008.

[137] J. W. Park and S. S. Im, “Phase behavior and morphology in blends of poly(L-lactic acid) and poly(butylene succinate),” *J. Appl. Polym. Sci.*, vol. 86, no. 3, pp. 647–655, Oct. 2002.

[138] M. Qahtani, F. Wu, M. Misra, S. Gregori, D. F. Mielewski, and A. K. Mohanty, “Experimental Design of Sustainable 3D-Printed Poly(Lactic Acid)/Biobased Poly(Butylene Succinate) Blends via Fused Deposition Modeling,” *ACS Sustain. Chem. Eng.*, vol. 7, no. 17, pp. 14460–14470, Sep. 2019.

[139] C. Lin, L. Liu, Y. Liu, and J. Leng, “The compatibility of polylactic acid and polybutylene succinate blends by molecular and mesoscopic dynamics,” *International Journal of Smart and Nano Materials*, vol. 11, no. 1. pp. 24–37, 2020.

[140] D. Wang, X. Lu, and J. Qu, “Role of In situ thermal-reduced graphene oxide on the morphology and properties of biodegradable poly(Lactic acid)/poly(butylene succinate) blends,” *Polym. Compos.*, vol. 39, no. 9, pp. 3057–3065, 2018.

[141] X. Wang, Y. Zhuang, and L. Dong, “Study of carbon black-filled poly(butylene succinate)/polylactide blend,” *J. Appl. Polym. Sci.*, vol. 126, no. 6, pp. 1876–1884, 2012.

[142] P. M. Chou, M. Mariatti, A. Zulkifli, and S. Sreekantan, “Evaluation of the flexural properties and bioactivity of bioresorbable PLLA/PBSL/CNT and PLLA/PBSL/TiO 2 nanocomposites,” *Compos. Part B Eng.*, vol. 43, no. 3, pp. 1374–1381, 2012.

[143] X. Tian, H. Bai, T. Chen, S. Sang, H. Deng, and X. Jiang, “Poly(lactic acid)/poly (butylene succinate)/boron nitride nanosheet composites with

high thermal conductivity: a novel biodegradable electronic packaging material," *Polym. Bull.*, no. 0123456789, 2023.

[144] G. X. Chen, H. S. Kim, E. S. Kim, and J. S. Yoon, "Compatibilization-like effect of reactive organoclay on the poly(l-lactide)/poly(butylene succinate) blends," *Polymer (Guildf).*, vol. 46, no. 25, pp. 11829–11836, 2005.

[145] T. F. Scientific, "Safety Data Sheet - Nanoclay, Hydrophilic Bentonite," 2019.

[146] V. S. Subramaniam, "reduced graphene oxide," in *Catalysis from A to Z*, Wiley, 2020.

[147] BSI Standards Publication, "Plastics — Determination of tensile properties Part 2 : Test conditions for moulding and extrusion plastics," 2012.

[148] T. Y. Qiu, M. Song, and L. G. Zhao, "Testing, characterization and modelling of mechanical behaviour of poly (lactic-acid) and poly (butylene succinate) blends," *Mech. Adv. Mater. Mod. Process.*, vol. 2, no. 1, 2016.

[149] J. W. Gooch, Ed., "Hagen–Poiseuille equation BT - Encyclopedic Dictionary of Polymers," New York, NY: Springer New York, 2007, p. 477.

[150] S. Ansari, M. A. I. Rashid, P. R. Waghmare, and D. S. Nobes, "Measurement of the flow behavior index of Newtonian and shear-thinning fluids via analysis of the flow velocity characteristics in a mini-channel," *SN Appl. Sci.*, vol. 2, no. 11, pp. 1–15, 2020.

[151] A. Patti, S. Acierno, G. Cicala, and D. Acierno, "Predicting the Printability of Poly(Lactide) Acid Filaments in Fused Deposition Modeling (FDM) Technology: Rheological Measurements and Experimental Evidence," *ChemEngineering*, vol. 7, no. 1, p. 1, Dec. 2022.

[152] E. Chailleux, G. Ramond, C. Such, C. De, and L. Roche, "A mathematical-based master-curve construction method applied to complex modulus of bituminous materials A mathematical-based master-curve construction

method applied to complex modulus of bituminous materials," pp. 75–92, 2017.

[153] J. Teng *et al.*, "Confined crystallization of poly(butylene succinate) intercalated into organoclays: Role of surfactant polarity," *RSC Adv.*, vol. 6, no. 72, pp. 68072–68080, 2016.

[154] O. Mysiukiewicz, M. Barczewski, K. Skórczewska, and D. Matykiewicz, "Correlation between processing parameters and degradation of different polylactide grades during twin-screw extrusion," *Polymers (Basel).*, vol. 12, no. 6, Jun. 2020.

[155] M. L. Di Lorenzo, "Calorimetric analysis of the multiple melting behavior of poly(L-lactic acid)," *J. Appl. Polym. Sci.*, vol. 100, no. 4, pp. 3145–3151, May 2006.

[156] N. Hongsriphan, C. Kaew-ngam, P. Saengdet, and N. Kongtara, "Mechanical Enhancement of Biodegradable Poly(Butylene Succinate) by Biobased Polyamide11," *Eng. J.*, vol. 25, no. 2, pp. 295–304, Feb. 2021.

[157] W. A. White and E. Pichler, "Water-sorption characteristics of clay minerals," *Illinois State Geol. Surv.*, vol. 266, p. 20 p., 1959.

[158] D. B. França *et al.*, "The versatility of montmorillonite in water remediation using adsorption: Current studies and challenges in drug removal," *J. Environ. Chem. Eng.*, vol. 10, no. 2, p. 107341, 2022.

Appendix A

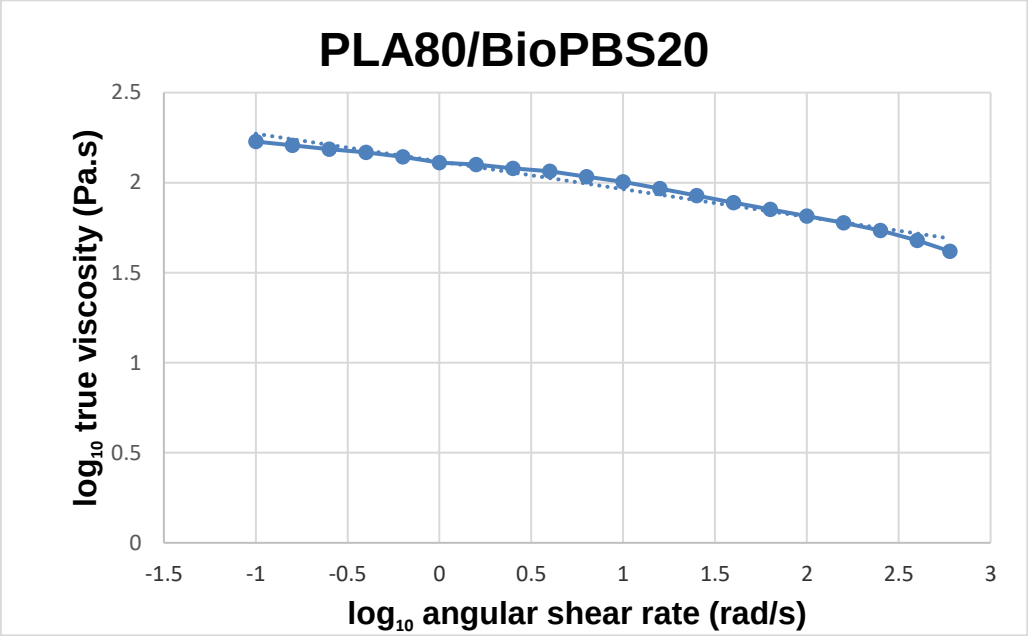

Figure 9-1 A.1 Log-log plots of angular shear rate against true viscosity for the fabricated composite at 210 °C.

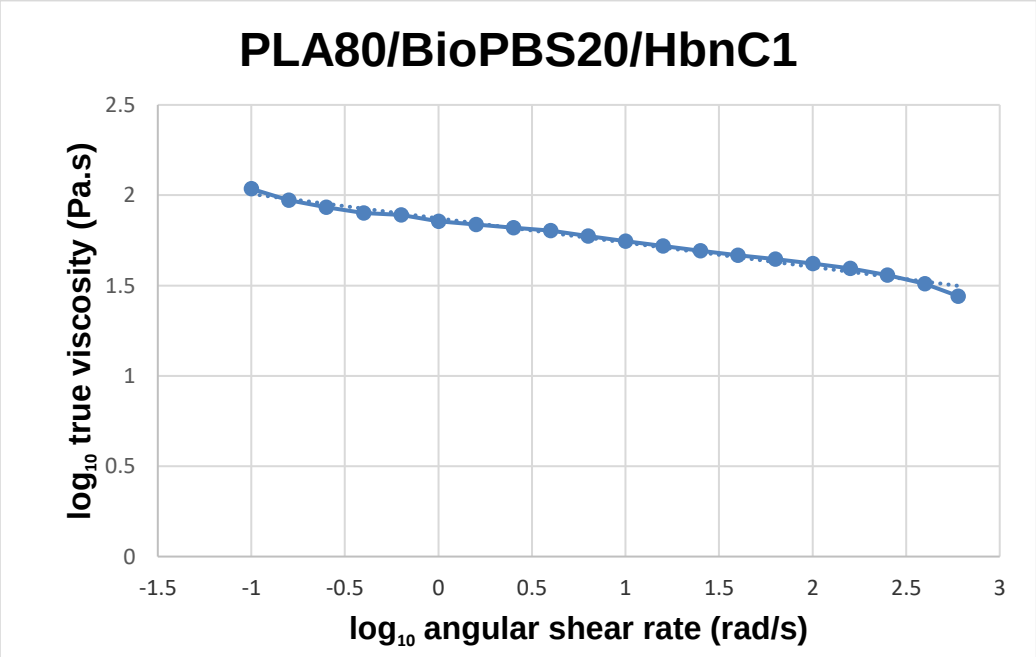

Figure 9-2 Log-log plots of angular shear rate against true viscosity for the fabricated composite at 210 °C.

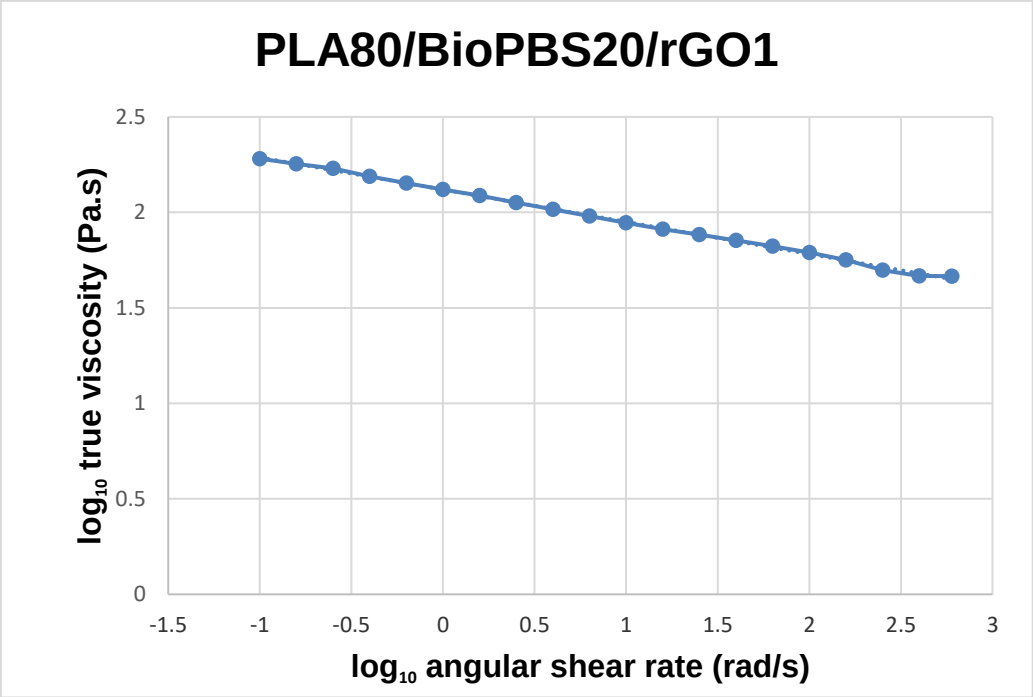

Figure 9-3 Log-log plots of angular shear rate against true viscosity for the fabricated composite at 210 °C.

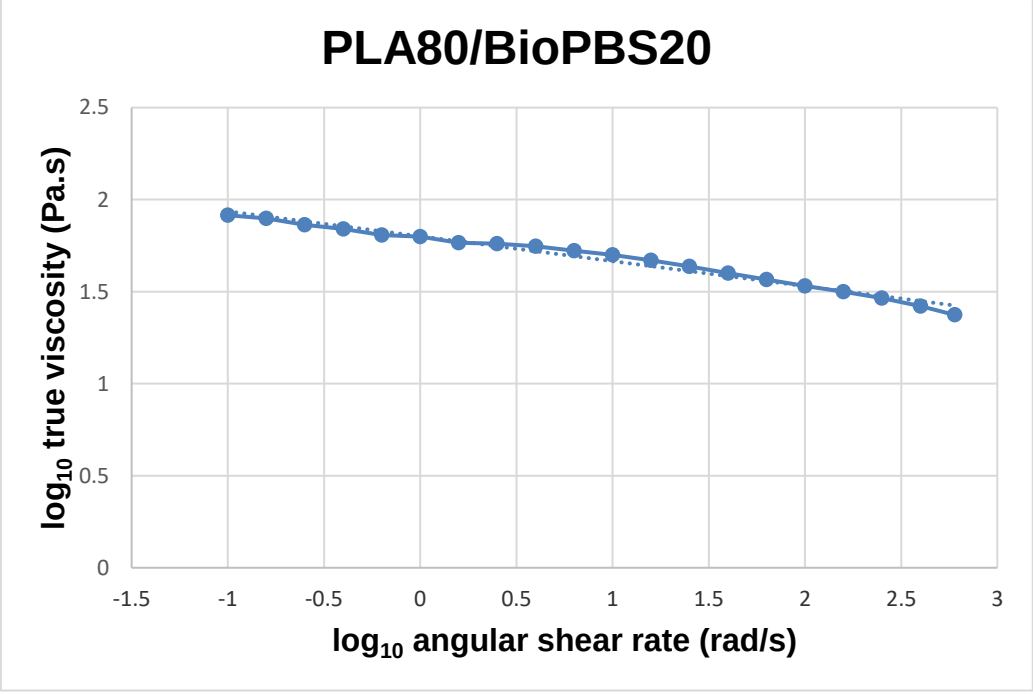

Figure 9-4 A.2 Log-log plots of angular shear rate against true viscosity for the fabricated composites at 220 °C.

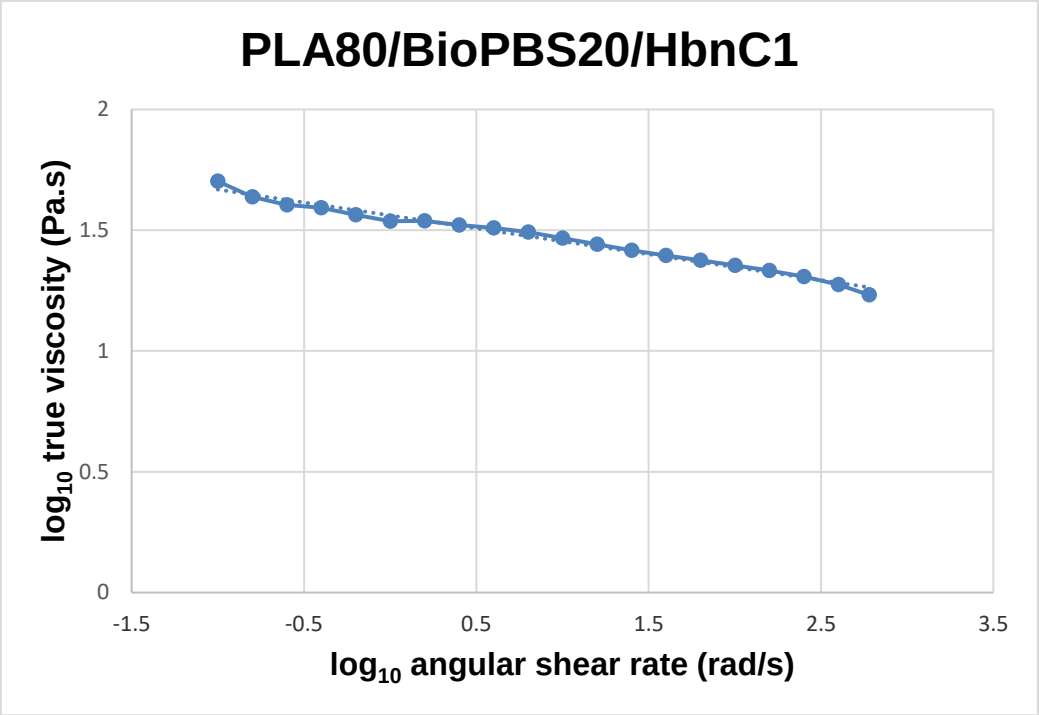

Figure 9-5 Log-log plots of angular shear rate against true viscosity for the fabricated composites at 220 °C.

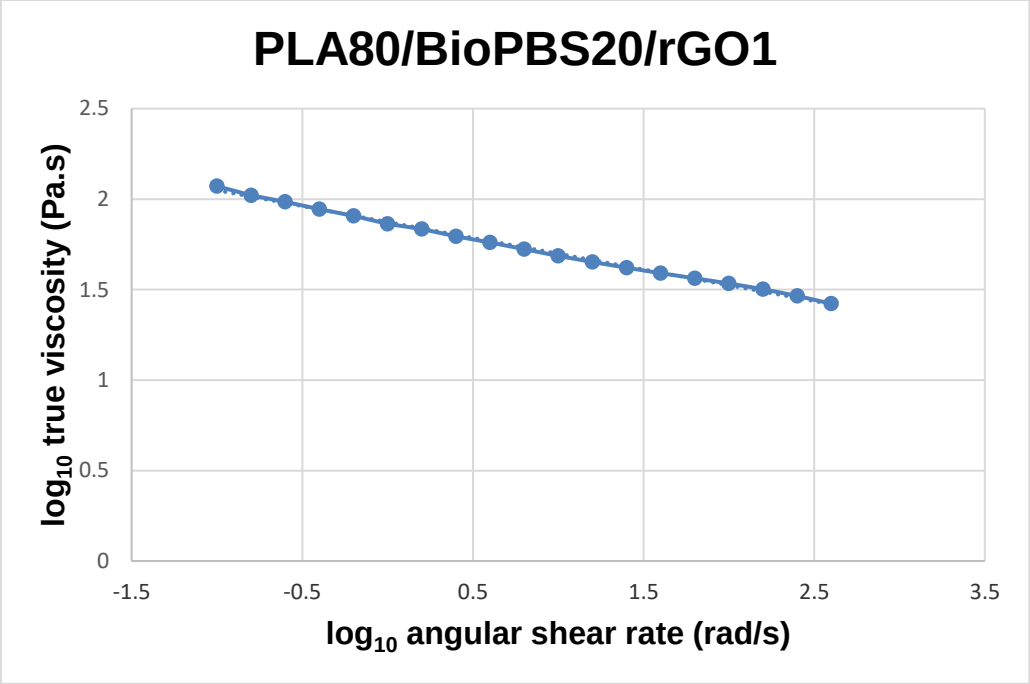

Figure 9-6 Log-log plots of angular shear rate against true viscosity for the fabricated composites at 220 °C.

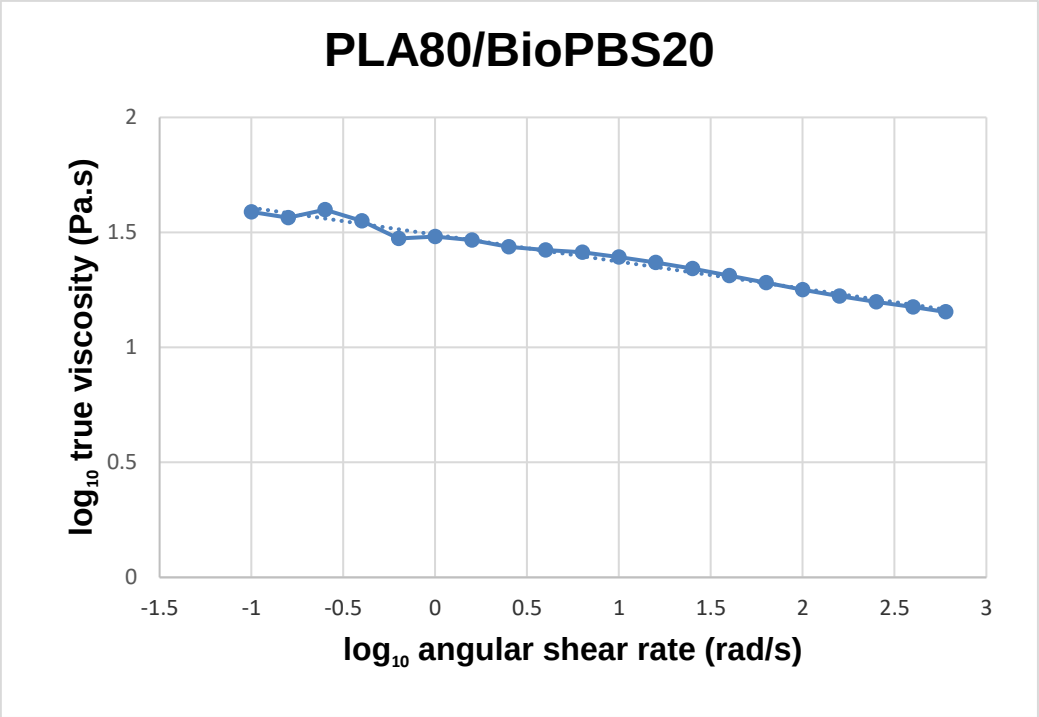

Figure 9-7 Log-log plots of angular shear rate against viscosity for the fabricated composites at 230 °C.

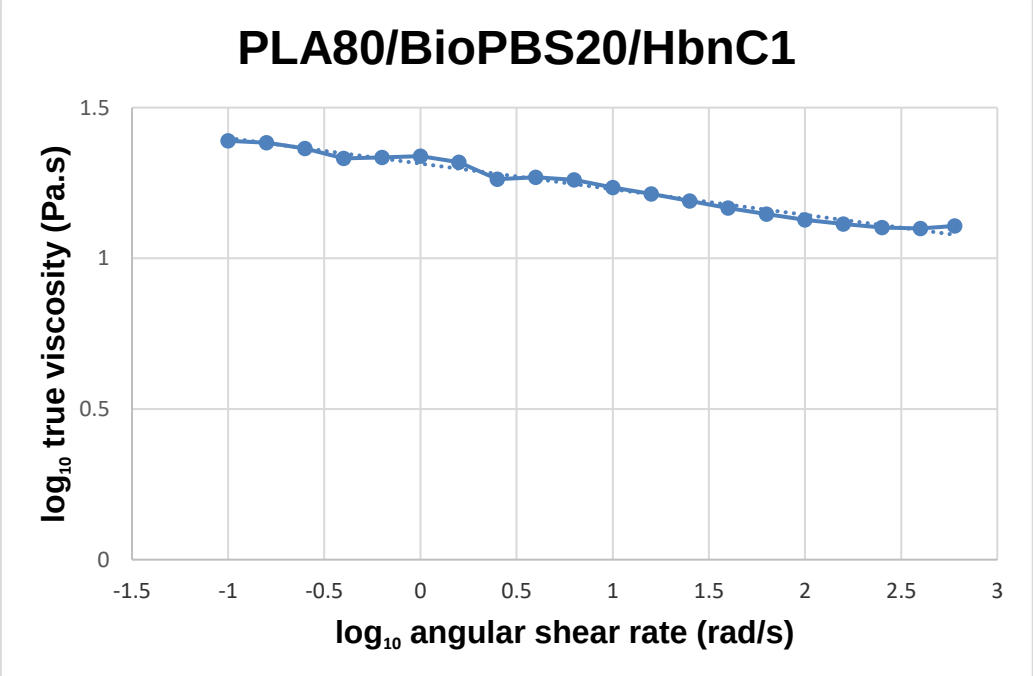

Figure 9-8 Log-log plots of angular shear rate against viscosity for the fabricated composites at 230 °C.

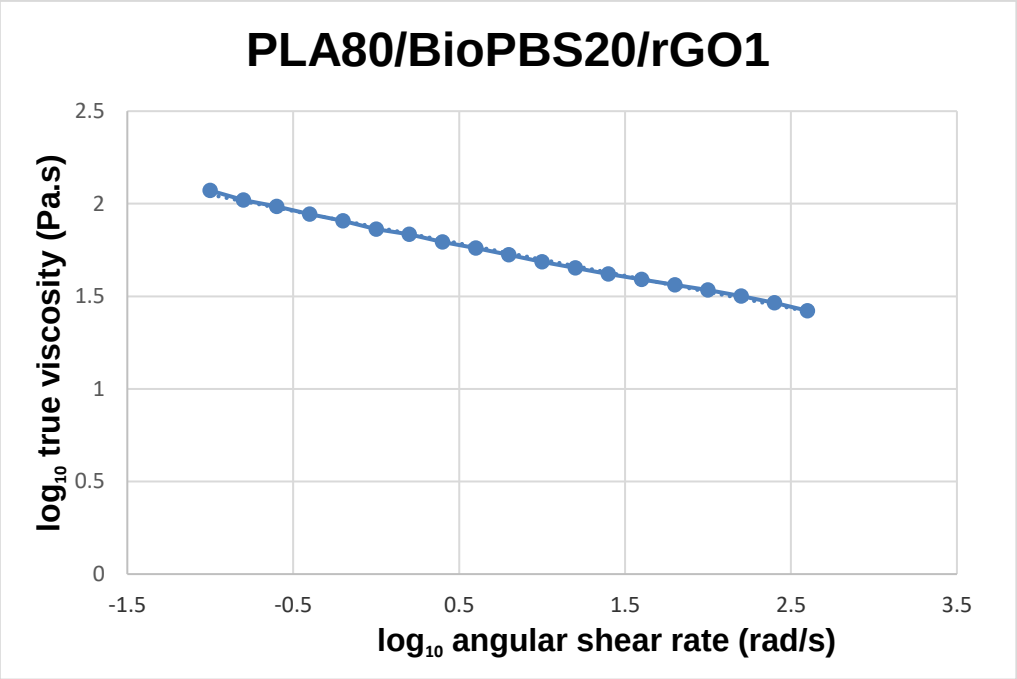

Figure 9-9 Log-log plots of angular shear rate against true viscosity for the fabricated composites at 230 °C.

Appendix B

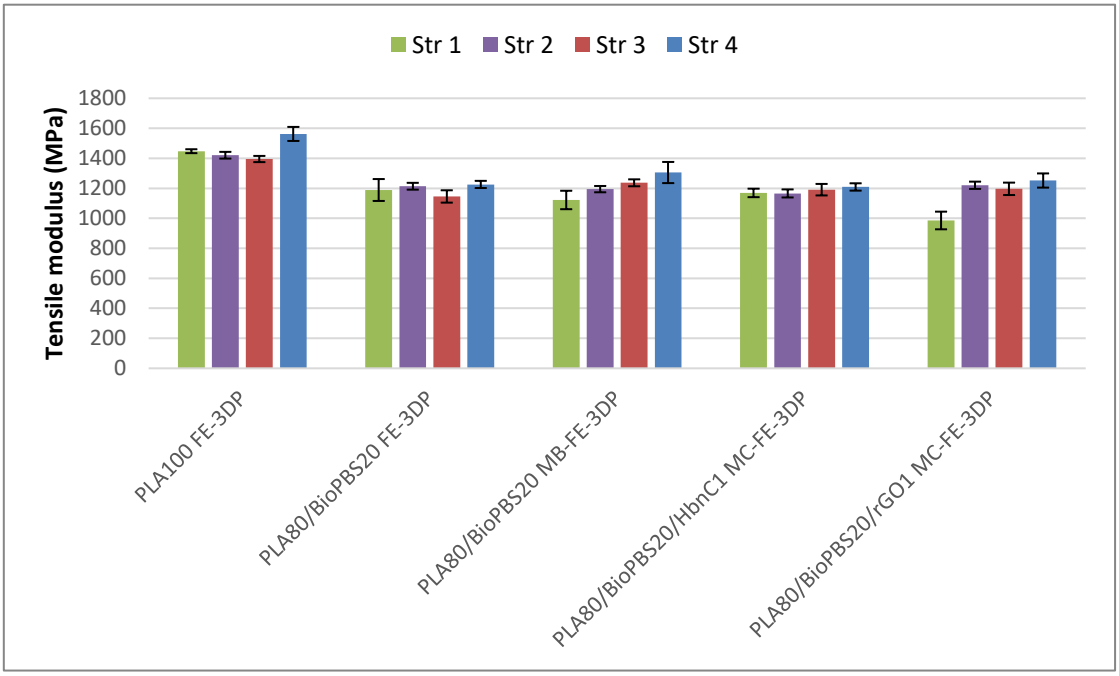

Figure 9-10 Tensile modulus of 3D-printed parts (by material category)

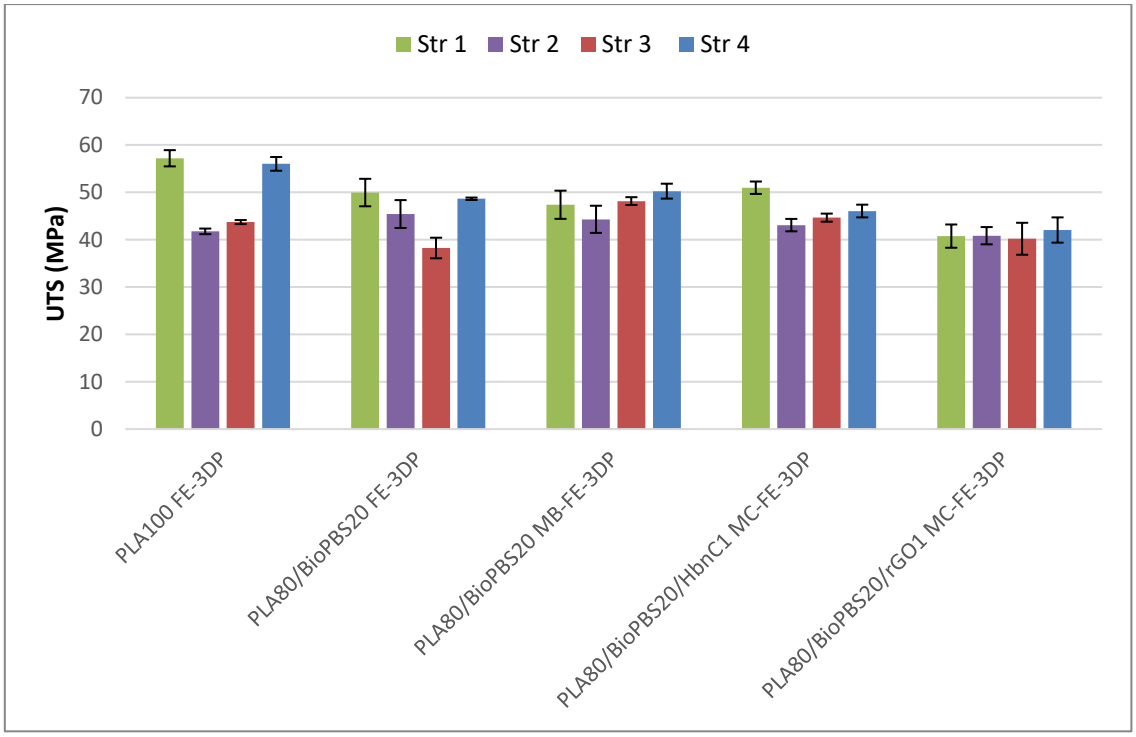

Figure 9-11 UTS of 3D-printed parts (by material category)

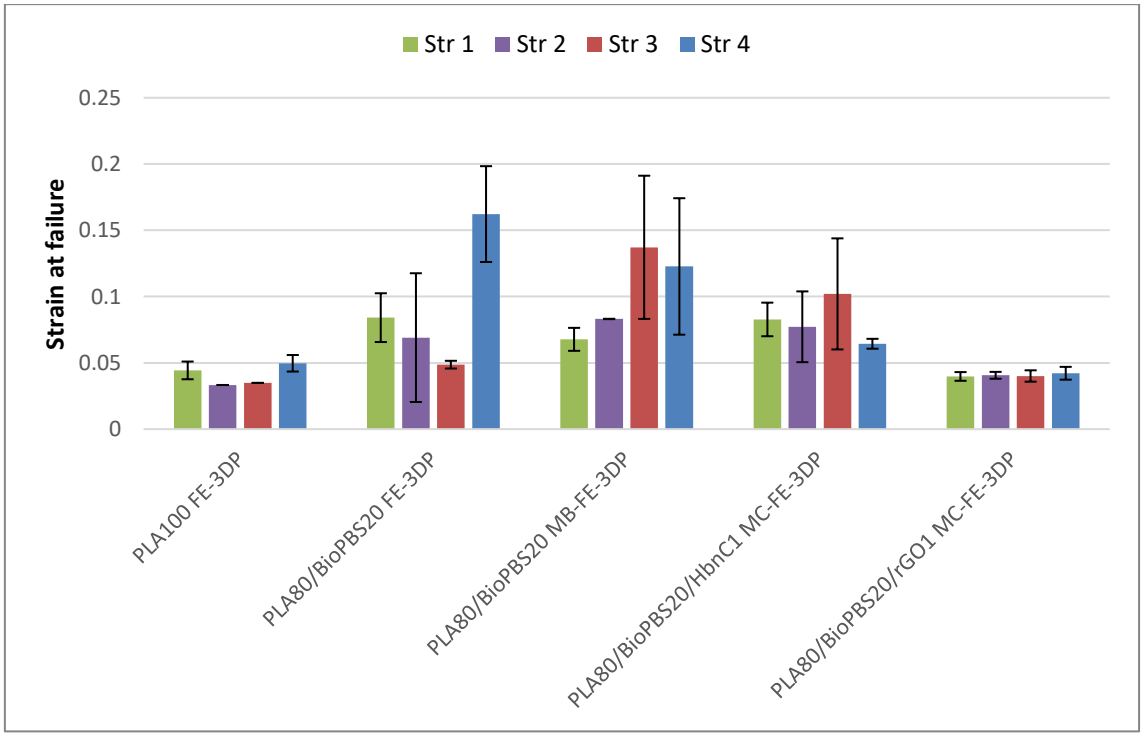

Figure 9-12 Strain at failure of 3D-printed parts (by material category)